Department of Materials Physics
UNIVERSIDAD DEL PAIS VASCO
THE UNIVERSITY OF THE BASQUE COUNTRY

eman ta zabal zazu

Universidad del País Vasco
Euskal Herriko Unibertsitatea

Theory of plasmon-enhanced spectroscopy of molecular excitations: infrared absorption, fluorescence, and Raman scattering

---

Thesis by
TOMÁŠ NEUMAN

for the degree of
DOCTOR OF PHILOSOPHY IN PHYSICS

Supervised by

Prof. Javier Aizpurua

Donostia-San Sebastián, Spain, October 2018

Acknowledgments

This thesis would never exist without my supervisor and advisor Javier Aizpurua, who has been guiding my steps through the jungle of academia already since five years ago. I thank Javier for his patience with me and for teaching me how to be a better scientist. I must also appreciate Javier's personal approach not just to me but to all members of the group.

We have spent long hours discussing with Ruben Esteban about physics and topics reaching beyond it. I thank Ruben for the time that he has invested into me and for his numerous advices and critical remarks. Often, Ruben has served as my unofficial supervisor.

I also had the opportunity to collaborate with many people both here in San Sebastian and abroad. I acknowledge Prof. Annemarie Pucci for giving me the opportunity to participate on projects regarding surface enhanced infrared spectroscopy and for hosting me in Heidelberg. I thank Garnett Bryant and Emily Townsend from NIST who hosted me there various times and who introduced me to the secrets of many-body theory of plasmons (and the vegetables garden at NIST). I also spent some time in Strasbourg in the group of Prof. Thomas Ebbesen. I thank all the members of Prof. Ebbesen's group for their hospitality. I acknowledge Prof. F. J. García-Vidal for bringing insight into the details of interaction between molecular excitons and plasmons. Here in San Sebastian I acknowledge Geza Giedke for long and constructive discussions about quantum optics, and David Casanova for discussions about quantum chemistry.

I thank all the people from our group, especially to my office mates, for creating such a friendly environment. We had many inspiring discussions with Mikolaj who now rides kangaroos in Australia, thanks Bruce! Gari has always been around and it was a pleasure for me to share with him so many trips to conferences where we enjoyed some fun together, thanks! Álvaro and Antton have brought into the group a fresh spirit, thanks for this guys!

Over the time I was lucky enough to meet a great amount of wonderful people who I thank for creating the friendly environment of the scientific community that we have here in Donostia. Thank you Andrea for your patience with me (I know, the kitchen!), for your support and friendship. I must also acknowledge Andrea for reading and commenting the thesis manuscript which was of great help. Many thanks to Berni, my (former) flatmate, friend, and binding element of the group here in Donostia. Without you Berni I would have never eaten as many txuletas!

Thanks to the Croatian gang, Ivor (I will always look at the ball) and Dino (the most random person ever). We have done some cycling and hiking with Fede, who has been a good friend to me all the time. Unai, and later Jose, convinced me to try climbing. We have played padel with the Croatians, Berni, Miguel, Unai, Julen and Mikel numerous times. Thanks guys! Lars, Divya, Malin, Chun Li, thanks for all the fun we had together!

Coffee and lunch breaks have been an important part of my (non) scientific activities here in CFM and over the years I had the opportunity to meet many people who were either visiting for a short while or working here or in the nearby centres. Thank you all for joining! I enjoyed deep philosophical debates that we used to have with Mathias and Moritz. It was also a pleasure for me to have been criticised by Miguel, in a milder form by Alba, and, as it became habitual, by everyone else, off course, always in a friendly spirit.

Last, I must acknowledge the firm support that I have always had from my family, even when I decided to live and study abroad. The rest in Czech: Děkuji rodičům za to, že mě podporovali po celou dobu studia, za to, že respektují a vždy respektovali má rozhodnutí, včetně toho odejít do zahraničí, a že i přes velkou vzdálenost, která nás dělí, nikdy nezapomněli zavolat a pohovořit si o novinkách života doma v Česku i tady ve Španělsku. Děkuji jim i bratrovi za to, že vždy vytvářeli rodinnu atmosféru, za to, že když jsem přijížděl domů, ač na krátkou dobu, vždy jsem cítil jejich lásku a péči. Mé díky patří i babičkám, které na mě vždy myslely, a které by mě jistě rády zásobily buchtami a koláči, ale velká vzdálenost jim to nedovolila. Děkuji vám všem za vaši trpělivost a pochopení, neb můj pobyt v zahraničí nedovoluje, abychom se viděli tak často, jak bychom si přáli.

Contents

I Methods 1

Resumen

Esta tesis aborda la cuestión de cómo la luz, o con más generalidad, la radiación electromagnética, interactúa con la materia. En nuestra vida cotidiana estamos rodeados de ondas electromagnéticas que cubren un amplio rango de energías desde las ondas de energías bajas, asociadas a las señales de radio, pasando por las microondas que calientan nuestra comida, y los rayos-x que ayudan a diagnosticar una pierna rota, hasta llegar a la luz que desvela la belleza del mundo a nuestros propios ojos. El ser humano ha sentido desde siempre fascinación por los milagros luminosos de la naturaleza que incluyen desde los agudos destellos producidos por descargas eléctricas en el cielo, hasta los relámpagos, o los colores vivos del arco iris. A lo largo de la historia, la humanidad ha desarrollado un control de la luz gracias a distintas herramientas ópticas que incluyen los telescopios que nos abren la puerta al universo, o los microscopios que nos permiten descifrar la intrincada estructura de la materia, base del mundo que nos rodea, así como de nosotros mismos.

El color de la luz, es decir, las propiedades de su espectro, no solo complace nuestra vista, sino que también permite analizar la estructura química de la materia mediante la espectroscopia. Tras iluminar una sustancia desconocida (la muestra), y detectar la luz transmitida o emitida para cada longitud de onda (color), es posible identificar las huellas espectrales características de los elementos químicos que constituyen dicha muestra, y de esta manera, descifrar la estructura de la misma. Por ejemplo, las vibraciones de las moléculas, al ser expuestas a radiación electromagnética, pueden absorber ondas infrarrojas (energía $\sim 100\,\mathrm{meV}$) o, al ser iluminadas con luz visible (energía $\sim 1\,\mathrm{eV}$), dar origen a picos de la señal vibracional tipo Raman en el espectro de dispersión. La materia iluminada también puede emitir fotones (fluorescencia) que encuentran aplicación en microscopía [1–3] y espectroscopia moderna [4], así como en campos más exóticos como la computación quántica.

Muchos de los logros de la óptica moderna y la espectroscopia de la luz son posibles gracias al hecho de que la luz interactúa con la materia. La refracción de la luz en el cristal de una lente óptica, al igual que el reflejo de la luz en un espejo encuentran sus orígenes en la escala microscópica, donde los electrones y los núcleos que forman la materia intercambian cuantos de energía con los fotones del campo electromagnético incidente y emitido. Con el desarrollo de la nanotecnología, ha sido posible lograr un control de la interacción entre la luz y la materia a una

escala menor que la longitud de onda de la luz visible ($\lambda_{\mathrm{vis}} \approx 400\,\mathrm{nm}$ - $700\,\mathrm{nm}$). Por ejemplo, la técnica de microscopía óptica de barrido por dispersión del campo cercano (s-SNOM) utiliza puntas metálicas de unos pocos nanómetros de radio que concentran el campo cercano de la luz por debajo del límite de difracción de Abbe, el límite teórico de los dispositivos ópticos habituales. Por otro lado, el desarrollo de metasuperficies con estructura nanométrica ha permitido manipular la fase de la luz de una manera controlada y, de este modo, construir dispositivos ópticos de dos dimensiones que presentan propiedades ópticas que a menudo superan las de los elementos ópticos convencionales [5].

Cuando la luz interactúa con los electrones de la banda de conducción de metales contenidos en nanopartículas de dimensiones que apenas alcanzan una fracción de su longitud de onda, la luz es capaz de excitar resonancias colectivas del gas electrónico en las interfases metal-aislante, conocidas como plasmones superficiales. Éstas resonancias constituyen oscilaciones de carga eléctrica en la superficie del metal que dan origen a campos electromagnéticos localizados en su proximidad. Los campos electromagnéticos asociados a estas resonancias presentan amplitudes especialmente intensas en ciertas regiones denominadas *hot spots* (puntos electromagnéticos calientes) que son m'as acusados, por ejemplo, en huecos estrechos entre las superficies de dos partículas cercanas, donde la interacción de Coulomb entre las densidades superficiales de carga de las dos partículas es más fuerte, produciendo, por tanto, una especial concentración de la carga plasmónica en dicha región (efecto nanoantena). Los plasmónes de estas antenas metálicas (partículas plasmónicas) [6] interactúan muy eficientemente con los fotones incidentes, y de esta manera, facilitan la interacción entre el haz de luz incidente y cualquier muestra (moléculas por ejemplo) localizada en la proximidad de la superficie de la antena. Este mecanismo de aumento de la señal da lugar, por ejemplo, a un aumento de la huella espectroscópica vibracional incluso de una sola molécula en la señal de dispersión Raman aumentada por superficie (SERS) [7–19] alcanzando varios órdenes de magnitud de aumento. El hallazgo del mecanismo de aumento electromagnético de la señal de SERS ha causado un gran desarrollo del campo de la plasmónica que, desde entonces, ha experimentado un gran auge. La capacidad de los plasmones de absorber la luz y producir calor ha logrado aplicaciones prácticas que incluyen la termoterapia inducida por plasmones, o el desarrollo de nuevos métodos de purificación del agua [20]. Se ha demostrado que la excitación de plasmones es capaz de provocar o inhibir reacciones químicas de moléculas situadas en las inmediaciones de superficies metálicas a través de varios mecanismos que incluyen el calentamiento local plasmónico, la generación de electrones calientes [21], o la modificación de la naturaleza de los estados quánticos de las moléculas tras el acoplamiento fuerte entre la luz y las nanopartículas metálicas [22].

Las partículas plasmónicas han sido diseñadas, entre otros, para mejorar el rendimiento de las espectroscopias ópticas e infrarrojas [23] como en SERS, en espectroscopia infrarroja aumentada por superficie (SEIRS) [24–39] o en fluorescencia aumentada por superficie (SEF). Aunque todas estas técnicas, SERS, SEIRS y SEF, aprovechan del aumento del campo cercano producido por las partículas plasmónicas, el aumento plasmónico desempeña en cada caso un papel diferente, que revisamos sucintamente a continuación.

En el caso de la técnica de SERS, las antenas plasmónicas simultáneamente actúan como (i) receptor de la radiación electromagnética, y (ii) emisor de la luz dispersada por las moléculas. Este mecanismo de dispersión resulta, por tanto, en un aumento total de la señal Raman producida en SERS, $\mathscr{R}_{\mathrm{St}}$, de la siguiente forma:

$$\mathscr{R}_{\mathrm{St}} \propto \underbrace{|f^{\mathrm{L}}_{\mathrm{inc}}|^2 |f^{\mathrm{St}}_{\mathrm{inc}}|^2}_{\substack{\text{Aumento}\\ \text{plasmónico}}} \times \underbrace{|E^{\mathrm{L}}_{\mathrm{inc}}|^2}_{\substack{\text{Intensidad}\\ \text{incidente}}} . \tag{1}$$

En la expresión anterior $f^{\mathrm{L}}_{\mathrm{inc}}$ y $f^{\mathrm{St}}_{\mathrm{inc}}$ son el aumento del campo eléctrico cercano producido por las antenas plasmónicas en la posición de la molécula a la frecuencia de la luz incidente y de la luz emitida, respectivamente, en forma de fotones Stokes de energía más baja (dispersodas inelásticamente), y $E^{\mathrm{L}}_{\mathrm{inc}}$ es el campo eléctrico asociado con la luz incidente.

En segundo lugar, en el caso de SEIRS, la situación es diferente a la de SERS, porque en la técnica de SEIRS la frecuencia del campo emitido por la muestra coincide con la del campo dispersado por la antena plasmonica (este caso se describe como dispersión elástica de la luz). Dado que la luz dispersada tanto por la antena como por la muestra llevan la misma frecuencia, no es posible discernir la señal de la antena de la señal originada por la muestra mediante métodos espectroscópicos como en SERS, sin embargo, el detector registra la señal compuesta por las dos contribuciones de manere combinada. Si la respuesta de la antena es conocida, las huellas espectrales de la muestra aparecen encima de las de la antena en forma de interferencia que puede reducir o aumentar la señal detectada, dependiendo de las condiciones de la interacción. Se puede demostrar que las huellas específicas de la muestra que aparecen en la señal, $\mathscr{A}_{AS}$, registrada en el detector, pueden ser expresadas de la siguiente forma:

$$\mathscr{A}_{AS} \propto \underbrace{|f^{\mathrm{L}}_{\mathrm{pl}}|^2}_{\substack{\text{Aumento}\\ \text{plasmónico}}} \times \underbrace{|E^{\mathrm{L}}_{\mathrm{inc}}|^2}_{\substack{\text{Intensidad}\\ \text{incidente}}} , \tag{2}$$

donde $f^{\mathrm{L}}_{\mathrm{pl}}$ es el aumento del campo cercano plasmónico responsable de la interacción entre la antena y la muestra.

Finalmente, la técnica de SEF es diferente a las descritas anteriormente ya que la excitación de los estados electrónicos de la molécula en este caso, no tiene por qué tener un origen óptico, es decir, la luz emitida puede resultar de la excitación puramente eléctrica de un estado electrónico molecular [40]. En el marco de la física quántica, una vez excitado, el estado electrónico de la molécula comienza a decaer y, durante ese proceso, es capaz de excitar los estados de los modos electromagnéticos de la luz y de los plasmones de las estructuras metálicas cercanas a la molécula. Cuantos más estados electromagnéticos interactúen con la transición electrónica de la molécula, más alto es el ritmo de decaimiento del estado excitado.

Los plasmones pueden acelerar este proceso de decaimiento de una manera muy eficiente gracias al aumento del campo cercano, que crea un entorno con alta densidad local de estados electromagnéticos (LDOS).

Pese a la rapidez de la transferencia de energía de la excitación molecular a los plasmones, no toda la energía se transforma en luz emitida hacia el campo lejano donde pueda ser detectada. Gran parte de dicha energía se pierde por culpa del decaimiento plasmónico no-radiativo que la convierte en calor producido en el metal. Por tanto, durante el diseño de las estructuras plasmónicas para su utilización en SEF, es imprescindible no sólo optimizar el aumento del decaimiento electrónico, sino también procurar evitar las pérdidas plasmónicas.

En esta tesis se abordan varios aspectos de la interacción entre plasmones y excitaciones moleculares con énfasis en la espectroscopia aumentada por los plasmones. En la Parte I de la tesis se establece la base teórica tanto de la descripción quántica, así como de la clásica, de las excitaciones estudiadas. Esta parte también dedica un apartado importante a la introducción de la teoría de sistemas quánticos abiertos que son ampliamente aplicados en los capítulos posteriores de la tesis.

En la Parte II de la tesis se desarrolla y utiliza la teoría dieléctrica clásica más allá de lo introducido en la Parte I referente a la metodología en el contexto de la espectroscopia infrarroja, SEIRS. Se presenta un modelo analítico sencillo, pero muy útil, para describir la interacción entre el modo plasmónico de una antena metálica y una excitación vibracional molecular en muestras situadas encima de la superficie de la antena. Se analiza el espectro de extinción de la radiación infrarroja de dicho sistema (habitualmente medido en modo de transmisión) separando las contribuciones que provienen de la dispersión y de la absorción del haz incidente. Así mismo, se explora cómo el contraste de las huellas espectroscópicas de las moléculas viene determinado por la absorción y la dispersión de la radiación en la plataforma plasmónica, es decir, la antena. Las antenas más grandes son capaces de dispersar la radiación de manera más eficaz de lo que la absorben, por lo que en esta parte, se diseña una serie de antenas lineales de diámetros y longitudes diferentes, de manera que la resonancia dipolar de éstas se encuentre a la misma frecuencia que la excitación vibracional, y se estudia la respuesta espectral tanto de la antena cubierta con las moléculas como sin ellas. De manera notable, se demuestra empíricamente que los sustratos formados por antenas que dispersan y absorben la radiación con eficiencias parecidas proporcionan el contraste óptimo de las huellas espectroscópicas de la muestra [37]. Este resultado tiene una importancia práctica para el diseño de los sustratos plasmónicos de cara a su utilización en SEIRS.

En la Parte III se estudia la interacción entre plasmones localizados y excitaciones electrónicas en moléculas localizadas en la proximidad de antenas metálicas. En el Capítulo 5 se examinan los detalles microscópicos del acoplamiento entre plasmones de partículas metálicas, capaces de localizar el campo electromagnético en la escala de un solo átomo, y las excitaciones moleculares. En esta situación se cuestiona la aproximación por la que la molécula se describe como un dipolo puntual que interactúa con el campo electromagnético de la cavidad, considerado a su vez homogéneo a lo largo de toda la extensión espacial de la molécula. Se identifican situaciones en las que la descripción puntual de la molécula no resulta válida y se muestra cómo se puede aprovechar esta situación para obtener más información sobre las moléculas. Por ejemplo, se pueden poner las moléculas objeto de estudio en proximidad a la punta de un microscopio de efecto túnel de modo que la punta del microscopio y el sustrato formen una cavidad plasmónica. De esta manera, mediante el desplazamiento de la punta respeto a la molécula y la medición de la respuesta óptica de la cavidad, esta configuración puede proporcionar información espacial sobre el acoplamiento plasmón-exciton de alta resolución, y de esa manera, permitir ver la estructura de la distribución de carga asociada con dicha excitación molecular. Finalmente, se muestra teóricamente que la inhomogeneidad de los campos electromagnéticos puede dar lugar a una ruptura de las reglas de selección ópticas, y hacer que las transiciones electrónicas moleculares de carácter cuadrupolar interactúen con la luz.

Si el acoplamiento entre las excitaciones de las moléculas y los plasmones supera las perdidas intrínsecas del metal y de las excitaciones de la molécula, los plasmones y los excitones forman nuevas excitaciones híbridas, llamadas polaritones (o plexcitones). Los polaritones han atraído mucho interés por sus propiedades especiales que permiten, entre otras, la transferencia de energía a larga distancia, la condensación de excitaciones, la emisión estimulada, y la generación de reacciones químicas. En el Capítulo 6 se hace un estudio de la emisión de luz originada por los polaritones previamente excitados con un láser monocromático. En este capítulo se demuestra teóricamente la importancia de la interacción entre los polaritones y las vibraciones internas de las moléculas, demostrando que las vibraciones dan lugar a una transferencia incoherente de energía entre los polaritones, y por tanto a una población incoherente predominante de los polaritónes de baja energía. Como consecuencia de este hecho, los espectros de luz emitida por polaritones plasmon-excitón muestran con frecuencia una asimetría espectral, tal y como se demuestra en varios experimentos.

Las vibraciones moleculares pueden desarrollar un papel activo, que va más allá del rol pasivo discutido anteriormente, por ejemplo en la inducción de reacciones químicas. Es, por tanto, deseable controlar de manera activa el estado de las vibraciones moleculares. En la Parte IV (Capítulo 7) de la tesis se explora el posible uso del mecanismo de espectroscopia de dispersión Raman aumentada por superficie como herramienta que permita controlar las vibraciones moleculares. Para describir teóricamente la dinámica del proceso Raman, así como la dinámica de las vibraciones, se adoptan métodos de la optomecánica cuántica, centrándonos en el régimen en el que la molécula es estimulada por un láser resonante con una de sus transiciones electrónicas - proceso Raman resonante. Se identifican las condiciones de iluminación externa que resultan en un aumento de las poblaciones de las vibraciones mediante el proceso de estimulación optomecánica. En el régimen resonante, dicho proceso puede ser selectivo con respeto a la energía de las vibraciones moleculares, por tanto, el proceso Raman resonante puede posibilitar el control selectivo de una vibración molecular específica deseada, y dar lugar a un aumento de su población para, de esta manera, influir en su reactividad química. Los procesos optomecánicos dejan sus huellas en los espectros de luz inelásticamente dispersada, por ello, en el Capítulo 7 de la tesis, se elabora una descripción teórica detallada de los espectros de luz emitida por estos sistemas y se identifican efectos novedosos de interferencia e incluso de división de los picos de los espectros. Por último, la tesis aborda la descripción de situaciones más exóticas en las que la estructura electrónica de la molécula es modificada por un láser intenso, o debido al acoplamiento fuerte entre el excitón molecular y el plasmón de la partícula metálica. En estas situaciones la modificación de la estructura electrónica de la molécula induce la interacción electrón-vibración en la misma, la cual puede ser interpretada como una ruptura de la aproximación de Born-Oppenheimer con la consiguiente influencia en la reactividad química del sistema.

En resumen, los capítulos de esta tesis tratan sobre la interacción entre las excitaciones moleculares, los plasmones y la radiación electromagnética, en un amplio abanico de situaciones que incluyen la interacción entre vibraciones moleculares y radiación infrarroja, así como la excitación y emisión de transiciones electrónicas en moléculas colorantes. Para describir la interacción luz-materia se desarrollan tanto herramientas clásicas como la teoría cuántica. Algunos resultados de esta tesis, tales como la optimización de la señal producida en la espectroscopia infrarroja aumentada por superficie, tienen importancia práctica directa, otros resultados apuntan a aspectos más fundamentes de la interacción entre luz y materia. Los detalles de la compleja dinámica de las vibraciones moleculares bajo estimulación óptica, o la dinámica de la emisión de luz involucrando los estados híbridos de luz y materia, es decir, los polaritones, pueden servir como claros ejemplos de este último aspecto. Los resultados de esta tesis aspiran a servir como inspiración de futura investigación teórica y experimental adicional sobre los fenómenos en ella descritos.

Introduction

The question of how light (or more generally electromagnetic radiation) interacts with matter is the focus of this thesis. In everyday life, we all are immersed in a sea of electromagnetic radiation ranging from low-energy waves that carry radio signals, through electromagnetic microwaves that heat up our food, x-rays that help to diagnose a broken bone, to visible light that reveals the beauties of the world to our naked eye. We have always been fascinated by the sharp flashes of light produced by lightnings or by the colourful spectrum of rainbow. In the course of time we have learned how to tame light by means of optical instruments such as telescopes, opening the gates of the universe, or microscopes which help us to understand the intriguing microscopic structure of matter forming the world around us and even ourselves.

The color of light, its spectral properties, not only please our eye but also help us to analyse the chemical nature of matter by means of spectroscopy. By shining light on an unknown chemical substance (sample) and collecting the emitted or transmitted light, it is possible to identify characteristic spectral fingerprints that reveal the sample's chemical structure [see Fig.1 with typical descriptions and the corresponding information attainable]. For example, molecular vibrations can result in absorption of electromagnetic radiation at the infrared end of the electromagnetic spectrum (energy $\sim$ 100 meV) or give rise to Raman peaks when illuminated by a coherent monochromatic visible laser (energy $\sim$ 1 eV). Upon illumination, matter can also emit fluorescence photons which find their application in modern microscopy [1–3], spectroscopy [4], and due to its unique properties, also in more exotic fields such as quantum computing.

All of the achievements of modern optics and light spectroscopy are possible owing to the fact that light interacts with matter. Light refraction on the glass of an optical lens as well as reflection of light by a mirror find their origins at the microscopic level, where the electrons and nuclei forming the matter interchange their energy with photons of the incident and emitted radiation. With the rise of nanotechnology, technologists have learnt how to engineer the light-matter interaction on scales much smaller than the wavelength of the visible light ($\lambda_{\text{vis}} \approx 400\,\text{nm}$ - $700\,\text{nm}$). For example, a technique called scanning near-field optical microscopy (SNOM) [41, 42] utilizes nanometrically sharp tips to focus light down to the level of a few tens of nanometers and thus to break the Abbe's diffraction limit that constraints conventional optical devices. The development of

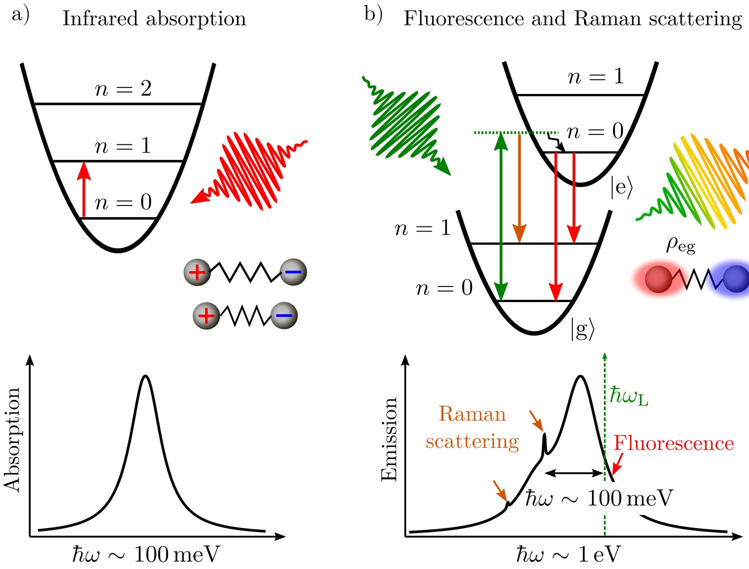

Figure 1: Schematic depiction of excitations in molecules studied in the thesis. (a) Molecular vibrations can be described as the (quantized) harmonic motion of nuclei on top of a parabolic potential determined by the electronic state of the molecule. The vibrational states are then characterised by a spectrum of equidistantly spaced vibrational energies for each n vibrational quanta. When such an infrared active vibration is illuminated, the radiation is resonantly absorbed at an energy of $\sim 100\,\mathrm{meV}$, resulting in a characteristic fingerprint spectral absorption peak. (b) A more complex picture of molecular electronic and vibrational states. Each electronic state, $|\mathrm{g}\rangle$ (the ground state) and $|\mathrm{e}\rangle$ (the excited state), support vibrational excitations. Upon illumination the molecule is excited and elastically and inelastically emits light. The inelastic light emission thus contains fluorescence (usually spectrally broad) and Raman scattering appearing as sharp peaks.

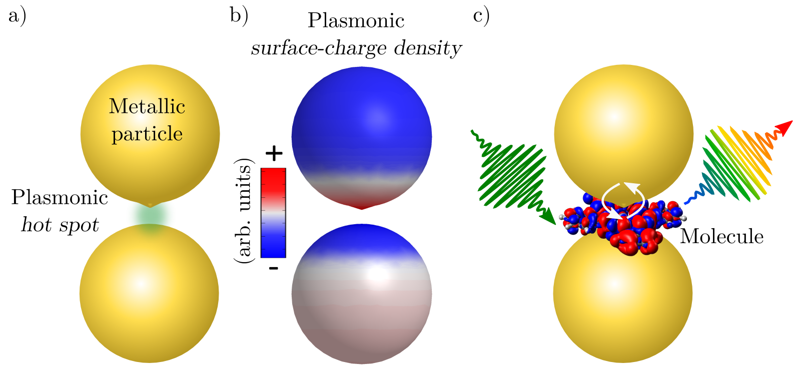

Figure 2: Conduction electrons of metallic particles are able to sustain surface plasmon excitations. (a) A dimer of metallic particles with a narrow gap formed between them. In the gap, the plasmonic fields are highly concentrated, forming a plasmonic *hot spot*. (b) Surface-charge distribution of a bonding-dipole surface plasmon of the particle dimer shown in non-linear scale. (c) Surface plasmons are able to enhance interaction of incident light (green arrow) with a molecule (white arrows) and modify the absorption or emission (rainbow-colored arrow) of the molecule.

nanostructured metasurfaces has allowed for manipulating the phase of light in a highly controlled manner and thus has enabled the construction of two-dimensional optical devices with unique focusing and spectral properties that are difficult to achieve by conventional means [5].

When light interacts with electrons of metals contained in the form of small particles of dimensions smaller than the wavelength of light, it can resonantly excite collective electronic excitations so-called surface plasmons (or surface plasmon polaritons). Surface plasmons carry strong oscillating electric charge at the surface of the metallic particle which induces highly localized electromagnetic near fields. The plasmonic field can be especially strong in the so-called *hot spots* formed in gaps between metallic nanoparticles, where the plasmonic surface charge is concentrated due to the inter-particle Coulomb interaction [Fig. 2 (a,b)]. The surface plasmons of such metallic *nanoantennas* (or plasmonic particles) [6] also efficiently interact with incident photons and thus facilitate efficient interaction between the incident light and samples placed in the vicinity of the antenna's surfaces. This mechanism, among others, has been recognised to enhance the spectroscopic fingerprint signal of even single molecules in surface-enhanced Raman scattering (SERS) spectroscopy [7–19] by many orders of magnitude. The discovery of SERS has led to a boom in the field of plasmonics, which, since that time, has undergone a rapid development. The ability of plasmonic particles to absorb light and produce heat has also led to practical thermal applications including novel plasmon-based cancer thermo-therapy [43] or water purification methods [20]. It has been shown that plasmons are also able to trigger or inhibit chemical reactions of molecules placed onto metallic surfaces by various mechanisms including local plasmonic heating, generation of hot electrons [21] or by changing the nature of the molecular states themselves via strong light-matter coupling [22].

Among others, plasmonics particles have been engineered to improve the performance of optical and infrared spectroscopies [23], such as in SERS, in surface-enhanced infrared spectroscopy (SEIRS) [24–39] or in surface-enhanced fluorescence (SEF) [44–48]. Although SERS, SEIRS and SEF all exploit the effect of near-field enhancement due to the plasmonic particles, the role of the plasmonic enhancement is different in each case:

Surface-enhanced Raman scattering (SERS): In SERS the plasmons of a metallic particle play the simultaneous role of (i) a receiver that is able to enhance the electric field of the incident light, $E^{\mathrm{L}}_{\mathrm{inc}}$, and thus efficiently excite a molecule attached to the particle's surface via its near field $E_{\mathrm{NF}} = f^{\mathrm{L}}_{\mathrm{pl}} E^{\mathrm{L}}_{\mathrm{inc}}$ ($f^{\mathrm{L}}_{\mathrm{pl}}$ being the plasmonic enhancement factor), and (ii) an efficient transmitter of the Raman photons generated in the molecule to the detector [see Fig. 3 (a)]. In particular, using a simplified qualitative classical picture, the plasmonic near field, $E^{(0)}_{\mathrm{NF}} \cos(\omega_{\mathrm{L}} t)$, at angular frequency ω_{L} induces a dipole moment, d_{tot}, in the molecule as:

$$d_{\mathrm{tot}} = \alpha_{\mathrm{mol}} E^{(0)}_{\mathrm{NF}} \cos(\omega_{\mathrm{L}} t), \tag{3}$$

where $\alpha_{\mathrm{mol}} = \alpha_{\mathrm{mol}}(q)$ is the molecular polarizability, which generally depends on the time-harmonic vibrational coordinate of the molecule, $q(t) = q_0 \cos(\Omega t)$, with Ω the vibrational frequency and q_0 the vibrational amplitude. The molecule's polarizability can be expanded to the first order in q to yield

$$\begin{aligned} d_{\mathrm{tot}} &\approx \alpha_{\mathrm{mol}}(0) E^{(0)}_{\mathrm{NF}} \cos(\omega_{\mathrm{L}} t) + \left.\frac{\partial \alpha_{\mathrm{mol}}}{\partial q}\right|_{q=0} q_0 \cos(\Omega t) E^{(0)}_{\mathrm{NF}} \cos(\omega_{\mathrm{L}} t) \\ &= \underbrace{\alpha_{\mathrm{mol}}(0) E^{(0)}_{\mathrm{NF}} \cos(\omega_{\mathrm{L}} t)}_{d_{\mathrm{Ray}}} \\ &+ \underbrace{\frac{1}{2}\frac{\partial \alpha_{\mathrm{mol}}}{\partial q} q_0 \cos[(\omega_{\mathrm{L}} - \Omega)t] E^{(0)}_{\mathrm{NF}}}_{d_{\mathrm{St}}} \\ &+ \underbrace{\frac{1}{2}\frac{\partial \alpha_{\mathrm{mol}}}{\partial q} q_0 \cos[(\omega_{\mathrm{L}} + \Omega)t] E^{(0)}_{\mathrm{NF}}}_{d_{\mathrm{aSt}}} . \end{aligned} \tag{4}$$

The induced dipole moment can be split into the elastic Rayleigh contribution, d_{Ray}, the Raman-Stokes contribution, d_{St}, oscillating at Raman-Stokes frequency $\omega_{\mathrm{St}} = \omega_{\mathrm{L}} - \Omega$, and the Raman-anti-Stokes contribution, d_{aSt}, oscillating at Raman-anti-Stokes frequency $\omega_{\mathrm{aSt}} = \omega_{\mathrm{L}} + \Omega$. Further on we are going to concentrate on the case of the Raman-Stokes scattering that is usually used for spectral fingerprinting. In this classical picture, the Raman dipole d_{St} radiates photons at the Raman-Stokes frequency to the detector via the plasmonic antenna. Using the reciprocity theorem of electromagnetism it can be shown that the amplitude of the far-field radiation, $E_{\mathrm{FF}}^{\mathrm{St}}$, is proportional to

$$E_{\mathrm{FF}}^{\mathrm{St}} \propto d_{\mathrm{St}} E_{\mathrm{NF}}^{\mathrm{St}}, \tag{5}$$

where $E_{\mathrm{NF}}^{\mathrm{St}} = f_{\mathrm{pl}}^{\mathrm{St}} E_{\mathrm{inc}}^{\mathrm{St}}$ (with $f_{\mathrm{pl}}^{\mathrm{St}}$ the respective plasmonic enhancement) is the near field of the plasmonic antenna produced by a virtual source placed in the far-field position of interest (the detector's position) radiating at frequency ω_{St} an electromagnetic field of incident amplitude $E_{\mathrm{inc}}^{\mathrm{St}}$. Finally, the measurable Raman-Stokes signal, $\mathscr{R}_{\mathrm{St}}$, is proportional to the square of the far-field amplitude, $\mathscr{R}_{\mathrm{St}} \propto |E_{\mathrm{FF}}^{\mathrm{St}}|^2$, which yields the following expression for the signal:

$$\mathscr{R}_{\mathrm{St}} \propto \underbrace{|f_{\mathrm{pl}}^{\mathrm{L}}|^2 |f_{\mathrm{pl}}^{\mathrm{St}}|^2}_{\substack{\text{Plasmonic}\\ \text{enhancement}}} \times \underbrace{|E_{\mathrm{inc}}^{\mathrm{L}}|^2}_{\substack{\text{Incident}\\ \text{intensity}}}. \tag{6}$$

The signal thus approximately scales with the intensity of the incident laser as $|E_{\mathrm{inc}}^{\mathrm{L}}|^2$ and is enhanced with respect to the signal obtained from the molecule in vacuum by a factor of $|f_{\mathrm{pl}}^{\mathrm{L}}|^2 |f_{\mathrm{pl}}^{\mathrm{St}}|^2$. Often the field enhancement at the Raman frequency is approximated as $f_{\mathrm{pl}}^{\mathrm{St}} \approx f_{\mathrm{pl}}^{\mathrm{L}}$, which yields the standard fourth-power dependence of the SERS electromagnetic enhancement, often cited in the literature [11]. Last, we note that the classical analysis of SERS outlined above fails to correctly address various aspects of the Raman process, such as the intensity-dependence of the anti-Stokes Raman signal, for which a full quantum theory is needed. We further develop the theory of SERS in Part IV of the thesis.

Surface-enhanced infrared spectroscopy (SEIRS): SEIRS is a method that relies on spectral analysis of elastically scattered (transmitted) electromagnetic radiation from a system composed of a plasmonic antenna and an infrared-active sample placed on the antenna's surface. Upon illumination, the incident electromagnetic field undergoes a complex multiple scattering process between the antenna and the sample, and is finally scattered into the far-field region where it is detected [see Fig. 3 (b)]. In the language of mathematics, the incident field $E_{\mathrm{inc}}^{\mathrm{L}}$ interacts with the antenna-sample system and induces a dipole moment in the antenna which then radiates the electromagnetic field of amplitude E_{A} into the far field. Let us decompose the total amplitude E_{A} into the contribution that would be induced by the incident light if no sample were present, E_{BG}, and the amplitude arising purely due to the complex antenna-sample interaction, $E_{\mathrm{AS}} = E_{\mathrm{A}} - E_{\mathrm{BG}}$, so that $E_{\mathrm{A}} = E_{\mathrm{BG}} + E_{\mathrm{AS}}$. The signal measured in the far field is then proportional to the square of the scattered amplitude as:

$$\mathscr{A} \propto |E_{\mathrm{A}}|^2 \approx \underbrace{|E_{\mathrm{BG}}|^2}_{\mathscr{A}_{\mathrm{BG}}} + \underbrace{2\mathrm{Re}\{E_{\mathrm{BG}} E_{\mathrm{AS}}^{*}\}}_{\mathscr{A}_{\mathrm{AS}}}, \tag{7}$$

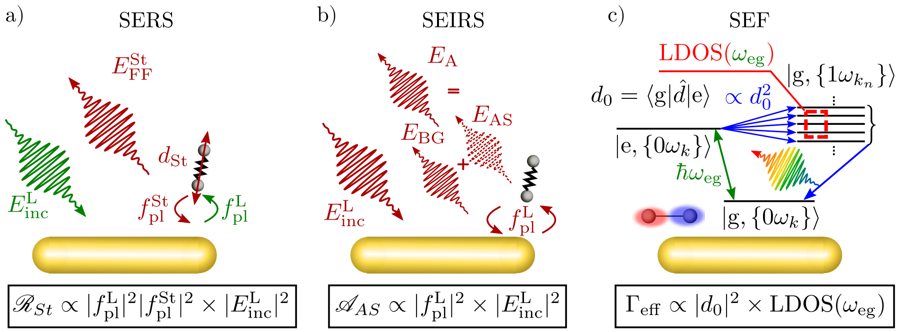

Figure 3: Schematics of the mechanisms of plasmon-enhanced processes: (a) SERS, (b) SEIRS, and (c) SEF. (a) In SERS the incident light, E_{inc}, stimulates plasmon-enhanced excitation of the Raman-Stokes dipole, d_{St}, in the molecule. This induced dipole then radiates the Raman-Stokes field, $E_{\mathrm{FF}}^{\mathrm{St}}$, via the plasmonic antenna into the far field. (b) In SEIRS the incident field induces a dipole moment in the antenna-sample (molecule) system. The induced dipole then radiates into the far field the amplitude $E_{\mathrm{A}} = E_{\mathrm{BG}} + E_{\mathrm{AS}}$. E_{A} can be decomposed into the background contribution E_{BG} arising purely due to scattering of the radiation off the antenna, and E_{AS} containing all the effects of the sample. (c) A molecule composed of an electronic ground, $|\mathrm{g}\rangle$, and an excited, $|\mathrm{e}\rangle$, state interacts with a continuum of (plasmonic) states $|\{1\omega_{k_n}\}\rangle$ containing one plasmonic excitation in mode k_n and zero excitations elsewhere. The molecule interacts with the plasmonic states via its transition dipole moment d_0, which is the expectation value of the molecule's electronic dipole operator $\hat{d}$, $d_0 = \langle \mathrm{g}|\hat{d}|\mathrm{e}\rangle$. The molecule's excited state first efficiently decays into the plasmonic states that subsequently radiatively decay into the ground state.

where we have neglected the usually small contribution from $|E_{\mathrm{AS}}|^2$ in the last step. The signal $\mathscr{A}$ naturally decomposes into the background signal due to the hosting antenna, $\mathscr{A}_{\mathrm{BG}}$, and the sought SEIRS spectral contrast, $\mathscr{A}_{\mathrm{AS}}$, that carries the information about the properties of the sample. Importantly, notice that $\mathscr{A}_{\mathrm{AS}}$ is linearly proportional to E_{AS}, which is a fundamental difference compared to SERS.

The underlying mechanism of the antenna-sample interaction and SEIRS enhancement is contained in the physical origin of E_{AS} and is described in more detail in Part II of the thesis. For simplicity here we further assume that the sample is only weakly perturbing the antenna's properties, in which case E_{AS} can be approximated in the double-scattering approximation. In this approximation, the antenna first enhances the incident field as $E_{\mathrm{NF}} = f_{\mathrm{pl}}^{\mathrm{L}} E_{\mathrm{inc}}^{\mathrm{L}}$, and E_{NF} polarizes the sample. In the second step, the polarized sample induces an electric field that interacts with the antenna and finally yields E_{AS}. Due to the reciprocity of electromagnetism, both the process of sample excitation and the subsequent re-excitation of the antenna take advantage of the plasmonic enhancement factor $f_{\mathrm{pl}}^{\mathrm{L}}$ (like in SERS), which leads to $E_{\mathrm{AS}} \propto {f_{\mathrm{pl}}^{\mathrm{L}}}^2 E_{\mathrm{inc}}^{\mathrm{L}}$. Putting all the above together, we obtain for the signal due to the sample:

$$\mathscr{A}_{AS} \propto \underbrace{|f_{\mathrm{pl}}^{\mathrm{L}}|^2}_{\substack{\text{Plasmonic}\\ \text{enhancement}}} \times \underbrace{|E_{\mathrm{inc}}^{\mathrm{L}}|^2}_{\substack{\text{Incident}\\ \text{intensity}}}. \tag{8}$$

The plasmonic enhancement in SEIRS is thus proportional to the square of the near-field enhancement of the hosting antenna, and the signal scales linearly with the intensity of the incident light.

Surface-enhanced fluorescence (SEF): We adopt a quantum viewpoint to qualitatively discuss the principle of SEF [see also schematic in Fig. 3 (c)]. The simplest model of SEF assumes a molecule that consists of a ground, $|\mathrm{g}\rangle$, and an excited, $|\mathrm{e}\rangle$, electronic states separated by energy $\hbar\omega_{\mathrm{eg}}$ (with $\hbar$ the reduced Plack's constant). Furthermore, the electronic states interact with a large number of plasmonic states

$$|\{1\omega_{k_n}\}\rangle \equiv |\ldots,\, 0\omega_{k_{n-1}},\, 1\omega_{k_n},\, 0\omega_{k_{n+1}}, \ldots\rangle$$

with one plasmon of energy $\hbar\omega_{k_n}$ excited and the rest of the plasmonic modes in the ground state. Altogether the state of the combined system can be spanned by the states $|\mathrm{g(e)},\, \{1\omega_{k_n}\}(\{0\omega_{k_n}\})\rangle$ and $|\mathrm{g},\, \{0\omega_{k_n}\}\rangle$, where $|\{0\omega_{k_n}\}\rangle$ denotes the plasmonic vacuum.

As we are interested in fluorescence of the molecule, we assume that at some initial time ($t = 0$) the molecule is prepared (e.g. by electrical or optical pumping) in the excited state and the plasmonic environment is in its ground state ($|\mathrm{e},\, \{0\omega_{k_n}\}\rangle$). Due to the strong interaction with the vacuum fluctuations of plasmons, the molecular excitation starts decaying and the population of the excited state approximately follows an exponential time dependence $\propto e^{-\Gamma_{\mathrm{eff}} t}$ for $t > 0$. The decay rate Γ_{eff} is a combination of the properties of the molecule via the molecule's transition dipole moment $d_0 = \langle \mathrm{g}|\hat{d}|\mathrm{e}\rangle$ (with $\hat{d}$ the electronic dipole moment operator), and properties of the plasmonic environment that are comprised into the so-called local density of electromagnetic states $\mathrm{LDOS}(\omega_{\mathrm{eg}}, \mathbf{r}_0) = \mathrm{LDOS}(\omega_{\mathrm{eg}})$ that counts the number of available plasmonic states around the frequency of the molecule's electronic transition, ω_{eg}, at the position of the molecule $\mathbf{r}_0$:

$$\Gamma_{\mathrm{eff}} \propto |d_0|^2 \times \mathrm{LDOS}(\omega_{\mathrm{eg}}). \tag{9}$$

The plasmonic LDOS is usually very high compared to the LDOS of photons in vacuum and hence the plasmonic environment yields a dramatic enhancement of the decay of the molecule's excited state. Finally, the plasmonic states decay rapidly to their ground state and give rise to an observable fluorescence signal in the far field. Usually, the final decay of the plasmons is much faster than the decay of the molecular excitation into plasmons, the latter being the *bottleneck* of the process.

Importantly, the plasmonic decay includes both radiative and non-radiative processes. Therefore, the molecular excitation is not converted into a radiated photon with 100 % efficiency. This is usually expressed via the quantum yield η defined as (neglecting the intrinsic non-radiative decay of the molecular excitation):

$$\eta = \frac{\Gamma_{\text{eff}}^{\text{rad}}}{\Gamma_{\text{eff}}}, \tag{10}$$

where $\Gamma_{\text{eff}}^{\text{rad}}$ is the part of the decay rate that results into the far-field radiation. For applications that rely on far-field photon emission, when designing plasmonic structures it is therefore necessary to consider not only the total decay rate, Γ_{eff}, but also the quantum yield, η. Notice that the quantum yield does not play any role in SERS nor in SEIRS and is thus specific for SEF [49].

Last we remark that for simplicity we have completely omitted the details of the mechanism that excites the molecule, which may or may not depend on its local plasmonic environment. However, the excitation mechanism can be important for quantitative analysis of the plasmonic enhancement in SEF [40].

In this thesis, we explore the interaction between plasmons and excitations in sample molecules placed onto the surface of the plasmonic particles. In Part I we first establish the theoretical basis for both the quantum and classical description of plasmonic and molecular excitations. Part I finally summarizes practical aspects of the theory of open quantum systems which is used extensively throughout the thesis.

We apply and further develop the classical methodology based on the solution of Maxwell's equations in Part II of the thesis in the context of SEIRS. We develop a simple but powerful analytical model that describes the interaction between the plasmonic mode of a metallic antenna and an infrared-active vibrational excitation in samples placed onto the antenna's surface. We dissect the extinction spectrum of such antenna-sample system (measured in transmission mode) into its spectral contributions originating from the antenna's absorption and scattering of the incident infrared electromagnetic wave and explore the influence of the scattering and absorption of radiation by the hosting linear plasmonic antennas on the fingerprint spectral contrast of infrared-active samples. As larger antennas have better ability to scatter electromagnetic radiation than to absorb it, we design a study of a series of plasmonic antennas of different length and diameter such that the resonance frequency of their lowest dipole mode is preserved and study the antenna's spectral response with and without the sample. Remarkably, we empirically demonstrate that substrates formed by antennas that scatter and absorb the incident radiation with similar efficiency provide an optimal fingerprint spectral contrast of the sample [37]. This result is of practical importance for design of SEIRS plasmonic substrates.

In Part III we study the interaction of particle surface plasmons with electronic excitations in molecules. We examine microscopic details of the coupling between plasmons of atomically sharp metallic cavities and molecular excitons in Chapter 5 [50]. There we test a standard approximation in which the molecule is treated as a point-like object interacting with the electric field of a cavity, homogeneous across the molecule. We clearly identify situations where the point-like description of molecules breaks down and show how additional information about molecular excitons can be extracted in such cases. For example, when molecules are placed under the tip of a scanning tunneling microscope, the spatial distribution of the excitonic oscillating charge can be optically mapped by shining light onto the sharp metallic tip of the microscope[51–57]. We also show that the highly inhomogeneous electric fields in plasmonic cavities can lead to breaking of optical selection rules and thus make quadrupolar excitonic transitions in molecules accessible to light spectroscopy.

If the coupling between optical (plasmonic) cavities and molecular excitons becomes large, new hybrid states of light and matter, so-called polaritons (or plexcitons), can be formed [58–88]. Polaritons have been at the center of scientific interest for many reasons, including coherent effects such as polariton lasing and condensation, polariton-mediated energy transfer, cavity-induced chemistry, or their fluorescence properties. In Chapter 6 we address the light emission from exciton-polaritons that are coherently excited by a monochromatic laser. We show that the fluorescence from exciton-polaritons is strongly influenced by the interaction of the hybrid states with the internal vibrational excitations of molecules or those of their environment [89]. We find that the interaction of polaritons with vibrations leads to incoherent transfer of the excitations between the polariton states that induces asymmetrical transfer of the polariton populations towards the energetically lower polariton state [90–94]. Consequently, light emission from polaritons originates predominantly from the incoherently populated lower-energy polaritons, a result often encountered in experiments of organic molecule's photon emission in cavities.

Beyond the role of a passive reservoir, molecular vibrations also play an active role e.g. in chemical reactions [95–100]. It is therefore desirable to control the state of molecular vibrations by active means. In Part IV of the thesis we explore the mechanism of surface-enhanced Raman scattering as an optical tool to control molecular vibrations [101–105]. By using an analogy between the Raman scattering and a quantum optomechanical process, we study both the spectral response and the underlying dynamics of molecular vibrations in *resonant* SERS. We identify the regime of optomechanical vibrational pumping that, in the case of resonant SERS, can become highly selective with respect to the frequency of vibrational modes. Such selective vibrational pumping could be applied to pump a vibrational mode of interest, for example, leading to breaking of specific chemical bonds of a molecule or molecular isomerization. Furthermore, we show that resonant Raman spectra can show complex interference features when the system is illuminated by a strong laser. An intense laser dresses molecular electronic excitation, which can trigger a coherent resonant interaction between the molecular electronic and vibrational states. This induced interaction between the nuclear and electronic motion can be interpreted as a breaking of the Born-Oppenheimer approximation, thus influencing the chemical properties of the molecule.

In summary, the following chapters describe the interaction among excitations in molecules, plasmons, and electromagnetic radiation, ranging from the vibrational excitations interacting resonantly with infrared electromagnetic radiation to optically active electronic excitations in organic dyes. Both classical and quantum approaches are combined to describe the interaction between light and matter. Some results of the thesis, such as the optimization of linear plasmonic antennas for SEIRS, are of practical importance, others, including the quantum description of plasmon-exciton coupling or the optomechanical description of resonant SERS, address more fundamental aspects of light-matter interaction. The intriguing aspects of plasmon-assisted dynamics of the optically pumped molecular vibrations, or the dynamics of combined molecular and cavity excited states can serve as examples of the latter. Perhaps, the theoretical results of this thesis might inspire further theoretical and experimental investigation of the phenomena addressed.

Part I

Methods

Chapter 1

Classical and quantum description of plasmons in small particles

The plasmon is defined as a quantum of a collective excitation of the electron gas. In this chapter we introduce the concept of plasmon from the classical theory of electromagnetism and quantize the oscillations of the electron gas using the canonical quantization procedure. To that end we first briefly review the classical electromagnetic theory of light scattering in dielectric media. This more than hundred-years-old classical approach developed by James Clerk Maxwell proves useful and accurate to describe the complex electromagnetic interaction between extended plasmonic antennas and their dielectric environment. In this classical linear-response theory, plasmons appear as resonances of the metallic structures described by their respective dielectric function. We employ Maxwell's equations to describe the process underlying surface-enhanced infrared spectroscopy in Part II of the thesis.

Further, we simplify the full machinery of Maxwell's equations by describing the interaction of light with small particles. To that end we exploit the concept of volume-integral equation for electromagnetic-field scattering that yields an insightful scheme for analytical modelling of the spectral response of small particles. By assuming that retardation effects connected with the finite speed of light are unimportant in certain circumstances, we introduce the *quasi-static* approximation which allows for a precise definition of localized plasmonic modes and opens the path towards their canonical quantization. We employ the canonical quantization of plasmons to study the interaction of particle plasmons with electronic transitions (excitons) in organic molecules in Parts III and IV of the thesis.

1.1 Maxwell's equations

The dynamics of interacting charged particles and electromagnetic fields is described by Maxwell's equations [106–109]. These equations are formulated as macroscopic equations that describe the dynamics of electromagnetic fields in materials described by their dielectric response. For further convenience we use here Maxwell's equations in the Fourier domain, where the harmonic time dependence $e^{-\mathrm{i}\omega t}$ of the fields is assumed even though some numerical implementations of Maxwell's equations, such as the Finite Differences in Time Domain (FDTD) method employed in the thesis, use the time-domain formulation. The electric charges and currents that emerge due to the dielectric response, both bound charges and bound currents, are incorporated into the effective response of the material as constants such as the frequency ω and position $\mathbf{r}$ dependent dielectric function $\varepsilon(\omega, \mathbf{r})$ and the relative permeability $\mu(\omega, \mathbf{r})$. Here we have implicitly assumed that the material response is isotropic, local in space and nonlocal in time. The material response functions thus depend only on the position $\mathbf{r}$ and on the frequency ω of the respective Fourier component of the field. On the other hand, the external charge density ρ_{ext} and current density $\mathbf{J}_{\mathrm{ext}}$ can serve as sources of electromagnetic radiation in the dielectric environment. In the Fourier domain, Maxwell's equations for the electric field $\mathbf{E}(\omega, \mathbf{r})$, the magnetic field $\mathbf{B}(\omega, \mathbf{r})$, the electric displacement field $\mathbf{D}(\omega, \mathbf{r})$, and the magnetic H-field $\mathbf{H}(\omega, \mathbf{r})$ read

$$\nabla \times \mathbf{E} = \mathrm{i}\omega \mathbf{B}, \tag{1.1}$$

$$\nabla \times \mathbf{H} = -\mathrm{i}\omega \mathbf{D} + \mathbf{J}_{\mathrm{ext}}, \tag{1.2}$$

$$\nabla \cdot \mathbf{D} = \frac{\rho_{\mathrm{ext}}}{\varepsilon_0}, \tag{1.3}$$

$$\nabla \cdot \mathbf{B} = 0, \tag{1.4}$$

and the respective fields are related via the relations

$$\mathbf{D} = \varepsilon_0 \mathbf{E} + \mathbf{P}, \tag{1.5}$$

$$\mathbf{H} = \frac{1}{\mu_0}\mathbf{B} - \mathbf{M}, \tag{1.6}$$

where $\mathbf{P}$ and $\mathbf{M}$ are the macroscopic polarization and magnetization density, respectively, μ_0 is the magnetic permeability and ε_0 the electric permittivity in vacuum. In the linear-response regime $\mathbf{P}$ and $\mathbf{M}$ are connected with the electromagnetic fields via $\varepsilon(\omega, \mathbf{r})$ and $\mu(\omega, \mathbf{r})$ as:

$$\mathbf{P} = \varepsilon_0[\varepsilon(\omega, \mathbf{r}) - 1]\mathbf{E}, \tag{1.7}$$

$$\mathbf{M} = \mu_0[\mu(\omega, \mathbf{r}) - 1]\mathbf{H}. \tag{1.8}$$

From now on we assume that the materials in question do not exhibit any magnetic response and therefore $\mu(\omega, \mathbf{r}) = 1$ in the whole space. Furthermore, we are interested in solutions of Maxwell's equations in regions without any free charges or currents. In such a case, Maxwell's equations can be rearranged into the form of the volume-integral (Lippmann-Schwinger) equation:

$$\boxed{\mathbf{E}(\omega,\mathbf{r}) = \mathbf{E}_{\text{ext}}(\omega,\mathbf{r}) + k^2 \iiint \mathbf{G}(\omega,\mathbf{r},\mathbf{r}')\cdot\left[\varepsilon(\omega,\mathbf{r}')-1\right]\mathbf{E}(\omega,\mathbf{r})\mathrm{d}^3\mathbf{r}',} \tag{1.9}$$

where $k=\omega/c$ with $c=1/\sqrt{\varepsilon_0\mu_0}$ the speed of light in vacuum, $\mathbf{E}_{\text{ext}}$ is an external (incident) electric field that drives the system and can be generated by distant external stimuli, and $\mathbf{G}(\mathbf{r},\mathbf{r}',\omega)$ is the dyadic Green's function that is a solution of the equation

$$\nabla\times\nabla\times\mathbf{G}(\omega,\mathbf{r},\mathbf{r}') - k^2\mathbf{G}(\omega,\mathbf{r},\mathbf{r}') = \mathbf{I}\delta(\mathbf{r}-\mathbf{r}'), \tag{1.10}$$

with $\mathbf{I}$ the identity tensor and $\delta(\mathbf{r}-\mathbf{r}')$ the Dirac's delta, and assuming radiation boundary conditions [109]. More explicitly, $\mathbf{G}(\omega,\mathbf{r},\mathbf{r}')$ in a vacuum reads:

$$\mathbf{G}(\omega,\mathbf{r},\mathbf{r}') = \frac{e^{\mathrm{i}kR}}{4\pi R}\left[\left(1+\frac{\mathrm{i}kR-1}{k^2R^2}\right)\mathbf{I} + \frac{3-3\mathrm{i}kR-k^2R^2}{k^2R^2}\frac{\mathbf{RR}}{R^2}\right], \tag{1.11}$$

where $\mathbf{R}=\mathbf{r}-\mathbf{r}'$ connects the source point $\mathbf{r}'$ with the observation point $\mathbf{r}$, and $R=|\mathbf{R}|$.

Equation (1.9) is the basis for the numerical method, the so-called *discrete dipole approximation* (DDA), to solve Maxwell's equations, which results from the discretization of the volume integral of the right-hand side of the equation. Nevertheless, the Lippmann-Schwinger equation also sheds light on some more general properties of light scattering on particles, which we apply in Chapter 4 to describe light scattering on plasmonic antennas electromagnetically interacting with thin layers of dielectric samples.

Before we proceed with the treatment of light scattering on small particles we discuss the so-called *quasi-static approximation* of the Maxwell's equations often employed to simplify the complex electromagnetic scattering problem.

1.1.1 The quasi-static approximation

In certain situations retardation effects of the electromagnetic fields caused by the finite speed of light do not play a significant role. Those situations are usually occurring when the size of the structures is considerably smaller than the wavelength of light. The complex machinery of Maxwell's equations then simplifies to solving the scalar Poisson's equation for the quasi-electrostatic potential in the *quasi-static* approximation.

The quasi-static approximation is obtained in the classical theory of electromagnetism in the limit when the speed of light is set to infinity, $c\to\infty$. The solution for the electric field can then be obtained from the quasi-electrostatic equations which can be derived, for example, from the Lippmann-Schwinger equation [Eq. (1.9)] by taking the limit $k \to 0$;

$$\mathbf{E}(\mathbf{r}) = \mathbf{E}_{\mathrm{ext}}(\mathbf{r}) + \iiint \mathbf{K}(\mathbf{r}, \mathbf{r}') \cdot [\varepsilon(\omega, \mathbf{r}') - 1]\, \mathbf{E}(\mathbf{r}')\mathrm{d}^3\mathbf{r}', \tag{1.12}$$

with the quasi-static dyadic kernel

$$\mathbf{K}(\mathbf{r}, \mathbf{r}') = \frac{1}{4\pi R^3}\left(\frac{3\mathbf{RR}}{R^2} - \mathbf{I}\right). \tag{1.13}$$

Equation (1.12) expresses the intuitive fact that the electric field induced by each polarized element of matter is distributed as the field around a static point dipole $\mathbf{P}(\mathbf{r})\mathrm{d}^3\mathbf{r} = \varepsilon_0 [\varepsilon(\omega, \mathbf{r}) - 1]\, \mathbf{E}(\mathbf{r})\mathrm{d}^3\mathbf{r}$ that is self-consistently acting on the material and producing the total material polarization. The quasi-static approximation further allows for formulating the electromagnetic scattering problem in terms of the quasi-static electric potential ϕ that generates the quasi-static electric field, $\mathbf{E} = -\nabla\phi$.

The quasi-static fields are solutions of Poisson's equation:

$$\nabla^2\phi = \frac{\rho_{\mathrm{tot}}}{\varepsilon_0}, \tag{1.14}$$

where $\rho_{\mathrm{tot}} = -\nabla \cdot \mathbf{P} + \rho_{\mathrm{ext}}$ is the total charge density including the induced charges due to the material polarization, $\rho_{\mathrm{ind}} = -\nabla \cdot \mathbf{P}$, and to the external charges ρ_{ext}.

The solution of Poisson's equation can be found using a variety of numerical and analytical methods, including the quasi-static DDA based on Eq. (1.12) or the boundary-element method (BEM)[110, 111] based on the boundary-integral formulation of Poisson's equation. The boundary-integral formulation of the theory is particularly useful in the description of the quasi-static modes of finite dielectric (metallic) particles. In its numerical implementation, BEM also allows for significant computational simplification as only the interfaces separating homogeneous materials (i.e. the particle boundaries) have to be discretized, compared to the volume-integral approach where the whole three-dimensional particle volume has to be discretized.

In the framework of the boundary-integral formulation, the surface charge σ of the particle composed of a homogeneous material described by the dielectric function ε surrounded by a vacuum, related to the particle polarization as $\sigma(\mathbf{s}) = \mathbf{n}_{\mathbf{s}} \cdot \mathbf{P}(\mathbf{s})$, fulfils the equation:

$$\iint_{\partial V_{\mathrm{pl}}} \mathcal{F}(\mathbf{s}, \mathbf{s}')\sigma(\mathbf{s}')\mathrm{d}^2\mathbf{s}' - 2\pi\frac{1+\varepsilon}{1-\varepsilon}\sigma(\mathbf{s}) = -\frac{\partial\phi_{\mathrm{ext}}}{\partial n} \tag{1.15}$$

with $\mathcal{F}(\mathbf{s}, \mathbf{s}') = -\frac{\mathbf{n}_{\mathbf{s}} \cdot (\mathbf{s} - \mathbf{s}')}{|\mathbf{s} - \mathbf{s}'|^3}$ for $\mathbf{s} \neq \mathbf{s}'$ and $\mathbf{n}_{\mathbf{s}}$ the outer surface normal at point $\mathbf{s}$ of the surface. The integral is evaluated over the particle surface ∂V_{pl}. The inhomogeneous term on the right hand side of Eq. (1.15) is the surface derivative of the external potential, ϕ_{ext}, imposed on the particle due to the external charges

ρ_{ext}, $\frac{\partial \phi_{\mathrm{ext}}}{\partial n} = \mathbf{n_s} \cdot \nabla \phi_{\mathrm{ext}}(\mathbf{s})$.

We use the quasi-static approximation to discuss plasmonic excitations in metals and define the plasmons as self-sustained oscillations of the conduction electrons in metals as obtained either from the boundary-integral equation [Eq. (1.15)] or from the volume-integral equation [Eq. (1.12)] in Section 1.2.1.

1.1.2 Interaction of light with small particles

The Lippmann-Schwinger equation [Eq. (1.9)] allows for a particularly insightful treatment of light scattering on particles of small size compared to the wavelength of the incident radiation. In such a case, the integral relationship for the total field at the position of the particle approximately simplifies into the algebraic form

$$\mathbf{E}(\mathbf{r},\omega) \approx \mathbf{E}_{\mathrm{ext}}(\mathbf{r},\omega) + \mathrm{i}\frac{k^3}{6\pi} V_{\mathrm{par}} \left[\varepsilon(\omega) - 1\right] \mathbf{E}(\omega,\mathbf{r}) - \mathbf{L} \cdot \left[\varepsilon(\omega) - 1\right] \mathbf{E}(\mathbf{r},\omega), \quad (1.16)$$

where V_{par} is the volume of the particle, $\varepsilon(\omega)$ is the dielectric function of the particle, and we approximate the dyadic Green's function via its regular part at the origin:

$$\mathrm{Im}\left\{\mathbf{G}(\mathbf{r},\mathbf{r},\omega)\right\} = \mathbf{I}\frac{k}{6\pi}, \quad (1.17)$$

and its singular part which yields the depolarization factor $\mathbf{L}$ [112]:

$$\mathbf{L} = \frac{1}{4\pi} \iint_{\partial V_{\mathrm{par}}} \frac{\mathbf{n_s} \mathbf{e}_{\mathrm{R}}}{R^2} \mathrm{d}^2\mathbf{s}. \quad (1.18)$$

Here the integral is evaluated over the surface of the particle with the outer normal $\mathbf{n_s}$ and with $\mathbf{e}_{\mathrm{R}} = \mathbf{R}/R$ the unit vector centred at a fixed point $\mathbf{r}'$ and pointing to point $\mathbf{s}$ on the particle surface. We note that the depolarization factor in Eq. (1.18) emerges already from the solution of the quasi-static form of the Lippmann-Schwinger equation [Eq. (1.12)] and is therefore not influenced by retardation effects [113], which we have neglected for simplicity. The external field $\mathbf{E}_{\mathrm{ext}}$ determines the polarization density $\mathbf{P}$ in the particle, via Eq. (1.16), as

$$\mathbf{P} = \varepsilon_0 \left[\varepsilon(\omega) - 1\right] \mathbf{E}, \quad (1.19)$$

which can be integrated to yield the total dipole moment induced in the particle. By assuming an homogeneous polarization of the particle's volume, the induced dipole moment becomes:

$$\mathbf{p} = V_{\mathrm{par}} \mathbf{P} = \boldsymbol{\alpha} \cdot \mathbf{E}_{\mathrm{ext}}, \quad (1.20)$$

where we have defined the (radiation-corrected) polarizability $\boldsymbol{\alpha}$ of the particle:

$$\boxed{\boldsymbol{\alpha} = \frac{\boldsymbol{\alpha}_0}{1 - \frac{ik^3}{6\pi\varepsilon_0}\boldsymbol{\alpha}_0},} \tag{1.21}$$

with the quasi-static polarizability:

$$\boxed{\boldsymbol{\alpha}_0 = \varepsilon_0 V_{\mathrm{par}} \frac{\varepsilon(\omega) - 1}{[\varepsilon(\omega) - 1]\mathbf{L} + 1}.} \tag{1.22}$$

The quasi-static polarizability determines the response of the particle to the field that is homogeneously polarized across the particle volume. Thus, in this framework only the lowest dipolar excitations of the particles contribute to the polarizability given by Eq. (1.21). Nevertheless, if the external field $\mathbf{E}_{\mathrm{ext}}$ considerably varies in space over the particle's dimensions, the role of higher-order modes become important. We discuss a more general approach to the description of particle's excitations in Section 1.2.1, where we describe the emergence of collective plasmonic modes in metallic particles.

The polarizability of a small particle given in Eq. (1.21) holds information about the particle shape, contained in $\mathbf{L}$, about its material via the dielectric function $\varepsilon(\omega)$, and about the particle size via the radiation correction. The value of $\mathbf{L}$ also determines the frequency of the particle's optical resonances via the condition $(\varepsilon - 1)L_i + 1 = 0$, where L_i is an element of the depolarization tensor written in its diagonal form. Since L_i are real positive numbers, $L_i \in (0, 1)$, the resonances of the particle appear only if $\varepsilon(\omega) \leq 0$ for some value of ω. We give examples of such dielectric functions when we discuss plasmons in Section 1.2.1 and phononic materials in Section 4.2.

1.1.3 Absorption, scattering and extinction of small particles

Upon illumination by an external electromagnetic field the particle absorbs the incident light and its induced oscillating dipole moment radiates the scattered electromagnetic field. Both of these processes contribute to the loss of energy carried by the incident electromagnetic field and give rise to extinction of the incident light by the particle (as schematically shown in Fig. 1.1). The extinction can also be interpreted as the power that the incident field exerts upon the induced currents in the particle. The latter interpretation allows for a simple and intuitive derivation of the extinction cross section of a small particle.

The average power exerted by the incident field on the particle is given by

$$P_{\mathrm{ext}} = \frac{1}{2} \iiint_{V_{\mathrm{par}}} \mathrm{Re}\left\{ \mathbf{J}_{\mathrm{ind}} \cdot \mathbf{E}_{\mathrm{ext}} \right\} \mathrm{d}^3\mathbf{r}, \tag{1.23}$$

where $\mathbf{J}_{\mathrm{ind}}$ is the induced-current density inside the particle and the integration

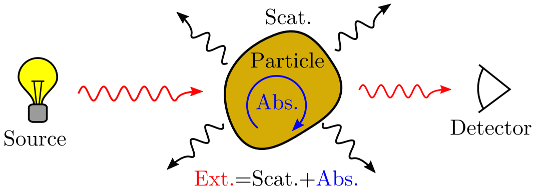

Figure 1.1: Schematic depiction of absorption, scattering and extinction of light on a small particle. The particle is illuminated by a source and the transmitted light is recorded by a detector. Upon illumination, the article absorbs the incident light (schematically shown by the blue arrow) and scatters the light to the far field (black arrows). The scattered and absorbed contributions are removed from the incident beam, together yielding the total extinction of the transmitted light.

is performed over the particle volume, V_{par}. Equation (1.23) can be compared to the expression of the absorption inside of the material:

$$P_{\mathrm{abs}} = \frac{1}{2} \iiint_{V_{\mathrm{par}}} \mathrm{Re}\left\{ \mathbf{J}_{\mathrm{ind}} \cdot \mathbf{E}_{\mathrm{tot}} \right\} \mathrm{d}^3\mathbf{r}, \tag{1.24}$$

where the external electric field, $\mathbf{E}_{\mathrm{ext}}$, is replaced by the total (i.e. external plus induced) field, $\mathbf{E}_{\mathrm{tot}}$, inside the particle. The scattered power, P_{sca}, is then obtained from the sum rule $P_{\mathrm{sca}} = P_{\mathrm{ext}} - P_{\mathrm{abs}}$. The induced current density is connected with the polarization density inside of the particle as $\mathbf{J}_{\mathrm{ind}} = -\mathrm{i}\omega\mathbf{P}$ and assuming a homogeneous polarization of the particle leads to the following expression for the power dissipated due to absorption, scattering and total extinction:

$$P_{\mathrm{abs}} = \sigma_{\mathrm{abs}} I_0, \tag{1.25}$$

$$P_{\mathrm{sca}} = \sigma_{\mathrm{sca}} I_0, \tag{1.26}$$

$$P_{\mathrm{ext}} = \sigma_{\mathrm{ext}} I_0, \tag{1.27}$$

where $I_0 = c\varepsilon_0 |\mathbf{E}_{\mathrm{ext}}|^2/2$ is the intensity of a plane wave and σ_{abs}, σ_{sca} and σ_{ext} are the absorption, scattering and extinction cross sections, respectively. For a point-like isotropic particle these expressions become [114, 115]:

$$\boxed{\begin{aligned}
\sigma_{\mathrm{abs}} &= \frac{k}{\varepsilon_0} \mathrm{Im}\{\alpha_0\} \left| \frac{\alpha}{\alpha_0} \right|^2, && (1.28)\\
\sigma_{\mathrm{sca}} &= \frac{k^4}{6\pi\varepsilon_0^2} |\alpha|^2 = \sigma_{\mathrm{ext}} - \sigma_{\mathrm{abs}}, && (1.29)\\
\sigma_{\mathrm{ext}} &= \frac{k}{\varepsilon_0} \mathrm{Im}\{\alpha\}, && (1.30)
\end{aligned}}$$

The Eqs. (1.28) to (1.30) are consistent with the laws of energy conservation as they include the effect of the radiation reaction introduced by the total particle polarizability α compared to the quasi-static polarizability α_0. When the particles are small, the scattering cross section becomes negligible compared to the absorption. In such a situation the absorption and extinction become practically identical as $\alpha \approx \alpha_0$, and the quasi-static approximation applies.

Last, we note that although the expressions for the particle polarizability [Eq. (1.21)] have been derived assuming that the particle consists of a homogeneous material, the results of this section can be generalized to more complicated systems as we show in Chapter 4 where the working principle of surface-enhanced infrared spectroscopy is discussed.

1.2 Plasmons

The free-electron gas has been in the focus of solid-state physicists already since early 1900's, when the Drude-Lorentz model of electrical conductivity was proposed [116, 117]. Surprisingly enough, the physical behavior of the electron gas, an inherent many-body system of electrons interacting via the long-range Coulomb force, is in many ways well described by models assuming independent non-interacting electrons. This independent-electron picture happens to be so successful thanks to the screening of the electron-electron interaction in metals which effectively causes that the electrons *avoid* each other and their collisions are therefore suppressed to a large extent. Nevertheless, the low-energy excitations of the electron gas often show a collective character where the electron gas behaves as an elastic body due to the long-range electron-electron interaction [63, 118–123]. Such excitations are called plasmons and we devote the following chapters to their description within the framework of the classical and quantum models.

1.2.1 Classical description of plasmons in a Drude-like metal

The simplest classical description of the optical response of the free-electron gas of density N_e, charge e and (effective) mass m_e in metals is provided by the Drude dielectric function. The Drude model assumes that the conduction electrons in a metal freely propagate except when they collide with the positive nuclei of the metal atoms. These collisions are instantaneous and give rise to a damping rate γ_e. The resulting dielectric function of the metal is the well-known Drude dielectric function:

$$\varepsilon = 1 - \frac{\omega_{\mathrm{p}}^2}{\omega^2 + \mathrm{i}\gamma_e\omega}, \tag{1.31}$$

with the plasma frequency $\omega_{\mathrm{p}} = \sqrt{N_e e^2/(\varepsilon_0 m_e)}$.

The collective plasma excitations inside a metallic particle described by the Drude dielectric function, the plasmons, can then be described as self-sustained oscillations of the polarization density $\mathbf{P}(\mathbf{r})$ inside the metal. At this stage

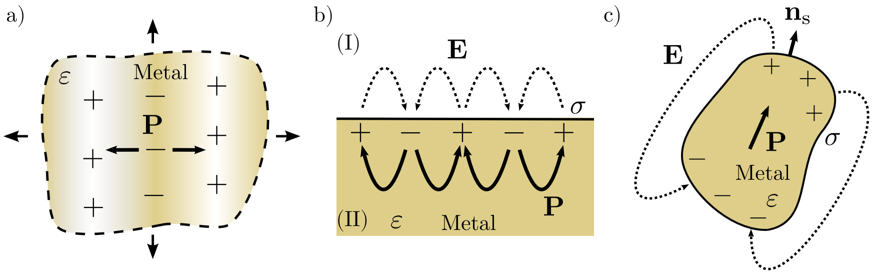

Figure 1.2: Schematics of (a) longitudinal bulk plasmons, (b) surface plasmon of a planar metal-vacuum interface and (c) localized surface plasmon in a metal, all of them described by a dielectric function ε. (a) The bulk plasmon is a longitudinal oscillation of free-electron gas polarization $\mathbf{P}$ in a bulk metal. (b) The surface plasmon is a wave of surface charge σ propagating along the metal-vacuum interface [vacuum in region (I) and metal in region (II)]. (c) The localized surface plasmon is a surface-charge oscillation confined to the boundary of a metallic particle.

of description we do not consider any interaction of the electrons with the (transverse) electromagnetic fields of vacuum and we include only the longitudinal electron-electron interaction [124], as it is commonly done in the many-body theory of solids. In other words, we treat the plasmons within the quasi-static approximation (Section 1.1.1). Below we examine some canonical examples of plasmonic excitations that can be found in the bulk, and on metal-vacuum interfaces.

Bulk plasmons

The simplest example of a plasmonic excitation is the longitudinal wave of the electronic density propagating in an infinitely extended metal as shown in Fig. 1.2 (a). In the bulk metal, the relationship between the electric field and the plasmonic polarization density can be expressed using the differential form of Gauss's law:

$$\nabla \cdot \mathbf{E} = \frac{\rho}{\varepsilon_0} = -\frac{1}{\varepsilon_0}\nabla \cdot \mathbf{P}, \tag{1.32}$$

where $\rho = -\nabla \cdot \mathbf{P}$. We further assume the bulk plasmons to be longitudinally polarized plane waves with a wave vector $\mathbf{q}$ and an amplitude $P_{\mathbf{q}}$ of the form

$$\mathbf{P}_{\mathbf{q}} = \frac{\mathbf{q}}{|\mathbf{q}|} P_{\mathbf{q}} \exp(\mathrm{i}\mathbf{q} \cdot \mathbf{r}). \tag{1.33}$$

We further assume the induced electric field to have the form of a longitudinally polarized wave, $\mathbf{E}_{\mathbf{q}}$, following the oscillating polarization density. The relationship between the electric field induced by such plane waves and the plasmon polarization density then simplifies to

$$\varepsilon_0 \mathbf{q} \cdot \mathbf{E}_\mathbf{q} = -\mathbf{q} \cdot \mathbf{P}_\mathbf{q} \tag{1.34}$$

and allows for determination of the relationship between $\mathbf{P}_\mathbf{q}$ and $\mathbf{E}_\mathbf{q}$ as $\varepsilon_0 \mathbf{E}_\mathbf{q} = -\mathbf{P}_\mathbf{q}$, which together with $\mathbf{P}_\mathbf{q} = \varepsilon_0(\varepsilon - 1)\mathbf{E}_\mathbf{q}$ leads to the well-known condition determining the frequency of the bulk plasmons

$$\varepsilon = 0. \tag{1.35}$$

Assuming that ε, the metal dielectric function, is well described by the Drude dielectric function (with negligible damping)

$$\varepsilon = 1 - \frac{\omega_\mathrm{p}^2}{\omega^2}, \tag{1.36}$$

the frequency of the bulk plasmons, ω_bulk, becomes

$$\boxed{\omega_\mathrm{bulk} = \omega_\mathrm{p}.} \tag{1.37}$$

Surface plasmons of a planar metal-vacuum interface

When the bulk metal is cut by a plane ($z = 0$) and one of the semi-infinite parts is replaced by a vacuum ($z > 0$), as shown in Fig. 1.2 (b), a new type of plasmon excitations arises at the interface. The new excitations are bound to the metal-vacuum interface and are called *surface plasmons*. Surface plasmons can be obtained from the *ansatz* that assumes that the oscillating charge has the form of a surface wave:

$$\sigma_{\mathbf{q}_\parallel}(\mathbf{r}_\parallel) = \sigma_{\mathbf{q}_\parallel} \exp(\mathrm{i}\mathbf{q}_\parallel \cdot \mathbf{r}_\parallel), \tag{1.38}$$

with $\mathbf{r}_\parallel$ and $\mathbf{q}_\parallel$ being the component of the position and momentum vectors in the plane of the interface (xy). The surface-charge density $\sigma_{\mathbf{q}_\parallel}$ produces an electrostatic potential in (I) the vacuum region ($z > 0$) and (II) the region filled with the metal ($z < 0$):

$$\phi^{(\mathrm{I})}(\mathbf{r}_\parallel, z) = \frac{\sigma_{\mathbf{q}_\parallel}}{2|\mathbf{q}_\parallel|\varepsilon_0} \exp(\mathrm{i}\mathbf{q}_\parallel \cdot \mathbf{r}_\parallel) \exp(-|\mathbf{q}_\parallel| z), \tag{1.39}$$

$$\phi^{(\mathrm{II})}(\mathbf{r}_\parallel, z) = \frac{\sigma_{\mathbf{q}_\parallel}}{2|\mathbf{q}_\parallel|\varepsilon_0} \exp(\mathrm{i}\mathbf{q}_\parallel \cdot \mathbf{r}_\parallel) \exp(|\mathbf{q}_\parallel| z), \tag{1.40}$$

which must fulfil the boundary condition

$$\left(\frac{\partial}{\partial z}\phi^{(\mathrm{I})}\right)\Big|_{z=0} = \varepsilon \left(\frac{\partial}{\partial z}\phi^{(\mathrm{II})}\right)\Big|_{z=0}. \tag{1.41}$$

This condition is satisfied if $\varepsilon = -1$, yielding the frequency for the surface plasmon resonance of a planar metal-vacuum interface. From the Drude-like dielectric function for the metal in Eq. (1.36) the surface-plasmon frequency in a metal-vacuum interface ω_{sp} can be determined as

$$\boxed{\omega_{\mathrm{sp}} = \frac{\omega_{\mathrm{p}}}{\sqrt{2}}.} \tag{1.42}$$

Localized surface plasmons

Next we consider that the metal is confined into a finite particle surrounded by a vacuum and search for the surface plasmonic modes sustained by the particle boundary. Such a situation is schematically depicted in Fig. 1.2 (c). According to Eq. (1.12) the electric field induced by the plasma oscillations is related to the polarization density via

$$\varepsilon_0 \mathbf{E}(\mathrm{r}) = \iiint \mathbf{K}(\mathbf{r}, \mathbf{r}') \cdot \mathbf{P}(\mathbf{r}') \mathrm{d}^3\mathbf{r}', \tag{1.43}$$

The self-sustained solutions, $\mathbf{P}_n(\mathbf{r})$, of Eq. (1.43) representing the plasmons are the $n-$th eigenmodes of the integral operator on its right-hand side:

$$\iiint \mathbf{K}(\mathbf{r}, \mathbf{r}') \cdot \mathbf{P}_n(\mathbf{r}') \mathrm{d}^3\mathbf{r}' = -L_n \mathbf{P}_n(\mathbf{r}). \tag{1.44}$$

The eigenvalues L_n are intimately related to the shape of the metallic particle but are independent of the particle's size. Once the eigenmodes are found, the frequency of the plasmonic modes is determined upon comparison of the right-hand side of Eq. (1.44) with the left-hand side of Eq. (1.43) and using $\mathbf{P}(\mathbf{r}) = \varepsilon_0(\varepsilon - 1)\mathbf{E}(\mathbf{r})$. One obtains:

$$\mathbf{P}_n(\mathbf{r}) = -(\varepsilon - 1) L_n \mathbf{P}_n, \tag{1.45}$$

yielding the condition for the existence of a localized plasmon mode n:

$$\varepsilon = \frac{L_n - 1}{L_n}. \tag{1.46}$$

If we assume that the metal is described by the lossless Drude-like dielectric function [Eq. (1.36)] the relationship in Eq. (1.46) yields a particularly simple expression for the localized plasmon frequencies, ω_{L_n}:

$$\boxed{\omega_{L_n} = \sqrt{L_n} \omega_{\mathrm{p}}.} \tag{1.47}$$

In the search for plasmonic excitations it is often more convenient to take advantage of different analytical and numerical approaches. A largely exploited tool that enables an efficient calculation of the plasmonic excitations is the boundary-integral approach introduced in Section 1.1.1. In the boundary-integral formulation plasmons are defined as self-sustained oscillations of the surface electric charge, σ, induced on the particle boundary. The boundary-integral formulation then connects σ with the electrostatic potential ϕ^{IN} inside the particle induced by the surface charges [111, 125, 126]:

$$\iint_{\partial V_{\mathrm{par}}} \mathcal{F}(\mathbf{s},\mathbf{s}')\sigma(\mathbf{s}')\mathrm{d}^2\mathbf{s}' + 2\pi\sigma(\mathbf{s}) = \frac{\partial\phi^{\mathrm{IN}}}{\partial n}4\pi\varepsilon_0, \tag{1.48}$$

where $\mathcal{F}(\mathbf{s},\mathbf{s}')$ has been defined in Eq. (1.15), and $\frac{\partial\phi^{\mathrm{IN}}}{\partial n} = \mathbf{n}_{\mathbf{s}}\cdot\nabla\phi^{\mathrm{IN}}(\mathbf{s})$. The surface plasmon modes σ_n are then obtained as solutions of the eigenvalue problem

$$\iint_{\partial V_{\mathrm{par}}} \mathcal{F}(\mathbf{s},\mathbf{s}')\sigma_n(\mathbf{s}')\mathrm{d}^2\mathbf{s}' = \lambda_n\sigma_n(\mathbf{s}), \tag{1.49}$$

where λ_n are real positive eigenvalues that solely depend on the particle shape and are independent of the particle absolute size. Importantly, the eigensolutions of Eq. (1.49), σ_n, are related to the eigensolutions, $\mathbf{P}_n$, of Eq. (1.44) as $\sigma_n = \mathbf{P}_n\cdot\mathbf{n}$. The respective eigenvalues obtained from Eq. (1.49), λ_n, and from Eq. (1.44), L_n, are connected via

$$L_n = \frac{1}{2} + \frac{\lambda_n}{4\pi}. \tag{1.50}$$

This result can be reached by substituting $\nabla\phi_n^{\mathrm{IN}} = L_n\mathbf{P}_n/\varepsilon_0$ and $\sigma_n = \mathbf{P}_n\cdot\mathbf{n}$, in Eq. (1.48), and using Eq. (1.49). Furthermore, it can be shown that the plasmonic modes $\mathbf{P}_n$ are mutually orthogonal functions [126] and can be normalized such that

$$\iiint_{V_{\mathrm{par}}} \mathbf{P}_n^*\cdot\mathbf{P}_m\,\mathrm{d}^3\mathbf{r} = \delta_{nm}. \tag{1.51}$$

with δ_{nm} the Kronecker delta.

For a certain class of geometries of the plamsonic particles, the plasmonic modes and frequencies can be found analytically. Such solutions can be obtained if the particle surfaces can be described as constant-coordinate surfaces in separable coordinates for the Laplace's equation. This problematic is described in detail by Morse and Feschbach [127] on p. 655 *et seq.* and later used on p. 828 *et seq.* in the context of the calculation of the Green's function fo the Laplace's and Helmholz's equations, and has been e.g. applied by Engelman and Ruppin for the treatment of phonon-polaritons in finite ionic crystals [128–130]. In Section 5.1.4 we use this method to find the surface-plasmon modes of a spherical particle.

1.3 Canonical quantization of localized surface plasmons

In the classical framework we have defined the surface plasmon modes as the self-sustained collective oscillations of the electron gas. Nevertheless, we have considered the eigensolutions either in the form of the surface charge σ [Eq. (1.49)] or the polarization density $\mathbf{P}$ [Eq. (1.44)] and defined a mathematically convenient normalization condition given by Eq. (1.51) without deeper physical significance. In this section we introduce the canonical quantization procedure for the localized surface plasmons that defines the quantum amplitude of a single plasmonic excitation (the amount of plasmonic quantum fluctuations) and thus completes the definition of surface plasmons as quanta of the collective charge oscillations. The quantized surface plasmons are the starting point for further theoretical developments in Parts III and IV of this thesis.

To quantize the surface plasmons we start with the classical Hamiltonian, H, expanded into the normal modes of the polarization density, $\mathbf{P}_n$:

$$H_{\mathrm{pl}} = \iiint_{V_{\mathrm{par}}} \sum_n \frac{m_e}{2N_e e^2}\dot{\mathbf{P}}_n^2 + \frac{L_n}{2\varepsilon_0}{\mathbf{P}_n}^2 \mathrm{d}^3\mathbf{r}, \tag{1.52}$$

where L_n is the corresponding eigenvalue [see Eq. (1.44)]. We identify $\mathbf{P}_n$, the (real) polarization density of the metal related to the plasmonic mode n, and $\mathbf{\Pi}_n \equiv \frac{m_e}{e}\dot{\mathbf{P}}_n$, as the canonical dynamical variables. We further introduce the mode functions, $\mathbf{f_n}$, which are vector fields defined in the particle volume V_{pl}, that describe the displacement of the electron gas at each point ($\mathbf{f}_n \propto \mathbf{P}_n$), and are normalized as:

$$\iiint_{V_{\mathrm{par}}} \mathbf{f}_n^* \cdot \mathbf{f}_m \,\mathrm{d}^3\mathbf{r} = \delta_{nm}. \tag{1.53}$$

It is further convenient to divide real functions ($x(t)$) into their respective positive ($x^{(+)}(t)$) and negative ($x^{(-)}(t)$) frequency parts as $x(t) = x^{(+)}(t) + x^{(-)}(t)$, with $x^{(+)}(t) = x^{(-)}(t)^*$ and $x^{(+)}(t) = \int_0^\infty x^{(+)}(\omega)e^{-\mathrm{i}\omega t}\,\mathrm{d}\omega$. The positive-frequency part of the polarization density of a mode n can be written as $\mathbf{P}_n^{(+)} = N_e e u_n^{(+)}\mathbf{f}_n$, with $u_n^{(+)}$ being the positive-frequency part of a scalar amplitude, u_n, of the displacement. For convenience, we also define $p_n^{(+)} \equiv N_e m_e \frac{\mathrm{d}u_n^{(+)}}{\mathrm{d}t}$. After some algebra we obtain the Hamiltonian of the plasmonic excitations (since the normal modes have a harmonic time dependence $u_n^{(+)}(t) = u_{n,0}^{(+)}e^{-\mathrm{i}\omega_{L_n}t}$):

$$H_{\mathrm{pl}} = \sum_n \frac{1}{2N_e m_e}p_n^2 + \frac{L_n N_e^2 e^2}{2\varepsilon_0}u_n^2. \tag{1.54}$$

This Hamiltonian describes a set of harmonic oscillators, where the oscillator frequency is $\omega_{L_n} = \sqrt{L_n N_e e^2/(\varepsilon_0 m_e)}$. Following the standard quantization procedure based on the correspondence with the quantization of a harmonic oscillator, we define the creation, $\hat{a}_n^\dagger$, and annihilation, $\hat{a}_n$, operators of the plasmonic excitation n and promote the amplitudes to operators to get the position and momentum operator of each mode as:

$$\hat{u}_n = \sqrt{\frac{\hbar}{2N_e m_e \omega_{L_n}}}(\hat{a}_n + \hat{a}_n^\dagger), \tag{1.55}$$

$$\hat{p}_n = -\mathrm{i}\sqrt{\frac{\hbar N_e m_e \omega_{L_n}}{2}}(\hat{a}_n - \hat{a}_n^\dagger), \tag{1.56}$$

with the commutation relation $[\hat{a}_n, \hat{a}_n^\dagger] = 1$ and $\hbar$ the reduced Planck's constant. These relationships define our *quantum* system in terms of the quantized polarization operator:

$$\begin{aligned}\hat{\mathbf{P}} &= \sum_n \hat{\mathbf{P}}_n^{(+)} + \hat{\mathbf{P}}_n^{(-)} = \sum_n \mathbf{P}_n^{(+)}\hat{a}_n + \mathbf{P}_n^{(-)}\hat{a}_n^\dagger \\ &= -\sum_n \sqrt{\frac{N_e e^2 \hbar}{2 m_e \omega_{L_n}}}(\hat{a}_n \mathbf{f}_n + \hat{a}_n^\dagger \mathbf{f}_n^*), \\ \dot{\hat{\mathbf{P}}} &= \frac{e}{m_e}\hat{\mathbf{\Pi}} = \mathrm{i}\sqrt{\frac{\hbar N_e e^2 \omega_{L_n}}{2m_e}}\left(\hat{a}_n \mathbf{f}_n - \hat{a}_n^\dagger \mathbf{f}_n^*\right),\end{aligned} \tag{1.57}$$

with $\mathbf{P}_n^{(-)} = [\mathbf{P}_n^{(+)}]^*$, which are time independent in the Schrödinger picture.

The result for the polarization operators can be applied to find the quantization condition for the surface charge density σ_n and the induced potential, ϕ_n (see Appendix A.1):

$$\boxed{\iint_{\partial V_{\mathrm{par}}} \phi_n^{(+)}\sigma_n^{(-)}\,\mathrm{d}^2\mathbf{s} = \frac{1}{2}\hbar\omega_{L_n},} \tag{1.58}$$

For completeness, we explicitly write the electrostatic potential operator, $\hat{\phi}_n^{\mathrm{pl}}$, of mode n, and the surface charge operator of the same mode, $\hat{\sigma}_n^{\mathrm{pl}}$, as

$$\hat{\phi}_n^{\mathrm{pl}} = \phi_n^{(+)}\hat{a}_n + \phi_n^{(-)}\hat{a}_n^\dagger, \tag{1.59}$$

$$\hat{\sigma}_n^{\mathrm{pl}} = \sigma_n^{(+)}\hat{a}_n + \sigma_n^{(-)}\hat{a}_n^\dagger. \tag{1.60}$$

Finally, the Hamiltonian of the plasmonic modes, $\hat{H}_{\mathrm{pl}}$, of the particle becomes in the notation of the creation and the annihilation operators

$$\boxed{\hat{H}_{\mathrm{pl}} = \sum_n \hbar\omega_{L_n}\hat{a}_n^\dagger\hat{a}_n,} \tag{1.61}$$

where we have left out the constant factor of $\sum_n \frac{1}{2}\hbar\omega_{L_n}$.

1.4 Summary

In this introductory chapter to the methodology we have presented the classical and quantum approaches to plasmonic excitations in metallic particles. We have started by reviewing Maxwell's equations in linear dielectrics to obtain practical tools allowing us to describe excitations in materials. We have described the dielectric response of metals via the Drude dielectric function and by using classical electrodynamics we have derived the conditions for the existence of bulk plasmons and of surface plasmon polaritons.

Special attention has been paid to the description of surface plasmons in finite metallic particles. We have discussed a general framework for calculation of the plasmonic mode functions and frequencies as eigenfunctions and eigenvalues of an integral operator.

Last, we have taken the classical results and by applying the canonical quantization procedure, a normalization condition for the plasmonic fields has been introduced such that their amplitude represents a single quantized plasmonic excitation.

We have left aside the quantization procedure of electromagnetic fields in dielectrics introduced by Huttner and Barnett where the material acts as a source of spatially-dependent fluctuating bosonic currents [131–136]. In this formalism the dielectric function carries the information about the current fluctuations in the material via the imaginary part of its dielectric function. Instead, we have opted in the thesis for a straightforward description of plasmons that emerges from the treatment of the interacting many-electron gas.

Chapter 2

Quantum description of electronic and vibrational excitations in molecules

One of the main goals of this thesis is to describe theoretically plasmon-mediated spectroscopy of molecular excitations. Plasmonic cavities are introduced as a structure that allows probing molecules more efficiently by squeezing electromagnetic fields down to the molecular scale. In this chapter we present a brief review of electronic and vibrational excitations in molecules. We start with the Hamiltonian description of the interacting system of many electrons and atomic nuclei, representing the molecule, and derive the basic equations governing the different molecular excitations.

This chapter sets stage for Parts II, III and IV which describe the interactions between plasmons and molecular excitations and their manifestation in plasmon-mediated infrared and optical response of molecules placed into the plasmonic cavities.

2.1 Hamiltonian of a molecule in a vacuum

The molecule is a highly complex system composed of mutually interacting negatively charged electrons and positively charged nuclei. In the non-relativistic limit, such system is generally described by the Hamiltonian (expressed in the position basis of the electrons [e] and the nuclei [n]):

$$H_{\mathrm{mol}} = H_{\mathrm{e}} + T_{\mathrm{n}}, \tag{2.1}$$

$$\begin{aligned} H_{\mathrm{e}} = &-\sum_i \frac{\hbar^2\nabla_i^2}{2m_e} + \sum_{\substack{i,j\\ i\neq j}} \frac{e^2}{8\pi\varepsilon_0|\mathbf{r}_i - \mathbf{r}_j|} \\ &+ \sum_{\substack{I,J\\ I\neq J}} \frac{Q_I Q_J}{8\pi\varepsilon_0|\mathbf{R}_I - \mathbf{R}_J|} + \sum_{Ij} \frac{eQ_I}{4\pi\varepsilon_0|\mathbf{R}_I - \mathbf{r}_j|}, \end{aligned} \tag{2.2}$$

$$T_{\mathrm{n}} = -\sum_I \frac{\hbar^2\nabla_I^2}{2M_I}. \tag{2.3}$$

where H_{e} and T_{n} are the electronic Hamiltonian (including the inter-nuclear interaction potential) and the nuclear kinetic energy, respectively, $\nabla_{i(I)}$ stands for the gradient operator in the electronic (nuclear) coordinates $\mathbf{r}_i = [r_{i,x}, r_{i,y}, r_{i,z}]$ ($\mathbf{R}_I = [R_{I,x}, R_{I,y}, R_{I,z}]$) and we have defined the electron (nucleus) charge, e (Q_I), and the mass of electron (nucleus), m_e (M_I). In the summations, the lower-case indices i, j run over the electrons and the upper-case indices I, J run over the nuclei. For brevity we will further use a simplified notation in which $\{\mathbf{r}\}$ ($\{\mathbf{R}\}$) labels the set of all the electronic (nuclear) coordinates. For later convenience we also define the electronic Hamiltonian free of the nuclear interaction energy, $\tilde{H}_{\mathrm{e}}$, as

$$\tilde{H}_{\mathrm{e}} = H_{\mathrm{e}} - \sum_{I\neq J} \frac{1}{2} \frac{Q_I Q_J}{4\pi\varepsilon_0|\mathbf{R}_I - \mathbf{R}_J|}, \tag{2.4}$$

which is commonly considered as the starting point for the many-body electronic problem as discussed below.

The standard way how to approach the solution of the Hamiltonian in Eq. (2.1) is to assume the *ansatz* in which the total wave function of the system, $\Psi(\{\mathbf{r}\}, \{\mathbf{R}\})$, is a sum of contributions that are factorized into the part describing the electronic degrees of freedom, $\varphi_\alpha(\{\mathbf{r}\}; \{\mathbf{R}\})$, which parametrically depends on the nuclear coordinates, and the nuclear wave function, $\chi_\alpha(\{\mathbf{R}\})$ (the Born-Oppenheimer approximation):

$$\Psi(\{\mathbf{r}\}, \{\mathbf{R}\}) = \sum_\alpha \varphi_\alpha(\{\mathbf{r}\}; \{\mathbf{R}\}) \chi_\alpha(\{\mathbf{R}\}). \tag{2.5}$$

The electronic wave functions $\varphi_\alpha(\{\mathbf{r}\}; \{\mathbf{R}\})$ are defined to be eigensolutions of the electronic Hamiltonian H_{e}:

$$[H_{\mathrm{e}} - E_\alpha(\{\mathbf{R}\})]\, \varphi_\alpha(\{\mathbf{r}\}; \{\mathbf{R}\}) = 0, \tag{2.6}$$

with $E_\alpha(\{\mathbf{R}\})$ the $\{\mathbf{R}\}$-dependent eigenenergy of the electronic state α.

The nuclear wave functions $\chi_\alpha(\{\mathbf{R}\})$ obey the coupled equations:

$$\left\{-\sum_I \frac{\hbar^2\nabla_I^2}{2M_I} + [E_\alpha(\{\mathbf{R}\}) - \epsilon]\right\}\chi_\alpha + \sum_\beta \left\{-\sum_I \left[\frac{\hbar^2}{2M_I}\tau^{(2)}_{I,\alpha\beta} + \frac{\hbar^2}{M_I}\tau^{(1)}_{I,\alpha\beta}\cdot\nabla_I\right]\chi_\beta\right\} = 0, \tag{2.7}$$

where ϵ is the sought vibrational eigenvalue and we have defined the non-adiabatic couplings $\tau^{(1)}_{I,\alpha\beta}$ and $\tau^{(2)}_{I,\alpha\beta}$

$$\tau^{(1)}_{I,\alpha\beta} = \langle\varphi_\alpha|\nabla_I\varphi_\beta\rangle_r \equiv \int\cdots\int \varphi^*_\alpha\nabla_I\varphi_\beta\,\mathrm{d}^{3N_\mathrm{el}}\mathbf{r}, \tag{2.8}$$

$$\tau^{(2)}_{I,\alpha\beta} = \langle\varphi_\alpha|\nabla_I^2\varphi_\beta\rangle_r \equiv \int\cdots\int \varphi^*_\alpha\nabla_I^2\varphi_\beta\,\mathrm{d}^{3N_\mathrm{el}}\mathbf{r}, \tag{2.9}$$

with N_el the number of electrons. The contributions of the coupling coefficients $\tau^{(1)}_{I,\alpha\beta}$ can be shown to be inversely proportional to the difference between the energies $E_\alpha(\{\mathbf{R}\})$ and $E_\beta(\{\mathbf{R}\})$, with $\tau^{(2)}_{I,\alpha\beta} \sim \left(\tau^{(1)}_{I,\alpha\beta}\right)^2$. Therefore, in situations where the energies of the electronic states are well separated, the non-adiabatic corrections usually become small and can be neglected. This is the so-called adiabatic Born-Oppenheimer approximation in which the nuclear wave functions become decoupled and can be obtained from the set of independent equations

$$\left\{-\sum_I \frac{\hbar^2\nabla_I^2}{2M_I} + [E_\alpha(\{\mathbf{R}\}) - \epsilon]\right\}\chi_\alpha = 0, \tag{2.10}$$

where the energies $E_\alpha(\{\mathbf{R}\})$ of the respective electronic states (including the Coulomb energy of the interacting nuclei), dependent on the nuclear coordinates $\{\mathbf{R}\}$, play the role of an effective potential experienced by the nuclear motion, known as the Born-Oppenheimer potential-energy surface (PES). In the upcoming section we will address the individual parts of the Hamiltonian that give rise to the vibrational and electronic excitations.

2.2 Electronic excitations

Practically all molecular properties directly or indirectly derive from the molecular electronic structure. For example, the vibrational modes of a molecule are defined by the potential energy surfaces determined by the electronic states. Similarly, also the interaction of molecules with light is largely determined by the electronic states of the molecule and the transitions among them. Here we address how the electronic excitations of the molecule can be obtained in the Born-Oppenheimer approximation (assuming frozen nuclei).

Due to the quantum nature of electrons, the electronic Hamiltonian $\tilde{H}_{\mathrm{e}}$ poses a complicated many-body problem that in general cannot be solved exactly and we are therefore forced to make use of approximate methods [137]. Some methods rely on semi-empirical models that result in an effective single-electron Hamiltonian, such as the Hückel theory of molecular orbitals or the tight binding methods. On the other hand, *ab-initio* methods are attempting to solve the electronic problem starting from the exact many-body Hamiltonian without making the use of additional input parameters. Approaches such as the Hartree-Fock method with its extensions (the post Hartree-Fock methods) [137–142] or a class of Monte-Carlo methods [143, 144] are based on solution of the Hamiltonian, making assumptions about the electronic wave-function. Other approaches circumvent the use of the wave-function by deriving the electronic properties from the electronic density. Such electronic-density based approach is known as the density-functional theory (DFT) [145–148].

We choose DFT to perform calculations of the molecular electronic structure as it has become a standard and efficient tool of quantum chemistry.

2.2.1 The Density-Functional Theory

The DFT is based on mathematical theorems bearing their author's names, the Hohenberg-Kohn theorems [145], which state that:

(I) The total energy of the many-body system is a unique functional of the electron density $n(\mathbf{r})$, and

(II) the ground-state energy can be obtained from a variational principle with the optimal density minimizing the energy functional. The optimal density is the electron density of the actual electronic ground state.

These theorems allow for defining the ground-state quantum many-body properties in terms of the electron charge density, however, they do not apply for calculation of the excited states, for which further extensions of the theory are needed [137, 149]. We address the density-functional approach to the calculation of low-lying excited states in the next subsection.

The ground-state density $n(\mathbf{r})$ is usually constructed from a set of auxiliary functions $\phi_i^{\mathrm{KS}}(\mathbf{r})$ termed Kohn-Sham orbitals as

$$n(\mathbf{r}) = \sum_i \phi_i^{\mathrm{KS}*}(\mathbf{r})\phi_i^{\mathrm{KS}}(\mathbf{r}). \tag{2.11}$$

The Kohn-Sham orbitals then fulfil the Kohn-Sham equation [150] that formally resembles the single-particle Schrödinger equation and contains an implicit dependence on the electron density $n(\mathbf{r})$:

$$\left\{-\frac{\hbar^2\nabla^2}{2m_e} + V_s(\mathbf{r})\right\}\phi_i^{\mathrm{KS}}(\mathbf{r}) = \lambda_i^{\mathrm{KS}}\phi_i^{\mathrm{KS}}(\mathbf{r}). \tag{2.12}$$

Here the first term in the braces represents the single-particle kinetic-energy operator, $V_s(\mathbf{r}) = V_s[\mathbf{r}; n(\mathbf{r})]$ plays the role of the density-dependent potential and λ_i^{KS} are the eigenvalues related to the Kohn-Sham orbitals ϕ_i^{KS}. $V_s(\mathbf{r})$ can be further expressed as

$$V_s(\mathbf{r}) = V_{\mathrm{ext}}(\mathbf{r}) + \int \frac{e^2 n(\mathbf{r}')}{4\pi\varepsilon_0|\mathbf{r}-\mathbf{r}'|}\,\mathrm{d}^3\mathbf{r}' + V_{\mathrm{XC}}(\mathbf{r}), \tag{2.13}$$

where $V_{\mathrm{ext}}(\mathbf{r})$ is the potential induced by the nuclei combined with the potential of any other external sources, the second term accounts for the effective screening by the electrons and V_{XC} is the exchange-correlation potential related to the exchange-correlation energy functional $f_{\mathrm{XC}}[n(\mathbf{r})]$ via the functional derivative:

$$V_{\mathrm{XC}} = \frac{\delta f_{\mathrm{XC}}[n(\mathbf{r})]}{\delta n(\mathbf{r})}. \tag{2.14}$$

Using this notation, the total electronic energy E_{el} becomes

$$\begin{aligned} E_{\mathrm{el}}[n(\mathbf{r})] =& T_{\mathrm{s}}[n(\mathbf{r})] + \iiint V_{\mathrm{ext}}(\mathbf{r})n(\mathbf{r})\,\mathrm{d}^3\mathbf{r} + \frac{1}{2}\iiint\iiint \frac{e^2 n(\mathbf{r})n(\mathbf{r}')}{4\pi\varepsilon_0|\mathbf{r}-\mathbf{r}'|}\,\mathrm{d}^3\mathbf{r}\,\mathrm{d}^3\mathbf{r}' \\ &+ f_{\mathrm{XC}}[n(\mathbf{r})], \end{aligned} \tag{2.15}$$

where $T_{\mathrm{s}}[n(\mathbf{r})] = -\frac{\hbar^2}{2m_e}\iiint \phi_i^{\mathrm{KS}*}(\mathbf{r})\nabla^2\phi_i^{\mathrm{KS}}(\mathbf{r})\,\mathrm{d}^3\mathbf{r}$, and $f_{\mathrm{XC}}[n(\mathbf{r})]$ contains all the other many-body exchange and correlation contributions so that Eq. (2.15) holds.

The subtlety of the DFT lies in the definition of f_{XC} as the exact functional is not known. Many different forms of f_{XC} have been developed combining various analytical and empirical approaches. In this thesis we do not aim at discussing the broad palette of available functionals and instead refer the interested reader to specialized literature about the DFT [146, 147, 151]. Nevertheless, the state-of-the-art exchange-correlation functionals make DFT to be the accurate and computationally inexpensive tool for quantum chemistry and solid-state physics as known nowadays.

The ground-state electronic density, $n(\mathbf{r})$, of the molecule is found by self-consistent solution of the Kohn-Sham equation [Eq. (2.12)]. Once $n(\mathbf{r})$ is determined, it is possible to calculate the ground-state properties of the molecule, such as the molecular vibrations by sampling the ground-state nuclear PES.

2.2.2 Time-Dependent Density-Functional Theory

The Time-Dependent Density-Functional Theory (TDDFT) [137, 149, 152, 153] is based on the generalizing theorems of Runge and Gross [149], which show that the time-dependent electronic density,

$$n(\mathbf{r},t) = \sum_i \phi_i^{\mathrm{KS}*}(\mathbf{r},t)\phi_i^{\mathrm{KS}}(\mathbf{r},t), \tag{2.16}$$

can be calculated from a time-dependent version of the Kohn-Sham scheme [Eq. (2.12)] introduced above:

$$\mathrm{i}\hbar \frac{\partial \phi_i^{\mathrm{KS}}(\mathbf{r},t)}{\partial t} = \left\{ -\frac{\hbar^2 \nabla^2}{2m_e} + V_s(\mathbf{r},t) \right\} \phi_i^{\mathrm{KS}}(\mathbf{r},t), \tag{2.17}$$

where

$$V_s(\mathbf{r},t) = V_{\mathrm{ext}}(\mathbf{r},t) + \int \frac{e^2 n(\mathbf{r}',t)}{4\pi\varepsilon_0 |\mathbf{r}-\mathbf{r}'|} \, \mathrm{d}^3\mathbf{r}' + \frac{\delta A_{\mathrm{XC}}[n(\mathbf{r},t)]}{\delta n(\mathbf{r},t)}, \tag{2.18}$$

where $V_{\mathrm{ext}}(\mathbf{r},t)$ contains the potential of the nuclei and any additional time-dependent external potentials, and A_{XC} is the exchange-correlation part of the action integral [149]. As in the case of the time-independent theory, the exchange-correlation term, A_{XC}, is again the key to the accuracy of the method and is not known in its exact form.

In this thesis we use TDDFT as implemented in NWChem [154] in the form of the linear-response TDDFT (LR-TDDFT) [137, 155], which allows for calculation of the lowest-lying excitation energies. In the following we consider that the change in the electronic density induced due to the external linear perturbation (the electronic transition density) of frequency ω is of the form

$$\delta n(\mathbf{r},\omega) = \sum_{ai} X_{ai} \phi_a^{\mathrm{KS}}(\mathbf{r}) \phi_i^{\mathrm{KS}*}(\mathbf{r}) + Y_{ai} \phi_i^{\mathrm{KS}}(\mathbf{r}) \phi_a^{\mathrm{KS}*}(\mathbf{r}), \tag{2.19}$$

where $\phi_p^{\mathrm{KS}}(\mathbf{r})$ are the Kohn-Sham orbitals of the time-independent problem and we use the convention in which a, $b, \dots$ run over the unoccupied Kohn-Sham orbitals and i, $j, \dots$ over the occupied orbitals. The coefficients X_{ai} can be understood in this context as contributions to the electronic transition density from the single-electron transitions annihilating an electron in the occupied Kohn-Sham orbitals an populating an unoccupied orbital, and Y_{ai} are responsible for the reverse process. Without further derivation, we state that the LR-TDDFT in the random-phase approximation (RPA) consists in solving an eigenvalue (Casida) equation [137, 155] for the energies of the electronic excitations, $\mathcal{W}$, following:

$$\begin{bmatrix} \mathcal{A} & \mathcal{B} \\ \mathcal{B}^* & \mathcal{A}^* \end{bmatrix} \begin{bmatrix} \mathbf{X} \\ \mathbf{Y} \end{bmatrix} = \mathcal{W} \begin{bmatrix} 1 & 0 \\ 0 & -1 \end{bmatrix} \begin{bmatrix} \mathbf{X} \\ \mathbf{Y} \end{bmatrix}, \tag{2.20}$$

where $\mathbf{X}$ and $\mathbf{Y}$ are vectors containing the coefficients X_{ai} and Y_{ai}, respectively. We have further defined

$$\mathcal{A}_{ia,jb} = \delta_{ij}\delta_{ab}(\lambda_a^{\mathrm{KS}} - \lambda_i^{\mathrm{KS}}) + (ia|jb) + (ia|g_{\mathrm{XC}}|jb), \tag{2.21}$$

$$\mathcal{B}_{ia,jb} = (ia|bj) + (ia|g_{\mathrm{XC}}|bj), \tag{2.22}$$

where $\lambda_{a(i)}^{\mathrm{KS}}$ are the energies of the respective Kohn-Sham orbitals (considered as real), and

$$(pq|rs) = \int\int \frac{\phi_p^{\mathrm{KS}}(\mathbf{r}_1)\phi_q^{\mathrm{KS}}(\mathbf{r}_1)\phi_r^{\mathrm{KS}}(\mathbf{r}_2)\phi_s^{\mathrm{KS}}(\mathbf{r}_2)}{4\pi\varepsilon_0|\mathbf{r}_1-\mathbf{r}_2|}\,\mathrm{d}^3\mathbf{r}_1\mathrm{d}^3\mathbf{r}_2, \tag{2.23}$$

$$(pq|g_{\mathrm{XC}}|rs) = \int\int \phi_p^{\mathrm{KS}}(\mathbf{r}_1)\phi_q^{\mathrm{KS}}(\mathbf{r}_1)g_{\mathrm{XC}}(\mathbf{r}_1,\mathbf{r}_2)\phi_r^{\mathrm{KS}}(\mathbf{r}_2)\phi_s^{\mathrm{KS}}(\mathbf{r}_2)\,\mathrm{d}^3\mathbf{r}_1\mathrm{d}^3\mathbf{r}_2. \tag{2.24}$$

In the expressions above, the integrals identically vanish if any two orbitals with the same spatial integration coordinate represent electrons of the same spin. $(pq|g_{\mathrm{XC}}|rs)$ depends on the approximation of the exchange-correlation kernel and is related to A_{XC} [137]. In particular, the exchange-correlation contribution can be obtained in the adiabatic approximation, where it is assumed that

$$\frac{\delta A_{\mathrm{XC}}}{\delta n} \approx \frac{\delta f_{\mathrm{XC}}}{\delta n}, \tag{2.25}$$

as

$$g_{\mathrm{XC}}(\mathbf{r}_1,\mathbf{r}_2) \approx \frac{\delta^2 f_{\mathrm{XC}}}{\delta n(\mathbf{r}_1)\delta n(\mathbf{r}_2)}, \tag{2.26}$$

with f_{XC} being the exchange-correlation functional of the time-independent theory.

The solution of the full Casida equation [Eq. (2.20)] is often simplified by assuming that the transition electronic density, $\delta n(\mathbf{r},\omega)$, is formed purely by transitions from the occupied to the unoccupied Kohn-Sham orbitals, neglecting the often small contribution from Y_{ai}:

$$\delta n(\mathbf{r},\omega) \approx \sum_{ai} X_{ai}\phi_a^{\mathrm{KS}}(\mathbf{r})\phi_i^{\mathrm{KS}}(\mathbf{r}). \tag{2.27}$$

This approximation, called the Tamm-Dancoff approximation (TDA) or the configuration interaction singles (CIS), yields the simplified eigenvalue problem

$$\mathcal{A}\mathbf{X} = \omega\mathbf{X}. \tag{2.28}$$

Equation (2.28) is usually more tractable computationally for larger electronic systems than the full Casida equation [Eq. (2.20)] and often yields a satisfactory accuracy.

Once the electronic excitations are found from Eq. (2.20) or (2.28), the eigenfrequencies $\mathcal{W}_I$ and the respective eigenvectors $\mathbf{X}^I$ and $\mathbf{Y}^I$ can be used to determine the molecule's properties in the excited electronic state $|\mathrm{e}_I\rangle$. The eigenfrequencies can be used to determine the excited-state PESs that, among others, define the excited-state vibrations of the molecule. The vectors $\mathbf{X}^I$ and $\mathbf{Y}^I$ then yield the electronic transition charge density, $\rho_{\mathrm{e}_I\mathrm{g}}$, between the ground state $|\mathrm{g}\rangle$ and the excited state $|\mathrm{e}_I\rangle$:

$$\boxed{\rho_{\mathrm{e}_I\mathrm{g}} = e\delta n^I(\mathbf{r},\omega) = e\sum_{ai} X^I_{ai}\phi^{\mathrm{KS}}_a(\mathbf{r})\phi^{\mathrm{KS}}_i(\mathbf{r}) + Y^I_{ai}\phi^{\mathrm{KS}}_i(\mathbf{r})\phi^{\mathrm{KS}}_a(\mathbf{r}).} \tag{2.29}$$

In Section 5.1.4 we use the transition charge density to calculate the interaction of the molecular electronic excitations (excitons) with the particle plasmons.

2.3 Molecular vibrations in the adiabatic Born-Oppenheimer approximation

The nuclear Hamiltonian in Eq. (2.10) is determinant for chemical properties of the molecules as the PESs represent the energy landscapes of chemical reactions [156, 157] and determines the vibrational properties of molecules which give rise to fingerprint signatures in optical and IR spectra. In this chapter we solve the nuclear Hamiltonian in the limit of small atomic displacements

Our starting point is the vibrational Hamiltonian in the adiabatic Born-Oppenheimer approximation on top of the PES belonging to the electronic state of interest

$$H_{\mathrm{vib}} = -\sum_I \frac{\hbar^2\nabla_I^2}{2M_I} + E(\{\mathbf{R}\}), \tag{2.30}$$

which we interpret as a Hamiltonian of a set of classical point-like nuclei

$$H_{\mathrm{vib}} = \sum_{I,\zeta=x,y,z} \frac{1}{2}M_I\left(\dot{R}_{I,\zeta}\right)^2 + E(\{\mathbf{R}\}), \tag{2.31}$$

where I runs over the nuclei and ζ runs over the spatial coordinates. We further assume that the PES can be approximated in the vicinity of the equilibrium geometry $\{\mathbf{R}\}_0$ as

$$E_\alpha(\{\mathbf{R}\}) \approx E(\{\mathbf{R}\}_0) + \frac{1}{2}\sum_{I,J}\sum_{\zeta,\xi=x,y,z}\left(\frac{\partial^2}{\partial R_{I,\zeta}\partial R_{J,\xi}}E(\{\mathbf{R}\})\right)\bigg|_{\{\mathbf{R}\}_0} R_{I,\zeta}R_{J,\xi}. \tag{2.32}$$

It is also convenient to introduce the mass weighted coordinates

$$\tilde{q}_{I,\zeta} = \sqrt{M_I}R_{I,\zeta} \tag{2.33}$$

and for simplicity define a new indexing convention

$$\tilde{q}_a \equiv \tilde{q}_{I,\zeta}, \tag{2.34}$$

$$R_a \equiv R_{I,\zeta}, \tag{2.35}$$

$$M_a \equiv M_{I,\zeta} \tag{2.36}$$

so that we can introduce the mass-weighted (column) vectors $(\tilde{\mathbf{q}})_a = \tilde{q}_a$. Using the above definitions, we arrive at the following Hamiltonian characterizing the motion of the nuclei:

$$\begin{aligned} H_{\text{vib}} &= \frac{1}{2}\sum_a \dot{\tilde{q}}_a^2 + \frac{1}{2}U_{ab}\tilde{q}_a\tilde{q}_b \\ &= \frac{1}{2}\dot{\tilde{q}}^{\mathrm{T}} \cdot \dot{\tilde{q}} + \frac{1}{2}\tilde{\mathbf{q}}^{\mathrm{T}} \cdot \mathbf{U} \cdot \tilde{\mathbf{q}}, \end{aligned} \tag{2.37}$$

where we have defined the dynamical matrix

$$(\mathbf{U})_{ab} = U_{ab} = \frac{1}{\sqrt{M_a M_b}} \frac{\partial^2 E(\{\mathbf{R}\})}{\partial R_a \partial R_b}\Big|_{\{\mathbf{R}\}_0} \tag{2.38}$$

and $(\cdot)^{\mathrm{T}}$ stands for transposition.

We transform now the Hamiltonian in Eq. (2.37) into a diagonal form. To that end we diagonalize the dynamical matrix $\mathbf{U} = \mathbf{S}^{\mathrm{T}} \cdot \mathbf{\Omega}^2 \cdot \mathbf{S}$, where $\mathbf{\Omega}$ is the diagonal matrix of frequencies Ω_α:

$$\mathbf{\Omega} = \begin{bmatrix} \Omega_1 & 0 & \cdots \\ 0 & \Omega_2 & \cdots \\ \vdots & \vdots & \ddots \end{bmatrix}, \tag{2.39}$$

and $\mathbf{S}$ is a unitary matrix with each α-th column being an eigenvector of the matrix $\mathbf{U}$. In the new basis, the Hamiltonian has the form of a sum of non-interacting classical Harmonic oscillators that we identify with the molecular vibrations:

$$H_{\text{vib}} = \sum_{\alpha=1}^{3N} \frac{1}{2}\dot{q}_\alpha^2 + \frac{1}{2}\Omega_\alpha^2 q_\alpha^2, \tag{2.40}$$

where the summation runs over all $3N$ degrees of freedom of the nuclear motion of a N-atomic molecule. However, there are only $3N-6$ degrees of freedom that lead to deformation of the molecular geometry which can represent the vibrational modes. The remaining 6 degrees of freedom contain the rigid translations and rotations of the entire molecule, which result in six solutions with vibrational frequency equal to zero (the so-called zero-frequency modes). In the vibrational Hamiltonian of the molecule we therefore subtract the zero-frequency modes and sum only over the $3N-6$ vibrational modes.

So far we have obtained a *classical* Hamiltonian of the molecular vibrations that has been derived from the originally fully *quantum* Hamiltonian of the molecule. In the final step we therefore canonically quantize the molecular vibrations. To that end we promote the displacements q_α and their canonical conjugates $p_\alpha = \dot{q}_\alpha$ to operators ($q_\alpha \to \hat{q}_\alpha$ and $p_\alpha \to \hat{p}_\alpha$) that obey the commutation relations $[\hat{q}_\alpha, \hat{p}_\alpha] = \mathrm{i}\mu_\alpha^{\mathrm{M}}\hbar$, where μ_α^{M} is the reduced mass of the mode α. The reduced mass μ_α^{M} is defined as a diagonal element of the transformed mass matrix $\boldsymbol{\mu}^{\mathrm{M}}$ connected to the original diagonal mass matrix $(\mathbf{M})_{ab} = \delta_{ab}M_a$ via $\boldsymbol{\mu}^{\mathrm{M}} = \mathbf{S}^{\mathrm{T}} \cdot \mathbf{M} \cdot \mathbf{S}$.

The canonical quantization also allows for defining the operators in the basis of the bosonic creation $\hat{b}_\alpha^\dagger$ and annihilation $\hat{b}_\alpha$ operators of the vibrational mode α (fulfilling the commutation relation $[\hat{b}_\alpha, \hat{b}_\alpha^\dagger] = 1$):

$$\hat{q}_\alpha = \sqrt{\frac{\hbar}{2\Omega_\alpha}}(\hat{b}_\alpha^\dagger + \hat{b}_\alpha), \tag{2.41}$$

$$\hat{p}_\alpha = \mathrm{i}\mu_\alpha\sqrt{\frac{\hbar\Omega_\alpha}{2}}(\hat{b}_\alpha^\dagger - \hat{b}_\alpha) \tag{2.42}$$

and finally writing the vibrational Hamiltonian as

$$\hat{H}_{\mathrm{vib}} = \sum_\alpha^{3N-6} \hbar\Omega_\alpha \left(\hat{b}_\alpha^\dagger \hat{b}_\alpha + \frac{1}{2}\right). \tag{2.43}$$

Under the Born-Oppenheimer approximation, similar Hamiltonian can be written for the vibrations sustained by each electronic state $|\mathrm{e}_i\rangle$ of the molecule. The Hamiltonian of the molecular electronic and vibrational states then becomes

$$\boxed{\hat{H}_{\mathrm{mol}} = \sum_i |\mathrm{e}_i\rangle\langle\mathrm{e}_i| \left(E_i + \sum_\alpha^{3N-6} \hbar\Omega_{i,\alpha}\hat{b}_{i,\alpha}^\dagger \hat{b}_{i,\alpha}\right),} \tag{2.44}$$

with E_i the energy of the electronic excited state $|\mathrm{e}_i\rangle$ (including the vibrational zero-point energy), in which the vibrational modes of frequencies $\Omega_{i,\alpha}$ are described by the respective bosonic annihilation (creation) operators $b_{i,\alpha}$ ($b_{i,\alpha}^\dagger$) in each electronic state. We use this form of the molecular electronic and vibrational Hamiltonian [Eq. (2.44)] in Section 7.4 to describe the Raman activity of molecules and to derive the model Hamiltonians describing the interaction of the molecule's states with plasmons and with incident light.

2.4 Summary

In this introductory chapter we have provided a brief summary of the physical origin of the molecular electronic and vibrational excitations. Starting from the general many-body Hamiltonian describing the interacting system of electrons and nuclei, we have derived in the Born-Oppenheimer approximation the effective vibrational and electronic Hamiltonians.

We have concentrated on the treatment of the electronic excitations in molecules within the framework of (TD)DFT as the (TD)DFT is nowadays a computationally efficient and accurate tool in quantum chemistry. We use TDDFT in Section 5.1.4 to describe the interaction of the molecular electronic excitations with plasmons in metallic particles.

Finally we have solved the effective nuclear Hamiltonian of the molecule in the approximation of small vibrations and we have derived the classical and quantized vibrational modes of the molecule. We use these results in Parts II and IV of the thesis.

Chapter 3

Quantum Electrodynamics (QED) description of plasmonic and molecular excitations

The spectral signal in plasmon-enhanced spectroscopies is a result of a mutual interaction between the excitations of the sample and those of the hosting plasmonic antenna. In this chapter we introduce cavity Quantum Electrodynamics (QED), as a key quantum methodology that allow for practically treating the complex interaction between the excitations of the hosting plasmonic antenna, the excitations of the sample and the incident or emitted light. We build the theory using the formalism of the open quantum systems that allows for including incoherent processes, such as decay and decoherence, arising form interactions of the system with its environment.

In this chapter we first introduce the basic concepts and definitions of cavity QED, and derive the dynamical equations of the theory. We then discuss a particular example of a two-level system interacting with electromagnetic modes in a generically structured environment (the Wigner-Weisskopf theory). Last, we derive the expressions for the emission and extinction spectra within the QED formalism.

3.1 The density matrix and the quantum master equation

3.1.1 Pure states, mixed states and observables

Any isolated physical system can be characterized by its state $|\Psi\rangle$ (using the Dirac notation) that evolves in time according to the Schrödinger equation:

$$\mathrm{i}\hbar\frac{\mathrm{d}}{\mathrm{d}t}|\Psi\rangle = \hat{H}|\Psi\rangle, \tag{3.1}$$

where the time evolution is determined by the time-independent Hamiltonian $\hat{H}$ of the system. A system that is driven by external stimuli which are not explicitly quantized (such as classical driving electromagnetic fields) is called a closed quantum system for which the dynamics of the state $|\Psi\rangle$ is governed by the Schrödinger equation according to the generally time-dependent Hamiltonian $\hat{H}(t)$.

Very often, the exact quantum state cannot be determined for practical reasons, or an experiment on an *ensamble* of identical quantum systems needs to be performed. In such a case, the state of the system (or the average state of the *ensamble*) is rather described as a probabilistic mixture of several pure quantum states $|\psi_\alpha\rangle$, called the mixed state. It is therefore necessary to generalize the description of a quantum state beyond the pure state vectors $|\Psi\rangle$.

The desired statistical operator that combines the purely quantum description of the quantum state $|\psi_\alpha\rangle$ with the classical probabilities w_α to find the system in the state $|\psi_\alpha\rangle$ is the density operator defined as:

$$\hat{\rho} = \sum_\alpha w_\alpha |\psi_\alpha\rangle\langle\psi_\alpha|, \tag{3.2}$$

where w_α satisfy $\sum\limits_\alpha w_\alpha = 1$. The classical probabilities w_α introduce the classical uncertainty about the pure quantum state $|\psi_\alpha\rangle$ of the system. We further assume that all quantum states are properly normalized, which yields the normalization condition for the density operator $\mathrm{Tr}\{\hat{\rho}\} = 1$.

The density operator plays an important role in the theory of open-quantum systems as well as in the theory of coherence that will become important in the following chapters. It is therefore necessary to clarify the difference between the so-called mixed state (introduced by the density operator) and a quantum superposition of pure states. As an example we consider the density operators of a quantum superposition of two orthonormal states $|\mathrm{g}\rangle$ and $|\mathrm{e}\rangle$, $|\psi_{\mathrm{eg}}\rangle = \frac{1}{\sqrt{2}}(|\mathrm{g}\rangle + |\mathrm{e}\rangle)$, or of a mixed state containing $|\mathrm{g}\rangle$ and $|\mathrm{e}\rangle$ with equal classical probabilities. The corresponding density operator, $\hat{\rho}_{\psi_{\mathrm{eg}}}$, of the former can be represented in the basis

$\{|\mathrm{g}\rangle,\, |\mathrm{e}\rangle\}$ by a matrix:

$$\boldsymbol{\rho}_{\psi_{\mathrm{eg}}} = \frac{1}{2}\begin{bmatrix} 1 & 1 \\ 1 & 1 \end{bmatrix}. \tag{3.3}$$

For the mixed state, on the other hand, the density operator $\hat{\rho}_{\mathrm{mix}}$ can be represented by a matrix:

$$\boldsymbol{\rho}_{\mathrm{mix}} = \frac{1}{2}\begin{bmatrix} 1 & 0 \\ 0 & 1 \end{bmatrix}. \tag{3.4}$$

The difference between the two matrix representations is apparent. The matrix representing the superposition state $|\psi_{\mathrm{eg}}\rangle$ contains nonzero off-diagonal terms named coherences, whereas the mixed state is expressed by a fully diagonal matrix where the coherences are absent. Exploiting this nomenclature we can thus say that $|\psi_{\mathrm{eg}}\rangle$ is a *coherent superposition* of $|\mathrm{g}\rangle$ and $|\mathrm{e}\rangle$, and the mixed state is an *incoherent superposition* of the two.

The density operator has a large number of properties that can be found in standard textbooks [158, 159] and that we omit here for brevity. Like the pure quantum state, the density operator also determines all observable quantities (observables) of the system. According to quantum mechanics, the observables are represented by operators acting on its Hilbert space. The outcome of an experiment that measures an observable $\hat{O}$ is in quantum mechanics a stochastic quantity with the mean value given by the well-known formula

$$\langle\hat{O}\rangle = \langle\psi|\hat{O}|\psi\rangle \tag{3.5}$$

if the system is in the pure state. In case that the system is described by the density matrix, the outcome of the measurement is still a stochastic value, determined not only by the quantum probability of the measurement but also by the classical probabilities w_α. The mean value of the observable is then given by

$$\langle\hat{O}\rangle = \mathrm{Tr}\{\hat{\rho}\,\hat{O}\}, \tag{3.6}$$

where $\mathrm{Tr}\{\cdot\}$ denotes the trace.

3.1.2 Time evolution of the density operator

We complete the discussion of the density operator by presenting the differential equation governing its time evolution. Provided that each pure state $|\psi_\alpha\rangle$ of an isolated or closed system obeys

$$\mathrm{i}\hbar\frac{\mathrm{d}}{\mathrm{d}t}|\psi_\alpha\rangle = \hat{H}|\psi_\alpha\rangle, \tag{3.7}$$

with $\hat{H}$ the system Hamiltonian, the density operator of an isolated (closed) system can be shown to evolve according to the equation of motion

$$\mathrm{i}\hbar\frac{\mathrm{d}}{\mathrm{d}t}\hat{\rho} = [\hat{H}, \hat{\rho}], \tag{3.8}$$

where $[\cdot, \cdot]$ is the commutator. Equation (3.8) is known as the Liouville-von Neumann equation or the master equation.

The Liouville-von Neumann equation also gives access to the time evolution of the operator mean values. Using Eq. (3.6) together with Eq. (3.8) it can be shown that

$$\mathrm{Tr}\left\{\frac{\mathrm{d}}{\mathrm{d}t}\hat{\rho}\hat{O}\right\} = \langle\dot{\hat{O}}\rangle = \frac{1}{\mathrm{i}\hbar}\langle[\hat{O}, \hat{H}]\rangle, \tag{3.9}$$

where in the last step we made use of the cyclic property of the trace.

3.1.3 Open quantum systems, the quantum master equation

In practice many systems are not isolated nor closed but instead they interact with a highly complex environment constituting thus only a part of a larger closed system. In such situations, the complete knowledge of the state combining the sub-system of interest as well as the environment would be required to fully describe the dynamics of the system. This poses a difficult problem that is generally not tractable due to the excess of environmental degrees of freedom or simply due to the lack of knowledge about the environment. In this section we present the equations determining the approximate dynamics of the smaller sub-system of interest influenced by the environment that is treated as an effective reservoir.

We assume that the state of the total system can be expressed as a direct product $|S_i\rangle \otimes |E_j\rangle$ of orthonormal bases of the sub-system $|S_i\rangle$ and of the environment $|E_j\rangle$. The state of the complete system is then expressed in this basis with help of its density operator $\hat{\rho}_\mathrm{T}$ that contains both the information about the sub-system and the environment. We further define the reduced density operator, $\hat{\rho}_\mathrm{S}$, of the sub-system

$$\hat{\rho}_\mathrm{S} = \mathrm{Tr}_\mathrm{E}\{\hat{\rho}_\mathrm{T}\} \equiv \sum_i \langle E_i|\hat{\rho}_\mathrm{T}|E_i\rangle, \tag{3.10}$$

where we have defined the partial trace $\mathrm{Tr}_\mathrm{E}\{\hat{\rho}_\mathrm{T}\}$ of the density operator $\hat{\rho}_\mathrm{T}$ over the environmental states. The reduced density operator $\hat{\rho}_\mathrm{S}$ contains only the information about the sub-system of interest, denoted as the *open quantum system* S, and has a substantially smaller dimension than $\hat{\rho}_\mathrm{T}$. Moreover, the expectation values of all observables $\hat{O}_\mathrm{S}$ operating only on the sub-system Hilbert space can be obtained from $\hat{\rho}_{\mathrm{S}}$ by applying the trace rule

$$\langle \hat{O}_{\mathrm{S}} \rangle = \mathrm{Tr}\{\hat{\rho}_{\mathrm{S}}\, \hat{O}_{\mathrm{S}}\}. \tag{3.11}$$

It is therefore convenient to derive an effective theory which can solely describe the physics of $\hat{\rho}_{\mathrm{S}}$ and treat the environment only perturbatively.

We start with the general formula for the time evolution of the reduced density operator $\hat{\rho}_{\mathrm{S}}$ that can be derived from Eq. (3.8) by applying the definition in Eq. (3.10), yielding

$$\mathrm{i}\hbar \frac{\mathrm{d}}{\mathrm{d}t}\hat{\rho}_S = \mathrm{Tr}_{\mathrm{E}} \left\{ \mathrm{i}\hbar \frac{\mathrm{d}}{\mathrm{d}t}\hat{\rho}_{\mathrm{T}} \right\} = \mathrm{Tr}_{\mathrm{E}}\{[\hat{H}, \hat{\rho}_{\mathrm{T}}]\}, \tag{3.12}$$

where the right-hand side is a partial trace of an expression containing the Hamiltonian of the total system, $\hat{H}$, and the total-system density operator, $\hat{\rho}_{\mathrm{T}}$. The time evolution of $\hat{\rho}_{\mathrm{S}}$ is not generally Hermitian and new incoherent loss mechanisms, such as *population decay* or *pure dephasing*, appear due to the partial trace. These processes result in time-irreversible dynamics of the system state and lead to loss of the system coherence. We further write the total Hamiltonian $\hat{H}$ in the form

$$\hat{H} = \hat{H}_{\mathrm{S}} + \hat{H}_{\mathrm{SE}} + \hat{H}_{\mathrm{E}}, \tag{3.13}$$

where $\hat{H}_{\mathrm{S}}$ is the Hamiltonian of the open system, $\hat{H}_{\mathrm{E}}$ is the Hamiltonian of the environment and $\hat{H}_{\mathrm{SE}}$ is the interaction Hamiltonian connecting the two. Next we invoke the interaction picture in which the Hamiltonian transforms as $\tilde{\hat{H}} = \hat{U}\hat{H}\hat{U}^{\dagger} + \mathrm{i}\hbar\dot{\hat{U}}\hat{U}^{\dagger}$ with $\hat{U} = \exp\left(\mathrm{i}\hat{H}_{\mathrm{NI}}\, t\right)$ and $\hat{H}_{\mathrm{NI}} = \hat{H}_{\mathrm{S}} + \hat{H}_{\mathrm{E}}$. The operators, including the density operator, acquire the explicit time dependence $\tilde{\hat{O}} = \hat{U}\, \hat{O}\, \hat{U}^{\dagger}$.

In the interaction picture, the time evolution of the density operator has the form

$$\dot{\hat{\rho}}_{\mathrm{T}}(t) = \frac{1}{\mathrm{i}\hbar} \left[\hat{H}_{\mathrm{SE}}(t), \hat{\rho}_{\mathrm{T}}(t) \right]. \tag{3.14}$$

Eq. (3.14) can be formally integrated

$$\hat{\rho}_{\mathrm{T}}(t + \Delta t) = \hat{\rho}_{\mathrm{T}}(t) + \frac{1}{\mathrm{i}\hbar} \int_{t}^{t+\Delta t} \mathrm{d}t' \, \left[\hat{H}_{\mathrm{SE}}(t'), \hat{\rho}_{\mathrm{T}}(t') \right] \tag{3.15}$$

and used consecutively to express $\hat{\rho}_{\mathrm{T}}(t')$ in Eq. (3.15), leading to the second-order expression

$$\begin{aligned}\hat{\rho}_{\mathrm{T}}(t+\Delta t)-\hat{\rho}_{\mathrm{T}}(t)=&\frac{1}{\mathrm{i}\hbar}\int_{t}^{t+\Delta t}\mathrm{d}t'\,\left[\hat{H}_{\mathrm{SE}}(t'),\hat{\rho}_{\mathrm{T}}(t)\right]\\&-\frac{1}{\hbar^{2}}\int_{t}^{t+\Delta t}\mathrm{d}t'\int_{t}^{t'}\mathrm{d}t''\,\left[\hat{H}_{\mathrm{SE}}(t'),\left[\hat{H}_{\mathrm{SE}}(t''),\hat{\rho}_{\mathrm{T}}(t'')\right]\right].\end{aligned}\tag{3.16}$$

The derivation of the effective dynamics of $\hat{\rho}_{\mathrm{S}}$ from Eq. (3.16) involves the use of a series of approximations including the Born approximation and the Markov approximation.

We assume that the first term on the right-hand side of Eq. (3.16) disappears because

$$\mathrm{Tr}_{\mathrm{E}}\left\{\left[\hat{H}_{\mathrm{SE}}(t'),\hat{\rho}_{\mathrm{T}}(t)\right]\right\}=0,\tag{3.17}$$

which follows if we assume that $\hat{\rho}_{\mathrm{T}}\approx\hat{\rho}_{\mathrm{S}}(t)\otimes\hat{\rho}_{\mathrm{E}}$, where $\hat{\rho}_{\mathrm{E}}$ is not affected by the system dynamics. This approximation states that the correlations in the environment decay fast compared to the time scale of the system-environment coupling and can be seen as the *Born approximation*[158, 160]. In order for Eq. (3.17) to be valid, the interaction between the interesting system and the reservoir further needs to have vanishing mean-contribution from the reservoir, i.e.

$$\mathrm{Tr}_{\mathrm{E}}\left\{\hat{H}_{\mathrm{SE}}(t)\hat{\rho}_{\mathrm{E}}\right\}=0,\tag{3.18}$$

which can usually be achieved by a suitable definition of $\hat{H}_{\mathrm{SE}}$. Equation (3.16) thus becomes

$$\hat{\rho}_{\mathrm{T}}(t+\Delta t)-\hat{\rho}_{\mathrm{T}}(t)\approx-\frac{1}{\hbar^{2}}\int_{t}^{t+\Delta t}\mathrm{d}t'\int_{t}^{t'}\mathrm{d}t''\,\left[\hat{H}_{\mathrm{SE}}(t'),\left[\hat{H}_{\mathrm{SE}}(t''),\hat{\rho}_{\mathrm{T}}(t'')\right]\right],\tag{3.19}$$

which can be recast into a more convenient form by a change of the integration variables (defining $\tau=t'-t''$)

$$\begin{aligned}&\hat{\rho}_{\mathrm{T}}(t+\Delta t)-\hat{\rho}_{\mathrm{T}}(t)\\&\quad\approx-\frac{1}{\hbar^{2}}\int_{0}^{\Delta t}\mathrm{d}\tau\int_{t+\tau}^{t+\Delta t}\mathrm{d}t'\,\left[\hat{H}_{\mathrm{SE}}(t'),\left[\hat{H}_{\mathrm{SE}}(t'-\tau),\hat{\rho}_{\mathrm{T}}(t'-\tau)\right]\right]\\&\quad\approx-\frac{1}{\hbar^{2}}\int_{0}^{\infty}\mathrm{d}\tau\int_{t}^{t+\Delta t}\mathrm{d}t'\,\left[\hat{H}_{\mathrm{SE}}(t'),\left[\hat{H}_{\mathrm{SE}}(t'-\tau),\hat{\rho}_{\mathrm{T}}(t)\right]\right],\end{aligned}\tag{3.20}$$

where the second step assumes that the integrand becomes negligibly small for $\tau_c\ll\Delta t$, i.e. the reservoir correlations disappear on the time scale τ_c smaller than Δt (the course-grained approximation), and we have applied the *Markov approximation* by setting $\hat{\rho}_{\mathrm{T}}(t'')\approx\hat{\rho}_{\mathrm{T}}(t)$ [158, 160].

For concreteness, we now assume that the interaction Hamiltonian is of the factorized Hermitian form

$$\hat{H}_{\mathrm{SE}} = \hbar \sum_{\alpha} \hat{\mathcal{A}}_{\alpha} \otimes \hat{\mathcal{B}}_{\alpha} = \hbar \sum_{\alpha} \hat{\mathcal{A}}_{\alpha}^{\dagger} \otimes \hat{\mathcal{B}}_{\alpha}^{\dagger}, \tag{3.21}$$

where $\hat{\mathcal{A}}_{\alpha}$ and $\hat{\mathcal{B}}_{\alpha}$ belong to the system and environment Hilbert space, respectively. In the first step we subtract from the interaction Hamiltonian the contributions containing non-zero expectation values of the environment operators $\langle \hat{\mathcal{B}}_{\alpha} \rangle_{\mathrm{res}}$ with respect to the reservoir reduced density matrix $\hat{\rho}_{\mathrm{E}} = \mathrm{Tr}_{\mathrm{S}}\{\hat{\rho}_{\mathrm{T}}\}$. We define $\delta \hat{\mathcal{B}}_{\alpha}(s) = \hat{\mathcal{B}}_{\alpha}(s) - \langle \hat{\mathcal{B}}_{\alpha} \rangle_{\mathrm{res}}$, and add the Hamiltonian

$$\hat{H}_{\mathrm{av}} = \hbar \sum_{\alpha} \hat{\mathcal{A}}_{\alpha} \otimes \langle \hat{\mathcal{B}}_{\alpha} \rangle_{\mathrm{res}}, \tag{3.22}$$

to the system Hamiltonian $\hat{H}_{\mathrm{S}}$, thus defining $\hat{H}_{\mathrm{S}}' = \hat{H}_{\mathrm{S}} + \hat{H}_{\mathrm{av}}$. The remaining part of the interaction Hamiltonian is then

$$\hat{H}_{\mathrm{SE}}' = \hbar \sum_{\alpha,\beta} \hat{\mathcal{A}}_{\alpha\beta}(\omega_{\alpha}) \otimes \delta \hat{\mathcal{B}}_{\beta} = \hbar \sum_{\alpha,\beta} \hat{\mathcal{A}}_{\alpha\beta}^{\dagger}(\omega_{\alpha}) \otimes \delta \hat{\mathcal{B}}_{\beta}^{\dagger}, \tag{3.23}$$

where $\hat{\mathcal{A}}_{\beta} = \sum_{\alpha} \hat{\mathcal{A}}_{\alpha\beta}(\omega_{\alpha})$ and $\hat{\mathcal{A}}_{\alpha\beta}(\omega_{\alpha})$ are the eigenoperators of $\hat{H}_{\mathrm{S}}'$ defined by

$$[\hat{H}_{\mathrm{S}}', \hat{\mathcal{A}}_{\alpha\beta}(\omega_{\alpha})] = -\,\omega_{\alpha} \hat{\mathcal{A}}_{\alpha\beta}(\omega_{\alpha}), \tag{3.24}$$

$$[\hat{H}_{\mathrm{S}}', \hat{\mathcal{A}}_{\alpha\beta}^{\dagger}(\omega_{\alpha})] = \omega_{\alpha} \hat{\mathcal{A}}_{\alpha\beta}^{\dagger}(\omega_{\alpha}). \tag{3.25}$$

By substituting Eq. (3.23) into Eq. (3.20), expanding the commutators, performing the integration[1] in Eq. (3.20) and using $\hat{\rho}_{\mathrm{T}} \approx \hat{\rho}_{\mathrm{S}}(t) \otimes \hat{\rho}_{\mathrm{E}}$, it can be shown that the Liouville-von Neumann equation for $\hat{\rho}_{\mathrm{S}}$ finally becomes [158, 160]

$$\boxed{\frac{\mathrm{d}}{\mathrm{d}t} \hat{\rho}_{\mathrm{S}} = \frac{1}{\mathrm{i}\hbar} [\hat{\tilde{H}}_{S}, \hat{\rho}_{\mathrm{S}}] + \sum_{\beta\beta'\alpha} \frac{\gamma_{\beta'\beta}^{\mathrm{Lin}}(\omega_{\alpha})}{2} \left(2\hat{\mathcal{A}}_{\alpha\beta} \hat{\rho}_{\mathrm{S}} \hat{\mathcal{A}}_{\alpha\beta'}^{\dagger} - \{\hat{\mathcal{A}}_{\alpha\beta'}^{\dagger} \hat{\mathcal{A}}_{\alpha\beta}, \hat{\rho}_{\mathrm{S}}\} \right).} \tag{3.26}$$

Here $\gamma_{\beta\beta'}^{\mathrm{Lin}}$ are the effective rates which depend on the reservoir two-time correlation functions

$$\gamma_{\beta'\beta}^{\mathrm{Lin}}(\omega_{\alpha}) = 2\mathrm{Re}\left\{ \int_{0}^{\infty} \langle \delta \hat{\mathcal{B}}_{\beta'}^{\dagger}(s) \delta \hat{\mathcal{B}}_{\beta}(0) \rangle e^{\mathrm{i}\omega_{\alpha} s} \, \mathrm{d}s \right\}, \tag{3.27}$$

The Hamiltonian $\hat{\tilde{H}}_{\mathrm{S}}$ in Eq. (3.26) is furthermore generally different from the bare system Hamiltonian $\hat{H}_{\mathrm{S}}$

$$\hat{\tilde{H}}_{S} = \hat{H}_{\mathrm{S}} + \hat{H}_{\mathrm{av}} + \hat{H}_{\mathrm{Lamb}}, \tag{3.28}$$

---

[1] The t' integration is performed as $\int_{t}^{t+\Delta t} \mathrm{d}t' \, I(t') \approx \Delta t \cdot I(t)$.

as it contains the contribution $\hat{H}_{\mathrm{av}}$ due to the reservoir averages [Eq. (3.22)] and the Lamb shift due to the reservoir:

$$\hat{H}_{\mathrm{Lamb}} = \hbar \sum_{\alpha} \sum_{\beta\beta'} S^{\mathrm{Lamb}}_{\beta\beta'}(\omega_\alpha) \hat{\mathcal{A}}^{\dagger}_{\alpha\beta}(\omega_\alpha) \hat{\mathcal{A}}_{\alpha\beta'}(\omega_\alpha), \tag{3.29}$$

with

$$S^{\mathrm{Lamb}}_{\beta'\beta}(\omega_\alpha) = \mathrm{Im}\left\{ \int_0^\infty \langle \delta\hat{\mathcal{B}}^{\dagger}_{\beta'}(s) \delta\hat{\mathcal{B}}_{\beta}(0) \rangle e^{\mathrm{i}\omega_\alpha s}\, \mathrm{d}s \right\}, \tag{3.30}$$

where $\mathrm{Im}\{\cdot\}$ is the imaginary part. The effective rates $\gamma^{\mathrm{Lin}}_{\beta'\beta}(\omega_\alpha)$ and frequencies $S^{\mathrm{Lamb}}_{\beta'\beta}(\omega_\alpha)$ arise from the τ integration in Eq. (3.20).

In practical calculations it is often possible to neglect the Hamiltonian terms H_{av} and H_{Lamb} or to incorporate them directly into the system Hamiltonian. Finally, the last term in Eq. (3.26) represents the damping and decoherence of the system and is commonly denoted as the Lindblad term (or the Lindblad-Kossakowski term):

$$\mathscr{L}(\hat{\rho}_{\mathrm{S}}) = \sum_{\beta\beta'\alpha} \frac{\gamma^{\mathrm{Lin}}_{\beta'\beta}(\omega_\alpha)}{2} \left(2\hat{\mathcal{A}}_{\alpha\beta}\, \hat{\rho}_{\mathrm{S}}\, \hat{\mathcal{A}}^{\dagger}_{\alpha\beta'} - \{\hat{\mathcal{A}}^{\dagger}_{\alpha\beta'} \hat{\mathcal{A}}_{\alpha\beta}, \hat{\rho}_{\mathrm{S}}\} \right). \tag{3.31}$$

In practice, the Lindblad terms can be often written as a sum of independent contributions

$$\mathscr{L}(\hat{\rho}) = \sum_i \mathscr{L}^{\gamma_{\mathcal{O}_i}}_{\hat{\mathcal{O}}_i}(\hat{\rho}) \tag{3.32}$$

of the form:

$$\boxed{\mathscr{L}^{\gamma_{\mathcal{O}_i}}_{\hat{\mathcal{O}}_i}(\hat{\rho}_{\mathrm{S}}) = \frac{\gamma_{\mathcal{O}_i}}{2} \left(2\hat{\mathcal{O}}_i\, \hat{\rho}_{\mathrm{S}}\, \hat{\mathcal{O}}^{\dagger}_i - \left\{ \hat{\mathcal{O}}^{\dagger}_i \hat{\mathcal{O}}_i, \hat{\rho}_{\mathrm{S}} \right\} \right),} \tag{3.33}$$

with $\hat{\mathcal{O}}_i$ being the respective system operators and $\gamma_{\mathcal{O}_i}$ the corresponding decay rates.

Practical construction of the effective Liouville-von Neumann equation

For convenience we provide here a condensed form of the procedure described above. The practical construction of the effective Liouville-von Neumann equation for the system density matrix can be summarized in the following practical steps:

- The total Hamiltonian of the interesting system and environment is conveniently split into the form of Eq. (3.13), with $\hat{H}_{\mathrm{SE}} = \hbar \sum_\beta \hat{\mathcal{A}}_\beta \otimes \hat{\mathcal{B}}_\beta$.

- The reservoir operators are re-expressed in the form $\hat{\mathcal{B}}_\beta(s) = \delta\hat{\mathcal{B}}_\beta(s) + \langle \hat{\mathcal{B}}_\beta \rangle_{\mathrm{res}}$ and the average $\langle \hat{B}_\beta \rangle_{\mathrm{res}}$ becomes part of the system Hamiltonian $\hat{H}'_{\mathrm{S}} = \hat{H}_{\mathrm{S}} + \hat{H}_{\mathrm{av}}$, with $\hat{H}_{\mathrm{av}} = \hbar \sum_{\alpha,\beta} \hat{\mathcal{A}}_{\alpha\beta}(\omega_\alpha) \otimes \langle \hat{\mathcal{B}}_\beta \rangle_{\mathrm{res}}$.

- The new interaction Hamiltonian is constructed as $\hat{H}'_{\mathrm{SE}} = \hbar \sum_{\alpha,\beta} \hat{\mathcal{A}}_{\alpha\beta}(\omega_\alpha) \otimes \delta\hat{\mathcal{B}}_\beta$, where $\hat{\mathcal{A}}_{\alpha\beta}(\omega_\alpha)$ are the eigenoperators of $\hat{H}'_{\mathrm{S}}$.
- The two-time correlators of the environment are calculated to obtain the effective rates $\gamma^{\mathrm{Lin}}_{\beta'\beta}(\omega_\alpha)$ [Eq. (3.27)] and frequencies $S^{\mathrm{Lamb}}_{\beta'\beta}(\omega_\alpha)$ [Eq. (3.30)] to finally construct the Liouville-von Neumann equation [Eq. (3.26)].

Dynamics of the operator mean values

Equation (3.26) represents the central expression of this chapter which becomes a powerful tool for calculation of incoherent dynamics of open-quantum systems. With Eq. (3.26) in hand, we can construct differential equations governing the evolution of the system operator averages $\langle \hat{O}_{\mathrm{S}}(t) \rangle$ under the influence of the environment:

$$\boxed{\begin{aligned}\left\langle \dot{\hat{O}}_{\mathrm{S}} \right\rangle &= \frac{1}{\mathrm{i}\hbar} \left\langle \left[\hat{O}_{\mathrm{S}}, \hat{\tilde{H}}_{\mathrm{S}} \right] \right\rangle + \\ &\left\langle \sum_{\beta\beta'\alpha} \gamma^{\mathrm{Lin}}_{\beta'\beta}(\omega_\alpha) \left(2\hat{\mathcal{A}}^\dagger_{\alpha\beta'}\, \hat{O}_{\mathrm{S}}\, \hat{\mathcal{A}}_{\alpha\beta} - \left\{ \hat{\mathcal{A}}^\dagger_{\alpha\beta'} \hat{\mathcal{A}}_{\alpha\beta}, \hat{O}_{\mathrm{S}} \right\} \right) \right\rangle .\end{aligned}} \tag{3.34}$$

Equation (3.34) generally yields a set of differential equations that are a useful starting point for further numerical or analytical treatment.

Another approach that leads to a numerically advantageous form of the master equation [Eq. (3.26)] consists in rewriting the density matrix of the system $\hat{\rho}_{\mathrm{S}}$ in the form of a column vector $\vec{\hat{\rho}}_{\mathrm{S}}$ and writing Eq. (3.26) formally as

$$\dot{\vec{\hat{\rho}}}_{\mathrm{S}} = \mathcal{L} \vec{\hat{\rho}}_{\mathrm{S}}, \tag{3.35}$$

where $\mathcal{L}$ is the Liouvillian superoperator governing the time evolution of $\hat{\rho}_{\mathrm{S}}$ constructed from the Hamiltonian and the Lindblad terms (see Appendix B.1 for details about the technical implementation).

3.1.4 Two-time averages, the quantum regression theorem

The dynamics of system operators has been introduced in Eq. (3.34). Nevertheless, it is often necessary to describe correlations of observable quantities measured at different times. For example, the optical spectra can be retrieved from two-time (auto-)correlation functions of electromagnetic field operators. Here we briefly introduce the basic concepts that can be used for calculation of the two-time correlators and present the quantum regression theorem as a powerful tool that facilitates their practical numerical and analytical calculation.

The two-time correlation function is conveniently defined in the *Heisenberg picture*, in which the quantum states $|\psi\rangle$ become time independent and the system dynamics is carried by the quantum operators $\hat{O}(t)$ [161]. If $\hat{H}$ is the Hamiltonian of the total system (i.e. containing both the interesting part of the system and the reservoir), the Heisenberg-picture operators evolve in time as

$$\hat{O}(t) = e^{\mathrm{i}\hat{H}t/\hbar}\,\hat{O}(0)\,e^{-\mathrm{i}\hat{H}t/\hbar} = \hat{U}^{\dagger}(t,0)\,\hat{O}(0)\,\hat{U}(t,0) = \hat{U}^{\dagger}(t,0)\,\hat{O}\,\hat{U}(t,0), \tag{3.36}$$

where on the right side of Eq. (3.36) the operator $\hat{O}(0) \equiv \hat{O}$ is the operator in the *Schrödinger picture*, i.e. the time-independent operator.

A two-time correlation function $\langle \hat{O}_1(t)\hat{O}_2(t+\tau)\rangle$ of two operators $\hat{O}_1$ and $\hat{O}_2$ is defined as

$$\begin{aligned}
\langle \hat{O}_1(t)\hat{O}_2(t+\tau)\rangle &= \mathrm{Tr}\left\{\hat{O}_1(t)\,\hat{O}_2(t+\tau)\,\hat{\rho}_{\mathrm{T}}\right\} && (3.37)\\
&= \mathrm{Tr}\{\hat{O}_1\,\hat{U}^{\dagger}(t+\tau,t)\,\hat{O}_2\,\hat{U}(t+\tau,t)\,\underbrace{\left[\hat{U}(t,0)\,\hat{\rho}_{\mathrm{T}}\,\hat{U}^{\dagger}(t,0)\right]}_{\hat{\rho}_{\mathrm{T}}(t)}\} && (3.38)\\
&= \mathrm{Tr}\left\{\hat{O}_2\left[\hat{U}(t+\tau,t)\,\hat{\rho}_{\mathrm{T}}(t)\,\hat{O}_1\,\hat{U}^{\dagger}(t+\tau,t)\right]\right\} && (3.39)\\
&= \mathrm{Tr}_{\mathrm{S}}\left\{\hat{O}_2\,\mathrm{Tr}_{\mathrm{E}}\left\{\hat{U}(t+\tau,t)\,\hat{\rho}_{\mathrm{T}}(t)\,\hat{O}_1\,\hat{U}^{\dagger}(t+\tau,t)\right\}\right\} && (3.40)
\end{aligned}$$

with $\hat{\rho}_{\mathrm{T}}$ the density matrix of the system and we used $\hat{U}(t+\tau,0) = \hat{U}(t+\tau,t)\hat{U}(t,0)$ [158]. If we further define

$$\hat{P}(t+\tau,t) = \mathrm{Tr}_{\mathrm{E}}\left\{\hat{U}(t+\tau,t)\,\hat{\rho}_{\mathrm{T}}(t)\,\hat{O}_1\,\hat{U}^{\dagger}(t+\tau,t)\right\} \tag{3.41}$$

and write

$$\langle \hat{O}_1(t)\hat{O}_2(t+\tau)\rangle = \mathrm{Tr}_{\mathrm{S}}\left\{\hat{O}_2\,\hat{P}(t+\tau,t)\right\}, \tag{3.42}$$

we notice that the two-time correlation function assumes the form of the average of the operator $\hat{O}_2$ where the system density matrix $\hat{\rho}_{\mathrm{S}}$ is replaced by $\hat{P}(t+\tau,t)$ that evolves as a function of τ. In case that the density matrix $\hat{\rho}_{\mathrm{T}}(t)$ approximately factorizes as $\hat{\rho}_{\mathrm{T}} \approx \hat{\rho}_{\mathrm{S}} \otimes \hat{\rho}_{\mathrm{E}}$ and assuming that $\hat{O}_1$ and $\hat{O}_2$ are the system operators, the expression in Eq. (3.41) simplifies

$$\hat{P}(t+\tau,t) = \hat{U}(t+\tau,t)\,\hat{\rho}_{\mathrm{S}}(t)\,\hat{O}_1\,\hat{U}^{\dagger}(t+\tau,t). \tag{3.43}$$

Moreover, if the system density matrix obeys Eq. (3.35), the operator $\hat{P}(t+\tau,t)$ does so as well (in the vectorized form):

$$\frac{\mathrm{d}}{\mathrm{d}\tau}\vec{\hat{P}}(t+\tau,t) = \mathcal{L}\vec{\hat{P}}(t+\tau,t), \tag{3.44}$$

with the initial condition $\hat{P}(t,t) = \hat{\rho}_{\mathrm{S}}(t)\,\hat{O}_1$. Eq. (3.44) is known as the *quantum regression theorem* (QRT). This theorem is also used in an alternate, more general, form. If the mean value of an operator $\hat{O}_2$ follows the dynamics

$$\langle \hat{O}_2(t+\tau)\rangle = \sum_j g_j^{\mathrm{te}}(\tau)\langle \hat{O}_{2j}(t)\rangle, \tag{3.45}$$

with τ-dependent coefficients $g_j^{\mathrm{te}}(\tau)$, the two-time average is

$$\langle \hat{O}_1(t)\,\hat{O}_2(t+\tau)\rangle = \sum_j g_j^{\mathrm{te}}(\tau)\langle \hat{O}_1(t)\,\hat{O}_{2j}(t)\rangle. \tag{3.46}$$

The form of QRT in Eq. (3.46) is especially advantageous for analytical calculations of two-time correlators.

3.2 Coupling of a two-level system (TLS) to a continuum of reservoir modes (the Wigner-Weisskopf theory)

The formalism of the *Markovian* theory of open quantum systems is powerful for handling the dynamics and spectral properties of quantum systems that are weakly interacting with large reservoirs (the environment). Sometimes, however, the interaction between the system and the reservoir is strong such that the separation into the system part and the environmental part becomes difficult. Such situation commonly occurs if the spectral function of the reservoir [i.e. $\gamma^{\mathrm{Lin}}_{\beta\beta'}(\omega)$ as defined in Eq. (3.27)] varies rapidly with ω around the eigenfrequency ω_α of the system operators $\hat{\mathcal{A}}_{\alpha\beta}$.

In this section we focus on the particular example of a two-level system consisting of the ground $|\mathrm{g}\rangle$ and the excited $|\mathrm{e}\rangle$ state, interacting with a continuum of electromagnetic-field modes and derive the equation of motion for the excited state amplitude following Ref. [158]. This problem has been originally tackled by Wigner and Weisskopf in the context of spontaneous decay of an atomic transition into the electromagnetic modes in vacuum. Here we consider that the TLS is describing an excitonic transition of a molecule that interacts with the electromagnetic modes of its environment. The Hamiltonian of such system becomes

$$\hat{H}_{\mathrm{sys}} = \hbar\omega_{\mathrm{eg}}\hat{\sigma}^\dagger\hat{\sigma} + \sum_k \hbar\omega_k \hat{a}_k^\dagger \hat{a}_k, \tag{3.47}$$

with ω_{eg} the molecular transition frequency, $\hat{\sigma} = |\mathrm{g}\rangle\langle\mathrm{e}|$ and $\hat{a}_k$ ($\hat{a}_k^\dagger$) the annihilation (creation) bosonic operators of the electromagnetic continuum fulfilling $[\hat{a}_k, \hat{a}_{k'}^\dagger] = \delta_{kk'}$. The molecular transition interacts with the electromagnetic-field modes via the interaction Hamiltonian

$$\hat{H}_{\mathrm{I}} = \hat{R}\hat{\sigma}^{\dagger} + \mathrm{H.c.}, \; \hat{R} = \sum_k g_k \hat{a}_k, \tag{3.48}$$

with H.c. standing for the Hermitian conjugate and coupling rates g_k.

We solve now the Schrödinger equation describing the time evolution of the system state with the following *ansatz*:

$$|\psi\rangle = c_0|\mathrm{g}, \{0\omega_k\}\rangle + c_{\mathrm{e}}|\mathrm{e}, \{0\omega_k\}\rangle + \sum_k c_k|\mathrm{g}, \{1\omega_k\}\rangle, \tag{3.49}$$

where the states $|\mathrm{g}(\mathrm{e}), \{0\omega_k\}\rangle$ contain zero excitations of the electromagnetic field modes and the states $|\mathrm{g}, \{1\omega_k\}\rangle$ contain exactly one excitation of the electromagnetic mode k and zero excitations elsewhere. With this *ansatz*, the Schrödinger equation in the interaction picture

$$\mathrm{i}\hbar\frac{\mathrm{d}}{\mathrm{d}t}|\psi\rangle = \hat{H}_{\mathrm{I}}|\psi\rangle \tag{3.50}$$

becomes

$$\begin{aligned} \frac{\mathrm{d}}{\mathrm{d}t}c_{\mathrm{e}}(t) &= -\frac{\mathrm{i}}{\hbar}\sum_k g_k \, e^{\mathrm{i}(\omega_{\mathrm{eg}}-\omega_k)t} c_k(t), \\ \frac{\mathrm{d}}{\mathrm{d}t}c_k(t) &= -\frac{\mathrm{i}}{\hbar}g_k^* \, e^{-\mathrm{i}(\omega_{\mathrm{eg}}-\omega_k)t} c_{\mathrm{e}}(t), \\ \frac{\mathrm{d}}{\mathrm{d}t}c_0(t) &= 0. \end{aligned} \tag{3.51}$$

Notice that the state $|\mathrm{g}, \{0\omega_k\}\rangle$ becomes decoupled from the rest of the dynamics as the total Hamiltonian $\hat{H}_{\mathrm{tot}} = \hat{H}_{\mathrm{sys}} + \hat{H}_{\mathrm{I}}$ conserves the total number of excitations, i.e. $[\hat{H}_{\mathrm{tot}}, \hat{N}] = 0$, with $\hat{N} = \hat{\sigma}^{\dagger}\hat{\sigma} + \sum_k \hat{a}_k^{\dagger}\hat{a}_k$.

The system in Eq. (3.51) can be formally solved by eliminating the amplitudes c_k from the second line of Eq. (3.51)

$$c_k(t) = -\frac{\mathrm{i}}{\hbar}g_k^* \int_0^t e^{-\mathrm{i}(\omega_{\mathrm{eg}}-\omega_k)t_1} c_{\mathrm{e}}(t_1)\,\mathrm{d}t_1 \tag{3.52}$$

and substituting the result back into the first line of Eq. (3.51)

$$\frac{\mathrm{d}}{\mathrm{d}t}c_{\mathrm{e}}(t) = -\int_0^t \underbrace{\frac{1}{\hbar^2}\sum_k |g_k|^2 \, e^{\mathrm{i}(\omega_{\mathrm{eg}}-\omega_k)(t-t_1)}}_{f(t-t_1)} c_{\mathrm{e}}(t_1)\,\mathrm{d}t_1. \tag{3.53}$$

Finally, the equation for the time-evolution of the amplitude $c_e(t)$ becomes an integro-differential equation

$$\boxed{\frac{\mathrm{d}}{\mathrm{d}t}c_{\mathrm{e}}(t) = -\int_0^t f(t-t_1)c_{\mathrm{e}}(t_1)\,\mathrm{d}t_1.} \tag{3.54}$$

We further note that the kernel $f(t-t_1)$ can be expressed using the operator $\hat{R}$ as

$$f(t-t_1) = \mathrm{Tr}_{\mathrm{em}}\left\{\hat{R}(t)\hat{R}^{\dagger}(t_1)\hat{\rho}_{\mathrm{em}}\right\} e^{\mathrm{i}\omega_{\mathrm{eg}}(t-t_1)}, \tag{3.55}$$

where the trace is taken with respect to the electromagnetic modes and $\hat{\rho}_{\mathrm{em}}$ is the density matrix of the electromagnetic modes in the vacuum state. Equation (3.55) becomes useful in cases when the correlation function $\langle\hat{R}(t)\hat{R}^{\dagger}(t_1)\rangle = \mathrm{Tr}_{\mathrm{em}}\left\{\hat{R}(t)\hat{R}^{\dagger}(t_1)\hat{\rho}_{\mathrm{em}}\right\}$ can be calculated by other means than the explicit summation of Eq. (3.53). It is particularly useful to define the so-called spectral function $J_{\mathrm{em}}(\omega)$ via the expression for the kernel $f(t-t_1)$ as:

$$f(t-t_1) \equiv \int_{-\infty}^{\infty} J_{\mathrm{em}}(\omega)\, e^{\mathrm{i}(\omega_{\mathrm{eg}}-\omega)(t-t_1)}\,\mathrm{d}\omega. \tag{3.56}$$

The spectral function $J_{\mathrm{em}}(\omega)$ then combines the information about the molecule-continuum coupling strength and the spectral structure of the continuum, and can bring an intuitive picture into the otherwise highly complex problem of the non-Markovian dynamics of the excited state of the molecule.

Equation (3.54) can be solved by standard mathematical methods involving the Laplace transform or direct numerical integration. In this thesis we adopt the general numerical approach suitable for integration of Eq. (3.54) with $J_{\mathrm{em}}(\omega)$ in a general form. The specifics of the numerical method are further described in Appendix B.2.

3.3 Emission and extinction spectra of quantum systems

We revise here the spectral response of quantum systems. The extinction and emission spectra are often the most accessible information about a quantum system, as implemented in optical experiments. In this chapter we derive the expressions for the emission and extinction spectra of quantum systems and define the spectral line shapes that we use in later chapters.

3.3.1 Photon emission spectrum

In this thesis we are be mostly interested in the calculation of emission spectra of systems involving a plasmonic particle and a molecule pumped by an incident laser. We further assume that the direct radiation of the molecule into the far-field is negligible compared to the indirect emission enhanced by the plasmonic particle. We show now that in such situations the emission spectrum can be obtained from a two-time correlation function of the plasmon annihilation and creation operators.

To that end we define the emission spectrum as the rate of absorption of the far-field photons that are emitted by the plasmonic particle in the detector. We further assume that the detector is composed of a series of absorbers, each of them sensitive to a particular frequency ω. We adopt this particular model of the detector for simplicity of the derivation, which can be performed in different ways [158, 161, 162]. In the linear regime, such detector can be realized as a set of harmonic bosonic absorbers of the respective frequencies ω. We assume each detector's absorber of frequency ω is described by the Hamiltonian $\hat{H}_{\mathrm{det},\omega}$,

$$\hat{H}_{\mathrm{det},\omega} = \hbar\omega \hat{d}_\omega^\dagger \hat{d}_\omega, \tag{3.57}$$

with $\hat{d}_\omega$ the annihilation operator of the absorber. We further assume that the detector mode of frequency ω interacts with the incident field via the detector-photon interaction Hamiltonian $\hat{H}_{\mathrm{det-ph}}$

$$\hat{H}_{\mathrm{det-ph}}(\omega) \propto \hat{E}^{(-)}\hat{d}_\omega + \hat{E}^{(+)}\hat{d}_\omega^\dagger, \tag{3.58}$$

where $\hat{E}^{(+)}$ $[\hat{E}^{(-)}]$ is the operator of the positive (+) [negative (−)] frequency part of the electromagnetic field measured at the position of the detector. The interaction between the measured field $\hat{E}^{(+)}$ $[\hat{E}^{(-)}]$ and the detector perturbs the density matrix of the total system and, in the linear response limit, within the interaction picture defined by the system and detector uncoupled Hamiltonian, it gives rise to the contribution

$$\delta\hat{\rho} \approx \frac{1}{\mathrm{i}\hbar}\int_{-\infty}^{t} \left[\hat{H}_{\mathrm{det-ph}}(t_1), \hat{\rho}\right] \mathrm{d}t_1, \tag{3.59}$$

where $\hat{\rho}$ is the density matrix of the non-interacting system and the detector. The rate of the photon absorption by the detector at the respective frequency ω, $W(\omega)$, proportional to the intensity measured at frequency ω, is then given by the increase of the detector's mode population with time:

$$W(\omega) \propto \frac{\mathrm{d}}{\mathrm{d}t}\langle \hat{d}_\omega^\dagger \hat{d}_\omega\rangle = \frac{\mathrm{i}}{\hbar}\left\langle \left[\hat{H}_{\mathrm{det-ph}}, \hat{d}_\omega^\dagger \hat{d}_\omega\right]\right\rangle. \tag{3.60}$$

In the linear-response regime, by using Eq. (3.59) this rate becomes

$$\begin{aligned} W(\omega) &\propto \mathrm{Tr}\left\{\int_{-\infty}^{t} \left[\hat{H}_{\mathrm{det-ph}}(t), \hat{d}_\omega^\dagger \hat{d}_\omega\right] \left[\hat{H}_{\mathrm{det-ph}}(s), \hat{\rho}\right] \mathrm{d}s\right\} \\ &\propto \mathrm{Tr}\Bigg\{ \int_{-\infty}^{t} \left[\hat{E}^{(-)}(t)\hat{d}_\omega e^{-\mathrm{i}\omega t} - \hat{E}^{(+)}(t)\hat{d}_\omega^\dagger e^{\mathrm{i}\omega t}\right] \\ &\times \left[\hat{E}^{(-)}(s)\hat{d}_\omega e^{-\mathrm{i}\omega s} + \hat{E}^{(+)}(s)\hat{d}_\omega^\dagger e^{\mathrm{i}\omega s}, \hat{\rho}\right] \mathrm{d}s\Bigg\}. \end{aligned} \tag{3.61}$$

We assume that the detector is initially in the ground state and thus $\langle \hat{d}_\omega \hat{d}_\omega \rangle = \langle \hat{d}_\omega^\dagger \hat{d}_\omega^\dagger \rangle = \langle \hat{d}_\omega^\dagger \hat{d}_\omega \rangle = 0$ and $\langle \hat{d}_\omega \hat{d}_\omega^\dagger \rangle = 1$, which yields for $W(\omega)$:

$$\begin{aligned} W(\omega) &\propto \mathrm{Tr}\left\{\int_{-\infty}^{t} \left[\hat{E}^{(-)}(t)\hat{E}^{(+)}(s)e^{\mathrm{i}\omega(s-t)} + \hat{E}^{(-)}(s)\hat{E}^{(+)}(t)e^{\mathrm{i}\omega(t-s)}\right] \mathrm{d}s\right\} \\ &= \mathrm{Tr}\left\{\int_{0}^{\infty} \left[\hat{E}^{(-)}(t)\hat{E}^{(+)}(t-\tau)e^{-\mathrm{i}\omega\tau} + \hat{E}^{(-)}(t-\tau)\hat{E}^{(+)}(t)e^{\mathrm{i}\omega\tau}\right] \mathrm{d}\tau\right\} \\ &= \int_{0}^{\infty} \left[\langle \hat{E}^{(-)}(t-\tau)\hat{E}^{(+)}(t)\rangle e^{\mathrm{i}\omega\tau} + \mathrm{H.~c.}\right] \mathrm{d}\tau \\ &= 2\mathrm{Re}\left\{\int_{0}^{\infty} \langle \hat{E}^{(-)}(t-\tau)\hat{E}^{(+)}(t)\rangle e^{\mathrm{i}\omega\tau}\, \mathrm{d}\tau\right\} \\ &= 2\mathrm{Re}\left\{\int_{0}^{\infty} \langle \hat{E}^{(-)}(t)\hat{E}^{(+)}(t+\tau)\rangle e^{\mathrm{i}\omega\tau}\, \mathrm{d}\tau\right\}. \end{aligned} \tag{3.62}$$

In the last step we used the identity $\langle \hat{E}^{(-)}(t-\tau)\hat{E}^{(+)}(t)\rangle = \langle \hat{E}^{(-)}(t)\hat{E}^{(+)}(t+\tau)\rangle$, which follows from the properties of the two-time correlation functions. In the steady state we set $t = 0$ and finally obtain the emission spectrum $s_\mathrm{e}(\omega) \propto W(\omega)$ in the form

$$s_\mathrm{e}(\omega) \propto \mathrm{Re}\left\{\int_{0}^{\infty} \left\langle \hat{E}^{(-)}(0)\hat{E}^{(+)}(\tau)\right\rangle e^{\mathrm{i}\omega\tau}\, \mathrm{d}\tau\right\}. \tag{3.63}$$

The electromagnetic field at the detector is generated by the radiation of the particle plasmon (assuming that the molecule radiates dominantly via the plasmon) and can be connected to the annihilation, $\hat{E}^{(+)} \propto \hat{a}$, and creation $\hat{E}^{(-)} \propto \hat{a}^\dagger$ operators of the radiative plasmonic mode. We are therefore led to define the plasmon emission spectrum as

$$\boxed{s_\mathrm{e}(\omega) \equiv 2\mathrm{Re}\left\{\int_{0}^{\infty} \mathrm{d}\tau\, \underbrace{\langle \hat{a}^\dagger(0)\hat{a}(\tau)\rangle}_{g_\mathrm{e}} e^{\mathrm{i}\omega\tau}\right\},} \tag{3.64}$$

where for further convenience we have introduced the two-time correlation function

g_e. Equation (3.64) does not include the effect of the electromagnetic-field propagation from the plasmonic particle to the detector. The signal that is actually measured at the detector $S_\mathrm{e}(\omega)$ thus contains an additional prefactor that reflects the spatial dependence of the plasmon radiation pattern and also encompasses the frequency-dependent factor $I(\mathbf{r},\omega)$ originating from the density of states of the radiating electromagnetic fields

$$S_\mathrm{e}(\omega) = I(\mathbf{r},\omega)\, s_\mathrm{e}(\omega). \tag{3.65}$$

For a radiating plasmonic particle in vacuum, the frequency dependence of $I(\mathbf{r},\omega)$ is $I(\mathbf{r},\omega) \propto \omega^4/|\mathbf{r}|^2$. In this thesis we will keep the convention of presenting the spectra in the more symmetrical form given by $s_\mathrm{e}(\omega)$ [Eq. (3.64)], free of far-field radiation effects.

3.3.2 Extinction spectrum

The linear extinction spectrum of a weak probe can be evaluated in close analogy with the emission spectra using the two-time correlation functions of the system operators [163–165]. We can calculate the extinction as the power that the probe field dissipates to drive the probed system.

We follow the argument of Mollow [164] that starts by defining the interaction of the system with the weak probe beam in the form

$$\hat{H}_\mathrm{P} = \hbar\mathcal{E}_\mathrm{P}\hat{a}^\dagger e^{-\mathrm{i}\omega_\mathrm{P}t} + \mathrm{H.c.}, \tag{3.66}$$

with $\mathcal{E}_\mathrm{P}$ the amplitude of the interaction of the system with the probe of frequency ω_P that is assumed to be close to the system resonance frequency such that the rotating-wave approximation applies. The system is represented by the annihilation (creation) operator $\hat{a}$ ($\hat{a}^\dagger$), which can be in general substituted by another system operator that appropriately describes the interaction with the probe. The weak driving represented by $\hat{H}_\mathrm{P}$ induces a small change in the density matrix $\delta\hat{\rho}$ of the probed system which is given by the following approximate expression within the lowest order of perturbation theory:

$$\delta\hat{\rho} \approx \frac{1}{\mathrm{i}\hbar}\int_{-\infty}^{t} \left[\hat{H}_\mathrm{P}(t_1), \hat{\rho}\right] \mathrm{d}t_1, \tag{3.67}$$

where $\hat{\rho}$ is the unperturbed density matrix of the system in the steady state. On the other hand, the probing field drives the system and therefore dissipates its energy. We derive the rate of the energy dissipation by explicitly quantizing the probe field and introduce the probe-field Hamiltonian $\hat{H}_\mathrm{PR}$

$$\hat{H}_\mathrm{PR} = \hbar\omega_\mathrm{P}\hat{c}^\dagger\hat{c}, \tag{3.68}$$

where $\hat{c}$ ($\hat{c}^\dagger$) are the bosonic annihilation (creation) operators. We further assume that the probing field is in a coherent state $|\mathcal{E}_{\mathrm{P}}(t)\rangle$, with $\mathcal{E}_{\mathrm{P}}(t)=\mathcal{E}_{\mathrm{P}}e^{-\mathrm{i}\omega_{\mathrm{P}}t}$ and

$$\hat{c}\,|\mathcal{E}_{\mathrm{P}}(t)\rangle=\mathcal{E}_{\mathrm{P}}(t)|\mathcal{E}_{\mathrm{P}}(t)\rangle. \tag{3.69}$$

Using Eq. (3.69), the probe-system coupling Hamiltonian in Eq. (3.66) can be formally written as

$$\hat{H}_{\mathrm{P}}=\hbar(\hat{c}^{\dagger}\hat{a}+\hat{c}\hat{a}^{\dagger}), \tag{3.70}$$

which becomes identical to Eq. (3.66) if the Hamiltonian (3.70) is averaged with respect to the probe degrees of freedom $\langle\mathcal{E}_{\mathrm{P}}(t)|\hat{H}_{\mathrm{P}}|\mathcal{E}_{\mathrm{P}}(t)\rangle$. The power dissipated by the probe, i.e. absorbed by the system, can then be found as

$$P_{\mathrm{abs}}=-\hbar\omega_{\mathrm{P}}\frac{\mathrm{d}}{\mathrm{d}t}\langle\hat{c}^{\dagger}\hat{c}\rangle. \tag{3.71}$$

From Eq. (3.9) we find the rate of dissipation of the probe energy as

$$\frac{\mathrm{d}}{\mathrm{d}t}\langle\hat{c}^{\dagger}\hat{c}\rangle\ =\frac{\mathrm{i}}{\hbar}\left\langle\left[\hat{H}_{\mathrm{P}},\hat{c}^{\dagger}\hat{c}\right]\right\rangle, \tag{3.72}$$

which, using Eq. (3.71) and applying the average with respect to the probe coherent state, leads to

$$P_{\mathrm{abs}}=\mathrm{i}\hbar\omega_{\mathrm{P}}\langle\mathcal{E}_{\mathrm{P}}^{*}e^{\mathrm{i}\omega_{\mathrm{P}}t}\hat{a}-\mathcal{E}_{\mathrm{P}}e^{-\mathrm{i}\omega_{\mathrm{P}}t}\hat{a}^{\dagger}\rangle\equiv\langle\hat{H}_{\mathrm{PW}}\rangle, \tag{3.73}$$

where the average is defined with respect to the perturbation of the density matrix $\delta\hat{\rho}$ and we have defined

$$\hat{H}_{\mathrm{PW}}(t)=\mathrm{i}\hbar\omega_{\mathrm{P}}\left(\mathcal{E}_{\mathrm{P}}^{*}e^{\mathrm{i}\omega_{\mathrm{P}}t}\hat{a}-\mathcal{E}_{\mathrm{P}}e^{-\mathrm{i}\omega_{\mathrm{P}}t}\hat{a}^{\dagger}\right). \tag{3.74}$$

The probe absorption P_{abs} is thus

$$\begin{aligned}P_{\mathrm{abs}}=\mathrm{Tr}\left\{\hat{H}_{\mathrm{PW}}(t)\delta\hat{\rho}\right\}=&\frac{1}{\mathrm{i}\hbar}\int_{-\infty}^{t}\mathrm{Tr}\left\{\hat{H}_{\mathrm{PW}}(t)\left[\hat{H}_{\mathrm{P}}(t_1),\hat{\rho}\right]\right\}\mathrm{d}t_1\\=&\frac{1}{\mathrm{i}\hbar}\int_{-\infty}^{t}\mathrm{Tr}\left\{\left[\hat{H}_{\mathrm{PW}}(t),\hat{H}_{\mathrm{P}}(t_1)\right]\hat{\rho}\right\}\mathrm{d}t_1.\end{aligned} \tag{3.75}$$

We further substitute Eqs. (3.66) and (3.74) into Eq. (3.75) and obtain the expression for the absorbed power

$$\begin{aligned}P_{\mathrm{abs}}\approx&\hbar\omega_{\mathrm{P}}|\mathcal{E}_{\mathrm{P}}|^2\int_{-\infty}^{t}\mathrm{Tr}\left\{\left[\hat{a}(t)\hat{a}^{\dagger}(t_1)e^{-\mathrm{i}\omega_{\mathrm{P}}(t_1-t)}-\hat{a}^{\dagger}(t)\hat{a}(t_1)e^{\mathrm{i}\omega_{\mathrm{P}}(t_1-t)}\right]\hat{\rho}\right\}\mathrm{d}t_1+\\&\mathrm{H.c.},\end{aligned} \tag{3.76}$$

where we have disregarded the fast-rotating terms of the form $\hat{a}(t)\hat{a}(t_1)e^{\mathrm{i}\omega_{\mathrm{P}}(t+t_1)}$. Notice also that the trace in Eq. (3.76) contains the steady-state density matrix

$\hat{\rho}$ and the absorbed power is therefore expressed as a property of the unperturbed system. We now define $t_1 = t + \tau$ and assume that the absorption is a stationary process

$$\begin{aligned} P_{\mathrm{abs}} &\approx \hbar\omega_{\mathrm{P}}|\mathcal{E}_{\mathrm{P}}|^2 \int_{-\infty}^{0} \left\langle \hat{a}(t)\hat{a}^\dagger(t+\tau)e^{-\mathrm{i}\omega_{\mathrm{P}}\tau} - \hat{a}^\dagger(t)\hat{a}(t+\tau)e^{\mathrm{i}\omega_{\mathrm{P}}\tau}\right\rangle \mathrm{d}\tau + \mathrm{H.c.} \\ &= \hbar\omega_{\mathrm{P}}|\mathcal{E}_{\mathrm{P}}|^2 \int_{-\infty}^{0} \left\langle \left[\hat{a}(t+\tau), \hat{a}^\dagger(t)\right]\right\rangle e^{\mathrm{i}\omega_{\mathrm{P}}\tau}\mathrm{d}\tau + \mathrm{H.c.} \\ &= \hbar\omega_{\mathrm{P}}|\mathcal{E}_{\mathrm{P}}|^2 \int_{0}^{\infty} \left\langle \left[\hat{a}(t+\tau), \hat{a}^\dagger(t)\right]\right\rangle e^{\mathrm{i}\omega_{\mathrm{P}}\tau}\mathrm{d}\tau + \mathrm{H.c.} \\ &= \hbar\omega_{\mathrm{P}}|\mathcal{E}_{\mathrm{P}}|^2 2\mathrm{Re}\left\{ \int_{0}^{\infty} \underbrace{\left\langle \left[\hat{a}(t+\tau), \hat{a}^\dagger(t)\right]\right\rangle}_{g_{\mathrm{ta}}} e^{\mathrm{i}\omega_{\mathrm{P}}\tau}\mathrm{d}\tau \right\}. \\ &= \hbar\omega_{\mathrm{P}}|\mathcal{E}_{\mathrm{P}}|^2 2\mathrm{Re}\left\{ \int_{0}^{\infty} \underbrace{\left\langle \left[\hat{a}(\tau), \hat{a}^\dagger(0)\right]\right\rangle}_{g_{\mathrm{ta}}} e^{\mathrm{i}\omega_{\mathrm{P}}\tau}\mathrm{d}\tau \right\}. \end{aligned} \tag{3.77}$$

Where we have defined the two-time correlation function $g_{\mathrm{ta}} = g_{\mathrm{a}} - g_{\mathrm{e}}$ that carries a component representing the pure absorption of the probe by the system

$$g_{\mathrm{a}} = \langle \hat{a}(\tau)\hat{a}^\dagger(0)\rangle \tag{3.78}$$

and a part representing the emission into the probe-field

$$g_{\mathrm{e}} = \langle \hat{a}^\dagger(0)\hat{a}(\tau)\rangle \tag{3.79}$$

that we have introduced in the previous section and that we have shown to yield the emission spectrum $s_{\mathrm{e}}(\omega)$

$$s_{\mathrm{e}}(\omega) = 2\mathrm{Re}\left\{ \int_{0}^{\infty} \left\langle \hat{a}^\dagger(0)\hat{a}(\tau)\right\rangle e^{\mathrm{i}\omega\tau}\mathrm{d}\tau \right\}.$$

In the context of weak-probe absorption, $s_{\mathrm{e}}(\omega)$ is the emission stimulated by the probe field. Using the above results we can define the direct probe-absorption spectrum $s_{\mathrm{a}}(\omega)$ as

$$\boxed{s_{\mathrm{a}}(\omega) \equiv 2\mathrm{Re}\left\{ \int_{0}^{\infty} \left\langle \hat{a}(\tau)\hat{a}^\dagger(0)\right\rangle e^{\mathrm{i}\omega\tau}\mathrm{d}\tau \right\},} \tag{3.80}$$

where we disregard the pre-factors appearing in Eq. (3.77).

The full expression for the absorption spectrum derived in Eq. (3.77) can be used to calculate the weak-probe absorption even in the case that the quantum system is driven by external stimuli. In such a case, the total probe absorption has to contain the part representing the direct absorption $s_{\mathrm{a}}(\omega)$ as well as the stimulated emission $s_{\mathrm{e}}(\omega)$. In case that the latter contribution prevails, the total absorption spectrum $s_{\mathrm{ta}}(\omega)$

$$s_{\mathrm{ta}}(\omega) = s_{\mathrm{a}}(\omega) - s_{\mathrm{e}}(\omega), \tag{3.81}$$

can be negative, implying that the system provides an overall gain.

3.4 Summary

The main purpose of this chapter is to provide a basic introduction to the concepts and expressions of the open-quantum system's theory in a compact way that we can later apply to study plasmon-assisted fluorescence in Part III and Raman scattering in Part IV of the thesis. This chapter also has the ambition to practically guide the reader through the theory as it does not pay too much attention to formal proofs but rather discusses the working principles of the quantum-mechanical tools that can be directly transfered to applications.

We have derived the basic equations that govern the dynamics of a system density matrix for closed and open quantum systems which is a starting point for the quantum-mechanical treatment of interacting systems relevant to plasmon-enhanced spectroscopies.

As this thesis deals mainly with optical and infrared molecular spectroscopy, special attention has been paid to the derivation of photon emission and extinction spectra of quantum systems interacting with light. We have provided these full derivations that allow us to express the system spectral response in terms of one-sided Fourier transforms of the system operators, often omitted in standard textbooks.

Part II

Surface-Enhanced Infrared Spectroscopy

Chapter 4

Dielectric theory of Surface-Enhanced Infrared Spectroscopy

The ability of nanometer- and micrometer-scaled metallic particles to squeeze incident electromagnetic field at their surface and thus strongly enhance the interaction of light with samples in their close vicinity has found applications in a broad range of plasmon-enhanced spectroscopic methods [23] including Surface-Enhanced Raman Spectroscopy (SERS) [8, 11, 15, 18, 166–174], Surface-Enhanced Infrared Spectroscopy (SEIRS, alternatively called Surface Enhanced Infrared Absorption: SEIRA) [24–39], Surface-Enhanced Fluorescence (SEF) [44–48] spectroscopy or optical absorption spectroscopy. In this chapter we focus on the classical description of the working principle standing behind SEIRS.

SEIRS is an extension of the conventional infrared (IR) absorption spectroscopy [175], where the incident infrared radiation is absorbed by infrared active vibrational modes of the sample (often molecules), and the absorption feature is manifested in the far-field optical absorption spectrum as a resonance peak. As the vibrational modes of molecules carry information about the molecular structure, the set of these vibrational absorption peaks can be used as a fingerprint which can unambiguously identify specific chemical substances and their bonding in different chemical compounds and materials [176–179]. This chemical fingerprinting finds its application in a broad range of fields ranging from basic research to applied science and industry.

Nevertheless, the interaction strength (the spectral cross-section) of molecules is usually extremely weak which in the conventional IR spectroscopy hinders the detection of the vibrational fingerprints of small amounts of molecules. In SEIRS this situation can be overcome by placing the molecules in the vicinity of metallic surfaces that support plasmonic resonances in the IR. The strongly enhanced interaction of the molecule with the incident light then allows for accessing the molecular vibrational fingerprints even for minute sample quantities [34].

In the following sections the basics of the IR activity of molecules is first outlined and then the focus is placed on the electromagnetic mechanism leading to SEIRS enhancement. In Section 4.4 we study a particular example of plasmonic structures utilized in SEIRS and perform a numerical study of their performance for enhancement of molecular signals in the IR.

4.1 IR activity of molecules

IR and Raman spectroscopy exploits the fact that molecular vibrations are able to interact with incident electromagnetic waves revealing fingerprint vibrational signatures in their respective spectra. However, not all molecular vibrations efficiently interact with probing light being *spectrally active*. Here we discuss the basic principles standing behind the vibrational spectral activity of molecules in infrared absorption spectroscopy.

IR spectroscopy is based on the direct excitation of molecular vibrations by the incident electromagnetic radiation. In the point-dipole approximation of the molecule, the vibrational modes interact with radiation via their ground-state dipole moment, $\mathbf{d}(q)$, which parametrically depends on the coordinate q[1] of a given vibrational mode. More precisely, the ground-state dipole moment of the molecule can be expressed as:

$$\mathbf{d}(q) = \int \mathbf{r}\, e\, n(\mathbf{r};q)\, \mathrm{d}^3\mathbf{r} + \sum_i \mathbf{R}_i(q) Q_i, \tag{4.2}$$

with $n(\mathbf{r};q)$ the position-dependent ground-state electron density parametrically depending on the vibrational coordinate q, e the electron charge, $\mathbf{R}_i(q)$ the q-dependent position and Q_i the charge of nucleus i. For a molecular vibration to be IR active, the derivative of the molecular dipole moment with respect to q must be non-vanishing. The condition for the IR activity of a molecular vibration therefore is:

$$\boxed{\left.\frac{\partial \mathbf{d}(q)}{\partial q}\right|_{q=0} \neq 0.} \tag{4.3}$$

An electromagnetic wave then upon interaction with the molecule creates an

---

[1] The real space displacements $R_{i,A}(q_\alpha)$ of atom A in direction $i \in \{x,y,z\}$ of mode α are constructed from the mass-weighted coordinate q_α as

$$R_{i,A}(q_\alpha) = \frac{1}{\sqrt{M_A}} S^{\alpha}_{i,A} q_\alpha, \tag{4.1}$$

where M_A is the mass of the atom and $S^{\alpha}_{i,A}$ are elements of a unit vector, $\sum_{i,A}(S^{\alpha}_{i,A})^2 = 1$, that arise from the diagonalization of the vibrational dynamical equations in the mass-weighted coordinates.

induced dipolar moment, $\delta\mathbf{d}$, that is proportional to the amplitude of the incident electromagnetic field, $\mathbf{E}(t)$, via the molecular vibrational polarizability tensor $\boldsymbol{\alpha}_{\text{vib}}$ as

$$\delta\mathbf{d}^{(+)} = \boldsymbol{\alpha}_{\text{vib}} \cdot \mathbf{E}^{(+)}(t), \tag{4.4}$$

where $\delta\mathbf{d}^{(+)}$ and $\mathbf{E}^{(+)}$ are the positive-frequency parts of the respective variables. The polarizability tensor $\boldsymbol{\alpha}_{\text{vib}}$ carries information about the IR active vibrational modes and yields the experimentally observable extinction signal σ_{ext}:

$$\sigma_{\text{ext}} = \frac{k}{\varepsilon_0} \text{Im} \left\{ \frac{1}{3} \text{Tr} \left[\boldsymbol{\alpha}_{\text{vib}} \right] \right\}, \tag{4.5}$$

where the trace $\text{Tr}\{\cdot\}$ arises from averaging over all molecular orientations and $k = \omega/c$.

The vibrational polarizability tensor $\boldsymbol{\alpha}_{\text{vib}}$ emerges from the dynamics of the vibrational mode driven by the incident electromagnetic wave. We can describe the coupling of the vibration with the incident radiation by the interaction potential energy $V_{\text{vib}-\text{rad}}(q)$:

$$V_{\text{vib}-\text{rad}}(q) = -\mathbf{d}(q) \cdot \mathbf{E}(t). \tag{4.6}$$

In the harmonic approximation, the molecular vibration is described as a harmonic oscillator of eigenfrequency Ω with kinetic, $T_{\text{vib}}(\dot{q})$, and potential, $V_{\text{vib}}(q)$, energy:

$$\begin{aligned} T_{\text{vib}} &= \frac{1}{2}\dot{q}^2, \\ V_{\text{vib}} &= \frac{1}{2}\Omega^2 q^2. \end{aligned} \tag{4.7}$$

Eq. (4.6) together with Eqs. (4.7) can be combined into the Lagrangian $\mathfrak{L}(q, \dot{q}, t)$ of the driven vibration as

$$\mathfrak{L} = T_{\text{vib}} - V_{\text{vib}} - V_{\text{vib}-\text{rad}}, \tag{4.8}$$

which yields the Euler-Lagrange equation of motion

$$\frac{\mathrm{d}}{\mathrm{d}t} \left(\frac{\partial \mathfrak{L}}{\partial \dot{q}} \right) = -\frac{\partial \mathfrak{L}}{\partial q}. \tag{4.9}$$

We further approximate $\mathbf{d}(q) \approx \mathbf{d}_0 + \frac{\partial \mathbf{d}}{\partial q}\big|_{q=0} q$ and obtain the differential equation

$$\ddot{q} = -\Omega^2 q + \frac{\partial \mathbf{d}}{\partial q} \cdot \mathbf{E}(t), \tag{4.10}$$

where for brevity we write $\frac{\partial \mathbf{d}}{\partial q} \equiv \frac{\partial \mathbf{d}}{\partial q}\big|_{q=0}$. We further assume that the incident electromagnetic light has a harmonic time dependence $\mathbf{E}(t) = \mathbf{E}^{(+)}(t) + \mathbf{E}^{(-)}(t) =$

$\mathbf{E}_0^{(+)}e^{-\mathrm{i}\omega t} + \mathbf{E}_0^{(-)}e^{\mathrm{i}\omega t}$, with $\mathbf{E}^{(+)}$ $[\mathbf{E}^{(-)}]$ the positive (negative) frequency part defined so that $\mathbf{E}^{(+)} = \left[\mathbf{E}^{(-)}\right]^*$. We further add into Eq. (4.10) the phenomenological damping force, $F_{\mathrm{damp}} = -\gamma_{\mathrm{v}}\dot{q}$, where γ_{v} is the damping coefficient of the particular vibration, and solve it for the particular solution given by the positive-frequency part of the driving field. To that end we assume a positive-frequency particular solution of q in the form $q^{(+)} = q_0^{(+)}e^{-\mathrm{i}\omega t}$ and obtain an algebraic equation for the amplitude $q_0^{(+)}$

$$(\Omega^2 - \omega^2)q_0^{(+)} - \mathrm{i}\gamma_{\mathrm{v}}\omega q_0^{(+)} = \frac{\partial \mathbf{d}}{\partial q} \cdot \mathbf{E}_0^{(+)}, \tag{4.11}$$

which yields

$$q_0^{(+)} = \frac{\frac{\partial \mathbf{d}}{\partial q} \cdot \mathbf{E}_0^{(+)}}{(\Omega^2 - \omega^2) - \mathrm{i}\gamma_{\mathrm{v}}\omega}. \tag{4.12}$$

The positive frequency part of the induced dipole moment, $\delta\mathbf{d}^{(+)} = \delta\mathbf{d}_0^{(+)}e^{-\mathrm{i}\omega t}$ (with $\mathbf{d}_0^{(+)}$ a time-independent amplitude), is then related to the vibrational displacement as $\delta\mathbf{d}^{(+)} = \frac{\partial \mathbf{d}}{\partial q}q^{(+)}$, which leads to:

$$\delta\mathbf{d}_0^{(+)} = \underbrace{\frac{\left(\frac{\partial \mathbf{d}}{\partial q} \otimes \frac{\partial \mathbf{d}}{\partial q}\right)}{(\Omega^2 - \omega^2) - \mathrm{i}\gamma_{\mathrm{v}}\omega}}_{\boldsymbol{\alpha}_{\mathrm{vib}}} \cdot \mathbf{E}_0^{(+)}, \tag{4.13}$$

where $\otimes$ stands for the Kronecker product. From Eq. (4.13) we identify the polarizability tensor of the molecular vibrational mode as:

$$\boxed{\boldsymbol{\alpha}_{\mathrm{vib}} = \frac{\mathbf{F}}{(\Omega^2 - \omega^2) - \mathrm{i}\gamma_{\mathrm{v}}\omega},} \tag{4.14}$$

with

$$\mathbf{F} = \left(\frac{\partial \mathbf{d}}{\partial q} \otimes \frac{\partial \mathbf{d}}{\partial q}\right).$$

The polarizability in Eq. (4.14) has the character of a Lorentz-like resonance with a resonance frequency $\approx \Omega$, and can be brought into the more standard Lorentzian form by further approximation. If one completes the square in the denominator in Eq. (4.14) and neglects the contributions of order $O(\gamma_{\mathrm{v}}^2)$, one obtains:

$$\begin{aligned}\boldsymbol{\alpha}_{\mathrm{vib}} &= \frac{\mathbf{F}}{(\Omega^2-\omega^2)-\mathrm{i}\gamma_{\mathrm{v}}\omega}\\ &\approx \frac{\mathbf{F}}{\left[\Omega-(\omega+\mathrm{i}\frac{\gamma_{\mathrm{v}}}{2})\right]\left[\Omega+(\omega+\mathrm{i}\frac{\gamma_{\mathrm{v}}}{2})\right]}\\ &= \frac{\mathbf{F}}{2\Omega\left[\Omega-(\omega+\mathrm{i}\frac{\gamma_{\mathrm{v}}}{2})\right]}+\underbrace{\frac{\mathbf{F}}{2\Omega\left[\Omega+(\omega+\mathrm{i}\frac{\gamma_{\mathrm{v}}}{2})\right]}}_{\text{off-resonant}}\\ &\approx \frac{\mathbf{F}}{2\Omega\left(\Omega-\omega-\mathrm{i}\frac{\gamma_{\mathrm{v}}}{2}\right)},\end{aligned} \tag{4.15}$$

Where in the last step we have dropped the off-resonant term as we are interested only in the polarizability evaluated close to the vibrational resonance. The final form of $\boldsymbol{\alpha}_{\mathrm{vib}}$ in Eq.(4.15) has the sought form of the Lorentzian resonance, i.e.,

$$\mathrm{Im}\left\{\boldsymbol{\alpha}_{\mathrm{vib}}\right\} \approx \frac{\gamma_{\mathrm{v}}\mathbf{F}}{4\,\Omega\left[(\omega-\Omega)^2+\left(\frac{\gamma_{\mathrm{v}}}{2}\right)^2\right]}, \tag{4.16}$$

and the extinction cross section of the IR active vibrational mode, Eq. (4.5), thus becomes:

$$\boxed{\sigma_{\mathrm{ext}} = \frac{k}{\varepsilon_0}\frac{\gamma_{\mathrm{v}}\mathrm{Tr}\left[\mathbf{F}\right]}{12\,\Omega\left[(\omega-\Omega)^2+\left(\frac{\gamma_{\mathrm{v}}}{2}\right)^2\right]}.} \tag{4.17}$$

The IR-active vibrational mode thus appears in the absorption spectrum as a Lorentzian peak positioned at the frequency of the molecular vibrational mode and its intensity is given by the IR activity of the mode contained in the oscillator strength $\mathbf{F}$.

4.2 Molecular layers and phononic materials

So far we have described the interaction of a single molecule with light. Nevertheless, in SEIRS we usually study an ensemble of molecules forming a layer on top of the surfaces of plasmonic antennas. In practise it is therefore more convenient to describe the material composed of the individual molecular samples as a continuous dielectric medium characterized by an effective dielectric function ε_{S}. The polarizability of a single molecule can be related to the dielectric function of the effective material via the Clausius-Mossotti relation [107, 180]. The Clausius-Mossotti relation self-consistently evaluates how a single molecule is polarized inside of a homogeneously polarized continuous medium composed of molecules of the same type. The permittivity of the effective homogeneous medium is then connected with the single-molecule polarizability, α_{vib} (for simplicity

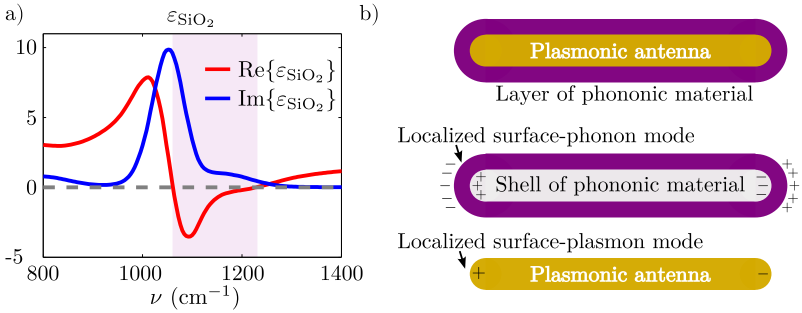

Figure 4.1: (a) Real (Re$\{\varepsilon_{\mathrm{SiO}_2}\}$ - red line) and imaginary (Im$\{\varepsilon_{\mathrm{SiO}_2}\}$ - blue line) part of the experimentally measured dielectric function $\varepsilon_{\mathrm{SiO}_2}$ of SiO$_2$ [181]. In the frequency region where Re$\{\varepsilon_{\mathrm{SiO}_2}\} < 0$ (region marked by the shaded area), structures fabricated of the phononic material can sustain collective surface-phonon modes. (b) An example of a system of a plasmonic antenna covered with a shell of a sample phononic material [e.g. described by the dielectric function shown in (a)]. Both the phononic sample and the plasmonic antenna can sustain collective surface-phonon and surface-plasmon modes, respectively. An example of such surface modes is schematically depicted as the positive (+) and negative (−) induced surface charges on the boundaries of the respective structures.

considered here as isotropic), via

$$\varepsilon_{\mathrm{S}} \approx \frac{3\varepsilon_0 + 2N_{\mathrm{mol}}^{\mathrm{d}}\alpha_{\mathrm{vib}}}{3\varepsilon_0 - N_{\mathrm{mol}}^{\mathrm{d}}\alpha_{\mathrm{vib}}}, \tag{4.18}$$

where $N_{\mathrm{mol}}^{\mathrm{d}}$ is the density of the molecules and ε_0 is the vacuum permittivity.

Another class of materials that yields a strong infrared response are phononic solids [128–130, 182–189]. Phononic materials are often crystalline, polycrystalline or amorphous solids whose structure contains infrared-active bonds. Similarly to the infrared-active molecules, the infrared-active bonds of the phononic materials are able to change the local polarization of the material and thus induce an interaction with the electromagnetic field. A typical example of such a phononic crystal is silicon oxide, whose Si − O bond oscillation induces a strong change of polarization that gives rise to strong IR response [190]. We plot an experimentally measured dielectric function of SiO$_2$, $\varepsilon_{\mathrm{SiO}_2}$, in Fig. 4.1 (a) [181].

In the following we describe the bulk properties of generic phononic materials and of molecular materials on the same footing via the dielectric formalism by considering a model dielectric function, which has the from of a Lorentz oscillator:

$$\varepsilon_{\mathrm{S}}(\omega) = \varepsilon_\infty + \frac{\omega_{\mathrm{OS}}^2}{\omega_{\mathrm{TO}}^2 - \omega^2 - \mathrm{i}\gamma_{\mathrm{v}}\omega}, \tag{4.19}$$

where ε_∞ is the background permittivity, ω_{OS} is the oscillator strength, ω_{TO}

is the frequency of the transverse-optical (TO) phonon and γ_v is the resonance broadening. The parameters of the dielectric function are commonly determined from experimental data. Nevertheless, in the following we use model parameters to freely tune the properties of a phononic sample in order to study the behavior of the phononic modes when interacting plasmonic antennas, such as in SEIRS.

4.2.1 Localized phononic resonances

Similar to the case of plasmonic resonances (see Chapter 1.2.1), if a vibrationally active material is shaped into a finite particle, the dielectric response of the particle results from its self-consistent interaction with the electromagnetic fields [128–130, 182–184]. Especially in case of strongly IR-active phononic crystals, this can give rise to localized surface phonon (phonon-polariton) resonances appearing at frequencies that fit into a range where the real part of the phononic dielectric function is negative [$\mathrm{Re}\{\varepsilon_\mathrm{S}\} < 0$ - shown for the example of $\mathrm{SiO_2}$ as the shaded area in Fig. 4.1 (a)]. The spectral features emerging in the infrared response of such samples deposited on plasmonic antennas [as schematically shown in Fig. 4.1 (b)] must be thus understood as a result of the interaction between the plasmonic modes of the metallic structure and the sample's localized collective phonon-polariton modes [188, 189].

4.3 Surface-Enhanced Infrared Spectroscopy (SEIRS)

As the direct interaction of molecules with electromagnetic radiation is usually very weak, the signal emerging from a few molecules is practically undetectable due to experimental noise. SEIRS provides a way to enhance the spectroscopic signal of molecules by placing them into the vicinity of plasmonic structures, which enhance the effective interaction of the molecule with the incident radiation.

Here we describe the underlying mechanism leading to the electromagnetic enhancement of the signal in SEIRS, which can be understood in the framework of scattering of an electromagnetic wave on a pair of point-like scatterers representing the molecule and the plasmonic particle. We develop here a classical model to describe this interaction and apply it to analyze the spectral response of a realistic system consisting of a linear plasmonic antenna and a sample in the form of a small material patch located on the antenna surface.

4.3.1 Interaction of plasmons with IR active molecular vibrations

When there is direct spectral overlap of the antenna plasmonic resonance and the molecular vibrational resonance, the spectral line shapes of SEIRS exhibit interference features that are often described as Fano-like resonances [191–194], where a pseudo-continuum of electromagnetic modes represented by a broad dipole resonance of the infrared antenna interferes with the narrow vibrational resonance of the analyzed molecules.

We introduce here an analytical model that yields closed-form analytical expressions for typical SEIRS spectra of a plasmonic antenna covered with a molecular sample. To that end we develop a coupled-dipole model, treating the plasmonic antenna and the molecular sample as two point-like polarizable objects, and describe the scattering of incident IR radiation on the antenna-sample system. We attribute to both the antenna and the sample an isotropic polarizability α_{A} and α_{S}, respectively, following the prescription of the previous section:

$$\alpha_{\mathrm{A(S)}} = \frac{f_{\mathrm{A(S)}}}{\Omega^2_{\mathrm{A(S)}} - \omega^2 - \mathrm{i}\gamma_{\mathrm{A(S)}}\omega}, \tag{4.20}$$

with $f_{\mathrm{A(S)}}$ being the antenna (sample) oscillator strength, $\gamma_{\mathrm{A(S)}}$ the antenna (sample) intrinsic damping and $\Omega_{\mathrm{A(S)}}$ the antenna (sample) resonance frequency. The quasistatic polarizability in Eq. (4.20) has the form of a Lorentzian-like resonance whose central frequency and line width are in principle established by the material properties and geometry of the respective scatterer. Note that the macroscopic polarizability $\alpha_{\mathrm{A(S)}}$ is generally determined by the full self-consistent solution of the Maxwell's equations for the antenna (sample) in vacuum defined by its shape and dielectric function. The sample polarizability α_{S} thus reduces to the single-molecule polarizability only if the sample is represented by a single molecule. The coupled-dipole equations describing the scattering of the IR plane-wave on the antenna-sample system can be expressed by means of the antenna and sample dipoles, $\mathbf{d}_{\mathrm{A}}$ and $\mathbf{d}_{\mathrm{S}}$ placed at their respective positions $\mathbf{r}_{\mathrm{A}}$ and $\mathbf{r}_{\mathrm{S}}$, as:

$$\mathbf{d}_{\mathrm{A}} = \alpha_{\mathrm{A}} \left(\mathbf{E}_0(\mathbf{r}_{\mathrm{A}}) + \frac{k^2}{\varepsilon_0} \mathbf{G}(\mathbf{r}_{\mathrm{A}}, \mathbf{r}_{\mathrm{S}}) \cdot \mathbf{d}_{\mathrm{S}} + \frac{k^2}{\varepsilon_0} \mathrm{Im}\left\{ \mathbf{G}(\mathbf{r}_{\mathrm{A}}, \mathbf{r}_{\mathrm{A}}) \right\} \cdot \mathbf{d}_{\mathrm{A}} \right), \tag{4.21}$$

$$\mathbf{d}_{\mathrm{S}} = \alpha_{\mathrm{S}} \left(\mathbf{E}_0(\mathbf{r}_{\mathrm{S}}) + \frac{k^2}{\varepsilon_0} \mathbf{G}(\mathbf{r}_{\mathrm{S}}, \mathbf{r}_{\mathrm{A}}) \cdot \mathbf{d}_{\mathrm{A}} \right), \tag{4.22}$$

where $\mathbf{G}(\mathbf{r}, \mathbf{r}')$ is the dyadic Green's function in vacuum [Eq. (1.11)], k is the vacuum wave number of the incident radiation and $\mathbf{E}_0$ is the incident plane-wave amplitude at the position of the respective scatterer. In Eq. (4.21) we have introduced the self-interaction term that is responsible for the radiation damping of the large plasmonic antenna $\propto \mathrm{Im}\{\mathbf{G}\}$, but we have neglected the radiation damping of the weakly polarizable molecular sample that is effectively dark for the incident radiation. Eqs. (4.21) and (4.22) can be solved for the respective dipole moments:

$$\mathbf{d}_{\mathrm{A}} = \left[\mathbf{I} - \mathrm{Im}\{\mathbf{G}_{\mathrm{AA}}\} \left(\mathbf{I} - \alpha_{\mathrm{A}} \mathbf{G}_{\mathrm{AS}} \alpha_{\mathrm{S}} \mathbf{G}_{\mathrm{SA}} \right)^{-1} \alpha_{\mathrm{A}} \right]^{-1}$$

$$\left(\mathbf{I} - \alpha_{\mathrm{A}} \mathbf{G}_{\mathrm{AS}} \alpha_{\mathrm{S}} \mathbf{G}_{\mathrm{SA}} \right)^{-1} \left(\alpha_{\mathrm{A}} \mathbf{E}_0^{\mathrm{A}} + \alpha_{\mathrm{A}} \mathbf{G}_{\mathrm{AS}} \alpha_{\mathrm{S}} \mathbf{E}_0^{\mathrm{S}} \right), \tag{4.23}$$

$$\mathbf{d}_{\mathrm{S}} = \alpha_{\mathrm{S}} \mathbf{E}_0^{\mathrm{S}} + \alpha_{\mathrm{S}} \mathbf{G}_{\mathrm{SA}} \mathbf{d}_{\mathrm{A}}. \tag{4.24}$$

Here we have introduced the notation $\frac{k^2}{\varepsilon_0}\mathbf{G}(\mathbf{r}_\mathrm{I},\mathbf{r}_\mathrm{J}) \equiv \mathbf{G}_\mathrm{IJ}$ and $\mathbf{E}_0(\mathbf{r}_\mathrm{I}) \equiv \mathbf{E}_0^\mathrm{I}$. We further simplify the tensorial character of the antenna-sample coupling, e.g., assuming that the two scatterers are suitably aligned with respect to each other and with respect to $\mathbf{E}_0$, and introduce the scalar form of Eq. (4.23) for this particular configuration:

$$d_\mathrm{A} = \underbrace{\frac{\dfrac{\alpha_\mathrm{A} E_0^\mathrm{A}}{1-\alpha_\mathrm{A}\alpha_\mathrm{S}G^2}}{1-\dfrac{\mathrm{i}k^3}{6\pi\varepsilon_0}\dfrac{\alpha_\mathrm{A}}{1-\alpha_\mathrm{A}\alpha_\mathrm{S}G^2}}}_{\text{Direct driving}} + \underbrace{\frac{\dfrac{\alpha_\mathrm{A} G\alpha_\mathrm{S} E_0^\mathrm{S}}{1-\alpha_\mathrm{A}\alpha_\mathrm{S}G^2}}{1-\dfrac{\mathrm{i}k^3}{6\pi\varepsilon_0}\dfrac{\alpha_\mathrm{A}}{1-\alpha_\mathrm{A}\alpha_\mathrm{S}G^2}}}_{\text{Indirect driving}}, \tag{4.25}$$

where $G_\mathrm{IJ} = G_\mathrm{JI} = G$ (the interaction is real in the quasi-static limit) is the relevant component of $\mathbf{G}_\mathrm{IJ}$. Assuming that the sample molecules are only weakly interacting with the incident radiation, so that $|G\alpha_\mathrm{S}| \ll 1$, we can neglect the indirect driving term in Eq. (4.25) with respect to the direct driving term. We then identify the effective polarizability of the plasmonic antenna in the presence of the molecular sample as

$$\alpha_\mathrm{eff} = \frac{\dfrac{\alpha_\mathrm{A}}{1-\alpha_\mathrm{A}\alpha_\mathrm{S}G^2}}{1-\dfrac{\mathrm{i}k^3}{6\pi\varepsilon_0}\dfrac{\alpha_\mathrm{A}}{1-\alpha_\mathrm{A}\alpha_\mathrm{S}G^2}} \equiv \frac{\alpha_\mathrm{eff}^\mathrm{AS}}{1-\dfrac{\mathrm{i}k^3}{6\pi\varepsilon_0}\alpha_\mathrm{eff}^\mathrm{AS}}, \tag{4.26}$$

where we have defined the quasi-static effective polarizability of the antenna, $\alpha_\mathrm{eff}^\mathrm{AS}$, which accounts for the antenna-sample interaction:

$$\alpha_\mathrm{eff}^\mathrm{AS} \equiv \frac{\alpha_\mathrm{A}}{1-\alpha_\mathrm{A}\alpha_\mathrm{S}G^2}. \tag{4.27}$$

For completeness we also define the effective polarizability of the sample, $\alpha_\mathrm{eff}^\mathrm{SA}$. Assuming that the molecular sample is dominantly excited by the near field of the plasmonic antenna, the induced dipole moment of the sample thus approximately becomes:

$$d_\mathrm{S} \approx \frac{\dfrac{\alpha_\mathrm{S} G\alpha_\mathrm{A} E_0^\mathrm{A}}{1-\alpha_\mathrm{A}\alpha_\mathrm{S}G^2}}{1-\dfrac{\mathrm{i}k^3}{6\pi\varepsilon_0}\dfrac{\alpha_\mathrm{A}}{1-\alpha_\mathrm{A}\alpha_\mathrm{S}G^2}}, \tag{4.28}$$

from which we can define the effective polarizability of the sample as:

$$\alpha_\mathrm{eff}^\mathrm{SA} \equiv \frac{\dfrac{\alpha_\mathrm{S} G\alpha_\mathrm{A}}{1-\alpha_\mathrm{A}\alpha_\mathrm{S}G^2}}{1-\dfrac{\mathrm{i}k^3}{6\pi\varepsilon_0}\dfrac{\alpha_\mathrm{A}}{1-\alpha_\mathrm{A}\alpha_\mathrm{S}G^2}}. \tag{4.29}$$

We remark that the results of the coupled dipole model can be generalized to extended objects in the form of a coupled-mode model [195] that leads to analogous physical conclusions. In this thesis we thus use the results derived in this point-dipole approximation to gain deeper understanding of the spectral response of the antenna-sample system.

Once the polarizability of the antenna is known, the absorption, extinction and scattering spectra can be calculated from the following relationships (see Chapter 1.1.3):

$$\boxed{\begin{aligned}\sigma_{\text{abs}} &\approx \frac{k}{\varepsilon_0}\text{Im}\{\alpha_{\text{eff}}^{\text{AS}}\}\left|\frac{\alpha_{\text{eff}}}{\alpha_{\text{eff}}^{\text{AS}}}\right|^2, &(4.30)\\ \sigma_{\text{ext}} &\approx \frac{k}{\varepsilon_0}\text{Im}\{\alpha_{\text{eff}}\}, &(4.31)\\ \sigma_{\text{sca}} &\approx \frac{k^4}{6\pi\varepsilon_0^2}\left|\alpha_{\text{eff}}\right|^2 = \sigma_{\text{ext}} - \sigma_{\text{abs}}. &(4.32)\end{aligned}}$$

In Eqs. (4.30), (4.31) and (4.32) we have neglected the contributions to the absorption, extinction and scattering emerging directly from the vibrational sample. Therefore, in our theory, the spectra result only from the absorption and scattering processes taking place on the antenna influenced by the presence of the sample's dark (or effectively dark) resonance.

The spectra of a typical antenna interacting with a molecular sample are plotted in Fig. 4.2 (a) for absorption (blue line), scattering (black line) and extinction (red line). The parameters of the model are chosen such that the antenna scattering dominates over the absorption and both the antenna and sample's resonances are made to spectrally overlap. The specific values of the parameters defining the system are given in the caption of Fig. 4.2. The spectral profiles of the absorption, scattering and extinction contain a Fano-like feature due to the molecular resonance that we further highlight in Fig. 4.2 (b), where we zoom in the spectra of Fig. 4.2 (a) and normalize them to the spectral response of the bare antenna (antenna's absorption, $\sigma_{\text{abs}}^{\text{A}}$, extinction, $\sigma_{\text{ext}}^{\text{A}}$, and scattering, $\sigma_{\text{sca}}^{\text{A}}$). The extinction and the scattering spectra feature a clear spectral dip at the position of the sample resonance. This dip, however, is not present in the absorption spectrum which exhibits a positive bump on top of the broad antenna resonance. The appearance of the positive feature in the absorption is rather surprising, inasmuch as in experimental SEIRS absorption dips are observed even for strongly scattering antennas [30, 34, 37, 39, 178, 196]. This seemingly paradoxical situation stems from the fact that in experiments it is the antenna extinction that is measured and not the antenna absorption.

We show in the following section how the line shapes of the respective spectra can be understood with help of the model presented above. We consider several modes of antenna operation depending on the ratio between the antenna intrinsic and radiation losses.

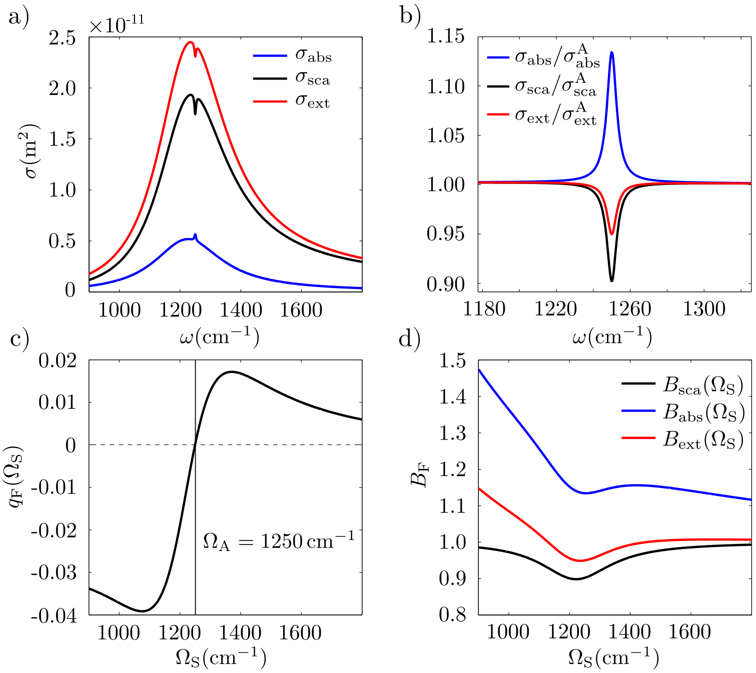

Figure 4.2: (a) Absorption, σ_{abs}, scattering, σ_{sca}, and extinction, σ_{ext}, spectra calculated with the use of the analytical model presented in Section 4.3.1 assuming dominant radiation losses of the antenna and $\Omega_{\mathrm{A}} = \Omega_{\mathrm{S}} = 1250\,\mathrm{cm}^{-1}$. A symmetric dip is observed at the position of the sample resonance in the extinction and in the scattering spectrum, whereas the absorption spectrum exhibits a positive bump. (b) Relative change of the absorption, scattering and extinction spectra induced by presence of the dark mode. (c) The asymmetry parameter q_{F} plotted as a function of sample resonance frequency Ω_{S}. (d) Amplitude of the Lorentzian curve added to the conventional Fano line, B_{F}, for scattering ($B_{\mathrm{sca}} = \beta$), extinction [$B_{\mathrm{ext}} = \beta(1 + \delta_{\mathrm{F}})$] and absorption [$B_{\mathrm{abs}} = \beta(1 + \delta'_{\mathrm{F}})$] spectra as a function of sample resonance frequency Ω_{S}. The amplitude $B_{\mathrm{sca}} = \beta$ never exceeds unity at the antenna resonance frequency and is represented by the lowest lying line. Close to the antenna resonance, the radiation corrected amplitude $B_{\mathrm{ext}} = \beta(1+\delta_{\mathrm{F}})$ is below unity which causes diminishing of the Fano dip in the extinction. The amplitude $B_{\mathrm{abs}} = \beta(1 + \delta'_{\mathrm{F}})$ exceeds unity leading to reversal of the original antiresonance towards positive resonance in the absorption. We used the following parameters to generate the plots: $f_{\mathrm{A}} = 1 \times 10^{-22}\,\mathrm{F}\cdot\mathrm{m}^2\cdot\mathrm{cm}^{-2}$, $f_{\mathrm{S}} = 6 \times 10^{-28}\,\mathrm{F}\cdot\mathrm{m}^2\cdot\mathrm{cm}^{-2}$, $\gamma_{\mathrm{A}} = 60\,\mathrm{cm}^{-1}$ and $\gamma_{\mathrm{S}} = 6\,\mathrm{cm}^{-1}$.

4.3.2 Spectral line shapes of σ_{abs}, σ_{sca} and σ_{ext}

The spectral response of a system of coupled modes is usually understood in terms of the Fano resonances [191, 197, 198]. The effectively dark mode of the sample coupled solely to the so-called bright mode of the antenna causes constructive or

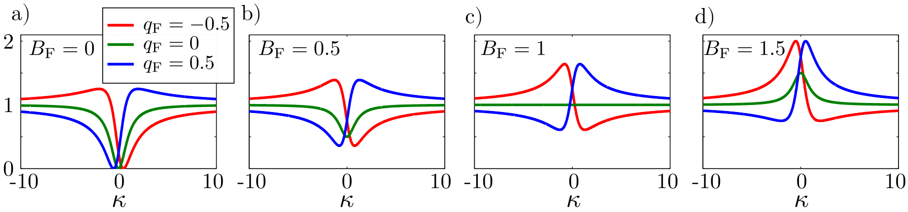

Figure 4.3: Corrected Fano spectral lineshape σ_{CF} for $q_{\mathrm{F}} = -0.5$, 0 and 0.5, and different values of B_{F}: (a) $B_{\mathrm{F}} = 0$, (b) $B_{\mathrm{F}} = 0.5$, (c) $B_{\mathrm{F}} = 1$, and (d) $B_{\mathrm{F}} = 1.5$. The value of the Fano asymmetry parameter q_{F} modifies the symmetry of the profile, showing a perfectly symmetric dip for $q_{\mathrm{F}} = 0$ and $B_{\mathrm{F}} < 1$, and an asymmetric dip for $q_{\mathrm{F}} \neq 0$. For $q_{\mathrm{F}} = 0$ and $B_{\mathrm{F}} = 1$ the Fano spectral feature completely disappears and for $q_{\mathrm{F}} = 0$ and $B_{\mathrm{F}} = 1.5$ the spectral dip turns into a positive peak on top of the background.

destructive interference leading to the formation of the characteristic asymmetric Fano line shape. It has been shown by Gallinet and Martin [199] that the original Fano formula must be corrected for the case of coupled electromagnetic modes and that in the formula for the spectral line shape, σ_{CF}, there appears a new parameter, B_{F}, responsible for smoothing off the resonance feature. The expression for the line shape is:

$$\sigma_{\mathrm{CF}} \propto \frac{(\kappa + q_{\mathrm{F}})^2 + B_{\mathrm{F}}}{\kappa^2 + 1} = \underbrace{\frac{(\kappa + q_{\mathrm{F}})^2}{\kappa^2 + 1}}_{\text{Fano}} + \underbrace{\frac{B_{\mathrm{F}}}{\kappa^2 + 1}}_{\text{Lorentzian}} . \tag{4.33}$$

Here κ is the frequency parameter and q_{F} is the Fano asymmetry parameter. The corrected Fano profile, σ_{CF}, thus contains the original Fano line and a Lorentzian peak of amplitude B_{F}. We plot σ_{CF} for different values of q_{F} and B_{F} in Fig. 4.3. The Fano line shape has the form of a generally asymmetric peak, which for the case of $q_{\mathrm{F}} = 0$ (green lines in Fig. 4.3) becomes a perfectly symmetric (Lorentzian) dip whose bottom reaches exactly zero and thus completely splits the spectrum. The Lorentzian contribution then mitigates the depth of the spectral dip which for $0 < B_{\mathrm{F}} < 1$ only shallowly perturbs the constant spectrum [Fig. 4.3 (a,b)]. When $B_{\mathrm{F}} = 1$ the Fano dip is perfectly cancelled and the spectrum σ_{CF} becomes constant for $q_{\mathrm{F}} = 0$ [Fig. 4.3 (c)]. Interestingly, by further increasing B_{F} to values $1 < B_{\mathrm{F}}$, it is possible to completely reverse the Fano dip into a positive peak on top of the constant background as shown in Fig. 4.3 (d).

In this section we show how the spectral response in absorption, extinction and scattering leads to different Fano-like line shapes and connect the parameters of the Fano curves to the actual physical parameters of the coupled-dipole model. We first derive the line shape induced by the coupling of the dark mode with the bright mode for the simplest and practically measured situation: the extinction spectrum. The extinction spectrum is given by the imaginary part of the total polarizability of the antenna coupled to the molecular vibrational modes [Eq. (4.31)]. We insert the formula for the polarizability of the antenna interacting with the sample from Eq. (4.26), using the bare antenna and sample polarizabilities from Eq. (4.20), into Eq. (4.31) and obtain the expression for the extinction spectral line shape:

$$\boxed{\begin{aligned}\sigma_{\mathrm{ext}} &\approx k\,\mathrm{Im}\{\alpha_{\mathrm{eff}}\}\\ &= k\,\mathrm{Im}\left\{f_{\mathrm{A}}\frac{c_{\mathrm{F}}+\mathrm{i}d_{\mathrm{F}}}{[a_{\mathrm{F}}c_{\mathrm{F}}-f_{\mathrm{A}}f_{\mathrm{S}}G^2-y_{\mathrm{F}}d_{\mathrm{F}}]+\mathrm{i}[c_{\mathrm{F}}y_{\mathrm{F}}+a_{\mathrm{F}}d_{\mathrm{F}}]}\right\}\\ &= \frac{-kf_{\mathrm{A}}y_{\mathrm{F}}}{a_{\mathrm{F}}^2+y_{\mathrm{F}}^2}\,\frac{c_{\mathrm{F}}^2+\frac{f_{\mathrm{A}}f_{\mathrm{S}}G^2d_{\mathrm{F}}}{y_{\mathrm{F}}}+d_{\mathrm{F}}^2}{(c_{\mathrm{F}}-\Delta_{\mathrm{F}})^2+\Gamma_{\mathrm{c}}^2+d_{\mathrm{F}}^2+2\Gamma_{\mathrm{c}}d_{\mathrm{F}}}\\ &= \frac{-kf_{\mathrm{A}}y_{\mathrm{F}}}{a_{\mathrm{F}}^2+y_{\mathrm{F}}^2}\,\frac{(\kappa+q_{\mathrm{F}})^2+\beta(1+\delta_{\mathrm{F}})}{\kappa^2+1}\\ &= \sigma_{\mathrm{ext}}^{\mathrm{A}}\frac{(\kappa+q_{\mathrm{F}})^2+\beta(1+\delta_{\mathrm{F}})}{\kappa^2+1}.\end{aligned}} \tag{4.34}$$

where for convenience we use a simplified notation for the Lorentzian-like oscillators and define the real parameters $a_{\mathrm{F}}=\Omega_{\mathrm{A}}^2-\omega^2$, $b_{\mathrm{F}}=-\gamma_{\mathrm{A}}\omega$, $c_{\mathrm{F}}=\Omega_{\mathrm{S}}^2-\omega^2$, $d_{\mathrm{F}}=-\gamma_{\mathrm{S}}\omega$, and $y_{\mathrm{F}}=b_{\mathrm{F}}-R_{\mathrm{F}}f_{\mathrm{A}}$ with $R_{\mathrm{F}}=k^3/(6\pi\varepsilon_0)$. We have further defined, following the notation of reference [199], the reduced frequency, $\kappa=(c_{\mathrm{F}}-\Delta_{\mathrm{F}})/\Gamma$, the asymmetry parameter, $q_{\mathrm{F}}=\Delta_{\mathrm{F}}/\Gamma$, the parameter $\beta=d_{\mathrm{F}}^2/\Gamma^2$ and its correction $\delta_{\mathrm{F}}=f_{\mathrm{A}}f_{\mathrm{S}}G^2/(y_{\mathrm{F}}d_{\mathrm{F}})$. We have also used the following definitions: $\Gamma=\Gamma_{\mathrm{c}}+d_{\mathrm{F}}$ having $\Gamma_{\mathrm{c}}=y_{\mathrm{F}}f_{\mathrm{A}}f_{\mathrm{S}}G^2/(a_{\mathrm{F}}^2+y_{\mathrm{F}}^2)$ and $\Delta_{\mathrm{F}}=a_{\mathrm{F}}f_{\mathrm{A}}f_{\mathrm{S}}G^2/(a_{\mathrm{F}}^2+y_{\mathrm{F}}^2)$. The expression in the last line of Eq. (4.34) represents a product of the bare antenna extinction spectrum, $\sigma_{\mathrm{ext}}^{\mathrm{A}}$, and a Fano-like spectral profile. By analogous algebraic manipulation we derive the line shape of the scattering spectrum:

$$\boxed{\begin{aligned}\sigma_{\mathrm{sca}} &\approx \frac{k^4}{6\pi\varepsilon_0^2}\left|\alpha_{\mathrm{eff}}\right|^2=\frac{f_{\mathrm{A}}^2}{a_{\mathrm{F}}^2+y_{\mathrm{F}}^2}\,\frac{(\kappa+q_{\mathrm{F}})^2+\beta}{\kappa^2+1}\\ &= \sigma_{\mathrm{sca}}^{\mathrm{A}}\frac{(\kappa+q_{\mathrm{F}})^2+\beta}{\kappa^2+1}\end{aligned}} \tag{4.35}$$

and of the absorption spectrum:

$$\boxed{\begin{aligned}\sigma_{\mathrm{abs}} &\approx k\,\mathrm{Im}\{\alpha_{\mathrm{eff}}^{\mathrm{AS}}\}\left|\frac{\alpha_{\mathrm{eff}}}{\alpha_{\mathrm{eff}}^{\mathrm{AS}}}\right|^2 = \frac{-kf_{\mathrm{A}}b_{\mathrm{F}}}{a_{\mathrm{F}}^2+b_{\mathrm{F}}^2}\frac{a_{\mathrm{F}}^2+b_{\mathrm{F}}^2}{a_{\mathrm{F}}^2+y_{\mathrm{F}}^2}\frac{\Gamma'^2}{\Gamma^2}\frac{(\kappa'+q'_{\mathrm{F}})^2+\beta'(1+\delta'_{\mathrm{F}})}{\kappa^2+1}\\ &= \sigma_{\mathrm{abs}}^{\mathrm{A}}\frac{\Gamma'^2}{\Gamma^2}\frac{(\kappa'+q'_{\mathrm{F}})^2+\beta'(1+\delta'_{\mathrm{F}})}{\kappa^2+1}\\ &= \sigma_{\mathrm{abs}}^{\mathrm{A}}\frac{(\kappa+q_{\mathrm{F}})^2+\beta(1+\delta'_{\mathrm{F}})}{\kappa^2+1}.\end{aligned}} \tag{4.36}$$

In the definition of the primed parameters, instead of the total damping y_{F} (i.e. the damping including radiation), we use only the intrinsic (quasi-static) antenna damping b_{F}. The explicit definitions are: $\delta'_{\mathrm{F}} = f_{\mathrm{A}}f_{\mathrm{S}}G^2/(b_{\mathrm{F}}d_{\mathrm{F}})$, $\Gamma' = \Gamma'_{\mathrm{c}} + d$, $\Gamma'_{\mathrm{c}} = b_{\mathrm{F}}f_{\mathrm{A}}f_{\mathrm{S}}G^2/(a_{\mathrm{F}}^2+b_{\mathrm{F}}^2)$, $\kappa' = (c_{\mathrm{F}}-\Delta'_{\mathrm{F}})/\Gamma'$, $q'_{\mathrm{F}} = \Delta'_{\mathrm{F}}/\Gamma'$, $\Delta'_{\mathrm{F}} = a_{\mathrm{F}}f_{\mathrm{A}}f_{\mathrm{S}}G^2/(a_{\mathrm{F}}^2+b_{\mathrm{F}}^2)$, $\beta' = d_{\mathrm{F}}^2/\Gamma'^2$. The final expressions for the scattering and absorption in Eqs. (4.35) and (4.36), respectively, have the form of a generalized Fano-like profile, but they differ in the correction parameter B_{F}. For the extinction $B_{\mathrm{ext}} = \beta$, for the scattering $B_{\mathrm{sca}} = \beta(1+\delta_{\mathrm{F}})$, and for the absorption $B_{\mathrm{abs}} = \beta(1+\delta'_{\mathrm{F}})$.

The symmetry of the pure Fano line shape is determined by the parameter q_{F}, which we plot in Fig. 4.2 (c) as a function of the sample frequency Ω_{S} at $\omega = \Omega_{\mathrm{S}}$. We note that the asymmetry parameter q_{F} has the same value for all of the spectra and its value depends on the detuning between the antenna and the sample $\Omega_{\mathrm{A}} - \Omega_{\mathrm{S}}$. The asymmetry parameter changes its sign from negative, below the antenna resonant frequency, to positive, above the antenna frequency, marking thus a change of the symmetry of the molecular Fano-like spectral signature. If the eigenfrequency of the sample is tuned to the resonance of the antenna ($\Omega_{\mathrm{A}} = \Omega_{\mathrm{S}}$), the pure Fano line features a fully symmetric antiresonance. The Fano line is further accompanied by the term in the form of a Lorentzian resonance with amplitude $B_{\mathrm{F}} \in \{B_{\mathrm{ext}}, B_{\mathrm{sca}}, B_{\mathrm{abs}}\}$ centred exactly at the position of the Fano dip. If the amplitude of the additional Lorentzian curve exceeds unity, the original Fano antiresonance is switched towards a positive resonance. We see in Fig. 4.2 (b), (d) that this situation occurs in the absorption spectrum for the set of parameters selected for our system, $B_{\mathrm{abs}}(\Omega_{\mathrm{S}} = \Omega_{\mathrm{A}}) > 1$. On the other hand, the parameters B_{ext} and B_{sca} diminish the antiresonance of the extinction and scattering spectra, respectively, but do not exceed unity and hence for $\Omega_{\mathrm{A}} = \Omega_{\mathrm{S}}$, both the extinction and the scattering profiles preserve the Fano-like dip.

We now show that for the exact tuning $\Omega_{\mathrm{A}} = \Omega_{\mathrm{S}}$ the positive feature can appear only in the absorption spectrum and that the extinction and the scattering always exhibit a spectral dip. It is interesting to rewrite the expression for the amplitudes B_{ext}, B_{sca} and B_{abs} in terms of the original oscillator parameters for practical relevant situations usually exploited in SEIRS, $\Omega_{\mathrm{A}} \approx \Omega_{\mathrm{S}}$ [28], and setting $\omega \approx \Omega_{\mathrm{S}}$, we get:

$$B_{\mathrm{sca}}(\omega \approx \Omega_{\mathrm{S}} \approx \Omega_{\mathrm{A}}) = \beta = \frac{d_{\mathrm{F}}^2 y_{\mathrm{F}}^2}{(f_{\mathrm{A}} f_{\mathrm{S}} G^2 + y_{\mathrm{F}} d_{\mathrm{F}})^2}, \tag{4.37}$$

$$B_{\mathrm{ext}}(\omega \approx \Omega_{\mathrm{S}} \approx \Omega_{\mathrm{A}}) = \beta(1+\delta_{\mathrm{F}}) = \frac{y_{\mathrm{F}} d_{\mathrm{F}}}{y_{\mathrm{F}} d_{\mathrm{F}} + f_{\mathrm{A}} f_{\mathrm{S}} G^2}, \tag{4.38}$$

$$B_{\mathrm{abs}}(\omega \approx \Omega_{\mathrm{S}} \approx \Omega_{\mathrm{A}}) = \beta(1+\delta'_{\mathrm{F}}) = \underbrace{\frac{y_{\mathrm{F}} d_{\mathrm{F}}}{y_{\mathrm{F}} d_{\mathrm{F}} + f_{\mathrm{A}} f_{\mathrm{S}} G^2}}_{F_1} \underbrace{\frac{b_{\mathrm{F}} d_{\mathrm{F}} + f_{\mathrm{A}} f_{\mathrm{S}} G^2}{y_{\mathrm{F}} d_{\mathrm{F}} + f_{\mathrm{A}} f_{\mathrm{S}} G^2} \frac{y_{\mathrm{F}}}{b_{\mathrm{F}}}}_{F_2}. \tag{4.39}$$

We immediately observe that the amplitudes B_{sca} and B_{ext} are limited for the case of the exact tuning and can never reach unity. The flip into the positive peak is therefore forbidden for the scattering and for the extinction. Note that this statement is not true for arbitrary antenna-sample detuning as B_{ext} can be larger than one for $\Omega_{\mathrm{A}} \neq \Omega_{\mathrm{S}}$ [see Fig. 4.2 (d)]. In the detuned situation, the Lorentzian contribution superposes with an asymmetric Fano line which in turn yields an asymmetric shape of the resulting spectrum [28]. The situation is more complicated for B_{abs} as it contains a product of terms that we denote as F_1 and F_2 and that are manifestly smaller and larger than one, respectively. The magnitude of B_{abs} thus results from the interplay of these two terms and its bounds, $B_{\mathrm{abs}} \lessgtr 1$, cannot be determined generally. To get further insight we thus assume that the coupling term between the antenna and the sample $f_{\mathrm{A}} f_{\mathrm{S}} G^2$ is small and we Taylor expand Eq. (4.39) as

$$\beta(1+\delta'_{\mathrm{F}}) \approx 1 + f_{\mathrm{A}} f_{\mathrm{S}} G^2 \frac{y_{\mathrm{F}} - 2b_{\mathrm{F}}}{b_{\mathrm{F}} y_{\mathrm{F}} d_{\mathrm{F}}} + \ldots \tag{4.40}$$

When the coupling is weak, the sign of the first order coefficient decides whether the spectral antenna-sample interaction results in a positive resonance or a negative antiresonance in the absorption spectrum. We find the condition for the formation of the positive resonance as $|y_{\mathrm{F}}| > 2|b_{\mathrm{F}}|$ by requiring the sign of the first order coefficient to be positive (note that by definition y_{F}, b_{F} and d_{F} are negative). In other words, the positive resonance occurs when the sample weakly couples with the antenna whose total damping is at least twice larger than the intrinsic damping, i.e., the radiation damping of the antenna is larger than its intrinsic damping. Furthermore, if the condition $|y_{\mathrm{F}}| = 2|b_{\mathrm{F}}|$ is satisfied, the absorption spectrum is, to the first order, virtually unperturbed by the sample resonance.

Such behavior of the absorption spectrum can be understood in terms of coupling regime of the antenna-electromagnetic field as defined in the coupled mode theory, as described by Adato *et al.* [196]. In this context, the antenna is seen as a resonator coupled to the incident and reflected fields. Depending on the antenna parameters, the regime of the antenna-field coupling can be classified as *under-coupled* ($|y_{\mathrm{F}}| < 2|b_{\mathrm{F}}|$), *over-coupled* ($|y_{\mathrm{F}}| > 2|b_{\mathrm{F}}|$) or as *critical-coupling* regime ($|y_\mathrm{F}| = 2|b_\mathrm{F}|$). In the critical coupling, the antenna absorption efficiency is maximized [196, 200, 201] and decreases towards both under- and over-coupled regimes when the antenna intrinsic damping is varied. If the sample is placed into the vicinity of the antenna, the antenna intrinsic damping is effectively increased for frequencies close to the sample resonance, which can be identified from the expression for the antenna quasi-static polarizability in Eq. (4.27) combined with Eq. (4.20) and considering $\alpha_\mathrm{S}(\Omega_\mathrm{S}) = \mathrm{i}f_\mathrm{S}/(\gamma_\mathrm{S}\Omega_\mathrm{S})$:

$$\alpha_\mathrm{eff}^\mathrm{AS}(\Omega_\mathrm{S}) = \frac{f_\mathrm{A}}{\Omega_\mathrm{A}^2 - \Omega_\mathrm{S}^2 - \mathrm{i}\left[\gamma_\mathrm{A}\Omega_\mathrm{S} + f_\mathrm{A}f_\mathrm{S}G^2/(\gamma_\mathrm{S}\Omega_\mathrm{S})\right]}, \tag{4.41}$$

where $f_\mathrm{A}f_\mathrm{S}G^2/(\gamma_\mathrm{S}\Omega_\mathrm{S}^2)$ is the effective increase of the antenna damping due to the coupling with the sample. The antenna-sample coupling then results either in enhancement or suppression of the antenna absorption in the narrow spectral range around the sample resonance. Depending if the bare antenna is in the over-coupled regime or in the under-coupled regime, the interaction of the antenna with the sample thus gives rise to the absorption positive feature or the negative dip, respectively. We demonstrate this behavior on an particular example of a linear plasmonic antenna later in Chapter 4.4.2.

4.3.3 Validation of the analytical model by numerical simulations: consequences of the model

In order to corroborate the validity of the analytical model we numerically calculate the spectra of a gold linear cylindrical spherically-capped plasmonic antenna (3.2 µm long, diameter 100 nm) with two kinds of phononic samples, a large patch coupled with the antenna providing medium strength of antenna-sample interaction (mildly interacting patch) and a thin patch leading only to much weaker coupling between the sample and the antenna (the weakly interacting patch). We model the sample as a cylindrical patch of thickness 7.5 nm in the case of the weakly interacting patch and of thickness 15 nm in case of the mildly interacting patch. The patches are constructed by intersecting a cylindrical capsule with spherical caps of length 180 nm (mildly interacting patch) or 150 nm (weakly interacting patch) by the body of the antenna as shown in Fig. 4.4 (a). We use the gold dielectric function by Palik [202]. The patch dielectric function is modelled as a single Lorentz oscillator [Eq.(4.19)] with $\varepsilon_\infty = 2.14$, $\omega_\mathrm{OS} = 969\,\mathrm{cm}^{-1}$, $\omega_\mathrm{TO} = 1085\,\mathrm{cm}^{-1}$ and $\gamma_\mathrm{v} = 10\,\mathrm{cm}^{-1}$, mimicking a phononic mode in the sample.

In the following we study interaction of the lowest dipole plasmonic mode (resonant at about $\Omega_\mathrm{A} \approx 1250\,\mathrm{cm}$) of the antenna with the excitations of the sample. The near-field distribution of the dipole mode of the bare plasmonic antenna, $|\mathbf{E}|$, excited on resonance by an incident plane wave polarized along x and propagating in the z direction is shown in Fig. 4.4 (b). The plasmonic near field is strongly localized at the surface of the antenna and increases in magnitude from the centre of the antenna towards the antenna's extremities where the plasmonic hot spots are localized.

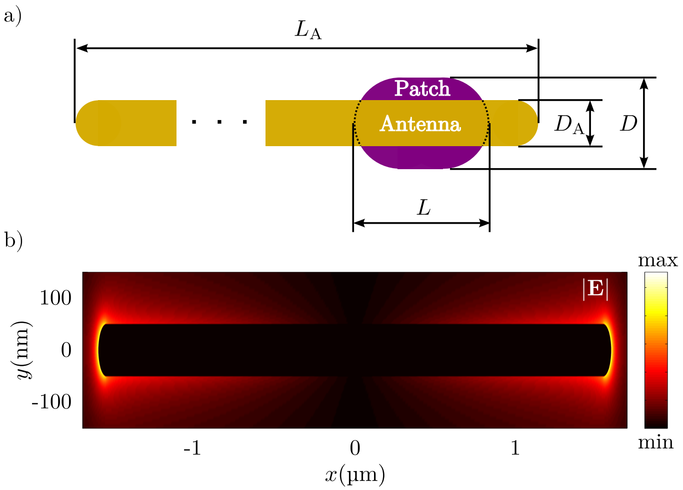

Figure 4.4: (a) The vibrational patch is modelled as a cylindrical object with hemispherical caps of length L and diameter D and is hollow in the centre as the body of the antenna passes through it. For the weakly interacting patch we used $L = 150\,\mathrm{nm}$, $D = 115\,\mathrm{nm}$ and for the mildly interacting patch we used $L = 180\,\mathrm{nm}$, $D = 130\,\mathrm{nm}$. The length of the antenna is $L_A = 3.2\,\mathrm{\mu m}$ with diameter $D_A = 100\,\mathrm{nm}$. (b) Normalized amplitude of the near field of the plasmonic antenna ($L_A = 3.2\,\mathrm{\mu m}$, $D_A = 100\,\mathrm{nm}$) illuminated by a monochromatic plane wave polarized along x and of frequency $\approx 1250\,\mathrm{cm}^{-1}$, which is resonant with the lowest dipole mode of the antenna. The near field amplitude increases from the centre of the antenna towards the antenna's extremities where it is maximized in the plasmonic hot spots.

We place the samples on top of the antenna onto different positions along the antenna's long axis and observe the changes in the total spectral response of the antenna-sample system. Finally we fit the analytical model to the numerically calculated spectra in order to obtain the model parameters as a function of the sample position. A commercial-grade simulator based on the Finite-Difference Time-Domain (FDTD) method was used to perform the numerical calculations [203]. We obtain the model parameters by fitting the scattering spectra and use them to calculate the absorption and the extinction. We choose to fit the scattering as it originates almost purely from the large antenna's dipole moment and practically does not contain any contributions from the direct scattering of the sample. The scattering, unlike the absorption and hence also the extinction, thus best complies with the assumption of the analytical model, which neglects the direct contribution of the sample absorption and scattering to the overall antenna-sample spectral response.

The waterfall plots of the numerically calculated extinction [Fig. 4.5 (a,b)], scattering [Fig. 4.5 (c,d)] and absorption [Fig. 4.5 (e,f)] spectra (black lines) of the antenna-sample system for gradually increasing the coupling between the sample

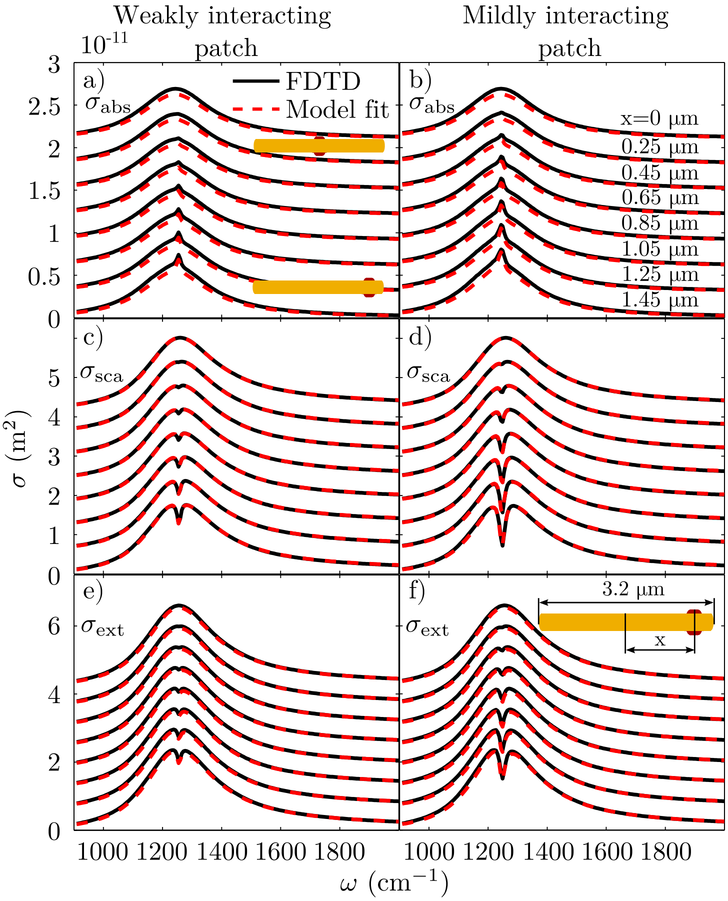

Figure 4.5: Numerically calculated (black lines) and model fit (red dashed lines) spectra [(a,b) absorption, (c,d) scattering and (e,f) extinction] of the plasmonic antenna with a patch of phononic material positioned along the antenna longitudinal axis onto a distance x from the antenna center. The model parameters are obtained from the fit to the scattering spectrum of the bare antenna and used for calculation of the absorption and extinction spectra. (a,c,e) Spectra calculated for a patch of small sample volume causing only slight perturbation to the original spectrum of the antenna (the weakly interacting patch). (b,d,f) Spectra calculated for a patch of larger sample volume (the mildly interacting patch); the dip in scattering spectrum almost completely splits the original antenna scattering peak. The antenna parameters obtained from the fit are: $f_{\mathrm{A}} = 9.97 \times 10^{-23}\,\mathrm{F}\cdot\mathrm{m}^2\cdot\mathrm{cm}^{-2}$, $\omega_{\mathrm{A}} = 1269\,\mathrm{cm}^{-1}$ and $\gamma_{\mathrm{A}} = 67\,\mathrm{cm}^{-1}$. We further use the following fixed parameters for the phononic sample: $f_{\mathrm{S}} = 1.15 \times 10^{-26}\,\mathrm{F}\cdot\mathrm{m}^2\cdot\mathrm{cm}^{-2}$, $\Omega_{\mathrm{S}} = 1255\mathrm{cm}^{-1}$ for the weakly interacting sample and $\Omega_{\mathrm{S}} = 1247\mathrm{cm}^{-1}$ for the mildly interacting sample, $\gamma_{\mathrm{S}} = 13\,\mathrm{cm}^{-1}$. The only parameter modified for the different position of the patches is the coupling strength G which was increased up to $G = 3.25 \times 10^{28}\,\mathrm{F}^{-1}\cdot\mathrm{m}^{-2}$ for the weakly interacting sample and $G = 5.76 \times 10^{28}\,\mathrm{F}^{-1}\cdot\mathrm{m}^{-2}$ for the mildly interacting sample.

and the antenna together with the results from the model fit (red dashed lines) are displayed in Fig. 4.5 (a, c, e) for the weakly interacting patch and in Fig. 4.5 (b, d, f) for the mildly interacting patch. The results from the model almost perfectly fit the scattering spectra [Fig. 4.5 (c,d)], but the absorption calculated from the fit parameters is somewhat underestimated [Fig. 4.5 (e,f)]. We attribute this to the simplified form of the initial expressions used for the calculation of the spectra [Eqs. (4.30)], which are derived for point-like polarizable objects. Despite this, the spectra obtained from the analytical model match those from the numerical calculations with remarkable accuracy.

We have chosen the parameters of the antenna such that the scattering spectrum of the bare antenna strongly overwhelms its absorption spectrum. The resonance feature that appears on top of the broad antenna spectrum at the frequency of the sample resonance is thus a positive bump in the absorption and an anti-resonance both in the scattering and in the extinction. When the mutual coupling between the antenna and the sample is increased, for example by moving the phononic patch towards the antenna extremities where its near field is larger, the originally almost unperturbed spectrum of the antenna displays a gradual increase of the spectral fingerprint of the sample resonance.

To understand this trend we calculate the antenna's normalized near-field amplitude $|\mathbf{E}_\mathrm{A}|$ and intensity $\propto |\mathbf{E}_\mathrm{A}|^2$ along the antenna axis and plot them in Fig. 4.6 (a) for the weakly interacting sample and in Fig. 4.6 (b) for the mildly interacting sample as red and blue lines, respectively. The dominantly radially polarized antenna near-field amplitude increases approximately linearly with the distance from the antenna center ($x = 0\,\mu\mathrm{m}$) towards the antenna's extremities. Alongside with the near fields we show the fitted antenna-sample coupling constant G (black crosses) obtained for the different positions of the sample along the antenna. We normalize all the quantities to the value obtained at the antenna extremity. The fitted coupling constant G almost perfectly reproduces the spatial distribution of the antenna's near-field amplitude for both the weakly and the mildly interacting sample. This can be understood if we realize that the coupling G is proportional to the overlap integral between the normalized distribution of the polarization $\tilde{\mathbf{P}}_\mathrm{S}(\mathbf{r}) = \mathbf{P}_\mathrm{S}(\mathbf{r})/\max[\mathbf{P}_\mathrm{S}(\mathbf{r})]$ inside the sample at the frequency of the phononic resonance and the antenna's near-field distribution $\mathbf{E}_\mathrm{A}(\mathbf{r})$, $G \propto \iiint \mathbf{E}_\mathrm{A}(\mathbf{r};x) \cdot \tilde{\mathbf{P}}_\mathrm{S}(\mathbf{r})\mathrm{d}^3\mathbf{r}$, as has been shown using more general theory elsewhere [195]. Since the distribution of $\tilde{\mathbf{P}}_\mathrm{S}(\mathbf{r})$ is independent of the sample position, the spatial dependence of G is thus determined by the near-field distribution at the antenna, in agreement with the result in Fig. 4.6.

The role of the coupling parameter G for practical sample sensing is however more challenging to interpret. We therefore investigate, as a spectroscopic figure of merit, the size of the spectral feature induced by the presence of the sample, when the sample's position is shifted along the infrared antenna. We subtract the spectral line of the bare antenna from the spectra of the total interacting system and plot in Fig. 4.6 (a,b) the difference between the maximum and minimum of the normalized spectral line as the spectroscopic contrast measured in the absorption (blue squares), scattering (black circles) and extinction (red triangles). We observe

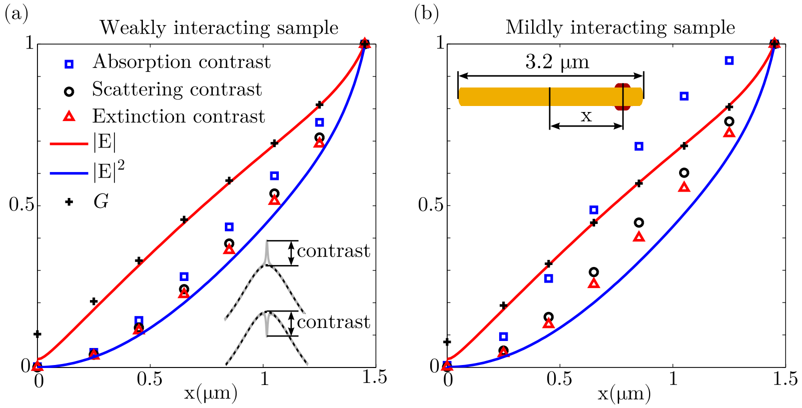

Figure 4.6: Comparison of the normalized size of the spectral contrast [see the inset in (a)] calculated in the absorption, scattering and extinction with the profile of the antenna near-field amplitude $|\mathbf{E}_\mathrm{A}|$ and intensity $|\mathbf{E}_\mathrm{A}|^2$, as a function of sample position along the antenna axis measured from the antenna center. The results are displayed for the weakly interacting sample (a) and for the mildly interacting sample (b). The coupling constant G obtained from the fit of the analytical model to the numerical data corroborates the prediction that the antenna-sample coupling is proportional to the bare antenna's near-field amplitude.

that the spectral contrast increases as both the weakly and the mildly interacting patch moves along the antenna axis out from the antenna centre. However, a closer look at the spectral contrast reveals strong discrepancies between the results for the weakly and the mildly interacting sample.

The spectral contrast of the weakly interacting sample follows a profile which is similar to the spatial variation of the near-field intensity $|\mathbf{E}_\mathrm{A}|^2$ in all the signals. The explanation of this behavior follows directly from the analytical form of the model spectra, in which the spectral contrast is dependent on the square of the coupling parameter, G^2. The Taylor expansion for the weak antenna–sample interaction therefore emerges in the form of a quadratic lowest-order term and gives rise to the quadratic dependence of the signal on the coupling G. Hence the observed tendency corroborates the commonly accepted enhancement mechanism of SEIRS for weakly interacting samples, which can understood as a succession of two steps: first, the sample interacts with the incident radiation which is enhanced by the infrared antenna on its surface (mediated by G) and then, the polarized sample scatters the infrared radiation via the radiative channels of the antenna to the far field (mediated again by G). More precisely, this double-scattering mechanism can be derived from Eqs. (4.21) and (4.22) by an iterative solution (the so-called multiple-scattering series) terminated in the second order in G (contained in $\mathbf{G}_{\mathrm{AS(SA)}}$). For the dipole moment of the antenna, $\mathbf{p}_{\mathrm{A}}$ we obtain:

$$\underbrace{\mathbf{p}_{\mathrm{A}}}_{\propto \mathbf{E}_{\mathrm{A}}} = \underbrace{\boldsymbol{\alpha}_{\mathrm{A}}\mathbf{E}_0^{\mathrm{A}}}_{\propto \mathbf{E}_{\mathrm{BG}}} + \underbrace{\boldsymbol{\alpha}_{\mathrm{A}}\mathbf{G}_{\mathrm{AS}}\boldsymbol{\alpha}_{\mathrm{S}}\mathbf{G}_{\mathrm{SA}}\boldsymbol{\alpha}_{\mathrm{A}}\mathbf{E}_0^{\mathrm{A}} + \ldots}_{\propto \mathbf{E}_{\mathrm{AS}}} \tag{4.42}$$

The electric field scattered by the antenna to the far field is proportional to the antenna's dipole moment, $\mathbf{E}_{\mathrm{A}} \propto \mathbf{p}_{\mathrm{A}}$. In the far field, the signal resulting from the antenna-sample interaction, $\mathbf{E}_{\mathrm{AS}}$, interferes with the background radiation including the response of the bare antenna, $\mathbf{E}_{\mathrm{BG}}$, and leads to the spectral contrast as follows:

$$\mathrm{Signal} \propto |\mathbf{E}_{\mathrm{A}}|^2 = |\mathbf{E}_{\mathrm{BG}} + \mathbf{E}_{\mathrm{AS}}|^2 \approx \underbrace{|\mathbf{E}_{\mathrm{BG}}|^2}_{\text{Antenna spectrum}} + \underbrace{2\mathrm{Re}\{\mathbf{E}_{\mathrm{BG}}^{*}\mathbf{E}_{\mathrm{AS}}\}}_{\text{Spectral contrast}}. \tag{4.43}$$

The first term is proportional to the original spectrum of the bare antenna. The second term represents the interference between the background scattering and the scattering due to the sample and leads to the formation of the characteristic spectral contrast. The spectral contrast is linearly proportional to the field emerging from the antenna-sample coupling, $\mathbf{E}_{\mathrm{AS}}$, which results in the quadratic dependence of the spectral contrast on the antenna near-field amplitude, as described above.

If the mutual coupling between the antenna and the sample is enhanced by increasing either G, or the sample oscillator strength f_{S} (for example by increasing its volume), the lowest order Taylor's approximation is not valid any more. In such a case, saturation effects which can be intuitively understood as a consequence of the electromagnetic multiple scattering between the sample and the antenna appear.

These saturation effects are responsible for the dependence of the signal contrast on the position of the sample, as calculated for the mildly interacting sample. The signal contrast starts to increase, roughly following a parabolic dependence when the sample is positioned close to the antenna center. When the sample is moved closer to the antenna apexes and the antenna-sample coupling increases, the signal contrast deviates significantly from the parabolic profile. This is more apparent when the signal contrast is measured in the absorption spectrum.

Last we remark that a further increase of the antenna-sample coupling would eventually lead to a splitting of the antenna peak due to the formation of new hybrid modes, as a result of the combined excitation of antenna and sample [189]. This limiting situation of fully developed hybridization is very interesting but will not constitute the object of current study, as our analyzis is focused on the enhancement signal originated by minute quantities of sample.

4.4 Optimization of linear plasmonic antennas for SEIRS

In the pioneering SEIRS experiments the sample molecules were adsorbed on surfaces of metal nanoparticle aggregates that were small enough to permit an interpretation of the observed absorption signals within the effective medium theory, where radiation losses were neglected [204]. In later developments it has been demonstrated that SEIRS can be significantly increased if metallic antennas are engineered to be resonant with the detected vibrational resonances [24, 26, 28–30, 32–35, 188, 205–208]. To that end plasmonic antennas in the form of linear metal wires of micrometer length and diameter of the order of $\approx 100\,\mathrm{nm}$ have been proposed. Such large metallic structures can experience large radiation damping and their radiation losses often prevail over the intrinsic damping and must be therefore correctly included in the description of the antenna's scattering. As by now, not much attention has been paid to the influence of the hosting antenna's radiation and intrinsic losses on the properties of the characteristic spectral feature, the SEIRS signal, that appears on top of the broad antenna resonance. Here we perform such a study.

We consider the representative case of a single linear gold nanoantenna (or arrays of them with large enough space between the antennas) illuminated by light polarized parallel to the antenna axis. We first examine the properties of the scattering and absorption of the bare IR resonant nanoantennas. After that, we study the influence of the scattering and absorption of radiation by the hosting linear plasmonic antennas on the on the fingerprint spectral contrast of the IR-active samples. Our findings, based on a combination of results obtained from finite-difference in time-domain (FDTD) simulations, corroborate a simple and practical rule for designing the optimal linear plasmonic antenna for SEIRS applications. The implementation of this rule requires a careful inspection of the scattering and the absorption cross sections of the plasmonic antenna, as key contributions of the total extinction cross section obtained in typical SEIRS experiments.

4.4.1 Extinction, scattering and absorption of linear plasmonic antennas

Localized plasmonic resonances usually experience large intrinsic and radiation losses. The intrinsic losses of plasmonic antennas are mostly given by the bulk material properties of the metal, which can be incorporated in the metal dielectric function, and arise due to the scattering of the metal conduction electrons on impurities, lattice oscillations (phonons), or due to electron-electron scattering. Other intrinsic loss mechanisms can emerge from the scattering of the metal electrons onto the surfaces of the metallic particles or from the electron confinement when the particles are small ($\lesssim 5\,\mathrm{nm}$). The dimensions of the plasmonic antennas considered in this chapter make suitable a description of

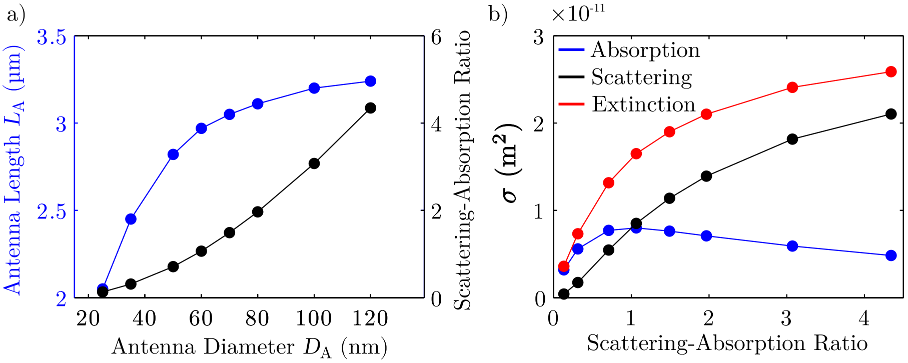

Figure 4.7: Scattering and absorption properties of individual linear plasmonic antennas of variable diameter D_A and length L_A tuned to show the same lowest-dipole resonance $\Omega_\mathrm{A} \approx 1250\,\mathrm{cm}^{-1}$. (a) The length of the plasmonic antennas L_A (blue circles) and the scattering-absorption ratio extracted from the maxima of the antenna scattering and absorption spectra (black circles) as a function of antenna diameter D_A. The antenna aspect ratio decreases with increasing antenna size, as the radiation reaction redshifts the resonances of larger antennas. The increasing importance of the antenna radiation is also reflected on the increasing antenna scattering-absorption ratio for larger antennas. (b) Maxima of the antenna absorption (blue), scattering (black) and extinction (red) cross sections calculated for the lowest dipole resonance, for the different antenna sizes given in (a), here represented by the scattering-absorption ratio. The absorption of the antenna is maximized when the scattering and the absorption of the antenna are approximately equal, whereas the scattering and the total extinction grow with increasing antenna size.

the metal dielectric response via its bulk properties. In this section we perform a full electromagnetic calculation of the scattering, absorption and extinction of linear metallic antennas of different sizes and study the dependence of the contributions from the intrinsic and radiation losses to the total antenna damping and subsequently the performance of such antennas for SEIRS sensing.

To evaluate the contribution of the intrinsic and radiation loss channels to the antenna damping we calculate the spectral response of the antenna in absorption and in scattering. The absorption spectrum is a measure of the energy that is lost due to the intrinsic loss mechanisms in the antenna's material and can be thus used to quantify the antenna's intrinsic losses. On the other hand, the scattering spectrum represents the flux of energy radiated away off the metallic antenna and thus gauges the antenna radiative losses. In SEIRS experiments, the signal is usually detected in transmission where the total extinction of the incident power containing both absorption and scattering losses of the antennas is recorded. To obtain the final measured signal we therefore sum up the absorption and scattering spectra into the experimentally relevant extinction spectrum and present it alongside with its constituents.

In particular, we design a series of cylindrical spherically capped linear plasmonic antennas of different geometrical size (length L_A and diameter D_A)

with the lowest dipole resonance kept at approximately the same frequency $\Omega_\mathrm{A} \approx 1250\,\mathrm{cm}^{-1}$, but differing in their scattering and absorption efficiency. The antennas of the smallest volume dominantly absorb the incident radiation, but have too small radiative dipole moment to significantly scatter light into the far field. On the other hand, large antennas are able to re-radiate the incident field into the far field at the expense of the light absorption in the material of the antenna. The dimensions of the antennas, their diameter D_A and length L_A, are depicted in Fig. 4.7 (a) as blue dots. The length of the antenna depends monotonically on the antenna diameter, but the functional dependence shows that the antenna aspect ratio $L_\mathrm{A}/D_\mathrm{A}$ decreases when the antenna size increases, despite the expectation arising from the quasi-static description in which $L_\mathrm{A}/D_\mathrm{A}$ fully determines the antenna resonance. Indeed, the smallest antenna considered has a diameter of $D_\mathrm{A} = 25\,\mathrm{nm}$ and a corresponding length of $L_\mathrm{A} = 2.05\,\mu\mathrm{m}$ with aspect ratio of $L_\mathrm{A}/D_\mathrm{A} = 82$, compared to the largest antenna that has $D_\mathrm{A} = 120\,\mathrm{nm}$ with $L_\mathrm{A} = 3.24\,\mu\mathrm{m}$ and aspect ratio $L_\mathrm{A}/D_\mathrm{A} = 27$. This large difference of $L_\mathrm{A}/D_\mathrm{A}$ with increasing antenna size is closely related to the radiation reaction of larger antennas, which aside of broadening the spectral peaks also red-shifts the quasi-static antenna resonances.

For each antenna we also calculate the absorption, $\sigma_\mathrm{abs}(\omega)$ and the scattering, $\sigma_\mathrm{sca}(\omega)$, spectra, and in Fig. 4.7 (a) the ratio of the scattering and absorption maxima obtained for the antenna's lowest dipole resonance, the scattering-absorption ratio, is shown:

$$\boxed{\text{Scattering-Absorption Ratio} \equiv \max[\sigma_\mathrm{sca}(\omega)]/\max[\sigma_\mathrm{abs}(\omega)]} \tag{4.44}$$

as black dots. The scattering-absorption ratio is monotonically increasing with antenna size, being practically negligible for the small, almost purely absorbing antenna, and reaching a value of ≈ 4 for the largest antenna. The designed antennas thus cover a broad range of operation regimes for which the antennas can be under-, over- or critically coupled as described in Section 4.3.2.

It is also interesting to study the dependence of the maxima of the antenna's absorption, scattering and extinction cross sections as a function of antenna size, here represented by the scattering-absorption ratio, which we plot in Fig. 4.7 (b). As the antenna size is increased, the antenna dipole plasmonic mode interacts more strongly with the radiation fields and thus gives rise to the monotonic increase of the scattering (black connected dots). On the other hand, the absorption of the antennas exhibits a resonance at around a value for which the antenna absorption and scattering are approximately equal (scattering-absorption ratio = 1). The maximized absorption that occurs for antennas whose radiation and intrinsic losses are even, which is known as the critical-coupling regime [196, 200, 201]. The antenna size is thus another important parameter that has to be taken into account for the design of SEIRS substrates. In the following section we thus explore the role of the antenna size (represented through the scattering-absorption ratio) for sensing of vibrational samples placed into the proximity of the plasmonic antennas.

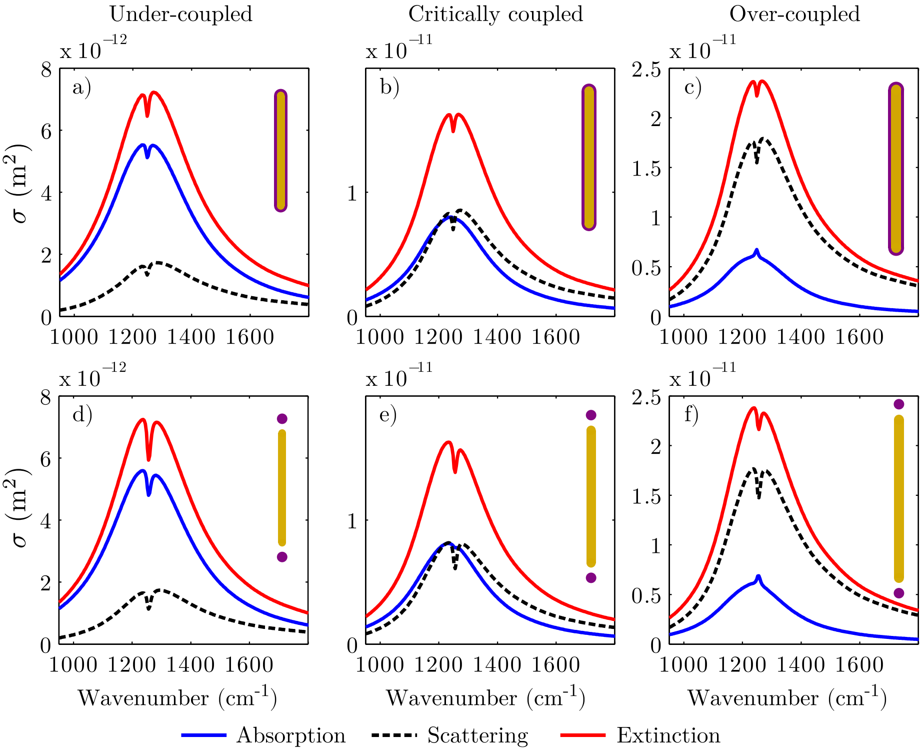

Figure 4.8: Absorption (blue), scattering (black dashed) and extinction (red) spectra of (a,d) a dominantly absorbing antenna ($L_\mathrm{A} = 2.45\,\mu\mathrm{m}$, $D_\mathrm{A} = 35\,\mathrm{nm}$), (b,e) a larger antenna that is approximately equally scattering and absorbing ($L_\mathrm{A} = 2.97\,\mu\mathrm{m}$, $D_\mathrm{A} = 60\,\mathrm{nm}$) and (c,f) a large antenna that is dominantly scattering ($L_\mathrm{A} = 3.2\,\mu\mathrm{m}$, $D_\mathrm{A} = 100\,\mathrm{nm}$). The resonance frequency of the lowest dipole mode of the hosting antenna is fixed to approximately $1250\,\mathrm{cm}^{-1}$ in all cases. In (a-c) the antennas are covered by a homogeneous ($t = 10\,\mathrm{nm}$ thick) layer of a vibrationally active material and in (d-f) a pair of phononic spheres with diameter $D_\mathrm{A} = 30\,\mathrm{nm}$ are placed close to the antenna apexes, such that the gap between the antenna and the sphere is 5 nm. The signal of the vibrationally active sample appears on top of the broad antenna resonance in the form of a dip in the extinction and scattering spectra, and as a dip or a positive bump in the absorption.

4.4.2 Importance of the scattering-absorption ratio of the plasmonic antenna for the SEIRS signal

We use the antennas introduced in Fig. 4.7 as a substrate for SEIRS and study the influence of the antenna's scattering-absorption ratio on the signal of the vibrationally active sample. To this end we choose the vibrational sample either in the form of a layer homogeneously covering the antenna's surface, which represents a layer of vibrationally active molecules, or in the form of spherical particles placed close to the extremities of the plasmonic antennas, which can represent e.g. small phononic crystals [128–130] (see the inset in Fig. 4.8). The spherical particle can also represent arrangement where the tip of a scattering-type near-field optical microscope probes the antenna's near field. We consider that the molecular layer has thickness $t = 10\,\mathrm{nm}$ and the gap between the particle of diameter $D_{\mathrm{phc}} = 30\,\mathrm{nm}$ and the antenna apexes is $5\,\mathrm{nm}$. The material of both the layer and the spherical particles is modeled via the dielectric function containing a single Lorentzian resonance [Eq. (4.19)], where the parameters are chosen to represent a weak vibrational oscillator in the case of the layer ($\varepsilon_\infty = 1$, $\omega_{\mathrm{OS}} = 56\,\mathrm{cm}^{-1}$, $\omega_{\mathrm{TO}} = 1248\,\mathrm{cm}^{-1}$ and $\gamma_{\mathrm{v}} = 10\,\mathrm{cm}^{-1}$) and to represent a strong phononic response (e.g of a SiO_2 crystal) for the phononic spherical particles ($\varepsilon_\infty = 2.14$, $\omega_{\mathrm{OS}} = 1033\,\mathrm{cm}^{-1}$, $\omega_{\mathrm{TO}} = 1157\,\mathrm{cm}^{-1}$ and $\gamma_{\mathrm{v}} = 10\,\mathrm{cm}^{-1}$). The parameters of the respective dielectric functions are chosen such that the resonance of the sample approximately matches the maximum of the antenna's dipole resonance peak and the effects of the background dielectric function ε_∞ are suppressed. The relatively strong phononic response of the spherical samples ensures that even the relatively small spherical samples can produce an observable spectral feature on top of the antenna's spectrum.

In Fig. 4.8 we plot the absorption (blue), scattering (black dashed) and extinction (red) spectra of antenna covered with the thin molecular layer (a-c) and of antenna with the pair of the identical spheres positioned at the antenna's extremities (d-f). We display the spectral response for three selected antenna sizes, representing (a,d) a small antenna that dominantly absorbs light, (b,e) a medium-sized antenna that approximately equally absorbs and scatters the incident radiation and (c,f) a large antenna that dominantly scatters the incident radiation. The geometrical parameters of the respective antennas are given in the caption of Fig. 4.8. On top of the broad resonance of the antenna, a characteristic vibrational feature of the sample is clearly observable. In the extinction and scattering this feature has the form of a spectral dip for all antenna sizes. In the absorption spectra there appears a dip slightly modifying the spectrum of the small antenna (a,d) which practically disappears for the medium-sized antenna and flips into a positive bump for the large, dominantly scattering, hosting antenna. This characteristic flip of the absorption dip into absorption bump is a signature of the behavior described in Section 4.3.2, where we showed that the presence of the sample's resonance leads to a decrease of the antenna's absorption, and hence to a formation of the dip, when the antenna is in the under-coupled regime. However, the absorption is enhanced when the antenna is over-coupled, as shown in Fig. 4.8.

Next we analyze the size of the characteristic spectral fingerprint of the sample as defined previously (the depth of the spectral dip or height of the spectral bump measured with respect to the smoothened spectrum of the antenna). We normalize the signal contrast to the volume of the phononic layer or the phononic spheres and plot the result in Fig. 4.9, obtained from the absorption (blue), scattering (black) and extinction (red), as a function of the scattering-absorption ratio of the hosting antennas. In Fig. 4.9 (a) the signal contrast is plotted for the antenna covered by the homogeneous layer of the vibrational sample and in (b) for the antennas with

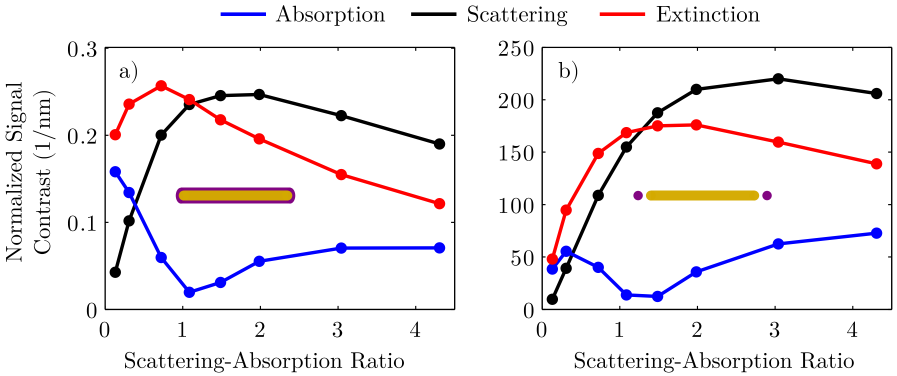

Figure 4.9: The vibrational signal contrast in the absorption (blue), scattering (black) and extinction (red) measured as the size of the characteristic spectral dip or the positive bump and normalized to the volume of the sample. The signal contrast is plotted in (a) for the antenna covered by a homogeneous layer of thickness $t = 10\,\mathrm{nm}$ and in (b) for the antenna with a pair of identical spheres at the antenna apexes as a function of the bare antenna's scattering-absorption ratio. The normalized signal contrast has a different functional dependence in the absorption, scattering and extinction spectra as discussed in the main text.

the two phononic spheres nearby.

In the case of the layer [Fig. 4.9 (a)] the signal contrast measured in the scattering and extinction first increases until it reaches a maximum value, and then starts decreasing for larger antennas. The decreasing tendency of the scattering signal can be explained as an effect of the smaller near-field enhancement provided by the large antennas with high radiative losses. Interestingly, the signal contrast in the scattering and in the extinction is optimized for different antenna sizes. From Fig. 4.9 (a) we can observe that the extinction signal is maximal for a scattering-absorption ratio of the antennas around ≈ 1, whereas the optimal scattering signal emerges for larger antennas. This is because the contribution of the large scattering dip is diminished by the positive absorption feature for large antennas. In the absorption, the initially large spectral dip practically disappears for the critically coupled antennas and flips into a positive bump for highly scattering antennas. This leads to the paradoxical situation in which the optimal SEIRS signal measured in the extinction almost exclusively emerges from the scattering of the hosting antenna.

A similar picture can be observed when we consider the samples of phononic spheres in Fig. 4.9 (b). In this case the optimal value of the signal contrast is encountered for antennas having slightly larger values of the scattering-absorption ratio. This is due to the relatively large geometrical size of the spheres that are exposed to the highly inhomogeneous field of the antennas. Nevertheless, as for the vibrationally active layer, the signal contrast measured in extinction spectra is maximized for antennas that are approximately equally scattering and absorbing.

In this optimal situation, again the spectral contrast is dominantly emerging from the dip of the scattering signal.

The straightforward observation from the results above is thus that the antennas whose scattering and absorption cross sections are approximately equal, $\sigma_{\mathrm{abs}} \approx \sigma_{\mathrm{sca}}$, provide the best sensing performance in SEIRS. The flat maximum of the extinction signal suggests that a relatively broad range of antenna sizes is able to provide a satisfactory signal contrast. Paradoxically, under the conditions when $\sigma_{\mathrm{abs}} \approx \sigma_{\mathrm{sca}}$, the extinction signal contrast emerges almost exclusively from the plasmonic scattering of the hosting antenna. These findings can be used as a practical rule to design hosting antennas for SEIRS. For optimal sensing, the sample should be positioned onto the plasmonic hot spot of the antenna, i.e. onto the position where the antenna near-field enhancement is the largest, and the antenna resonance should be tuned to the vibrational resonance of the detected sample. Moreover, as we have demonstrated here for linear plasmonic antennas, the size of the antennas should be chosen such that the scattering and the absorption of the antenna are approximately equal. This condition can be in practice most easily verified by numerical simulations, e.g. using the FDTD method.

4.5 Summary

This chapter has presented the underlying mechanisms behind the formation of the spectral fingerprints from a sample onto the spectra of plasmonic antenna that allow for sensitive identification of molecular vibrations. After having discussed the IR activity of a bare molecule, materials composed of many molecules and ionic solids, we have presented the coupled dipole model that allows for understanding the mechanism of the SEIRS signal enhancement.

We have further dissected the spectral response of the antenna-sample system into its scattering and absorption contributions. We have shown that in situations where the antenna scattering and absorption are similar, the SEIRS signal (the spectral fingerprint) in the extinction spectrum is given almost exclusively by the antenna-sample scattering. In such a situation, the sample fingerprint practically disappears in the absorption spectrum.

We have applied an analytical model to analyze the fully numerically calculated spectral response of a realistic system consisting of a single linear-rod antenna covered with a patch of a vibrationally active sample. The analytical modeling has allowed for interpreting the system's spectral response and extract information about the spatial dependence of the antenna-sample coupling and the vibrational spectral contrast observed in the absorption, scattering, and extinction.

Full numerical calculations verify that in common situations where tiny quantities of biomolecules are to be detected, the signal measured in any of the spectra follows a quadratic dependence on the mutual antenna-sample coupling parameter and hence linearly follows the near-field intensity in the surrounding of the plasmonic antenna. This conclusion, however, breaks for stronger antenna-sample coupling where saturation effects start to play role, due to the increasing importance of the multiple scattering between the sample and the antenna.

Linear plasmonic antennas have served us as a canonical example of a plasmonic hosting structure for SEIRS. We have performed an extensive numerical study of the antenna's scattering and absorption properties based on their geometrical size and established a simple rule that leads to the optimal antenna's performance for sensing.

Using numerical calculations we have empirically shown that the optimal extinction spectral contrast of a sample's vibrational fingerprint is found when the scattering and absorption of the hosting antennas are approximately equal. However, the exact optimal condition may slightly vary depending on the spatial distribution of the vibrational sample. Under these conditions, the extinction fingerprint arises predominantly due to the antenna's scattering in full accordance with the theory introduced in Section 4.3.2.

The findings of this chapter are of a practical importance for the experimental design of SEIRS-based sensors. In addition to the standard positioning of the sample into a plasmonic hot spot, i.e. positions of high plasmonic near-field enhancement, these results point out towards the requirement that the size of the antennas also needs to be adjusted such that $\sigma_{\mathrm{abs}} \approx \sigma_{\mathrm{sca}}$.

The generalization of this optimization scheme requires further numerical and analytical studies, however, a similar result can be expected for antennas of more general shapes. In practice, general distribution of the sample layer over the surface of the antenna influences the optimal antenna geometry (compare the results for a homogeneously covered antenna and the antenna interacting with the spherical sample shown in Fig. 4.9).

Part III

Surface-Enhanced Fluorescence

Chapter 5

Coupling of molecular emitters and plasmonic cavities beyond the point-dipole approximation

Upon interaction with an external electromagnetic field, an emitter can undergo a transition from the ground electronic state to an excited electronic state, produced by the absorption of a quantum of the driving field at the frequency of the respective electronic transition. This absorption event yields a characteristic spectral fingerprint which identifies the electronic transition in the measured absorption spectrum. Conversely, the excited state of the emitter can decay into the ground state and give rise to the emission of light, the so-called photoluminescence, at the specific frequency of the emitter's electronic transition. Both the emitter's absorption and emission properties are modified when the emitter couples with the electromagnetic modes of an optical cavity [209]. This coupling is enhanced when the quality factor of the cavity is high or the effective cavity mode volume is small, and when the electronic transition of the molecule possess a large transition dipole moment. In this context, the transition dipole moment of the molecules is usually considered to be point-like as the extent of the cavity modes is often large and the spatial variation of the cavity field occurs on scales much larger than the geometrical size of the emitters. Nevertheless, nanoscale plasmonic cavities represent a class of optical resonators that are able to squeeze the electromagnetic fields into deeply subwavelength dimensions, reaching effective mode volumes as small as a few nm^3. Under such conditions, emitters such as quantum dots [210–220] or organic molecules [52–56, 105, 221–223] cannot be approximated as point-like objects since the fields of the cavity modes vary considerably on the scale of the emitter's geometrical size [224]. In this chapter we present a formalism that allows for describing the coupling of the spatially extended excitonic transitions in organic molecules (molecular excitons) with the strongly confined modes of plasmonic cavities.

We describe the molecule as an electronic two-level system (TLS) interacting with the electromagnetic modes of the plasmonic environment. As a key quantity that steers the regime of plasmon-exciton coupling and determines the dynamical response of the system containing the plasmons and the exciton, we calculate the Jaynes-Cummings [225] plasmon-molecule coupling strength g. In the point-dipole approximation, g is usually estimated as the scalar product of the molecular transition dipole moment $\mathbf{d}_0$ and the local electric field $\tilde{\mathbf{E}}$ of the quantized cavity mode, as

$$\hbar g \approx -\mathbf{d}_0 \cdot \tilde{\mathbf{E}}. \tag{5.1}$$

Here we go beyond this approximation and evaluate g from a more complete quantum description of the plasmon-exciton coupling that fully considers the extension of the molecular exciton in the inhomogeneous plasmonic field.

To set the stage for the treatment of the plasmon-exciton interaction, we first briefly review the physics of the interaction between the molecular electronic excitations (excitons) and an incident electric field. After that we introduce the quantum formalism of the plasmon-exciton coupling which combines the description of the molecular excitons at the level of TDDFT with the canonical quantization of the localized plasmonic modes. Using this model we approach the problem of spatial mapping of the coupling g between the particle plasmon and a single-molecule's exciton, which is closely related to experiments where single molecules placed into the gap formed under the tip of a scanning tunneling microscope (STM) are electrically excited and emit photons into the far-field [52–56]. We further apply the model to demonstrate that the strong inhomogeneities of the plasmonic electromagnetic field can lead to breaking of the standard optical selection rules governing the interaction of the incident light with the molecular exciton and the exciton's radiation properties. Moreover, as the interaction strength between the plasmons and the molecular excitons is usually large, it significantly modifies the dynamics of the molecular excitons via the Purcell effect or, if the coupling between the plasmons and the exciton overcomes the system losses, even leads to the formation of new hybrid states combining molecular excitons and plasmons into the so-called *plexcitons* [226]. Using the quantum model we also show situations where the spatial extent of the molecule's excitons becomes important for a correct qualitative and quantitative description of the plasmon-exciton dynamics.

5.1 Coupling of a molecular electric-type electronic transition with a cavity mode

The scheme of the coupling between a molecular emitter and a cavity described in this section is schematically shown in Fig. 5.1. The simplest approach to the interaction of the molecule with light treats the molecule as a point-like two level

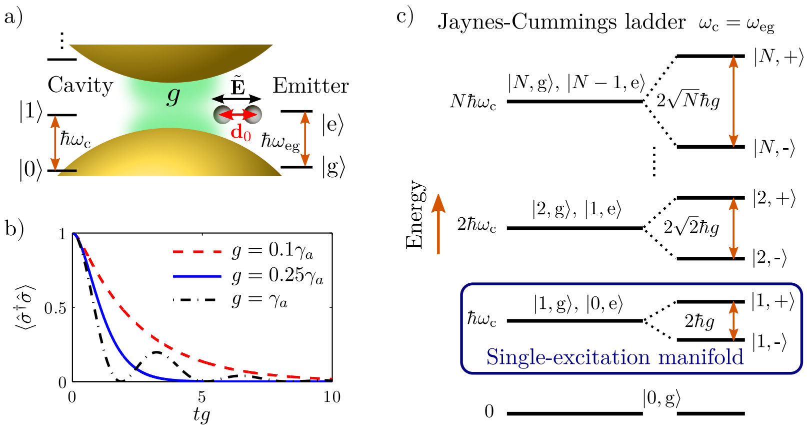

Figure 5.1: Coupling of a molecular electric-dipole electronic transition with a cavity mode. (a) Schematic of a plasmonic cavity interacting with a point-dipole emitter. The cavity is described as a bosonic mode described by Fock states $|0\rangle$, $|1\rangle \ldots$ with energy spacing $\hbar\omega_c$ given by the cavity-mode frequency. The emitter is described as a TLS with excitation energy between the ground, $|g\rangle$, and excited, $|e\rangle$, state $\hbar\omega_{eg}$. In the point-dipole approximation, the coupling between the cavity mode and the emitter's exciton is given by the scalar product of the emitter's transition dipole moment $\mathbf{d}_0$ and the electric field of the cavity mode $\tilde{\mathbf{E}}$ at the emitter's position. (b) The decay of the emitter's population into the mode of the cavity, as given by Eq. (5.20) for $g = 0.1\gamma_a$, (red dashed line), $0.25\gamma_a$ (blue solid line) and γ_a (black dash-dotted line), with γ_a the decay rate of the mode of the cavity. (c) Energy diagram of the states of the cavity and the emitter (assuming $\omega_c = \omega_{eg}$) if the coupling g is switched off (left) and after the coupling is turned on (right) as discussed in the main text. The blue frame marks the single-excitation manifold where either the cavity or the emitter are singly excited.

electronic system described by the Hamiltonian $\hat{H}_e$

$$\hat{H}_e = \hbar\omega_{eg}|e\rangle\langle e|, \tag{5.2}$$

with $\hbar\omega_{eg}$ the energy of the electronic excitation measured with respect to the ground-state energy. We further assume that this transition carries an oscillating transition dipole moment $\mathbf{d}_0$ associated with the electric-dipole-allowed electronic transition between the two electronic levels of the molecule: the ground state, $|g\rangle$, and the excited state of interest, $|e\rangle$:

$$\mathbf{d}_0 = \langle g|\hat{\mathbf{d}}|e\rangle. \tag{5.3}$$

Here $\hat{\mathbf{d}} = e\hat{\mathbf{r}}$ is the electron dipole-moment operator with e the electron charge and $\hat{\mathbf{r}}$ the position operator.

We assume that the molecule interacts with a single mode of a cavity that is described by the Hamiltonian $\hat{H}_{\mathrm{c}}$

$$\hat{H}_{\mathrm{c}} = \hbar\omega_{\mathrm{c}}\hat{a}^{\dagger}\hat{a}, \tag{5.4}$$

where $\hat{a}$ and $\hat{a}^{\dagger}$ are the bosonic annihilation and creation operators, respectively.

The interaction Hamiltonian, $\hat{H}_{\mathrm{c-e}}$, between the single electromagnetic mode of the cavity and the exciton is expressed in the point-dipole approximation in the form of the potential energy of the transition dipole of the molecule exposed to the electric field of the mode:

$$\hat{H}_{\mathrm{c-e}} = -\hat{\mathbf{d}} \cdot \hat{\mathbf{E}}, \tag{5.5}$$

where $\hat{\mathbf{E}}$ is the operator of the electromagnetic field evaluated at the position of the molecule. In the basis of the molecular ground and the excited state, the transition-dipole operator becomes

$$\hat{\mathbf{d}} = \langle \mathrm{g}|\hat{\mathbf{d}}|\mathrm{e}\rangle |\mathrm{g}\rangle\langle \mathrm{e}| + \mathrm{H.c.} = \mathbf{d}_0\hat{\sigma} + \mathrm{H.c.}, \tag{5.6}$$

where we have assumed that the molecule's charge density does not carry a dipole moment in the ground nor in the excited state and we have defined the TLS lowering operator $\hat{\sigma} \equiv |\mathrm{g}\rangle\langle \mathrm{e}|$. The electric field operator of the cavity mode can be expressed using the bosonic annihilation and creation operators as

$$\hat{\mathbf{E}} = \tilde{\mathbf{E}}\,(\hat{a} + \hat{a}^{\dagger}), \tag{5.7}$$

with $\tilde{\mathbf{E}}$ the quantum amplitude of the electric field of the cavity mode. In cavity quantum electrodynamics (QED), the quantum amplitude of the cavity mode is usually associated with the mode's effective volume V_{eff} [72, 209, 227–230] as

$$\tilde{\mathbf{E}} = \sqrt{\frac{\hbar\omega_{\mathrm{c}}}{2\varepsilon_0 V_{\mathrm{eff}}}}\frac{\mathbf{E}(\mathbf{r}_{\mathrm{mol}})}{\max\{|\mathbf{E}(\mathbf{r})|\}}, \tag{5.8}$$

where ω_{c} is the resonance frequency of the cavity mode and $\mathbf{E}(\mathbf{r})$ is the spatial distribution of the mode's electric field with $\mathbf{r}_{\mathrm{mol}}$ being the position of the molecule. For simplicity we now assume that both the electric field $\mathbf{E}(\mathbf{r}_{\mathrm{mol}})$ at the position of the molecule and the transition dipole moment $\mathbf{d}_0$ are real and write the interaction Hamiltonian as

$$\hat{H}_{\mathrm{c-e}} \equiv \hat{H}_{\mathrm{Rabi}} = \hbar g(\hat{a} + \hat{a}^{\dagger})(\hat{\sigma} + \hat{\sigma}^{\dagger}), \tag{5.9}$$

where $\hbar g = -\mathbf{d}_0 \cdot \tilde{\mathbf{E}}$ is the point-dipole approximation for the Jaynes-Cummings coupling constant. The Hamiltonian in Eq. (5.9) represents the Rabi interaction term between the bosonic cavity mode and the TLS and is usually approximated in the rotating-wave approximation (RWA). The RWA consists in neglecting the terms that contain the simultaneous creation or annihilation of both a quantum of the cavity excitation and the electronic excitation, $\hbar g\hat{a}\hat{\sigma}$ and $\hbar g\hat{a}^{\dagger}\hat{\sigma}^{\dagger}$, respectively, resulting in the Jaynes-Cummings coupling Hamiltonian:

$$\hat{H}_{\mathrm{J-C}} = \hbar g(\hat{a}\hat{\sigma}^{\dagger} + \hat{a}^{\dagger}\hat{\sigma}). \tag{5.10}$$

The RWA is used under the assumption that the coupling rate is smaller than the excitonic frequency [small Bloch-Siegert shift [231, 232] $\sim (g^2/\omega_{\mathrm{eg}}) \ll \omega_{\mathrm{eg}}$], and if the detuning between the plasmon and the exciton frequency is not too large (i.e. $\omega_{\mathrm{eg}} - \omega_{\mathrm{c}} \ll \omega_{\mathrm{eg}} + \omega_{\mathrm{c}}$).

The total Hamiltonian of the emitter coupled with the cavity mode can then be expressed as:

$$\hat{H}_{\mathrm{tot}} = \hat{H}_{\mathrm{c}} + \hat{H}_{\mathrm{e}} + \hat{H}_{\mathrm{J-C}}, \tag{5.11}$$

known as the Jaynes-Cummings model.

The Hamiltonian in Eq. (5.11) describes the coherent dynamics of the coupled cavity-emitter system. However, in practice, both the cavity and the emitter experience incoherent losses that are commonly added into the system's master equation [Eq. (3.26)] for the density matrix $\hat{\rho}$, via the Lindblad terms [Eq. (3.33)]

$$\mathscr{L}_{\hat{a}}^{\gamma_a}(\hat{\rho}) = \frac{\gamma_a}{2}\left(2\hat{a}\hat{\rho}\hat{a}^{\dagger} - \left\{\hat{a}^{\dagger}\hat{a}, \hat{\rho}\right\}\right), \tag{5.12}$$

$$\mathscr{L}_{\hat{\sigma}}^{\gamma_\sigma}(\hat{\rho}) = \frac{\gamma_\sigma}{2}\left(2\hat{\sigma}\hat{\rho}\hat{\sigma}^{\dagger} - \left\{\hat{\sigma}^{\dagger}\hat{\sigma}, \hat{\rho}\right\}\right), \tag{5.13}$$

where $\mathscr{L}_{\hat{a}}^{\gamma_a}(\hat{\rho})$ and $\mathscr{L}_{\hat{\sigma}}^{\gamma_0}(\hat{\rho})$ represent the losses of the cavity and the emitter, respectively, with γ_a the cavity decay rate and γ_σ the intrinsic decay rate of the molecule. The relationship between the system losses, represented by the decay rates γ_a and γ_σ, and the coupling constant, g, determines the coupling regime between the cavity and the emitter. In most common situations, the losses of the cavity (e.g. a plasmonic mode) are much larger than the coupling constant g and than the internal losses of the emitter, γ_σ. In such a case we can say that the cavity and the emitter are in the *weak-coupling* regime (or if $\gamma_a \ll g \ll \gamma_\sigma$ in the *bad-cavity* limit). The emitter states and the cavity states then represent a good basis for the description of the system and the interaction g only perturbatively influences the emitter's dynamics. On the other hand, if the coupling g overcomes the system losses ($g > \gamma_a, \gamma_\sigma$) the system is said to be in the *strong-coupling* regime. In the strong coupling regime the emitter states hybridize with the cavity states and form a new set of so-called polariton states (if the cavity mode is a plasmon the new states are also called plexcitonic states).

5.1.1 The weak-coupling regime

In the weak-coupling regime, the effective dynamics of the emitter in the presence of the cavity can be described as an irreversible decay of the exciton into the cavity mode. The cavity mode thus effectively acts for the emitter as an incoherent reservoir and can be eliminated using the method described in Section 3.1.3. The effective decay of the molecule into the plasmonic mode (the Purcell effect), assuming that the plasmon cavity is not incoherently populated, can then be expressed by the following Lindblad term:

$$\mathscr{L}_{\hat{\sigma}}^{\Gamma_{\text{eff}}}(\hat{\rho}) = \frac{\Gamma_{\text{eff}}}{2}\left(2\hat{\sigma}\hat{\rho}\hat{\sigma}^\dagger - \left\{\hat{\sigma}^\dagger\hat{\sigma},\hat{\rho}\right\}\right), \tag{5.14}$$

with the decay rate

$$\Gamma_{\text{eff}} = 2g^2\text{Re}\left\{\int_0^\infty \langle\hat{a}(\tau)\hat{a}^\dagger(0)\rangle e^{\text{i}\omega_{\text{eg}}\tau}\text{d}\tau\right\}, \tag{5.15}$$

which, assuming that the plasmon obeys a dynamics unperturbed by the presence of the molecule, yields

$$\Gamma_{\text{eff}} = \frac{g^2\gamma_a}{(\omega_{\text{c}}-\omega_{\text{eg}})^2 + (\gamma_a/2)^2}. \tag{5.16}$$

The interaction of the emitter with the cavity mode also yields a shift of the emitter's resonance frequency which vanishes for $\omega_{\text{eg}} = \omega_{\text{c}}$, and we neglect it here for simplicity. After elimination of the cavity, the emitter dynamics can be described by the Hamiltonian $\hat{H}_{\text{e}}$, accompanied by the Lindblad terms $\mathscr{L}_{\hat{\sigma}}^{\Gamma_{\text{eff}}}(\hat{\rho})$ and $\mathscr{L}_{\hat{\sigma}}^{\gamma_\sigma}(\hat{\rho})$. The effective dynamics of the emitter's excited state $|\text{e}\rangle$ is then obtained from the equation of motion for the operator's average $\langle\hat{\sigma}^\dagger\hat{\sigma}\rangle = \langle|\text{e}\rangle\langle\text{e}|\rangle$, following Eq. (3.34):

$$\frac{\text{d}}{\text{d}t}\langle\hat{\sigma}^\dagger\hat{\sigma}\rangle = -(\Gamma_{\text{eff}}+\gamma_\sigma)\langle\hat{\sigma}^\dagger\hat{\sigma}\rangle, \tag{5.17}$$

which yields an exponentially decaying population of the emitter

$$\langle\hat{\sigma}^\dagger\hat{\sigma}\rangle(t) = \langle\hat{\sigma}^\dagger\hat{\sigma}\rangle(0)e^{-(\Gamma_{\text{eff}}+\gamma_\sigma)t}, \tag{5.18}$$

with $\langle\hat{\sigma}^\dagger\hat{\sigma}\rangle(0)$ the initial value of the operator's average. This enhanced decay of the emitter due to the interaction with the cavity mode is the so-called Purcell effect.

5.1.2 The vacuum strong-coupling regime

When the coupling constant g is sufficiently large, the cavity mode can reversibly interchange energy with the emitter and thus give rise to Rabi oscillations. We show now how the Rabi oscillations emerge from the Jaynes-Cummings model [Eqs. (5.11), (5.12) and (5.13)] and discuss the criteria for the vacuum strong-coupling regime on more rigorous grounds. To obtain the effective dynamics of the strongly coupled system we use again Eq. (3.34) (under the simplified conditions which assume: $\omega_{\mathrm{eg}} = \omega_{\mathrm{c}}$ and $\gamma_\sigma \ll \gamma_a$) to arrive at:

$$\frac{\mathrm{d}}{\mathrm{d}t}\begin{bmatrix}\langle\hat{\sigma}^\dagger\hat{\sigma}\rangle\\ \langle\hat{a}\hat{\sigma}^\dagger\rangle\\ \langle\hat{a}^\dagger\hat{\sigma}\rangle\\ \langle\hat{a}^\dagger\hat{a}\rangle\end{bmatrix} \approx \begin{bmatrix}0 & -ig & ig & 0\\ -ig & -\gamma_a/2 & 0 & ig\\ ig & 0 & -\gamma_a/2 & -ig\\ 0 & ig & -ig & -\gamma_a\end{bmatrix}\begin{bmatrix}\langle\hat{\sigma}^\dagger\hat{\sigma}\rangle\\ \langle\hat{a}\hat{\sigma}^\dagger\rangle\\ \langle\hat{a}^\dagger\hat{\sigma}\rangle\\ \langle\hat{a}^\dagger\hat{a}\rangle\end{bmatrix}. \tag{5.19}$$

Eq. (5.19) yields the solution

$$\langle\hat{\sigma}^\dagger\hat{\sigma}\rangle(t) = e^{-\frac{\gamma_a}{2}t}\,\frac{\left(4\tilde{\Omega}^2 - 8g^2\right)\cos(\tilde{\Omega}t) + 2\gamma_a\tilde{\Omega}\sin(\tilde{\Omega}t) + 8g^2}{4\tilde{\Omega}^2}, \tag{5.20}$$

with $\tilde{\Omega} = \sqrt{4g^2 - \left(\frac{\gamma_a}{2}\right)^2}$, and assuming that initially $\langle\hat{\sigma}^\dagger\hat{\sigma}\rangle(0) = 1$ and $\langle\hat{a}\hat{\sigma}^\dagger\rangle = \langle\hat{a}^\dagger\hat{\sigma}\rangle = \langle\hat{a}^\dagger\hat{a}\rangle = 0$. The solution for the emitter's population $\langle\hat{\sigma}^\dagger\hat{\sigma}\rangle(t)$ has a character of an exponentially decaying oscillation of frequency $\tilde{\Omega}$, which for $g \gg \gamma_a$ approximately yields the well known Rabi frequency $\tilde{\Omega} \approx 2g$. The criterion of the vacuum strong coupling,

$$g \geq \gamma_a/4, \tag{5.21}$$

then ensures $\tilde{\Omega}$ to be real. We plot the dynamics of the emitter's excited state in Fig. 5.1 (b) for three different values of g: $g = 0.1\gamma_a$ (red dashed line), $g = 0.25\gamma_a$ (blue solid line), and $g = \gamma_a$ (black dashed-dotted line). For the smallest coupling the emitter's population exponentially irreversibly decays into the cavity mode. When the coupling reaches the strong-coupling condition, $g = \gamma_a/4$, the dynamics still has the form of an exponential decay as $\tilde{\Omega} = 0$. When we set the coupling equal to the decay rate of the cavity, the dynamics dramatically changes into an oscillation of the population between the emitter and the cavity, which is known as the Rabi oscillation.

Assuming that $g \gg \gamma_a$, we can see the strong coupling as a hybridization of the original cavity and emitter states into new polariton states. The new polariton states inherit the nonlinearity of the two-level emitter and form the so-called Jaynes-Cummings ladder in the energy diagram. The Jaynes-Cummings ladder is sketched in Fig. 5.1(c) together with the levels of the uncoupled system, assuming $\omega_{\mathrm{c}} = \omega_{\mathrm{eg}}$ for simplicity. In the case that the cavity-mode-exciton interaction is switched off, the system can be represented in the basis of eigenstates $|N, \mathrm{g(e)}\rangle = |N\rangle \otimes |\mathrm{g(e)}\rangle$ (with $\otimes$ the direct product), combining the cavity mode number states $|N\rangle$ and the electronic ground (excited) state $|\mathrm{g(e)}\rangle$ of the emitter.

For $\omega_{\mathrm{eg}} = \omega_{\mathrm{c}}$ and negligible interaction g, the states $|N-1, \mathrm{e}\rangle$ and $|N, \mathrm{g}\rangle$ are degenerate and their energies form an equally spaced ladder (on the left of the scheme). When g overcomes the system losses, the system enters the strong coupling regime and the degeneracy is lifted, resulting in a new set of hybrid polaritonic states $|N, +\rangle$ and $|N, -\rangle$ [$|N, \pm\rangle = (|N-1, \mathrm{e}\rangle \pm |N, \mathrm{g}\rangle)/\sqrt{2}$ shown on the right]. The energy splitting between these pairs of states, $\Delta E_{\mathrm{J-C}}(N)$, is proportional to the square root of the number of cavity-mode excitations present in the system and to the coupling constant g via $\Delta E_{\mathrm{J-C}}(N) = 2\sqrt{N}\hbar g$ and therefore the system exhibits nonlinear optical response upon strong illumination [233, 234] and leads to effects such as photon blockade [235, 236]. Nevertheless, many physical phenomena, such as the decay of the initially fully excited emitter into the cavity mode discussed above, can be described within the so-called single-excitation manifold (marked in Fig. 5.1 (c) by the blue frame), where either the molecule or the cavity mode are singly excited. Among others, also the optical absorption and photon emission of the Jaynes-Cummings system illuminated by a weak probing field is correctly captured by the dynamics of the ground state and the single-excitation manifold. We use this in Chapter 6 to describe the absorption and emission properties of coherently driven exciton polaritons.

5.1.3 Setting the regime of coupling between a single plasmonic mode and a single molecule's exciton

As we have seen, to correctly describe the dynamics of the system of a molecular excitonic emitter coupled with a plasmonic cavity, it is of utmost importance to establish the relation between the plasmon-exciton coupling and the internal system losses. To that end we briefly estimate the parameters that can be achieved in the configuration when a single molecule is placed into a plasmonic cavity using the point-dipole approximation.

The Jaynes-Cummings coupling constant g can be estimated as a product of the maximal quantized field amplitude of a plasmonic mode and the transition dipole moment of a common molecular emitter, $\mathbf{d}_0$. The latter usually reaches values of the order of $|\mathbf{d}_0| \sim 0.1\,e\cdot\mathrm{nm}$. The amplitude of the plasmonic electric field can be estimated from the mode volume achieved in the plasmonic cavity and the frequency of the plasmonic mode. The plasmonic energy usually reaches values of units of eV and for the estimation we choose $\hbar\omega_{\mathrm{c}} \approx 2\,\mathrm{eV}$. The mode volumes of plasmonic modes squeezed into plasmonic gaps can be as small as $V_{\mathrm{eff}} \sim 10\,\mathrm{nm}^3$ [105, 227, 230, 237, 238]. Using these values we estimate that g can reach values of up to approximately $\hbar g \sim 100\,\mathrm{meV}$. This value must be compared with the intrinsic losses of the plasmonic cavities that are often large. The cavity losses are usually expressed in the form of the quality factor $Q \approx \omega_{\mathrm{c}}/\gamma_a$, which for plasmonic cavities commonly ranges around $Q \sim 10-20$, yielding $\gamma_a \sim 100\,\mathrm{meV}$, or even smaller values $Q \sim 1$ for bad cavities formed, e.g., under the tip of a scanning tunneling microscope, giving $\gamma_a \sim 1\,\mathrm{eV}$. Nevertheless, higher quality factors, $Q \sim 60-70$, have been reached for silver particles [227].

The regime of the plasmon-exciton coupling thus balances on the edge between the strong and the weak couping, depending on the type of the cavity used or the position and orientation of the emitters in the cavity. It is therefore important to correctly estimate the coupling constant g between the plasmonic modes and the molecule's excitons. Moreover, the morphology of the plasmonic particles causes distorsion of the electromagnetic fields in the proximity of their surface which spatially vary on a scale similar to the geometrical size of the molecule, which often hinders the use of the point-dipole approximation to estimate g. Below we therefore describe how the plasmon-exciton coupling g can be estimated beyond the point-dipole approximation taking into account the spatial extent of the molecule's excitonic transitions.

5.1.4 Model of plasmon-exciton coupling beyond the point-dipole approximation

To describe the interaction between plasmons and the excitons of organic molecules we use a quantum treatment that combines the canonical quantization of plasmons with first-principles calculations of the molecular electronic excitations based on TDDFT, as schematically depicted in Fig. 5.2 (a). Plasmonic modes are considered as harmonic oscillations of the incompressible free electron gas characterized by an electron density, N_e, and effective electron mass m_e [63, 110, 118, 239–242] that is contained in the metallic nanoparticles. The dielectric function describing the response of the corresponding bulk metal is thus given by the Drude model (Section 1.2.1). Each n-th plasmonic mode of frequency ω_n of the nanoparticle is then characterized by its quantized electric potential $\phi_n^{(+)}$ [$\phi_n^{(-)}$] and surface charge density $\sigma_n^{(\pm)}$, obtained from the canonical quantization of surface modes introduced in Section 1.3, with the superscripts $(+)$ [$(-)$] labelling the positive (negative) frequency part. Such a plasmonic system can be described by a Hamiltonian, $\hat{H}_{\mathrm{pl}}$, resembling a set of non-interacting harmonic oscillators:

$$\hat{H}_{\mathrm{pl}} = \sum_n \hbar\omega_n \hat{a}_n^\dagger \hat{a}_n, \tag{5.22}$$

where $\hat{a}_n$ ($\hat{a}_n^\dagger$) are the bosonic annihilation (creation) operators of the n^{th} plasmonic mode. In principle, this model can be extended to the quantization of non-local plasmonic modes [243, 244], nevertheless, the local classical description adopted in this thesis can effectively describe the inhomogeneous screened fields in many representative plasmonic cavities [245–248].

We consider the molecular excitations (excitons) using linear-response TDDFT at the level of the Tamm-Dancoff approximation in vacuum (see also Section 2.2.2). From the TDDFT calculations we obtain the transition density, $\rho_{\mathrm{eg}}(\mathbf{r})$, which describes the oscillating electric charge associated with the electronic transition of the molecule. The transition-charge density can be formally defined as the expectation value of the electronic-density operator $\hat{\rho}_{\mathrm{c}}(\mathbf{r})$ ($\rho_{\mathrm{eg}}(\mathbf{r}) = e\langle \mathrm{e}|\hat{\rho}_{\mathrm{c}}(\mathbf{r})|\mathrm{g}\rangle$), accounting for the electronic transitions between the ground $|\mathrm{g}\rangle$ and the excited $|\mathrm{e}\rangle$ states. The transition-charge density is defined in relation with the TDDFT in Section 2.2.2. Throughout the thesis we consider that the plasmons interact with molecules physisorbed or physically separated from the surface of the metallic particles by a dielectric spacer and thus neglect the orbital overlap between the molecular and metal wave functions.

Within this quantum framework, the coupling g_n between the molecular exciton and the n^{th} plasmonic mode is calculated as a convolution integral of the plasmonic

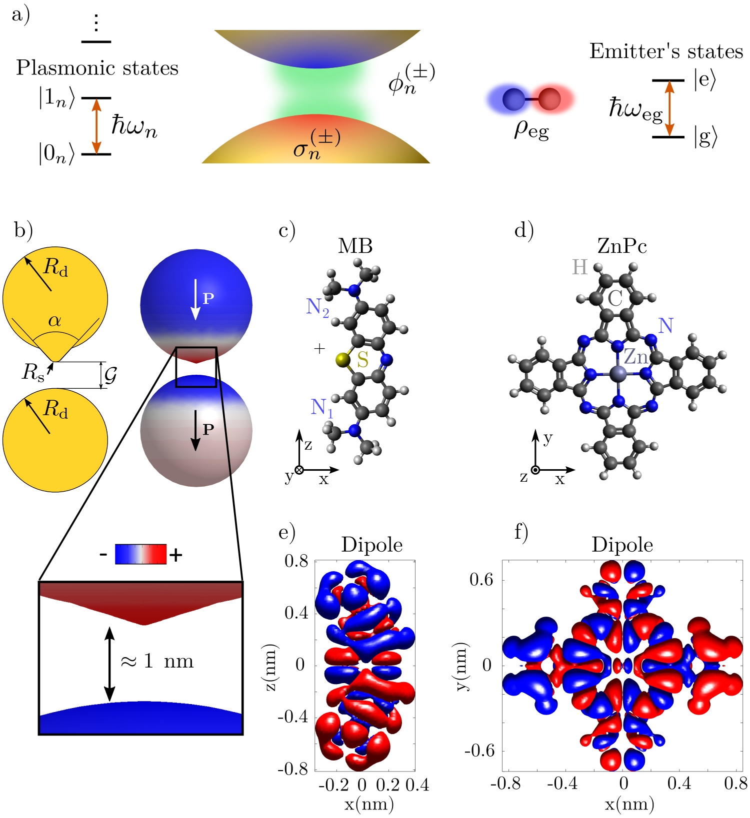

Figure 5.2: (a) Schematics of the plasmonic resonator-emitter system. The plasmon is described as a harmonic oscillation of an incompressible electron gas. Molecular excitations are addressed as two-level systems of energy $\hbar\omega_{\mathrm{eg}}$. The plasmon interacts with the molecular transition density ρ_{eg}. (b) Schematics of the geometry used to map the coupling strength (left). A plasmonic dimer of radii $R_\mathrm{d} = 5$ nm, with a protrusion of $R_\mathrm{s} = 0.2$ nm (cone opening angle $\alpha = 72.5^\circ$) hosts a molecule located at position $(x, y, z = 0)$ within the gap of width $\mathcal{G}$. MB ($\mathcal{G} = 2$ nm) and ZnPc ($\mathcal{G} = 1$ nm) molecules are considered. Surface charge distribution of the bonding-dimer plasmonic mode considered for the mapping of the molecular excitons (right). The surface charge density is highly concentrated in the gap around the sharp protrusion, as shown in the zoom. (c,d) Atomic structure of (c) methylene blue (MB) and (d) zinc phtalocyanine (ZnPc). (e,f) Isosurface plots of the transition densities (MB, ZnPc) corresponding to the transition between the ground and the singlet excited state calculated within the TDDFT framework (blue: negative values of the density, and red: positive ones).

potential and the molecular transition density (considering here that the transition density is real):

$$\boxed{\hbar g_n = \int \rho_{\mathrm{eg}}(\mathbf{r})\phi_n^{(+)}(\mathbf{r})\,\mathrm{d}^3\mathbf{r},} \tag{5.23}$$

where the integral is evaluated over the distribution of the molecular transition-charge density. The Hamiltonian describing the plasmon-exciton interaction is:

$$\hat{H}_{\mathrm{pl-mol}} = \hbar \sum_{i,n} \left[g_{n,i}^{*} \hat{a}_n^{\dagger} |\mathrm{g}\rangle\langle \mathrm{e}_i| + g_{n,i}\hat{a}_n |\mathrm{e}_i\rangle\langle \mathrm{g}| \right], \tag{5.24}$$

where $|\mathrm{g}\rangle$ ($|\mathrm{e}_i\rangle$) are the electronic ground state (excited state i).

5.2 Spatial mapping of g for realistic organic molecules

In many practical plasmonic cavities the near-field can be highly confined due to particle special morphologies such as protrusions emerging on the facets inside gaps, leading to extreme field localization at the atomic scale [249]. A similar effect can be also obtained, for instance, in the gap between a metallic substrate and an atomically sharp tip of a scanning probe microscope [51–57]. The latter situation allows to optically map the magnitude of plasmon-exciton coupling, as the sharp tip is scanned over the molecule. We reproduce this situation in a plasmonic dimer with an atomistic protrusion in the gap whose geometry is depicted in Fig. 5.2(b). Such a model is able to quantitatively reproduce the near-field distribution around atomic-scale features in plasmonic cavities, as recently validated by comparison with TDDFT results [248]. In the following, we use the plasma frequency ω_{p} as a parameter that allows us for tuning the low-energy bonding-dipole plasmon of the dimer [the surface charge density of the mode is shown in Fig. 5.2(b), on the right] with frequency $\omega_1 \equiv \omega_{\mathrm{pl}}$, to be resonant with the exciton of the molecule, and calculate the coupling strength between the two as the gap is scanned over the molecule in the horizontal plane xy, while keeping z constant.

We illustrate the importance of the quantum treatment of the molecular electronic transitions in two specific cases of dye molecules: methylene blue (MB) [Fig. 5.2 (c)] and zinc phtalocyanine (ZnPc) [Fig. 5.2 (d)], due to their relevance in experimental situations [54, 55, 238]. MB is a molecule with an electronic transition S_z of a strong dipole transition moment (optically active) oriented along the z axis, $d_z = 0.23$ e·nm [axes marked in Fig. 5.2 (c,d)]. ZnPc is a *flat* molecule with all the atoms lying on the xy plane showing two degenerate optically active transitions, S_x and S_y, on the same plane, with transition dipole moment $d_{x,y} = 0.17$ e·nm. The transition charge densities of the molecular excitons are shown as isosurface plots in Fig. 5.2 (e,f) for the S_z transition of MB (e) and the transition S_x of ZnPc (f), respectively. The positive (red) and negative (blue) transition charge densities are clearly observable at opposite sides of both molecules, corroborating the dipole character of the transitions, continuously distributed over the entire extent of the molecules (~ 2 nm).

We first place into the gap the MB molecule oriented vertically (electronic transistion S_z), and compare the map of the coupling strength, calculated within the full quantum model (FQM) [Fig. 5.3 (b)] with that obtained with the point-dipole model (PDM) [Fig. 5.3 (c)]. The coupling is maximized when the molecule is positioned at the center of the gap and reaches values of up to 120 meV, being larger in the FQM by $\approx 10\,\mathrm{meV}$ than in the PDM. The magnitude of the coupling decreases as the molecule is displaced off the center, following the decay of the electric field component along the dimer axis. The point-dipole approximation [Fig. 5.3 (c)] in this case reproduces well both the qualitative and quantitative features of the first-principles calculation [Fig. 5.3 (b)], validating the use of this approach in this highly symmetric situation.

A more dramatic situation occurs when the ZnPc molecule is considered (with the plane of the molecule perpendicular to the dimer axis). As ZnPc has two degenerate transitions, S_x and S_y, we calculate the map of the effective coupling defined as:

$$g^{\mathrm{ZnPc}}_{S_{\mathrm{x(y)}}}(\mathbf{r}_0) = \sqrt{|g^{\mathrm{ZnPc}}_{S_{\mathrm{x}}}(\mathbf{r}_0)|^2 + |g^{\mathrm{ZnPc}}_{S_{\mathrm{y}}}(\mathbf{r}_0)|^2}. \tag{5.25}$$

We show the corresponding maps in Figs. 5.3 (d,e) calculated using the FQM (d) and the PDM (e), respectively. When the molecule is placed at the center of the cavity, both maps exhibit a minimum (zero) originated by the vanishing overlap integral between a rotationally symmetrical plasmon mode and a horizontal electronic dipolar transition in the molecule. Away from the center, the $\mathrm{C}_{4\mathrm{v}}$ symmetry is broken and the map shows a doughnut-like shape, following the pattern of the radial component of the electric local field in the proximity of the atomistic protrusion [51, 105, 249]. Interestingly, whereas the result of the PDM [Fig. 5.3 (e)] is fully rotationally symmetric, the FQM map [Fig. 5.3 (d)] acquires the four-fold symmetry of the molecular sample ($\mathrm{D}_{4\mathrm{h}}$). We highlight this effect by plotting in Fig. 5.3 (f) a cut along the circular trajectory marked by the blue circle in Fig. 5.3 (d) and the green circle in Fig. 5.3 (e). The FQM result exhibits experimentally accessible oscillations of the coupling constant, characterized by $\approx 10\%$ variation, whereas the PDM yields a constant profile. Importantly, the FQM yields a coupling constant reaching roughly one half of the coupling strength obtained from the PDM. These values are fully consistent with the experimental ones reported for this kind of systems [52, 53].

5.3 Breaking of optical selection rules in plasmonic cavities

The effect of the extreme field localization in plasmonic cavities can also have a dramatic impact on the optical selection rules governing the interaction of incident

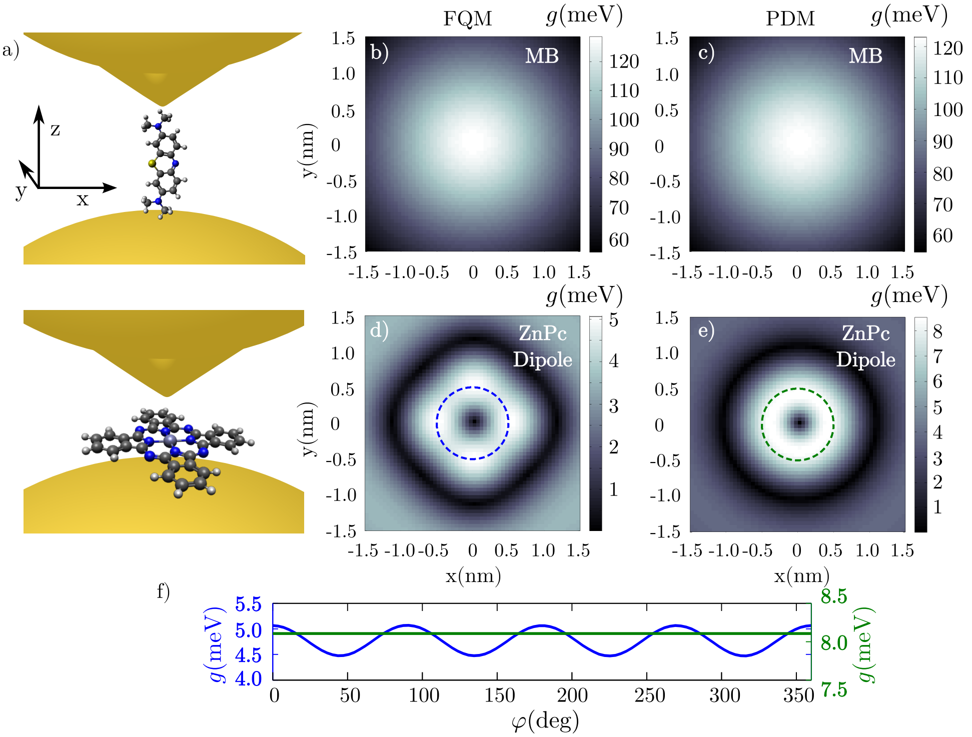

Figure 5.3: (a) Schematics of the molecular orientation in the plasmonic gap. The MB is oriented vertically (top) and the ZnPc molecule horizontally (bottom). The plasmonic cavity is scanned in the xy plane. (b-e) Maps of the coupling constant $g(\mathbf{r}_0)$ between the plasmon dipolar gap mode and the molecular electronic transition as a function of the lateral displacement of the center of the molecule around the gap (center of the gap at $x = y = 0$). (b,c) Maps of g calculated for a vertically oriented MB molecule. (d,e) Maps of effective g for a horizontally positioned ZnPc molecule, which considers both lowest-energy degenerated dipole transitions. Maps to the left obtained within the FQM, and maps to the right within the PDM. (f) Circular cut of g at a distance of 0.5 nm from the center as indicated with dashed lines in (d,e). FQM (blue) and PDM (green) are compared.

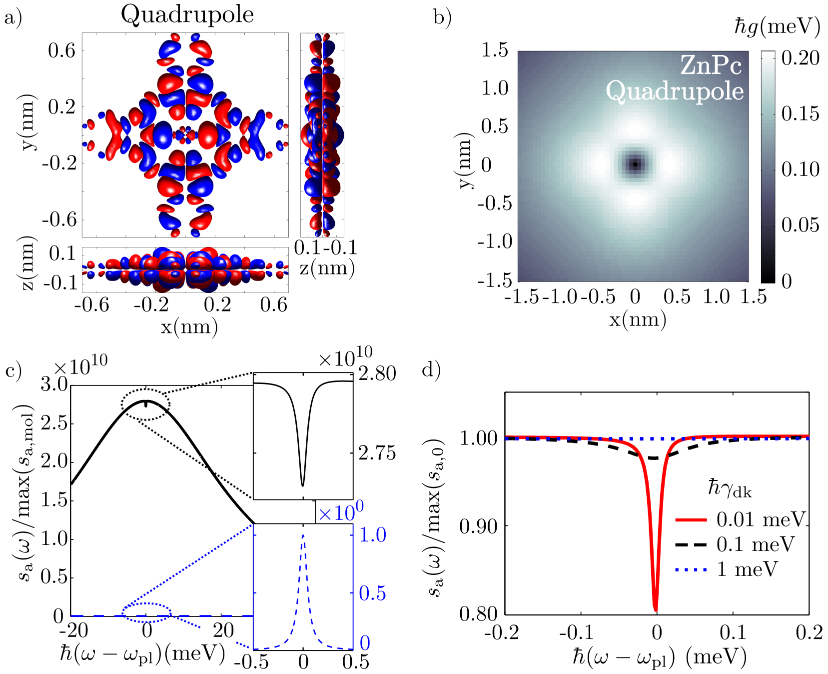

Figure 5.4: Breaking of optical selection rules for the quadrupolar transition of ZnPc. (a) Isosurface plot of the transition charge density produced by the quadrupolar electronic transition of the ZnPc molecule. The positive values are red, the negative values are blue. (b) Map of the plasmon-exciton effective coupling constant $g^{\mathrm{ZnPc}}_{S_{xz(yz)}}$, as the plasmonic cavity is scanned across the molecule in the xy plane (see inset). (c) Absorption spectra of the plasmonic cavity with the molecule inside (black line) and of the bare molecule in vacuum (blue-dashed line). The broadening of the molecular excitation is considered to be $\hbar\gamma_{\mathrm{dk}} = 0.1\,\mathrm{meV}$. The spectra are normalized to the maximum of the bare-molecule absorption, $s_{\mathrm{a}}(\omega)/\max(s_{\mathrm{a,mol}})$. The absorption spectrum of the bare molecule in vacuum has a form of a Lorentzian peak of ≈ 9 orders of magnitude smaller amplitude compared to the depth of the Fano-like dip in the absorption of the coupled plasmon-exciton system. (d) Absorption spectra of the particle-molecule system normalized to the maximum of the absorption spectrum of the bare plasmonic dimer, $s_a(\omega)/\max(s_{a,0})$, for $\hbar\gamma_{\mathrm{dk}} = 0.01\,\mathrm{meV}$, $0.1\,\mathrm{meV}$ and $1\,\mathrm{meV}$. The magnitude of the absorption dip reaches $\approx 20\,\%$ of the absorption maximum for $\hbar\gamma_{\mathrm{dk}} = 0.01\,\mathrm{meV}$ (red solid line), gets shallower but still visible for $\hbar\gamma_{\mathrm{dk}} = 0.1\,\mathrm{meV}$ [the value used in (c)], with a magnitude of $\approx 2.5\,\%$ of the absorption maximum (black dashed line), and almost completely disappears for $\hbar\gamma_{\mathrm{dk}} = 1\,\mathrm{meV}$ (blue dotted line).

light with molecular transitions. To demonstrate this, we calculate the charge transition densities of a degenerate quadrupolar electronic transition S_{xz} (S_{yz}) of ZnPc (quadrupolar moment $\mathcal{Q}_{yz} = \mathcal{Q}_{xz} = \int xz\rho_{S_{xz}}\mathrm{d}^3\mathbf{r} \approx 2.74 \times 10^{-4}\,\mathrm{e}\cdot\mathrm{nm}^2$ and energy $\hbar\omega_{\mathrm{dk}} \approx 2.97\,\mathrm{eV}$) which does not carry any dipole moment and is thus effectively dark for an incident plane wave in vacuum. We show the corresponding transition density $\rho_{S_{xz}}$ in Fig. 5.4 (a). Following the same procedure as for the degenerate dipole transitions S_x and S_y in the previous section, we calculate the spatial map of the effective coupling constant $g^{\mathrm{ZnPc}}_{S_{xz(yz)}} = \sqrt{|g^{\mathrm{ZnPc}}_{S_{xz}}|^2 + |g^{\mathrm{ZnPc}}_{S_{yz}}|^2}$ between the quadrupolar excitonic transitions and the same bonding dipolar plasmon as in the dimer structure of Fig. 5.3(a). The map of $g^{\mathrm{ZnPc}}_{S_{xz(yz)}}$ is shown in Fig. 5.4 (b). The spatial distribution of $g^{\mathrm{ZnPc}}_{S_{xz(yz)}}$ exhibits four-fold symmetry $\mathrm{D}_{4\mathrm{h}}$, as was also found for the dipolar transition. The maximum value of the plasmon-exciton coupling obtained for this situation reaches $\approx 0.2\,\mathrm{meV}$, which sets the interaction into the weak coupling regime. Nevertheless, the calculated value of $g^{\mathrm{ZnPc}}_{S_{xz(yz)}}$ is large enough to allow for detection of the originally dark excitonic transition in the plasmon-enhanced absorption spectrum.

To demonstrate this breaking of optical selection rules we consider the values of $g^{\mathrm{ZnPc}}_{S_{xz(yz)}}$ obtained for a position of the molecule in the atomically sharp plasmonic gap at $x = 0.4\,\mathrm{nm}$, $y = 0\,\mathrm{nm}$, and calculate the optical absorption spectra [163–165], $s_{\mathrm{a}}(\omega)$, of the coupled system and that of the bare molecule in vacuum. We describe the plasmonic excitations by the Hamiltonian in Eq. (5.22) and treat the *dark* (dk) excitation of the molecule as a two-level system with $\hbar\omega_{\mathrm{dk}} = E_{\mathrm{e_{dk}}} - E_{\mathrm{g}}$. This Hamiltonian can be expressed as:

$$\hat{H}^{\mathrm{dk}}_{\mathrm{mol}} \approx E_{\mathrm{g}}|\mathrm{g}\rangle\langle\mathrm{g}| + E_{\mathrm{e_{dk}}}|\mathrm{e}\rangle\langle\mathrm{e}| \equiv \hbar\omega_{\mathrm{dk}}\hat{\sigma}^\dagger\hat{\sigma}, \tag{5.26}$$

where we assume that only one excited state $|\mathrm{e_{dk}}\rangle$ actively contributes to the absorption. To simplify the notation, on the right-hand side of Eq. (5.26) we have rewritten the Hamiltonian $\hat{H}^{\mathrm{dk}}_{\mathrm{mol}}$ in terms of the Pauli operators, setting $E_{\mathrm{g}} = 0$, without loss of generality. In this notation, the plasmon-exciton coupling Hamiltonian is:

$$\hat{H}^{\mathrm{dk}}_{\mathrm{pl-mol}} = \hbar\sum_{i,n}\left[g^{\mathrm{dk}*}_n\hat{a}^\dagger_n\hat{\sigma} + g^{\mathrm{dk}}_n\hat{a}_n\hat{\sigma}^\dagger\right], \tag{5.27}$$

where g^{dk}_n is the exciton-plasmon coupling constant as defined above for the dipole electronic transitions.

We further add the broadening of the plasmons, γ_a, and of the dark exciton, γ_{dk}, via the master equation [Eq. (3.26)] for the density matrix $\hat{\rho}$,

$$\dot{\hat{\rho}} = \frac{1}{\mathrm{i}\hbar}[\hat{H}^{\mathrm{dk}}_{\mathrm{mol}}, \hat{\rho}] + \sum_n \mathscr{L}^{\gamma_{a_n}}_{\hat{a}_n}(\hat{\rho}) + \mathscr{L}^{\gamma_{\mathrm{dk}}}_{\hat{\sigma}}(\hat{\rho}), \tag{5.28}$$

with the Lindblad superoperators

$$\mathscr{L}_{\hat{a}_n}^{\gamma_{a_n}}(\hat{\rho}) = \frac{\gamma_{a_n}}{2}\left(2\hat{a}_n\hat{\rho}\hat{a}_n^\dagger - \{\hat{a}_n^\dagger\hat{a}_n, \hat{\rho}\}\right), \tag{5.29}$$

$$\mathscr{L}_{\hat{\sigma}}^{\gamma_{\mathrm{dk}}}(\hat{\rho}) = \frac{\gamma_{\mathrm{dk}}}{2}\left(2\hat{\sigma}\hat{\rho}\hat{\sigma}^\dagger - \{\hat{\sigma}^\dagger\hat{\sigma}, \hat{\rho}\}\right). \tag{5.30}$$

We set the intrinsic broadening of the molecular resonance $\hbar\gamma_{\mathrm{dk}} = 0.1\,\mathrm{meV}$ and that of the plasmonic modes $\hbar\gamma_{a_n} = \hbar\gamma_a = 50\,\mathrm{meV}$ for all n modes.

We calculate the probe-absorption spectrum of the plasmon [163–165] (dropping the pre-factors) by generalizing Eq. (3.80) as the one-sided Fourier transformation of the plasmonic dipole operator's two-time auto-correlation function $\langle\hat{\mathcal{D}}(\tau)\hat{\mathcal{D}}^\dagger(0)\rangle$

$$\begin{aligned} s_{\mathrm{a}}(\omega) =& 2\mathrm{Re}\left\{\int_0^\infty \langle\hat{D}(\tau)\hat{\mathcal{D}}^\dagger(0)\rangle e^{\mathrm{i}\omega\tau}\,\mathrm{d}\tau\right\} \\ &= 2\sum_{mn}\mathcal{D}_m\mathcal{D}_n\mathrm{Re}\left\{\int_0^\infty \langle\hat{a}_m(\tau)\hat{a}_n^\dagger(0)\rangle e^{\mathrm{i}\omega\tau}\,\mathrm{d}\tau\right\}, \end{aligned} \tag{5.31}$$

where the plasmonic dipole operator $\hat{\mathcal{D}} = \sum_n \mathcal{D}_n\hat{a}_n$, with $\mathcal{D}_n$ the projections of the respective plasmon dipole moments along the assumed polarization of the incident light. We assume that the plasmonic mode n couples to an incident probing plane wave of amplitude E_0 and for the calculation of the absorption spectra, we consider the plasmon-probe coupling constant $\propto -\mathcal{D}_n$, normalized to the incident light amplitude. We neglect here the direct and much weaker coupling of the molecular quadrupolar transition with the incident light.

To show the effect of selection rules breaking in a specific situation, we calculate the probe-absorption spectrum of the dimer cavity with an atomistic protrusion in the gap [Fig. 5.2 (b)] and assume that the probing light is polarized along the z axis of the dimer and therefore effectively couples mainly to the bonding dimer plasmon. The dipole moments $\mathcal{D}_n$ are then defined as

$$\mathcal{D}_n = \iint_{\partial V} \sigma_n^{(+)} z\,\mathrm{d}^2\mathbf{s}, \tag{5.32}$$

where $\sigma_n^{(+)}$ is the quantized surface-charge density of the plasmonic mode n and the integration is performed over the surfaces of the plasmonic particles.

In order to evaluate the two-time autocorrelation function $\langle\hat{a}_m(\tau)\hat{a}_n^\dagger(0)\rangle$ we apply the quantum regression theorem (see Section 3.1.4) which allows for obtaining the correlation functions as solutions of the set of differential equations:

$$\begin{aligned} \frac{\mathrm{d}\langle\hat{a}_i(\tau)\hat{a}_j^\dagger(0)\rangle}{\mathrm{d}\tau} &= (-\mathrm{i}\omega_i - \gamma_a/2)\langle\hat{a}_i(\tau)\hat{a}_j^\dagger(0)\rangle - \mathrm{i}g_i^{\mathrm{dk}}\langle\hat{\sigma}(\tau)\hat{a}_j^\dagger(0)\rangle, \\ \frac{\mathrm{d}\langle\hat{\sigma}(\tau)\hat{a}_j^\dagger(0)\rangle}{\mathrm{d}\tau} &= (-\mathrm{i}\omega_{\mathrm{dk}} - \gamma_{\mathrm{dk}}/2)\langle\hat{\sigma}(\tau)\hat{a}_j^\dagger(0)\rangle - \mathrm{i}\sum_i g_i^{\mathrm{dk}}\langle\hat{a}_i(\tau)\hat{a}_j^\dagger(0)\rangle. \end{aligned} \tag{5.33}$$

Assuming that the plasmon and the exciton are in the ground state when the probing field is not present, the initial conditions become:

$$\langle \hat{a}_m(0)\hat{a}_n^\dagger(0)\rangle = \delta_{mn}, \tag{5.34}$$

$$\langle \hat{\sigma}(0)\hat{a}_m^\dagger(0)\rangle = 0, \tag{5.35}$$

with δ_{mn} the Kronecker delta. We solve the set of Eqs. (5.33) numerically and perform the one-sided Fourier transformation to obtain the absorption spectrum. The set of equations yields

$$s_\mathrm{a}(\omega) = 2\mathrm{Im}\left\{\sum_{mn}\left[\frac{\mathcal{D}_m\mathcal{D}_n\delta_{mn}}{\Delta_m - \mathrm{i}\gamma_a/2} + \frac{\frac{g_m^\mathrm{dk}\mathcal{D}_m\mathcal{D}_n g_n^\mathrm{dk}}{(\Delta_m - \mathrm{i}\gamma_a/2)(\Delta_n - \mathrm{i}\gamma_a/2)}}{(\delta - \mathrm{i}\gamma_\mathrm{dk}/2) - \sum_k \frac{g_k^{\mathrm{dk}\,2}}{\Delta_k - \mathrm{i}\gamma_a/2}}\right]\right\}, \tag{5.36}$$

where $\Delta_n = \omega_n - \omega$, $\delta = \omega_\mathrm{dk} - \omega$, and $\mathrm{Im}\{\cdot\}$ stands for the imaginary part.

For comparison we additionally calculate the probe-absorption spectrum of the molecular quadrupolar mode in a vacuum (i.e. without the plasmon). To do that, we calculate the normalized coupling strength of the quadrupolar excitonic transition in the molecule, $\mathcal{E}_\mathrm{mol}$, for an incident plane-wave with $z-$polarized electric field of unit amplitude, propagating in the x direction as

$$\mathcal{E}_\mathrm{mol} \approx -\mathrm{i}k \iiint zx\rho_\mathrm{dk}\,\mathrm{d}^3\mathbf{r}, \tag{5.37}$$

with $k = 2\pi/\lambda^\mathrm{inc}$, where λ^inc is the vacuum wavelength of the incident light that is resonant with the molecular transition, and ρ_dk the transition-charge density of the *dark* (dk) quadrupolar exciton (carrying zero net dipole moment).

The absorption spectrum of the bare molecule, $s_\mathrm{a,mol}(\omega)$, is then calculated as in the case of the plasmonic particle, but now assuming that the incident probe directly interacts with the molecule:

$$s_{a,\mathrm{mol}}(\omega) = 2|\mathcal{E}_\mathrm{mol}|^2\mathrm{Re}\left\{\int_0^\infty \langle\hat{\sigma}(\tau)\hat{\sigma}^\dagger(0)\rangle e^{\mathrm{i}\omega\tau}\,\mathrm{d}\tau\right\}. \tag{5.38}$$

We resolve the two-time correlation function from the differential equation

$$\frac{\mathrm{d}\langle\hat{\sigma}(\tau)\hat{\sigma}^\dagger(0)\rangle}{\mathrm{d}\tau} = (-\mathrm{i}\omega_\mathrm{dk} - \gamma_\mathrm{dk}/2)\langle\hat{\sigma}(\tau)\hat{\sigma}^\dagger(0)\rangle, \tag{5.39}$$

with the initial condition

$$\langle\hat{\sigma}(0)\hat{\sigma}^\dagger(0)\rangle = 1. \tag{5.40}$$

The absorption spectrum of the bare molecule in vacuum can be finally obtained in the form

$$s_{a,\mathrm{mol}}(\omega) = \frac{|\mathcal{E}_{\mathrm{mol}}|^2 \gamma_{\mathrm{dk}}}{(\omega_{\mathrm{dk}} - \omega)^2 + (\gamma_{\mathrm{dk}}/2)^2}. \tag{5.41}$$

For this calculation we assume that the intrinsic width of the molecular transition is $\hbar\gamma_{\mathrm{dk}} = 0.1\,\mathrm{meV}$, taken as a representative intermediate value characterising fluorescent molecules. In Fig. 5.4 (c) we compare the spectrum of the coupled molecule-cavity system (black line) with the absorption of the molecule in a vacuum (blue dashed line). The spectra are normalized to the maximal value of the bare-molecule absorption $s_{\mathrm{a,mol}}(\omega)$. The spectrum of the cavity-molecule system shows the shape of a broad Lorentzian resonance originated from light absorbed by the bonding dimer plasmon perturbed by a small spectral dip that emerges due to the ZnPc quadrupolar electronic transition (Fano-like profile). On the other hand, the absorption peak of the bare molecule in a vacuum cannot be resolved on the selected scale and the blue dashed line appears to be flat. In the inset of Fig. 5.4 (c) we therefore zoom in the molecular absorption features and compare their relative spectral intensities. Strikingly, the size of the absorption dip obtained in the plasmonic cavity is ≈ 9 orders of magnitude larger than the absorption peak of the bare molecule, thus making the quadrupolar excitonic transition accessible to optical absorption spectroscopy.

Nevertheless, in practice, the value of the excitonic broadening γ_{dk} determines the magnitude of the absorption dip. To demonstrate this effect we compare the absorption dip calculated for the quadrupolar excitonic transition of ZnPc considering three different values of the intrinsic broadening: $\hbar\gamma_{\mathrm{dk}} = 0.01\,\mathrm{meV}$, $0.1\,\mathrm{meV}$ and $1\,\mathrm{meV}$. The respective spectra, normalized to the maximum of the plasmonic absorption without the molecule, $s_{\mathrm{a},0}$, are shown in Fig. 5.4 (d). For $\hbar\gamma_{\mathrm{dk}} = 0.01\,\mathrm{meV}$ the magnitude of the molecular Fano-like absorption dip reaches $\approx 20\,\%$ of the plasmonic-peak amplitude. For $\hbar\gamma_{\mathrm{dk}} = 0.1\,\mathrm{meV}$, the value used in Fig. 5.4 (c), the dip reaches $\approx 2.5\,\%$ of the plasmonic absorption maximum and could be still experimentally observed. When the intrinsic molecular broadening is considered relatively large, $\hbar\gamma_{\mathrm{dk}} = 1\,\mathrm{meV}$, the spectral dip practically disappears.

In conclusion, we have shown that plasmonic cavities that highly localize electromagnetic fields are able to enable optical spectroscopy of molecular excitons that are otherwise dark to standard optical methods. The dark excitations can manifest themselves in the extiction spectra of the plasmonic system in the form of Fano-like dips, whose visibility, however, strongly depends on the broadening of the molecular excitations.

5.4 Dynamics of molecular excitons in plasmonic cavities beyond the point-dipole approximation

So far we have discussed the position dependence of the plasmon-exciton coupling that arises due to the distribution of the transition-charge electronic density of the molecular excitons. The coupling of the excitons to the plasmonic cavity also results in a modification of the temporal evolution of the molecular excited states that we address in this section.

To that end we apply the hybrid quantization scheme to explore the role of the finite size of the molecule and calculate the dynamics of the population of the excited electronic state $|c_{\mathrm{e}}(t)|^2$ by solving the integro-differential equation for the amplitude, $c_{\mathrm{e}}(t)$, based on the Wigner-Weisskopf approach that we introduced in Section 3.2 [158, 250]:

$$\dot{c}_{\mathrm{e}}(t) = -\int_0^t \int_{-\infty}^{\infty} J_{\mathrm{em}}(s) e^{\mathrm{i}(\omega_{\mathrm{eg}}-s)(t-\tau)} c_{\mathrm{e}}(\tau)\, \mathrm{d}s\, \mathrm{d}\tau, \tag{5.42}$$

where $J_{\mathrm{em}}(s)$ is the spectral density characterizing the coupling of the molecule with the plasmonic system:

$$J_{\mathrm{em}}(s) = \frac{\gamma_a}{2\pi} \sum_n \frac{|g_n|^2}{(\omega_n - s)^2 + (\gamma_a/2)^2}, \tag{5.43}$$

with ω_n being the frequency of n^{th} plasmonic mode and $\hbar\omega_{\mathrm{eg}} = 2.3$ eV (2.8 eV) is the excitation frequency of the dipole transition (S_x, S_y, S_z) in the ZnPc (MB) molecule. For convenience we consider that the plasmon decay is proportional to the plasma frequency, $\gamma_a = 0.01\,\omega_{\mathrm{p}}$. In practice, γ_a phenomenologically accounts for the intrinsic losses in the metal and can be estimated from the classical dielectric function of the particle material [227]. In Appendix D we have also performed a set of calculations of the system dynamics involving larger values of γ_a (accounting for larger losses of conventional plasmonic materials) to test its influence on the results presented here. We have found that large values of γ_a affect the coherence of the dynamics, however, the general trends of the results presented here are generally valid. Note that in Eq. (5.42) we are neglecting the extremely slow intrinsic molecular decay. We solve Eq. (5.42) for the initial condition $|c_{\mathrm{e}}(0)|^2 = 1$, thus treating the decay of the initially fully excited molecular exciton.

We first consider the MB molecule [Fig. 5.2(c,e)] oriented perpendicularly to the surface of a spherical metal nanoparticle of radius $R_{\mathrm{d}} = 5$ nm. We plot in Fig. 5.5(a,b) the spectral density as a function of the distance, z_0, between the center of the molecule and the particle's surface. We compare the spectral density obtained using the full quantum model (FQM) in which the transition density is obtained within TDDFT [Fig. 5.5(a)], with that obtained with the use of the simplified point-dipole model (PDM) to describe the molecule [Fig. 5.5(b)]. The

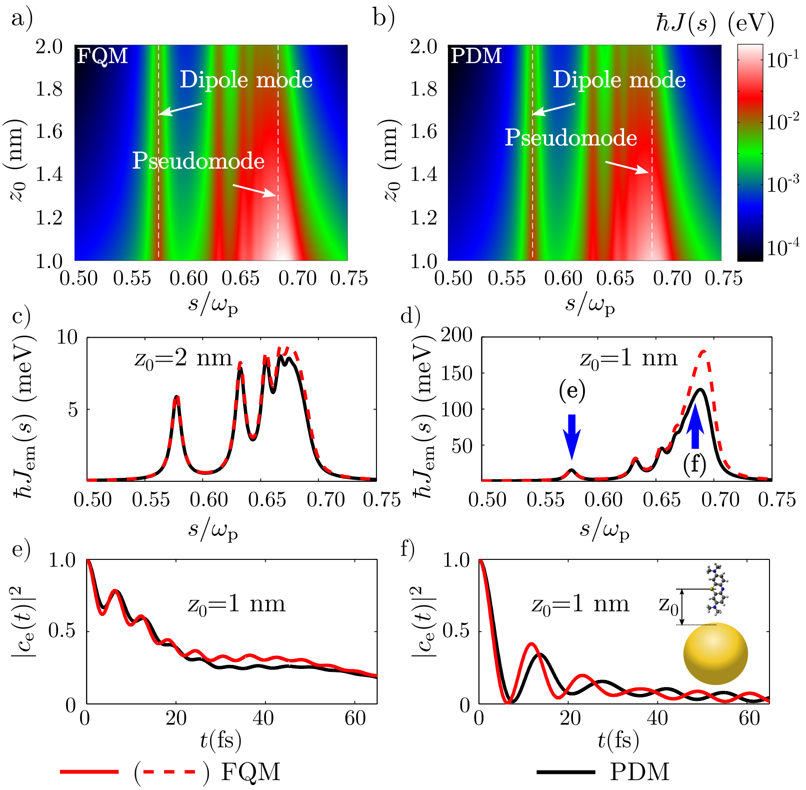

Figure 5.5: Dynamics of the MB molecular exciton in the proximity of a spherical plasmonic resonator. (a,b) Spectral densities calculated with the FQM (a) and with the PDM (b), as a function of the distance z_0 of the center of the molecule to the particle's surface (radius $R_d = 5$ nm). (c,d) Spectral densities extracted from (a) and (b), for $z_0 = 2$ nm (c) and for $z_0 = 1$ nm (d). (e,f) Selected decay dynamics for the exciton resonant with the dipolar plasmon (e) and with the pseudomode (f) for a separation distance of $z_0 = 1$ nm, as marked in (d). FQM results are displayed with red lines and PDM results with black ones.

same color scale is used for straightforward comparison. For a more quantitative comparison, in Fig. 5.5 (c,d) we extract the spectral densities for the smallest $z_0 = 2\,\text{nm}$ (c), and largest $z_0 = 1\,\text{nm}$ (d) within the PDM (black lines) and FQM (red lines). The spectral density maps calculated within both models feature the same qualitative behavior, showing several peaks starting at the frequency of the dipole mode of the sphere (the Fröhlich frequency $\omega_{\text{dip}} = \omega_\text{p}/\sqrt{3}$), and continuing with a number of higher-order modes that build up a strong resonance at around the frequency of the surface plasmon, $\omega_{\text{ps}} \approx \omega_\text{p}/\sqrt{2}$, the so-called pseudomode.[251]

One of the most striking effects of considering the spatial distribution of the transition density is revealed in the dynamics of the exciton decay, $|c_\mathrm{e}(t)|^2$. We analyze in Fig. 5.5(e) this situation when the MB exciton is resonant with the dipolar plasmon, and in Fig. 5.5(f) when is resonant with the plasmonic pseudomode (tuning ω_p of the metal). In both cases, the molecule is placed at $z_0 = 1$ nm. When the exciton is resonant with the dipolar mode, the spectral densities, $J(s)$, of the FQM and the PDM are almost identical in the spectral region close to the exciton resonance, thus leading to similar qualitative and quantitative features of the corresponding decay dynamics within both models. In the first stages of the decay, the exciton population shows fast but shallow oscillations that modulate the overall slower non-exponential decay process driven by low-order plasmonic modes. We have checked that the fast dynamics arises mainly due to presence of the pseudomode peak in $J(s)$, despite its large spectral detuning from the exciton frequency. A different picture can be observed in Fig. 5.5(f), where the pseudomode frequency coincides with the excitonic frequency, $\omega_\mathrm{ps} \approx \omega_\mathrm{eg}$. In this case, the decay dynamics features a clear coherent exchange of the exciton population with the plasmonic pseudomode. In this strong coupling regime, we find that the spectral density is larger in the FQM than in the PDM [Fig. 5.5(d)] resulting in about $\approx 20\,\%$ faster vacuum Rabi oscillations due to the proximity of one side of the molecule to the metallic surface. Notice that the coupling of the molecular exciton to the pseudomode is much more sensitive spatially than in the dipolar case due to the extremely localized character of the pseudomode.

We also consider an alternative situation of coupling by analyzing the exciton dynamics of a transition of the ZnPc molecule, which is oriented horizontally with respect to the metal nanoparticle. The spectral densities obtained from the two approaches are shown in Fig. 5.6 (a) and (b), using the same color scale in both cases. Both the FQM and the PDM exhibit a single peak at the pseudomode frequency. However, opposite to the MB case, the amplitude of this peak is substantially reduced in the FQM with respect to that obtained within PDM. This occurs because the higher order plasmon modes show a high spatial modulation which exceeds that of the transition density, thus softening the plasmon-exciton interaction. For analyzing the dynamics, we first focus on a situation where the exciton weakly interacts with a far blue-detuned plasmonic resonance. We select this detuned case by assuming a value of the plasma frequency ($\hbar\omega_\mathrm{p} \approx 9$ eV) which locates the frequency of the pseodomode ($\hbar\omega_\mathrm{ps} \approx 6.4\,\mathrm{eV}$) far away from the ZnPc exciton ($\hbar\omega_\mathrm{eg} = 2.3\,\mathrm{eV}$). We checked that the RWA also describes correctly the dynamics under these conditions. In this case the molecule is weakly coupled to the plasmonic excitations, so that the exciton decays exponentially, $|c_\mathrm{e}(t)|^2 = e^{-\Gamma_\mathrm{eff} t}$ (Purcell effect). The decay rate Γ_eff can be related to the spectral function of the plasmons as $\gamma = 2\pi J_\mathrm{em}(\omega_\mathrm{eg})$, which for the PDM reduces to the well-known expression $\Gamma_\mathrm{eff} = \frac{2\omega_\mathrm{eg}^2}{c^2\varepsilon_0}\left[\mathbf{d}_0 \cdot \mathrm{Im}\{\mathbf{G}(\mathbf{r}_0, \mathbf{r}_0)\} \cdot \mathbf{d}_0\right]$ (with c the speed of light in vacuum) [109] involving the imaginary part ($\mathrm{Im}\{\cdot\}$) of the (quasi-static) electric dyadic Green's function $\mathbf{G}(\mathbf{r}_0, \mathbf{r}_0)$ evaluated at position $\mathbf{r}_0$ of the dipolar emitter.

In Fig. 5.6 (c) we show the dependence of the plasmon-induced decay rate, Γ_eff,

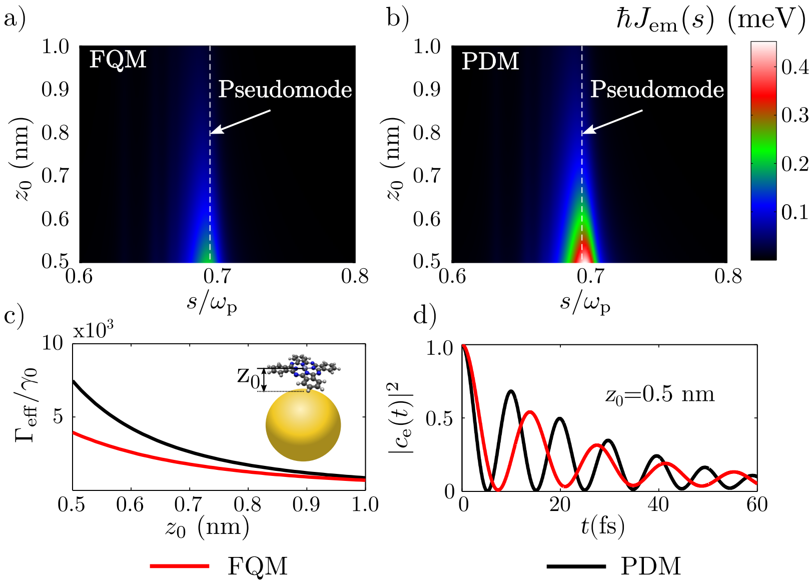

Figure 5.6: Dynamics of the ZnPc molecular exciton near a spherical plasmonic resonator. (a,b) Spectral densities as a function of the distance of the molecule to the particle's surface z_0 [see inset in (c)] within the FQM (a) and within the PDM (b). (c) Plasmonic enhancement of the total decay rate as a function of z_0, when the plasmon resonance is strongly blue-detuned from the molecular exciton. (d) Dynamics of the exciton for $z_0 = 0.5\,\mathrm{nm}$ when the exciton frequency corresponds to the pseudomode peak. The red line corresponds to the FQM and the black line to the PDM.

normalized to the vacuum decay of the transition, γ_0, as a function of the distance of the molecule (the central Zn atom) to the surface of the metal nanoparticle, as calculated with the FQM (red lines) and with the PDM (black lines). The values of the decay rate enhancement $\Gamma_{\mathrm{eff}}/\gamma_0$ (the Purcell factor) reach almost up to 10^4 for the closest separation distance ($z_0 = 0.5\,\mathrm{nm}$) when a point-like dipole is considered. At this distance, the decay rate calculated with the quantum model, dominated by the interaction with the pseudomode, is reduced by a factor of around 2 with respect to the PDM result. When the distance from the surface increases, the values of the decay rate from both models become closer, recovering the limit of the point-dipole approximation from distances of approximately $z_0 \approx 1\,\mathrm{nm}$. In a second scenario, we make the pseudomode frequency to coincide with the molecular exciton, $\omega_{\mathrm{ps}} \approx \omega_{\mathrm{eg}}$, also for a distance of $z_0 = 0.5\,\mathrm{nm}$. Under these conditions the plasmon-exciton coupling is strong and the calculated dynamics of the excited state, $|c_{\mathrm{e}}(t)|^2$, results in clear Rabi oscillations [Fig. 5.6 (d)]. The comparison of the dynamics obtained from the FQM (red lines) with that of the PDM (black lines) yields quantitative differences in the period of the Rabi oscillations, around 40 % smaller in the FQM than in the PDM. Hence, the FQM reveals the limitations of the PDM to address the exciton dynamics both in weak and strong coupling regimes.

Importantly, we have found that each particular geometrical configuration of the molecule with respect to the plasmonic cavity requires a detailed analysis of the plasmon-exciton coupling, as in some occasions the point-dipole approximation overestimates the coupling, as shown for the ZnPc molecule, whereas it underestimates its strength in others, as in the case of the vertically oriented MB molecule.

5.5 Summary

We have studied the interaction between plasmonic excitations in metallic particles and molecular excitons within the framework of cavity QED. We have extended the description of the plasmon-exciton coupling beyond the standard point-dipole approximation and discussed the consequences of treating the molecule as a spatially extended object.

We have found that the more complete quantum model, describing the plasmon-exciton interaction as an overlap of the excitonic transition-charge density of the molecule and the quantized electric potential of the plasmons, nicely corresponds with the experimentally reported photon maps of molecular excitons measured in electroluminescence of STM [52, 53].

Furthermore, we have shown that the interplay of the spatial distribution of the plasmonic potential and the excitonic transition-charge density of the molecule can lead to breaking of the optical selection rules governing the light-exciton interaction. The originally dark excitations (e.g. electric quadrupolar transitions) can become bright if their interaction with light is mediated by the highly confined fields of cavity plasmons. The spectral signatures of these excitons can be thus observed in the far-field spectra as Fano-like features on top of the broad optical response of the plasmons.

Finally, it has been found that the plasmonic environment strongly modifies the temporal evolution of the molecular excited states. We have identified situations where a correct excitonic dynamics is obtained only if the full spatial distribution of the molecular excitonic transition-charge density is considered. In other cases the commonly assumed point-dipole approximation may be sufficient to account for the physics of the plasmon-exciton couping. Each geometrical arrangement of the molecule in a plasmonic cavity thus requires specific inspection.

The model introduced in this chapter is a first step towards a more complex description of the plasmon-molecule interaction. As for now, the model assumes that the molecular geometry and hence also its excitations are described correctly by the vacuum properties of the molecule. It is worthwhile to note that in practical experiments concerning molecules in atomically-sharp plasmonic cavities, as those considered here, there might be additional effects that would require more sophisticated treatments of the metal-molecule interface regarding both the electronic structure as well as the electromagnetic interaction. The extreme localization in plasmonic cavities often relies on atomic-scale corrugations at the metal-nanoparticle surface which have been shown to vary along time due to thermal diffusion of the metallic surface atoms [105]. Low temperature experiments are thus required under certain circumstances to stabilize the particle morphology. Additionally, the ground-state geometry as well as the energies of the molecular excitons will be influenced by screening effects of the nearby metallic surfaces and, in the case of experiments performed in air or solvent, also of the wetting layer present in the plasmonic gap. These effects will generally modify the quantum-chemical properties of the molecules and require more complex ab-initio modelling. Nevertheless, we believe that the first-principles approach presented here provides a good qualitative and quantitative picture of the coupling between plasmons and single-molecular excitations under well-controlled conditions [52, 53, 238].

Chapter 6

Effects of a dephasing reservoir in photon emission of coherently driven organic exciton-polaritons

When placed into optical (plasmonic) cavities, excitons in organic molecules can strongly interact with the cavity modes and form new mixed exciton-photon (plasmon) excitations, so-called exciton polaritons [58–88], as described in Chapter 5. Exciton polaritons have been broadly analyzed in connection with their fluorescence properties, cavity-induced (photo)chemistry [77, 78, 252–256], polariton lasing and polariton condensation [257–265], and polariton-mediated energy transfer [266, 267].

The inelastic photon emission from the polariton modes has been found to exhibit spectral asymmetries that favour the emission from the lower polariton branch, while often suppressing the emission from the upper polariton [59, 76, 268–270]. This asymmetry has been attributed to vibrationally driven decay processes between the polaritonic states [271]. It has been shown that the vibrational states of the molecules play a key role in the formation of new vibron-polariton states that lead to the appearance of new peaks in the emission spectra [81, 82, 84, 86, 87, 272, 273]. The excitons in organic molecules are also exposed to interactions with their local environment (the solvent) that produces additional exciton dephasing. The interaction with the solvent molecules also contributes to significant solvent-dependent Stokes shift of the photoluminescence induced by the reorganization of the solvent molecules when the solute molecule changes the electronic state [274, 275]. It is therefore necessary to correctly treat the interaction of the polariton states with the dephasing reservoir when describing the strong coupling between a cavity mode and molecular excitons.

In this chapter we address the inelastic light emission spectra of polaritonic systems pumped by a coherent monochromatic laser. We present a quantum-optical model based on the solution of the quantum master equation [158] that describes the spectral asymmetries observed experimentally in the polariton emission and action (excitation) spectra [59, 76, 270]. We show that the dominant emission from the lower polariton state is a consequence of the interaction between the excitons and the dephasing reservoir, which in principle includes both the effects of the internal molecular vibrations and the solvent.

We first introduce the theoretical model in Section 6.1. In Section 6.2 we demonstrate consequences of the model on an example of a single molecule in a cavity. We address the more general case of N_{mol} molecules in a cavity in Section 6.3.

6.1 Open quantum system theory of (collective) exciton-cavity mode coupling

We describe the molecules as two-level electronic systems with a ground, $|\mathrm{g}\rangle$, and an excited state, $|\mathrm{e}\rangle$, interacting with their respective reservoirs, including both the internal molecular vibrational modes and the fluctuations of the local environment of each molecule [275]. The local environment of the molecule is responsible for the electronic dephasing processes [e.g. vibrations of the molecule or the environment [91, 271, 272, 276–279], fluctuations of solvent polarization etc.], as schematically represented in Fig. 6.1. The excitonic term of the Hamiltonian of the $i-$th molecule is

$$\hat{H}_{\mathrm{e},i} = \hbar\omega_{\mathrm{eg}}\hat{\sigma}_i^{\dagger}\hat{\sigma}_i, \tag{6.1}$$

where $\hat{\sigma}_i$ is the two-level-system lowering operator between the many-body excited state, $|\mathrm{e}_i\rangle$, and the many-body ground state, $|\mathrm{g}_i\rangle$, of the $i-$th molecule, $\hat{\sigma}_i = |\mathrm{g}_i\rangle\langle\mathrm{e}_i|$, and $\hbar\omega_{\mathrm{eg}}$ is the energy of $|\mathrm{e}_i\rangle$ with respect to $|\mathrm{g}_i\rangle$, considered equal for all molecules. Each molecule interacts with its local dephasing reservoir described by the Hamiltonian

$$\hat{H}_{\mathrm{res,i}} = \hbar\Omega_{\mathrm{R}}\hat{B}_i^{\dagger}\hat{B}_i, \tag{6.2}$$

with $\hbar\Omega_{\mathrm{R}}$ the effective energy of the mode of the reservoir, via the exciton-reservoir interaction Hamiltonian

$$\hat{H}_{\mathrm{e-res,i}} = d_{\mathrm{R}}\Omega_{\mathrm{R}}\hat{\sigma}_i^{\dagger}\hat{\sigma}_i(\hat{B}_i^{\dagger} + \hat{B}_i). \tag{6.3}$$

Here $\hat{B}_i$ are the bosonic annihilation operators of the collective reservoir mode i interacting locally with the exciton of the $i-$th molecule [91, 274, 278, 280–283], and † stands for the Hermitian conjugate. We have assumed that the reservoir modes have the same frequency $\Omega_{\mathrm{R,e},i} = \Omega_{\mathrm{R,g},i} = \Omega_{\mathrm{R}}$ in the excited state ($\Omega_{\mathrm{R,e},i}$) and the ground state ($\Omega_{\mathrm{R,g},i}$). The equilibrium position of the reservoir mode

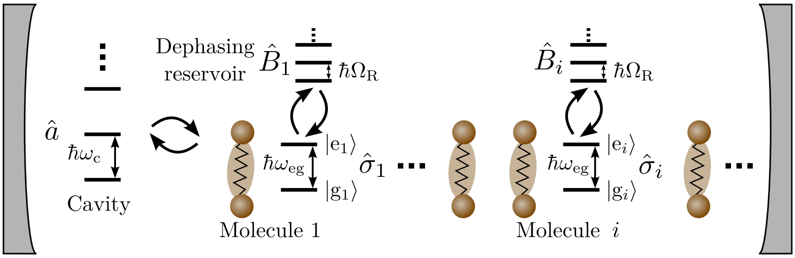

Figure 6.1: Schematic representation of the cavity containing a bosonic mode (with $\hat{a}$ the bosonic annihilation operator of the cavity excitation) of energy $\hbar\omega_c$ interacting with a series of molecules modelled as electronic two-level systems. Each i-th molecule is composed of its ground, $|g_i\rangle$, and excited, $|e_i\rangle$, electronic state separated by energy $\hbar\omega_{eg}$ (with $\hat{\sigma}_i = |g_i\rangle\langle e_i|$), which further interact with a dephasing reservoir that is modelled as an effective bosonic mode of energy $\hbar\Omega_R$, independently for each molecule ($\hat{B}_i$ being the respective bosonic annihilation operator).

is rigidly displaced in the electronic excited state of the $i-$th molecule by a dimensionless constant d_R with respect to its equilibrium position in the ground electronic state.

We describe the inter-molecular excitonic interactions through the Hamiltonian

$$\hat{H}_{e-e} = \sum_{ij} G_{ij}\hat{\sigma}_i^\dagger\hat{\sigma}_j + \text{H.c.}, \tag{6.4}$$

where G_{ij} are coupling constants that generally depend on the spatial distribution of the individual molecules as well as on their mutual orientation.

The molecular excitons interact with a single bosonic cavity mode of frequency ω_c

$$\hat{H}_c = \hbar\omega_c\hat{a}^\dagger\hat{a}, \tag{6.5}$$

where $\hat{a}$ ($\hat{a}^\dagger$) is the bosonic annihilation (creation) operator of the cavity mode. The i-th molecule interacts with the cavity mode via the coupling Hamiltonian

$$\hat{H}_{e-c,i} = \hbar g_i\hat{\sigma}_i^\dagger\hat{a} + \text{H.c.}, \tag{6.6}$$

where g_i is the respective cavity-mode-exciton coupling constant. The total Hamiltonian describing the cavity and molecular excitations thus becomes

$$\hat{H}_{tot} = \hat{H}_c + \hat{H}_{e-e} + \sum_i \left(\hat{H}_{e,i} + \hat{H}_{res,i} + \hat{H}_{e-res,i} + \hat{H}_{e-c,i}\right). \tag{6.7}$$

The Hamiltonian $\hat{H}_{tot}$ contains information about the coherent dynamics of the system, but also accounts for the the coupling of molecular excitons with their respective dephasing reservoirs. Importantly, $\hat{H}_{\mathrm{tot}}$ does not account for exciton decay and photon leakage. To properly account for this, we describe the dynamics of the system via the master equation for the density matrix $\hat{\rho}$, including the effects of the environment via the phenomenological Lindblad terms of the form $\mathscr{L}_{\hat{\mathcal{O}}_i}^{\gamma_{\mathcal{O}_i}}(\hat{\rho}) = \frac{\gamma_{\mathcal{O}_i}}{2}\left(2\hat{\mathcal{O}}_i\hat{\rho}\hat{c}_i^\dagger - \{\hat{\mathcal{O}}_i^\dagger\hat{\mathcal{O}}_i, \hat{\rho}\}\right)$, with $\hat{\mathcal{O}}_i$ the (annihilation) operator of the respective excitation, the phenomenological damping constants of the respective excitations $\gamma_{\mathcal{O}_i}$, and with $\{\cdot,\cdot\}$ the anticommutator. The quantum master equation that includes all the necessary Hamiltonian and Lindblad terms becomes:

$$\dot{\hat{\rho}} = \frac{1}{\mathrm{i}\hbar}\left[\hat{H}_{\mathrm{tot}}, \hat{\rho}\right] + \sum_i \mathscr{L}_{\hat{\mathcal{O}}_i}^{\gamma_{\mathcal{O}_i}}(\hat{\rho}), \tag{6.8}$$

where $\hat{\mathcal{O}}_i$ depends on the model under consideration. In the following we address the dynamics encompassed in Eq. (6.8) and analyse the spectral features arising in the optical response of the strongly-coupled system influenced by the coupling to a dephasing reservoir.

6.2 Single molecule in a cavity

6.2.1 Reservoir-induced incoherent processes for a single molecule

In the strong coupling regime the plasmon-exciton interaction $g_i = g$ becomes so significant that it overcomes the intrinsic electronic (γ_{σ_i}) and cavity (γ_a) decay rates and leads to the formation of new hybrid states, polaritonic states. The simplest situation arises when a single cavity mode couples with a single two-level electronic system (we omit the index i to denote the molecule's excitations when considering a single molecule) in the single excitation manifold, where only the bare states $|\mathrm{g},0\rangle$, $|\mathrm{e},0\rangle$ and $|\mathrm{g},1\rangle$ are considered, with 0 (1) the number of cavity excitations. The new polaritonic eigenstates $|+\rangle$ and $|-\rangle$ become a coherent admixture of the exciton and the cavity excitation depending on the magnitude of the coupling strength and the detuning of their respective frequencies:

$$\begin{aligned} |+\rangle &= \cos\theta|\mathrm{e},0\rangle + \sin\theta|\mathrm{g},1\rangle, \\ |-\rangle &= -\sin\theta|\mathrm{e},0\rangle + \cos\theta|\mathrm{g},1\rangle, \end{aligned} \tag{6.9}$$

$$\tan(2\theta) = \frac{2g}{\omega_{\mathrm{eg}} - \omega_{\mathrm{c}}} \text{ and } 0 < 2\theta < \pi. \tag{6.10}$$

The scheme of the newly arising energy level structure is drawn in Fig. 6.2 (a). The operators of the three-level system consisting originally of the states $|0\rangle = |\mathrm{g},0\rangle$, $|2\rangle = |\mathrm{e},0\rangle$ and $|3\rangle = |\mathrm{g},1\rangle$ can be more conveniently expressed in the new basis $\{|0\rangle, |+\rangle, |-\rangle\}$ with help of Eq. (6.9). Most importantly, the operator $\hat{\sigma}^\dagger\hat{\sigma}$ responsible for the interaction with the dephasing reservoir in $\hat{H}_{\mathrm{e-res}}$ becomes [91]

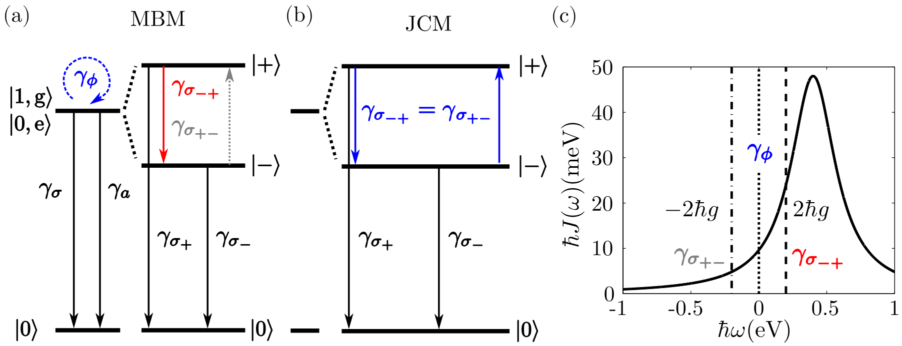

Figure 6.2: Role of the dephasing processes on the light emission from a single exciton strongly coupled with a cavity mode. (a) Schematic level diagram of the exciton in a cavity that is decoupled (left) and after the coupling is turned on (right) within the Markovian-bath model (MBM). The cavity-exciton coupling gives rise to new polariton states, $|+\rangle$ and $|-\rangle$, and opens new incoherent decay paths between $|+\rangle$ and $|-\rangle$ with respective rates $\gamma_{\sigma_{-+}} > \gamma_{\sigma_{+-}}$. (b) Energy level diagram marking the incoherent population transfer between the polariton states as in (a), but for the Jaynes-Cummings model (JCM) where the rates $\gamma_{\sigma_{-+}}$ and $\gamma_{\sigma_{+-}}$ are equal ($\gamma_{\sigma_{-+}} = \gamma_{\sigma_{+-}}$). (c) Spectral density $J(\omega)$ of the bath given by Eq. (6.22) for parameters $\hbar\gamma_\mathrm{R} = 400$ meV, $\hbar\Omega_\mathrm{R} = 400$ meV (chosen such that the reservoir spectral function $J(\omega)$ spans the range of vibrational frequencies of the molecule) and $d_\mathrm{R} = 0.173$ (for which $\hbar J(0) \approx 20\,\mathrm{meV}$). Calculations of selected emission and absorption spectra for smaller values of Ω_R are shown in Appendix E. The vertical lines mark the positions where the spectral density is evaluated to obtain the values of the Markovian decay rates $\gamma_{\sigma_{+-}}$, $\gamma_{\sigma_{-+}}$ and γ_ϕ.

(approximated in the single-excitation subspace):

$$\begin{aligned}\hat{\sigma}^\dagger\hat{\sigma} \approx |2\rangle\langle 2| &= \cos^2\theta|+\rangle\langle +| + \sin^2\theta|-\rangle\langle -| \\ &- \sin\theta\cos\theta\,(|-\rangle\langle +| \,+\, |+\rangle\langle -|)\,.\end{aligned} \tag{6.11}$$

We further introduce the simplifying notation $\hat{\sigma}_{\xi\zeta} = |\xi\rangle\langle\zeta|$, with $\xi, \zeta \in \{+, -\}$, and rewrite the electron-vibration coupling Hamiltonian as:

$$\begin{aligned}\hat{H}_{\mathrm{e-res}} &= \hbar d_\mathrm{R}\Omega_\mathrm{R}\hat{\sigma}^\dagger\hat{\sigma}(\hat{B}^\dagger + \hat{B}) = \hbar\hat{\sigma}^\dagger\hat{\sigma}\hat{F} \\ &= \hbar\left[\cos^2\theta\hat{\sigma}_{++} + \sin^2\theta\hat{\sigma}_{--} - \sin\theta\cos\theta\,(\hat{\sigma}_{-+} + \hat{\sigma}_{+-})\right]\hat{F},\end{aligned} \tag{6.12}$$

where we have defined $\hat{F} = d_\mathrm{R}\Omega_\mathrm{R}(\hat{B}^\dagger + \hat{B})$.

Following the standard procedure [158] (see also Section 3.1.3), we now eliminate the dephasing reservoir and derive the incoherent dynamics of the strongly coupled system. To that end we notice that the operators $\hat{\sigma}_{+-}$, $\hat{\sigma}_{-+}$, $\hat{\sigma}_{++}$, and $\hat{\sigma}_{--}$ are eigenoperators of the polaritonic Hamiltonian $\hat{H}_\mathrm{pol} = \hat{H}_\mathrm{c} + \hat{H}_\mathrm{e} + \hat{H}_{\mathrm{e-c}}$ (eigenoperator $\hat{O}_\mathrm{eig}$ of Hamiltonian $\hat{H}_\mathrm{pol}$ defined as $[\hat{H}_\mathrm{pol}, \hat{O}_\mathrm{eig}] = \lambda_{O_\mathrm{eig}}\hat{O}$ with λ_{O_eig}

a complex number) and in the interaction picture of $\hat{H}_{\mathrm{pol}}$, these operators have the following time dependence:

$$\hat{\sigma}_{+-} = \hat{\sigma}_{+-}(0)e^{-i(\omega_+ - \omega_-)t}, \tag{6.13}$$

$$\hat{\sigma}_{-+} = \hat{\sigma}_{-+}(0)e^{-i(\omega_- - \omega_+)t}, \tag{6.14}$$

$$\hat{\sigma}_{++} = \hat{\sigma}_{++}(0), \tag{6.15}$$

$$\hat{\sigma}_{--} = \hat{\sigma}_{--}(0), \tag{6.16}$$

where $\hat{\sigma}_{+-}(0)$, $\hat{\sigma}_{-+}(0)$, $\hat{\sigma}_{++}(0)$, and $\hat{\sigma}_{--}(0)$ are the Schrödinger picture operators, and with

$$\omega_\pm = \frac{\omega_{\mathrm{eg}} + \omega_{\mathrm{c}}}{2} \pm \sqrt{g^2 + \frac{(\omega_{\mathrm{eg}} - \omega_{\mathrm{c}})^2}{4}} \tag{6.17}$$

the frequency of the upper (ω_+) and lower (ω_-) polaritons, respectively.

In the secular approximation, the incoherent processes are represented by the Lindblad terms describing the dephasing of the polariton states, $\mathscr{L}^{\gamma_\phi}_{\hat{\sigma}_{++--}}(\hat{\rho})$, the decay of $|+\rangle$ to $|-\rangle$, $\mathscr{L}^{\gamma_{\sigma_{-+}}}_{\hat{\sigma}_{-+}}(\hat{\rho})$, and the reverse process, $\mathscr{L}^{\gamma_{\sigma_{+-}}}_{\hat{\sigma}_{+-}}(\hat{\rho})$. For brevity we have defined $\hat{\sigma}_{++--} = \cos^2\theta\hat{\sigma}_{++} + \sin^2\theta\hat{\sigma}_{--}$. The respective dephasing and decay rates, $\gamma_\phi = \gamma_{\sigma_{++--}}$, $\gamma_{\sigma_{-+}}$ and $\gamma_{\sigma_{+-}}$, are determined from the properties of the dephasing reservoir characterized by its spectral density $J(\omega)$:

$$\gamma_{\sigma_{-+}} = \cos^2\theta\sin^2\theta J(\omega_+ - \omega_-), \tag{6.18}$$

$$\gamma_{\sigma_{+-}} = \cos^2\theta\sin^2\theta J(\omega_- - \omega_+), \tag{6.19}$$

$$\gamma_\phi = J(0). \tag{6.20}$$

The spectral density of the reservoir [274, 278, 281–283] is obtained as the Fourier transform of the reservoir's two-time correlation function $\langle\hat{F}^\dagger(t+s)\hat{F}(t)\rangle$ [158],

$$J(\omega) = 2\mathrm{Re}\left\{\int_0^\infty \mathrm{d}s\, e^{\mathrm{i}\omega s}\langle\hat{F}^\dagger(t+s)\hat{F}(t)\rangle\right\}. \tag{6.21}$$

In particular, $J(\omega)$ emerging from Eq. (6.2) and Eq. (6.3) together with the Lindblad term $\mathscr{L}^{\gamma_B}_{\hat{B}}(\hat{\rho})$ (damped harmonic-oscillator reservoir [274, 282] with damping rate γ_B) calculated for zero temperature, $T = 0\,\mathrm{K}$, is

$$J(\omega) = \frac{2\gamma_B d_{\mathrm{R}}^2\Omega_{\mathrm{R}}^2}{(\Omega_{\mathrm{R}} - \omega)^2 + \gamma_B^2}. \tag{6.22}$$

The spectral density $J(\omega)$ of the considered vibrational bath [Eq. (6.22)] is shown in Fig. 6.2 (c). $J(\omega)$ has the form of a broad Lorentzian peak positioned at the positive side of the frequency axis. This stems from the condition $T = 0\,\mathrm{K}$, for which the polariton decay can result only in spontaneous generation of excitations (vibrations) in an otherwise unpopulated reservoir. We note that for $T > 0\,\mathrm{K}$ (a situation not considered here), when the reservoir acquires thermal population, processes including absorption of a thermal reservoir excitation (appearing for negative ω) would also contribute to $J(\omega)$ [90–94]. The model parameters used in our study are given in the caption of Fig. 6.2. As $J(\omega)$ is not symmetrical with respect to the zero frequency, the transition $|+\rangle \rightarrow |-\rangle$ given by the rate $\gamma_{\sigma_{-+}} = \cos^2\theta \sin^2\theta J(2|g|)$ is therefore favored compared to the $|-\rangle \rightarrow |+\rangle$ transition occuring with rate $\gamma_{\sigma_{+-}} = \cos^2\theta \sin^2\theta J(-2|g|)$, [marked by the vertical lines in Fig. 6.2(c)]. We stress that this asymmetry is a general property of dephasing reservoirs and robustly appears in a wide range of non-Markovian dephasing models [278, 280, 281, 283].This imbalance of the transfer of energy between the polariton states gives rise to the asymmetries observed in the emission spectra [59, 76, 270] that we address below.

Last, in strong coupling we employ the polariton Lindblad operators $\mathscr{L}_{\hat{\sigma}_+}^{\gamma_{\sigma_+}}(\hat{\rho})$ and $\mathscr{L}_{\hat{\sigma}_-}^{\gamma_{\sigma_-}}(\hat{\rho})$ ($\hat{\sigma}_+ = |0\rangle\langle +|$ and $\hat{\sigma}_- = |0\rangle\langle -|$), where the decay rates of the upper, γ_{σ_+}, and the lower, γ_{σ_-}, polariton are defined as

$$\gamma_{\sigma_+} = \gamma_a \sin^2\theta, \tag{6.23}$$

$$\gamma_{\sigma_-} = \gamma_a \cos^2\theta, \tag{6.24}$$

where γ_a is the decay rate of the bare cavity decoupled from the molecules. The phenomenological Lindblad terms $\mathscr{L}_{\hat{\sigma}_+}^{\gamma_{\sigma_+}}(\hat{\rho})$ and $\mathscr{L}_{\hat{\sigma}_-}^{\gamma_{\sigma_-}}(\hat{\rho})$ can be related to the commonly assumed phenomenological Lindblad superoperator describing the decay of the bare cavity, $\mathscr{L}_{\hat{a}}^{\gamma_a}(\hat{\rho})$. Under the strong-coupling condition we write the photon annihilation operator $\hat{a}$ in terms of the polariton operators $\hat{\sigma}_+$ and $\hat{\sigma}_-$ (in the single-excitation subspace):

$$\hat{a} \approx \sin\theta\,\hat{\sigma}_+ + \cos\theta\,\hat{\sigma}_-, \tag{6.25}$$

and apply the secular approximation. Under such conditions, the Lindblad superoperator $\mathscr{L}_{\hat{a}}^{\gamma_a}(\hat{\rho})$ transforms into the pair of Lindblad terms, $\mathscr{L}_{\hat{\sigma}_+}^{\gamma_{\sigma_+}}(\hat{\rho})$ and $\mathscr{L}_{\hat{\sigma}_-}^{\gamma_{\sigma_-}}(\hat{\rho})$:

$$\mathscr{L}_{\hat{a}}^{\gamma_a}(\hat{\rho}) \rightarrow \mathscr{L}_{\hat{\sigma}_+}^{\gamma_{\sigma_+}}(\hat{\rho}) + \mathscr{L}_{\hat{\sigma}_-}^{\gamma_{\sigma_-}}(\hat{\rho}). \tag{6.26}$$

We also phenomenologically include the intrinsic molecular losses via $\mathscr{L}_{\hat{\sigma}}^{\gamma_\sigma}(\hat{\rho})$, considering $\gamma_\sigma \ll \gamma_a$.

6.2.2 Polariton light emission spectra under coherent driving conditions for a single molecule

In the following we consider several different approaches to the implementation of the dephasing due to the reservoir. First, we implement explicitly the reservoir defined by $\hat{H}_{\mathrm{res}}$, $\hat{H}_{\mathrm{e-res}}$ [Eq. (6.2) and Eq. (6.3)] and $\mathscr{L}_{\hat{B}}^{\gamma_B}(\hat{\rho})$ into the master

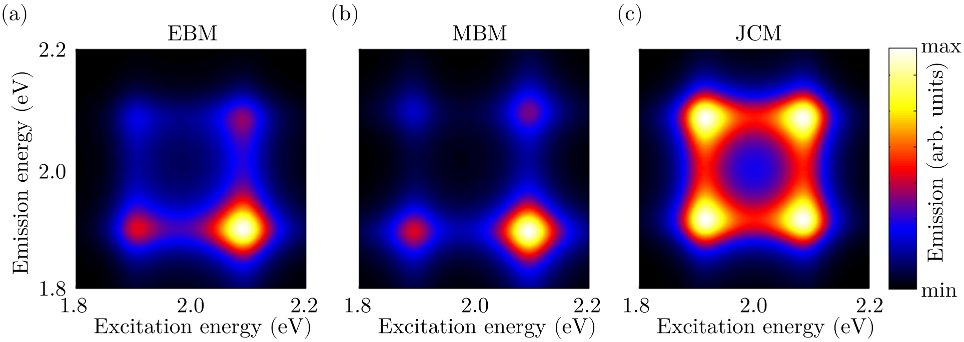

Figure 6.3: Photon emission spectra normalized to the incident laser intensity $|\mathcal{E}|^2$ as a function of the excitation frequency ω_L within (a) the explicit-bath model (EBM), (b) the Markovian-bath model (MBM) and (c) the Jaynes-Cummings model (JCM). In all calculations we have considered the parameters $\hbar\omega_\mathrm{eg} = \hbar\omega_\mathrm{c} = 2$ eV, $\hbar\gamma_a = 150$ meV, $\hbar\gamma_\sigma = 2 \times 10^{-2}$ meV and $\hbar g = 100$ meV. The pure dephasing constant for the JCM is $\gamma_\phi = J(0)$. The parameters of the bath are: $\hbar\gamma_B = 400$ meV, $\hbar\Omega_\mathrm{R} = 400$ meV and $d_\mathrm{R} = 0.173$.

equation as a part of the simulated system (the explicit bath model - EBM) and solve it for the spectral emission response (See Appendix E for details about the implementation of the reservoir degrees of freedom). In the second approach we approximate the EBM and eliminate the dephasing reservoir from Eq. (6.8) using the Born-Markov and secular approximations, as described in the previous section, and introduce the effective dephasing and damping terms via the Lindblad superoperators $\mathscr{L}_{\hat\sigma}^{\gamma_\sigma}(\hat\rho)$, $\mathscr{L}_{\hat\sigma_+}^{\gamma_{\sigma+}}(\hat\rho)$, $\mathscr{L}_{\hat\sigma_-}^{\gamma_{\sigma-}}(\hat\rho)$, $\mathscr{L}_{\hat\sigma_{++--}}^{\gamma_\phi}(\hat\rho)$, $\mathscr{L}_{\hat\sigma_{-+}}^{\gamma_{\sigma-+}}(\hat\rho)$ and $\mathscr{L}_{\hat\sigma_{+-}}^{\gamma_{\sigma+-}}(\hat\rho)$ (the Markovian bath model - MBM). The effective rates are schematically depicted in Fig. 6.2 (a). As a third approach we consider the commonly adopted Jaynes-Cummings model (JCM) where the effective dephasing and decay rates are first defined for the exciton of the molecule and the bare cavity mode, which are mutually decoupled. Note that this is in contrast with the MBM where the incoherent dynamics is derived in the polariton basis. The decay of the cavity and the molecular exciton are described in the JCM by $\mathscr{L}_{\hat a}^{\gamma_a}(\hat\rho)$ and $\mathscr{L}_{\hat\sigma}^{\gamma_\sigma}(\hat\rho)$, as defined earlier, and the pure dephasing is implemented via

$$\mathscr{L}_{\hat\sigma^\dagger\hat\sigma}^{\gamma_\phi}(\hat\rho) = \frac{\gamma_\phi}{2}\left(2\hat\sigma^\dagger\hat\sigma\hat\rho\,\hat\sigma^\dagger\hat\sigma - \{\hat\sigma^\dagger\hat\sigma, \hat\rho\,\}\right). \tag{6.27}$$

In the JCM the interaction with the reservoir given in Eq. (6.2) and Eq. (6.3) is not considered. Upon transformation into the polariton basis, the dephasing term in the JCM model yields (among others) interaction terms between $|+\rangle$ and $|-\rangle$, with equal rates for the $|+\rangle \to |-\rangle$ and $|-\rangle \to |+\rangle$ transitions, as schematically depicted in Fig. 6.2 (b).

As we are interested in the response of the system under illumination by a monochromatic laser light, we introduce the driving term

$$\hat{H}_{\mathrm{pump}} = \mathcal{E}\left(\hat{a}^{\dagger}e^{-\mathrm{i}\omega_{\mathrm{L}}t} + \hat{a}e^{\mathrm{i}\omega_{\mathrm{L}}t}\right), \tag{6.28}$$

with $\mathcal{E}$ the amplitude of the laser pumping and ω_{L} the laser frequency. We make sure that the pumping amplitude is small enough to conform with the single-excitation approximation.

We calculate the absorption spectra $s_{\mathrm{A}}(\omega)$ of the system (assuming that only the cavity interacts with the radiation field) and the inelastic emission spectra $s_{\mathrm{E}}(\omega;\omega_{\mathrm{L}})$ for different frequencies ω_{L} of the incident pumping laser. The spectra are calculated from the quantum regression theorem as one-sided Fourier transforms of the two-time correlation functions (see also Section 3.3)

$$s_{\mathrm{a}}(\omega) = 2\mathrm{Re}\int_0^{\infty} \langle\langle\hat{a}(\tau)\hat{a}^{\dagger}(0)\rangle\rangle_{\mathrm{ss}}\, e^{\mathrm{i}\omega\tau}\mathrm{d}\,\tau, \tag{6.29}$$

$$s_{\mathrm{e}}(\omega;\omega_{\mathrm{L}}) = 2\mathrm{Re}\int_0^{\infty} \langle\langle\hat{a}^{\dagger}(\tau)\hat{a}(0)\rangle\rangle_{\mathrm{ss}}\, e^{-\mathrm{i}\omega\tau}\mathrm{d}\,\tau, \tag{6.30}$$

where the double-angle brackets are defined as

$$\langle\langle\hat{a}^{\dagger}(\tau)\hat{a}(0)\rangle\rangle_{\mathrm{ss}} = \langle a^{\dagger}(\tau)\hat{a}(0)\rangle_{\mathrm{ss}} - \lim_{\tau\to\infty}\langle\hat{a}^{\dagger}(\tau)\hat{a}(0)\rangle_{\mathrm{ss}}. \tag{6.31}$$

The calculated emission spectra for the reservoir spectral density considered in Fig. 6.2 (c) are shown in Fig. 6.3 within both the EBM and the MBM and are compared to the result obtained from the JCM. To simplify the discussion, in the following we concentrate on the special case when the energies of the plasmonic and excitonic transition are matched ($\omega_{\mathrm{c}} = \omega_{\mathrm{eg}}$). In Fig. 6.3 (a-c) we plot the emission spectra of the strongly coupled single-molecule exciton with the cavity mode as a function of the excitation frequency ω_{L} within (a) the EBM, (b) the MBM, and (c) the JCM. For both the EBM and the MBM, the color maps offer the same qualitative and very similar quantitative result. The inelastic emission arises mainly from the transition of the lower polariton to the ground state and thus leads to a clear dominance of the lower polariton emission peak. Contrarily, the JCM yields a fully symmetrical result independently of the excitation frequency, which contradicts the experimental evidences of molecular emission [59, 76, 270]. The implementation of the dephasing within the JCM is thus unable to correctly describe the imbalance in the population transfer between the polaritonic states driven by the dephasing.

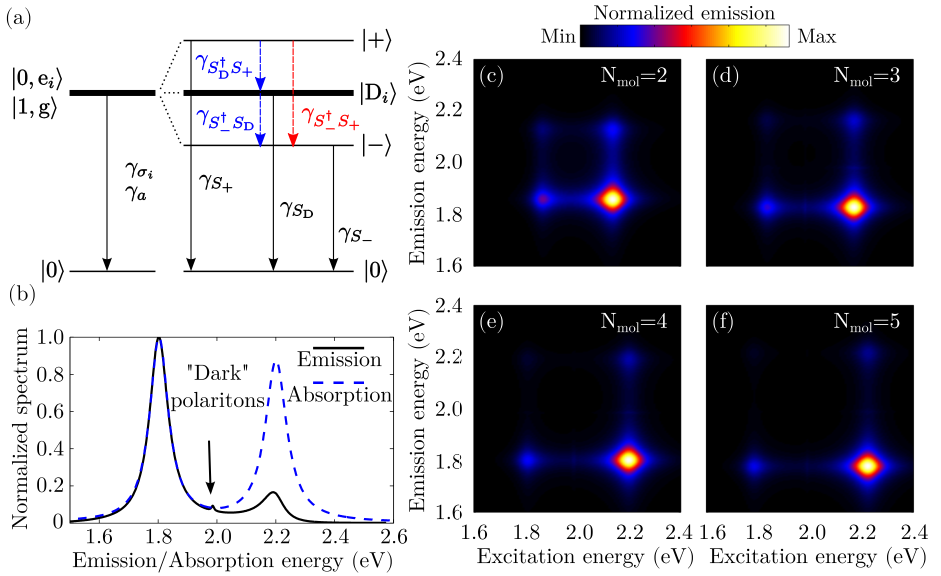

Figure 6.4: (a) Schematic representation of the polariton incoherent dynamics. The strong coupling leads to the formation of bright upper, $|+\rangle$, and lower, $|-\rangle$, polaritons that are decoupled from the dark states, $|\mathrm{D}_i\rangle$. The coupling of the polariton and the dark states with the dephasing reservoir gives rise to the incoherent transfer of populations from the higher-energy states to the lower energy states. The bare cavity incoherently decays with rate γ_a, the excitons of the bare molecules incoherently decay with rates $\gamma_{\sigma_i} = \gamma_\sigma$. The bright polariton states $|+\rangle$ and $|-\rangle$ then experience the incoherent decay into the ground state $|0\rangle$ with rates γ_{S_+} and γ_{S_-}, respectively. The dark polaritons decay to the ground state with equal rates $\gamma_{S_i} = \gamma_\sigma$. Finally, population transfer among the polariton branches occurs with rates $\gamma_{S^\dagger_\mathrm{D} S_+}$, $\gamma_{S^\dagger_- S_\mathrm{D}}$ and $\gamma_{S^\dagger_- S_+}$, as marked in the schematic. The population transfer is accompanied by the dephasing processes (not shown). (b) Emission (black line) and absorption (blue dashed line) spectra of four molecular excitons ($N_\mathrm{mol} = 4$) coupled to the cavity mode. The emission from $|-\rangle$ prevails over $|+\rangle$ emission due to the incoherent population transfer caused by the dephasing reservoir. The absorption spectrum, on the other hand, contains both $|+\rangle$ and $|-\rangle$ peaks of similar intensity. Last, the emission and the absorption spectra contain a peak appearing close to the frequency of the decoupled molecules that arises from the dark polariton states $|\mathrm{D}_i\rangle$ that are now coupled to the bright polaritons $|+\rangle$ and $|-\rangle$. (c-f) Emission spectra as a function of the excitation energy $\hbar\omega_\mathrm{L}$ for $N_\mathrm{mol} = 2, 3, 4, 5$ molecules, respectively. In all cases (b-f) the molecular excitons of equal energies $\hbar\omega_\mathrm{eg} = 2\,\mathrm{eV}$ are perfectly tuned to the cavity resonance $\hbar\omega_\mathrm{c} = 2\,\mathrm{eV}$ and interact with the cavity mode via $\hbar g_i = \hbar g = 100\,\mathrm{meV}$. The system is pumped by a laser of amplitude $\hbar\mathcal{E} = 0.1\,\mathrm{meV}$. The additional parameters are $\hbar\gamma_a = 150\,\mathrm{meV}$, $\hbar\gamma_B = 400\,\mathrm{meV}$, $\hbar\gamma_\sigma = 2 \times 10^{-2}\,\mathrm{meV}$, $d_\mathrm{R} = 0.173$, $\hbar\Omega_\mathrm{R} = 400\,\mathrm{meV}$.

6.3 N_{mol} molecules in a cavity

6.3.1 Reservoir-induced incoherent processes for N_{mol} molecules

Strong-coupling between a single-molecule exciton and a cavity mode is fundamentally important but in realistic systems the cavity is usually coupled to several molecular samples [238]. We therefore extend our description to cavities containing N_{mol} molecules and transform the system Hamiltonian $\hat{H}_{\mathrm{tot}}$ into the picture of collective polariton excitations. To that end we introduce a new set of operators $\hat{S}_i = \sum_\alpha c_{i\alpha}\hat{\sigma}_\alpha$, where $c_{i\alpha}$ are coefficients that are elements of a unitary matrix such that $(c_{i1},\, c_{i2},\, \ldots,\, c_{iN_{\mathrm{mol}}})$ form a set of N_{mol} orthonormal vectors. It is convenient to make the choice

$$(c_{11},\, c_{12},\, \ldots,\, c_{1N_{\mathrm{mol}}}) = \frac{1}{\sqrt{\sum_\alpha |g_\alpha|^2}}(g_1,\, g_2,\, \ldots,\, g_{N_{\mathrm{mol}}}) \tag{6.32}$$

and the remaining vectors orthonormal to the first vector. With this choice, $\hat{S}_1$ becomes fully coupled to the plasmonic cavity via a new effective coupling constant $g_{\mathrm{eff}} = \sqrt{\sum_\alpha |g_\alpha|^2}$. In the following we consider that all the coefficients $g_\alpha = g$ are equal $(c_{1\alpha} = 1/\sqrt{N_{\mathrm{mol}}})$ and recover the result $g_{\mathrm{eff}} = \sqrt{N_{\mathrm{mol}}}g$. We further consider the low-excitation limit where the new operators $\hat{S}_i$ become approximately bosonic and independent

$$[\hat{S}_i, \hat{S}_j^\dagger] \approx \delta_{ij}, \tag{6.33}$$

with the transformation rules

$$\sum_\alpha \hat{\sigma}_\alpha^\dagger \hat{\sigma}_\alpha = \sum_i \hat{S}_i^\dagger \hat{S}_i, \tag{6.34}$$

$$\sum_\alpha \hat{\sigma}_\alpha \hat{\rho} \hat{\sigma}_\alpha^\dagger = \sum_{ij} \left(\sum_\alpha c_{\alpha i} c_{\alpha j} \right) \hat{S}_i \hat{\rho} \hat{S}_j^\dagger = \sum_i \hat{S}_i \hat{\rho} \hat{S}_i^\dagger, \tag{6.35}$$

where in the second line we used the orthogonality of the coefficient vectors that we assumed to be real.

The transformation rules allow for rewriting the Hamiltonian as:

$$\begin{aligned}\hat{H}_{\mathrm{tot}} = {} & \sum_i \hbar\omega_{\mathrm{eg}} \hat{S}_i^\dagger \hat{S}_i + \hbar\omega_{\mathrm{c}} \hat{a}^\dagger \hat{a} + g_{\mathrm{eff}} \left(\hat{S}_1 \hat{a}^\dagger + \hat{S}_1^\dagger \hat{a} \right) + \sum_\alpha \hbar\Omega_{\mathrm{R}} \hat{B}_\alpha^\dagger \hat{B}_\alpha \\ & + \hbar d_{\mathrm{R}} \Omega_{\mathrm{R}} \sum_{ij} \left[\sum_\alpha c_{\alpha i} c_{\alpha j} \left(\hat{B}_\alpha + \hat{B}_\alpha^\dagger \right) \right] \hat{S}_i^\dagger \hat{S}_j \\ & + \sum_{ij} \left(\sum_{\alpha\beta} G_{\alpha\beta} c_{\alpha i} c_{\beta j} \right) \hat{S}_i^\dagger \hat{S}_j + \mathrm{H.c.}\end{aligned} \tag{6.36}$$

The Lindblad terms of the excitons of the individual molecules transform in the collective picture as

$$\sum_{\alpha} \mathscr{L}^{\gamma_{\sigma_\alpha}}_{\hat{\sigma}_\alpha}(\hat{\rho}) = \sum_{i} \mathscr{L}^{\gamma_{S_i}}_{\hat{S}_i}(\hat{\rho}). \tag{6.37}$$

As in the case of a single molecule, we can proceed to diagonalize the Hamiltonian part involving the bright excitonic mode strongly coupled with the cavity [neglecting for now the inter-molecular coupling in the last line of Eq. (6.36)]. We thus generate a new set of annihilation operators of the lower, $\hat{S}_{-}$, and the upper, $\hat{S}_{+}$, polaritons

$$\hat{S}_{+} = \cos\theta_{\text{eff}}\, \hat{S}_1 + \sin\theta_{\text{eff}}\, \hat{a}, \tag{6.38}$$

$$\hat{S}_{-} = -\sin\theta_{\text{eff}}\, \hat{S}_1 + \cos\theta_{\text{eff}}\, \hat{a}, \tag{6.39}$$

with θ_{eff} defined in analogy with the single-exciton case [Eq. (6.10)]:

$$\tan(2\theta_{\text{eff}}) = \frac{2g_{\text{eff}}}{\omega_{\text{eg}} - \omega_{\text{c}}} \text{ and } 0 < 2\theta < \pi. \tag{6.40}$$

To simplify the discussion we further denote the bright polaritons in analogy with the single-molecular case as $|+\rangle$ and $|-\rangle$ (such that in the single-excitation approximation $\hat{S}_{+} = |0\rangle\langle +|$ and $\hat{S}_{-} = |0\rangle\langle -|$), and the dark polariton states $|\mathrm{D}_i\rangle$ (such that $\hat{S}_i = |0\rangle\langle \mathrm{D}_i|$ for $i > 1$). The level diagram of the polaritonic system is schematically depicted in Fig. 6.4 (a).

In the polaritonic picture, the system Hamiltonian $\hat{H}_{\mathrm{tot}}$ becomes:

$$\hat{H}_{\mathrm{tot}} = \hbar\omega_+ \hat{S}_+^\dagger \hat{S}_+ + \hbar\omega_- \hat{S}_-^\dagger \hat{S}_- + \sum_{i=2}^{N_{\mathrm{mol}}} \hbar\omega_{\mathrm{eg}} \hat{S}_i^\dagger \hat{S}_i + \sum_\alpha \hbar\Omega_{\mathrm{R}} \hat{B}_\alpha^\dagger \hat{B}_\alpha \tag{6.41a}$$

$$+ \hbar d_{\mathrm{R}}\Omega_{\mathrm{R}} \left[\sum_\alpha c_{\alpha 1} c_{\alpha 1} \left(\hat{B}_\alpha + \hat{B}_\alpha^\dagger \right) \right] \times \left[\cos^2\theta_{\mathrm{eff}}\, \hat{S}_+^\dagger \hat{S}_+ + \sin^2\theta_{\mathrm{eff}}\, \hat{S}_-^\dagger \hat{S}_- - \sin\theta_{\mathrm{eff}} \cos\theta_{\mathrm{eff}} (\hat{S}_+^\dagger \hat{S}_- + \hat{S}_-^\dagger \hat{S}_+) \right] \tag{6.41b}$$

$$+ \left[\hbar \cos\theta_{\mathrm{eff}}\, d_{\mathrm{R}}\Omega_{\mathrm{R}} \sum_{i=2}^{N_{\mathrm{mol}}} \left[\sum_\alpha c_{\alpha i} c_{\alpha 1} \left(\hat{B}_\alpha + \hat{B}_\alpha^\dagger \right) \right] \hat{S}_i^\dagger \hat{S}_+ + \mathrm{H.c.} \right] \tag{6.41c}$$

$$- \left[\hbar \sin\theta_{\mathrm{eff}}\, d_{\mathrm{R}}\Omega_{\mathrm{R}} \sum_{i=2}^{N_{\mathrm{mol}}} \left[\sum_\alpha c_{\alpha i} c_{\alpha 1} \left(\hat{B}_\alpha + \hat{B}_\alpha^\dagger \right) \right] \hat{S}_i^\dagger \hat{S}_- + \mathrm{H.c.} \right] \tag{6.41d}$$

$$+ \hbar d_{\mathrm{R}}\Omega_{\mathrm{R}} \sum_{i,j=2}^{N_{\mathrm{mol}}} \left[\sum_\alpha c_{\alpha i} c_{\alpha j} \left(\hat{B}_\alpha + \hat{B}_\alpha^\dagger \right) \right] \hat{S}_i^\dagger \hat{S}_j \tag{6.41e}$$

$$+ \left[\sum_{j=2}^{N_{\mathrm{mol}}} \left(\sum_{\alpha\beta} G_{\alpha\beta} c_{\alpha 1} c_{\beta j} \right) \left[\cos\theta_{\mathrm{eff}} \hat{S}_+^\dagger - \sin\theta_{\mathrm{eff}} \hat{S}_-^\dagger \right] \hat{S}_j + \mathrm{H.c.} \right] \tag{6.41f}$$

$$+ \left[\left(\sum_{\alpha\beta} G_{\alpha\beta} c_{\alpha 1} c_{\beta 1} \right) \left[\cos\theta_{\mathrm{eff}} \hat{S}_+^\dagger - \sin\theta_{\mathrm{eff}} \hat{S}_-^\dagger \right] \left[\cos\theta_{\mathrm{eff}} \hat{S}_+ - \sin\theta_{\mathrm{eff}} \hat{S}_- \right] \right] \tag{6.41g}$$

$$+ \sum_{ij=2}^{N_{\mathrm{mol}}} \left(\sum_{\alpha\beta} G_{\alpha\beta} c_{\alpha i} c_{\beta j} \right) \hat{S}_i^\dagger \hat{S}_j . \tag{6.41h}$$

Here ω_+ and ω_- are defined as:

$$\omega_\pm = \frac{\omega_{\mathrm{eg}} + \omega_{\mathrm{c}}}{2} \pm \sqrt{g_{\mathrm{eff}}^2 + \frac{(\omega_{\mathrm{eg}} - \omega_{\mathrm{c}})^2}{4}} . \tag{6.42}$$

The coupling of the various polaritonic modes with the dephasing reservoir is given by (6.41b) to (6.41e). The interaction with the reservoir leads to population transfer among $|+\rangle$, $|-\rangle$, and the dark polaritons $|\mathrm{D}_i\rangle$. The coherent laser pumping is included in (6.58). The term in (6.41f) of the transformed Hamiltonian introduces mixing of the dark states with the bright modes. Equation (6.41h) represents additional interactions among the dark modes that are weak for the selected parameters.

The incoherent damping of the dephasing reservoir is included via $\mathscr{L}_{\hat{B}_\alpha}^{\gamma_{B_\alpha}}(\hat{\rho})$, with $\gamma_{B_\alpha} = \gamma_B$. The intrinsic damping of the molecules is included via

$\sum_i \mathscr{L}_{\hat{\sigma}_i}^{\gamma_{\sigma_i}}(\hat{\rho}) = \sum_i \mathscr{L}_{\hat{S}_i}^{\gamma_{S_i}}(\hat{\rho})$. The transformation into the basis of the polariton states further changes the form of the incoherent damping of the cavity. In the secular approximation, the cavity damping Lindblad term, $\mathscr{L}_{\hat{a}}^{\gamma_a}(\hat{\rho})$, transforms as

$$\mathscr{L}_{\hat{a}}^{\gamma_a}(\hat{\rho}) \approx \mathscr{L}_{\hat{S}_+}^{\gamma_{S_+}}(\hat{\rho}) + \mathscr{L}_{\hat{S}_-}^{\gamma_{S_-}}(\hat{\rho}), \tag{6.43}$$

with the respective decay rates

$$\gamma_{S_+} = \sin^2\theta_{\text{eff}}\gamma_a, \tag{6.44}$$

$$\gamma_{S_-} = \cos^2\theta_{\text{eff}}\gamma_a. \tag{6.45}$$

The contribution of the intrinsic molecular decay γ_σ to the decay of $|+\rangle$ and $|-\rangle$ can be neglected compared to the large cavity losses γ_a. Last we remark that the model outlined above, including explicitly the reservoir modes $\hat{B}_i$ is further denoted as the explicit bath model – EBM.

6.3.2 Reservoir-induced incoherent processes in Born-Markov approximation

To bring an intuitive insight into the reservoir-induced incoherent population transfer among the polariton states, we now eliminate the reservoir degrees of freedom in the Born-Markov and secular approximation and introduce effective incoherent Lindblad terms. For simplicity, we further assume that the intermolecular coupling is negligible and only weakly perturbs the dynamics given by Eq. (6.41a) to Eq. (6.41e). We eliminate the reservoir whose dynamics is given by the Hamiltonian term $\hat{H}_{\text{res}} = \sum_\alpha \hbar\Omega_{\text{R}}\hat{B}_\alpha^\dagger\hat{B}_\alpha$ and the Lindblad terms $\sum_\alpha \mathscr{L}_{\hat{B}_\alpha}^{\gamma_{B_\alpha}}(\hat{\rho})$, with $\gamma_{B_\alpha} = \gamma_B$ by standard methods of the theory of open-quantum systems using the secular approximation [158].

Equation (6.41b) represents incoherent interaction between the upper, $|+\rangle$, and the lower, $|-\rangle$, polariton, in close analogy with the single-excitonic case, and leads to the Lindblad terms $\mathscr{L}_{\hat{S}_+^\dagger\hat{S}_-}^{\gamma_{S_+^\dagger S_-}}(\hat{\rho})$ and $\mathscr{L}_{\hat{S}_-^\dagger\hat{S}_+}^{\gamma_{S_-^\dagger S_+}}(\hat{\rho})$. We further define $\hat{F}_\alpha = d_{\text{R}}\Omega_{\text{R}}(\hat{B}_\alpha + \hat{B}_\alpha^\dagger)$ ($\hat{F}_\alpha = \hat{F}$ as the reservoir modes are equivalent) and note that

$$\langle\hat{F}_\alpha^\dagger(t+s)\hat{F}_\beta(t)\rangle = \delta_{\alpha\beta}\langle\hat{F}_\alpha^\dagger(t+s)\hat{F}_\alpha(t)\rangle = \delta_{\alpha\beta}\langle\hat{F}^\dagger(t+s)\hat{F}(t)\rangle \tag{6.46}$$

as the respective bath modes are locally interacting with each molecule and are assumed to be uncorrelated. The respective rates then become

$$\gamma_{S_\mp^\dagger S_\pm} = \frac{\sin^2\theta_{\text{eff}}\cos^2\theta_{\text{eff}}}{N_{\text{mol}}}J(\omega_\pm - \omega_\mp), \tag{6.47}$$

where either the upper or the lower signs apply. This result can be found from

$$\begin{aligned}
&\frac{\gamma_{S_\mp^\dagger S_\pm}}{\sin^2\theta_{\mathrm{eff}}\cos^2\theta_{\mathrm{eff}}} = \\
&= 2\mathrm{Re}\left\{\int_0^\infty \mathrm{d}s\, e^{\mathrm{i}(\omega_\pm-\omega_\mp)s}\left\langle \sum_\alpha c_{\alpha 1}c_{\alpha 1}\hat{F}_\alpha^\dagger(t+s)\sum_\beta c_{\beta 1}c_{\beta 1}\hat{F}_\beta(t)\right\rangle\right\} \\
&= 2\mathrm{Re}\left\{\int_0^\infty \mathrm{d}s\, e^{\mathrm{i}(\omega_\pm-\omega_\mp)s}\left\langle \sum_\alpha c_{\alpha 1}^2 c_{\alpha 1}^2\hat{F}_\alpha^\dagger(t+s)\hat{F}_\alpha(t)\right\rangle\right\} \\
&= \sum_\alpha c_{\alpha 1}^2 c_{\alpha 1}^2 J(\omega_\pm-\omega_\mp) = \frac{1}{N_{\mathrm{mol}}}J(\omega_\pm-\omega_\mp), \qquad (6.48)
\end{aligned}$$

where we have used the definition of the coefficients $c_{\alpha 1} = 1/\sqrt{N_{\mathrm{mol}}}$ and

$$J(\omega) = 2\mathrm{Re}\left\{\int_0^\infty \mathrm{d}s\, e^{\mathrm{i}\omega s}\langle\hat{F}^\dagger(t+s)\hat{F}(t)\rangle\right\} \qquad (6.49)$$

to obtain the final result.

From Eq. (6.41c) we obtain for the decay of the upper polariton into the dark polaritons (and vice versa) the terms:

$$\mathscr{L}^{\gamma_{\sum_{i=2}^{N_{\mathrm{mol}}} S_i^\dagger S_+}}_{\sum_{i=2}^{N_{\mathrm{mol}}}\hat{S}_i^\dagger\hat{S}_+}(\hat{\rho}) \approx \sum_{i=2}^{N_{\mathrm{mol}}}\mathscr{L}^{\gamma_{S_i^\dagger S_+}}_{\hat{S}_i^\dagger\hat{S}_+}(\hat{\rho}), \qquad (6.50)$$

$$\mathscr{L}^{\gamma_{\sum_{i=2}^{N_{\mathrm{mol}}} S_+^\dagger S_i}}_{\sum_{i=2}^{N_{\mathrm{mol}}}\hat{S}_+^\dagger\hat{S}_i}(\hat{\rho}) \approx \sum_{i=2}^{N_{\mathrm{mol}}}\mathscr{L}^{\gamma_{S_+^\dagger S_i}}_{\hat{S}_+^\dagger\hat{S}_i}(\hat{\rho}), \qquad (6.51)$$

where we have neglected the Lindblad superators containing the cross-terms. In analogy with $\gamma_{S_\mp^\dagger S_\pm}$, the respective rates are:

$$\gamma_{S_i^\dagger S_+} \equiv \gamma_{S_{\mathrm{D}}^\dagger S_+} = \frac{\cos^2\theta_{\mathrm{eff}}}{N_{\mathrm{mol}}}J(\omega_+-\omega_{\mathrm{eg}}), \qquad (6.52)$$

$$\gamma_{S_+^\dagger S_i} \equiv \gamma_{S_+^\dagger S_{\mathrm{D}}} = \frac{\cos^2\theta_{\mathrm{eff}}}{N_{\mathrm{mol}}}J(\omega_{\mathrm{eg}}-\omega_+), \qquad (6.53)$$

where we have defined $\gamma_{S_{\mathrm{D}}^\dagger S_+}$ and $\gamma_{S_+^\dagger S_{\mathrm{D}}}$ assuming that the dark polaritons are equivalent. In close analogy, from Eq. (6.41d) we get for the decay of the dark polaritons into the lower polariton (and vice versa):

$$\mathscr{L}^{\gamma_{\sum_{i=2}^{N_{\mathrm{mol}}} S_{-}^{\dagger} S_i}}_{\sum_{i=2}^{N_{\mathrm{mol}}} \hat{S}_{-}^{\dagger} \hat{S}_i}(\hat{\rho}) \approx \sum_{i=2}^{N_{\mathrm{mol}}} \mathscr{L}^{\gamma_{S_{-}^{\dagger} S_i}}_{\hat{S}_{-}^{\dagger} \hat{S}_i}(\hat{\rho}), \tag{6.54}$$

$$\mathscr{L}^{\gamma_{\sum_{i=2}^{N_{\mathrm{mol}}} S_{i}^{\dagger} S_-}}_{\sum_{i=2}^{N_{\mathrm{mol}}} \hat{S}_{i}^{\dagger} \hat{S}_-}(\hat{\rho}) \approx \sum_{i=2}^{N_{\mathrm{mol}}} \mathscr{L}^{\gamma_{S_{i}^{\dagger} S_-}}_{\hat{S}_{i}^{\dagger} \hat{S}_-}(\hat{\rho}), \tag{6.55}$$

The respective rates are

$$\gamma_{S_{-}^{\dagger} S_i} \equiv \gamma_{S_{-}^{\dagger} S_{\mathrm{D}}} = \frac{\sin^2 \theta_{\mathrm{eff}}}{N_{\mathrm{mol}}} J(\omega_{\mathrm{eg}} - \omega_-), \tag{6.56}$$

$$\gamma_{S_{i}^{\dagger} S_-} \equiv \gamma_{S_{\mathrm{D}}^{\dagger} S_-} = \frac{\sin^2 \theta_{\mathrm{eff}}}{N_{\mathrm{mol}}} J(\omega_- - \omega_{\mathrm{eg}}), \tag{6.57}$$

where we have defined $\gamma_{S_{\mathrm{D}}^{\dagger} S_-}$ and $\gamma_{S_{-}^{\dagger} S_{\mathrm{D}}}$.

Last, in the Markovian model we also obtain the pure dephasing and energy transfer among the dark polariton states. These terms, however, do not contribute to the population decay that we discuss later and we will not consider them in the following.

In summary, we have obtained effective rates of incoherent transfer of populations among the polariton states in the Born-Markov approximation. The obtained decay rates all feature $\propto 1/N_{\mathrm{mol}}$ dependence, $\gamma_{S_{+}^{\dagger} S_-}$, $\gamma_{S_{-}^{\dagger} S_+}$, $\gamma_{S_{-}^{\dagger} S_{\mathrm{D}}}$, $\gamma_{S_{\mathrm{D}}^{\dagger} S_-}$, $\gamma_{S_{+}^{\dagger} S_{\mathrm{D}}}$, $\gamma_{S_{\mathrm{D}}^{\dagger} S_+} \propto 1/N_{\mathrm{mol}}$, and are proportional to the reservoir spectral function $J(\omega)$ evaluated at the frequency corresponding to the difference between the respective energies of the involved polariton states. Hence, the transitions from polaritons of higher energy towards polaritons of lower energy ($|+\rangle \to |-\rangle$, $|+\rangle \to |\mathrm{D}_i\rangle$, and $|\mathrm{D}_i\rangle \to |-\rangle$) are favoured with respect to the reverse processes due to the asymmetry of $J(\omega)$ $[J(-|\omega|) < J(|\omega|)]$ discussed above.

6.3.3 Polariton light emission spectra under coherent driving conditions for N_{mol} molecules

We now calculate the absorption and emission spectra of the system including N_{mol} molecules as defined in Eq. (6.29) and Eq. (6.30) using the EBM. We assume that the cavity is coherently pumped via the Hamiltonian term $\hat{H}_{\mathrm{pump}}^{\mathrm{col}}$:

$$\hat{H}_{\mathrm{pump}}^{\mathrm{col}} = \hbar \mathcal{E} \left(\left[\sin\theta_{\mathrm{eff}}\, \hat{S}_+ + \cos\theta_{\mathrm{eff}}\, \hat{S}_- \right] e^{\mathrm{i}\omega_{\mathrm{L}} t} + \left[\sin\theta_{\mathrm{eff}}\, \hat{S}_+^{\dagger} + \cos\theta_{\mathrm{eff}}\, \hat{S}_-^{\dagger} \right] e^{-\mathrm{i}\omega_{\mathrm{L}} t} \right). \tag{6.58}$$

In the following we also assume the inter-molecular coupling of the form

$$\begin{aligned} G_{ij} &= \frac{G_0}{|i-j|^3} \text{ for } i \neq j \text{ and} \\ G_{ij} &= 0 \text{ for } i = j \end{aligned} \tag{6.59}$$

and set

$$\hbar G_0 = \frac{d_0^2}{4\pi\varepsilon_0 r_0^3}, \tag{6.60}$$

with the transition dipole moment of the exciton $d_0 = 0.2\,\mathrm{e{\cdot}nm}$, the effective intermolecular distance $r_0 = 2\,\mathrm{nm}$ and ε_0 the vacuum permittivity. This choice of G_{ij} describes a set of interacting molecules whose dipoles are arranged along a line (e.g. in the x direction) with constant spacing r_0 and with parallel dipole moments d_0 (e.g. oriented along z). The intermolecular interaction given by Eq. (6.59) weakly perturbs the polariton structure given by the collective cavity-mode-exciton Hamiltonian, however, it breaks the symmetry of the Hamiltonian (makes the molecules inequivalent). Due to this symmetry breaking, the originally dark polariton states $|\mathrm{D}_i\rangle$ couple with the cavity mode and become observable in the spectra. We note that the symmetry of the system Hamiltonian can be broken in different ways, for example by introducing disorder into the system.

As an illustrative example we calculate the emission and absorption spectra of four mutually interacting molecules that are coupled to the cavity with $\hbar g_i = \hbar g = 100\,\mathrm{meV}$. The system is pumped at the upper polariton frequency $\hbar\omega_{\mathrm{L}} = 2.2\,\mathrm{eV}$. The result is shown in Fig. 6.4 (b) for $N_{\mathrm{mol}} = 4$ molecules interacting with the cavity mode. The emission spectrum (black solid line) shows a dominant peak originating from the lower polariton $|-\rangle$ (appearing at $\approx 1.8\,\mathrm{eV}$) as in the single-molecular case. Another sharp emission peak of low intensity, which was not present in the single-molecular case, emerges at a frequency around that of the decoupled molecules $\approx 2\,\mathrm{eV}$. This new peak is a signature of the polariton states $|\mathrm{D}_i\rangle$ that are dark in the collective-coupling model where the excitons do not interact directly among themselves, but become bright after introducing the inter-molecular coupling in Eq. (6.4). Experiments where large numbers of molecules couple with a cavity show that the dark-polariton photoluminescence peak can have comparable intensity to the emission peak of the lower polaritons [76, 270]. On the other hand, the absorption spectrum (blue dashed line) features two absorption peaks of similar intensity at frequencies of the polariton branches $|+\rangle$ and $|-\rangle$. As a result of the inter-polariton transfer induced by the reservoir, the lower-polariton peak has slightly higher spectral intensity and is narrower than the upper-polariton peak, since the upper-polariton peak is broadened by the decay processes induced by the dephasing reservoir [91].

Finally, in Fig. 6.4 we present the two-dimensional maps containing the emission (vertical axis) and excitation (horizontal axis) spectra of systems containing (c) $N_{\mathrm{mol}} = 2$, (d) $N_{\mathrm{mol}} = 3$, (e) $N_{\mathrm{mol}} = 4$ and (f) $N_{\mathrm{mol}} = 5$ molecules (considering $\hbar g = 100\,\mathrm{meV}$). The emission pattern is in all the cases similar to the single-molecule case [Fig. 6.3(a,b)], exhibiting a doublet of the emission peaks originating from $|+\rangle$ and $|-\rangle$ that are split by the collectively enhanced coupling $g_{\text{eff}} = \sqrt{N_{\text{mol}}}g$. Between the $|+\rangle$ and $|-\rangle$ polariton peaks, in this collective scenario there appears an additional feature corresponding to the dark polaritons in both the emission and the excitation spectra (although hardly distinguishable in the spectral maps). The dominance of the lower-polariton peak in all the calculated spectra is in accordance with the mechanism of incoherent population transfer in strongly-coupled systems discussed above. We can observe that the inelastic emission is most efficient from the lower polariton branch when the upper polariton is pumped. In this case, the interaction with the reservoir efficiently incoherently populates $|-\rangle$ which in turn emits the inelastic photons. We now briefly analyze the polariton dynamics in the collective scenario that gives rise to the asymmetry of the inelastic photon emission.

6.4 Polariton dynamics in the collective scenario

We have shown that the dephasing reservoir gives rise to incoherent transitions between the polariton states that preferentially lead from the states of higher energy towards the states of lower energy ($|+\rangle \to |\mathrm{D}_i\rangle$, $|+\rangle \to |-\rangle$ and $|\mathrm{D}_i\rangle \to |-\rangle$). This phenomenology has been addressed in details by other authors [90–94]. Here we focus on the dynamics of these decay processes and calculate the time evolution of the polariton populations $n_+ = \langle \hat{S}_+^\dagger \hat{S}_+ \rangle$, $n_- = \langle \hat{S}_-^\dagger \hat{S}_- \rangle$ and $n_{\mathrm{D}} = \frac{1}{N_{\text{mol}}-1}\sum_i \langle \hat{S}_i^\dagger \hat{S}_i \rangle$, where N_{mol} is the number of molecules, assuming that the populations evolve according to the master equation [Eq. (6.8) with Eq. (6.26)] that explicitly includes the dephasing reservoir (the EBM). We compare the EBM population dynamics with a rate-equation model (REM) based on the diagram of levels and decays displayed in Fig. 6.4 (a). The effective polariton dynamics derived in Section 6.3.2 leads to the following rate equations (we do not consider the coherent driving term $\hat{H}_{\text{pump}}^{\text{col}}$):

$$\begin{bmatrix} \dot{n}_+ \\ \dot{n}_{\mathrm{D}} \\ \dot{n}_- \end{bmatrix} = \begin{bmatrix} \gamma_{n_+} & (N_{\text{mol}}-1)\gamma_{S_+^\dagger S_{\mathrm{D}}} & \gamma_{S_+^\dagger S_-} \\ \gamma_{S_{\mathrm{D}}^\dagger S_+} & \gamma_{n_{\mathrm{D}}} & \gamma_{S_{\mathrm{D}}^\dagger S_-} \\ \gamma_{S_-^\dagger S_+} & (N_{\text{mol}}-1)\gamma_{S_-^\dagger S_{\mathrm{D}}} & \gamma_{n_-} \end{bmatrix} \begin{bmatrix} n_+ \\ n_{\mathrm{D}} \\ n_- \end{bmatrix}, \tag{6.61}$$

$$\tag{6.62}$$

with

$$\gamma_{n_+} = \gamma_{S_+} + \gamma_{S_-^\dagger S_+} + (N_{\text{mol}}-1)\gamma_{S_{\mathrm{D}}^\dagger S_+}, \tag{6.63}$$

$$\gamma_{n_{\mathrm{D}}} = \gamma_{S_{\mathrm{D}}} + \gamma_{S_-^\dagger S_{\mathrm{D}}} + \gamma_{S_+^\dagger S_{\mathrm{D}}}, \tag{6.64}$$

$$\gamma_{n_-} = \gamma_{S_-} + (N_{\text{mol}}-1)\gamma_{S_{\mathrm{D}}^\dagger S_-} + \gamma_{S_+^\dagger S_-}. \tag{6.65}$$

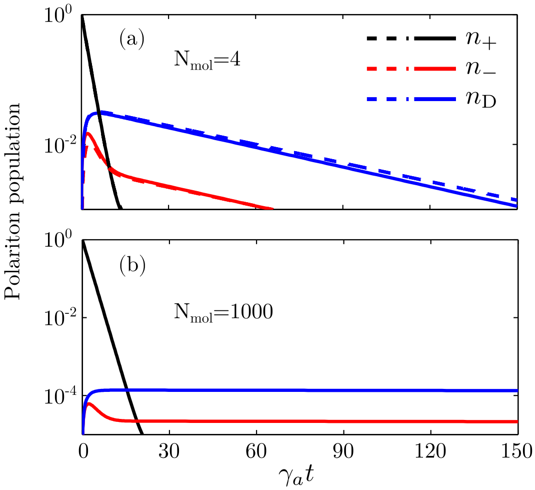

Figure 6.5: Decay of polariton populations n_+ (upper polariton - black), n_- (lower polariton - red) and n_{D} (dark polariton - blue), in logarithmic scale, as a function of time assuming that initially $n_+ = 1$ and $n_- = n_{\text{D}} = 0$. (a) The full calculation (EBM - dashed lines) is compared to the rate-equation model (REM - full lines) for $N_{\text{mol}} = 4$ molecules and $g = 100\,\text{meV}$. (b) The populations calculated from the REM for $N_{\text{mol}} = 1000$ molecules, using $\sqrt{N_{\text{mol}}}g = 200\,\text{meV}$. The remaining parameters are $\hbar\gamma_a = 150\,\text{meV}$, $\hbar\gamma_B = 400\,\text{meV}$, $\hbar\gamma_\sigma = 2\times10^{-2}\,\text{meV}$, $d_{\text{R}} = 0.173$, $\hbar\Omega_{\text{R}} = 400\,\text{meV}$.

In the REM, only the incoherent dynamics of the populations of the respective states is studied (the population decay) and processes related with the pure dephasing are not considered. We calculate the dynamics assuming that the upper polariton is initially fully populated $n_+ = 1$ and $n_- = n_{\text{D}} = 0$ and then spontaneously decays (the coherent driving [Eq. (6.28)] is switched off) into the ground state $|0\rangle$ and into the other polariton states, $|-\rangle$ and $|\text{D}_i\rangle$.

In Fig. 6.5 we plot the polariton populations in logarithmic scale as a function of time obtained from the numerical time evolution of the full system-reservoir density matrix (EBM - dashed lines) together with the solution of the REM (full lines) for (a) $N_{\text{mol}} = 4$ molecules and (b) $N_{\text{mol}} = 1000$ molecules (using REM only). For $N_{\text{mol}} = 4$, the REM matches well with the results from the EBM with only slight deviations from the exact population dynamics. n_+ (black) exhibits a rapid decay with total rate γ_{n_+} from its original population into the ground state, $|0\rangle$ (γ_{S_+}), but also into the lower polariton, $|-\rangle$ ($\gamma_{S_-^\dagger S_+}$), and the dark polaritons, $|\text{D}_i\rangle$, with rate $[(N_{\text{mol}}-1)\gamma_{S_{\text{D}}^\dagger S_+}]$, which pumps the lower polariton population (n_- - red lines) and dark polariton population (n_{D} - blue lines). After this initial impulse, the dark polariton population starts to steadily decay into the ground state ($\gamma_{S_{\text{D}}}$) and into the lower-polariton state ($\gamma_{S_-^\dagger S_{\text{D}}}$). Similarly to the dark polaritons, the lower polariton first gets populated due to the fast-decaying upper polariton. After that $|-\rangle$ rapidly decays into the ground state (γ_{S_-}), but only until it reaches the regime when n_- is dominantly pumped by the slowly decaying dark-polariton ($\gamma_{S_-^\dagger S_\mathrm{D}}$). In this regime, the decay of n_- becomes limited by the pumping and resembles that of the dark polaritons [the *bottleneck* effect, red lines in Fig. 6.5 (a)].

We have shown that the decay rates connecting the polariton states are inversely proportional to the number of molecules, $\gamma_{S_+^\dagger S_-}$, $\gamma_{S_-^\dagger S_+}$, $\gamma_{S_-^\dagger S_\mathrm{D}}$, $\gamma_{S_\mathrm{D}^\dagger S_-}$, $\gamma_{S_+^\dagger S_\mathrm{D}}$, $\gamma_{S_\mathrm{D}^\dagger S_+} \propto 1/N_\mathrm{mol}$. Since the upper and the lower polaritons in our model decay fast to the ground state ($\gamma_{S_+}, \gamma_{S_-} \propto \gamma_a$) regardless of N_mol, the initial stages of their respective population dynamics are practically independent of the number of molecules. However, as N_mol is increased, the dark polariton decay rate into the lower polariton becomes progressively smaller ($\gamma_{S_-^\dagger S_\mathrm{D}} \propto 1/N_\mathrm{mol}$) until it becomes fully limited by the intrinsic rate γ_σ for $N_\mathrm{mol} \to \infty$. This tendency is apparent in Fig. 6.5 (b), where we plot the population decay for $N_\mathrm{mol} = 1000$ molecules as obtained from the rate-equation model. In this case the bright polariton, $|+\rangle$, initially decays into the dark polariton states, $|\mathrm{D}_i\rangle$, which only slowly decay into the lower polariton $|-\rangle$.

Finally we remark that the model described in this chapter is able to address the dynamics of population transfer among the polaritonic states, but does not explain the long lifetime of the lower polariton state that has been reported in the literature [91, 271, 284–286]. In our approach, the terminal slow decay of n_- arises due to the *bottleneck* in the form of a slowly decaying *dark* polariton states. The explanation of the long lower-polariton lifetime requires further modelling of the microscopic decay mechanisms of coupled cavity mode and molecular excitons.

6.5 Summary

In summary, we have demonstrated that the dephasing reservoir in strongly coupled cavity-mode-exciton systems can lead to asymmetries in the observed emission spectra, favouring light emission from the lower polariton and suppressing the upper polariton emission. The asymmetry in the inelastic light emission from a cavity arises naturally from the model which explicitly considers the dephasing bath as an effective damped harmonic oscillator. The coupling with the reservoir in the strong coupling regime naturally favours the transfer of the population of the higher-energy polaritons towards the polaritons of lower energy ($|+\rangle \to |\mathrm{D}_i\rangle$, $|+\rangle \to |-\rangle$ and $|\mathrm{D}_i\rangle \to |-\rangle$), including the dark polaritons if many molecules are considered. This process leads to the prevalence of the inelastic photon emission from the lower polariton $|-\rangle$ and considerably shorter lifetime of the upper polariton $|+\rangle$. Moreover, if many mutually interacting molecules are coupled to the cavity, the dark polariton states can become bright and give rise to a new peak in the polariton emission spectrum. This new peak is then positioned approximately at the frequency of the uncoupled excitons, which is consistent with experimental observations of light emission from molecules [59, 76, 270].

The results of this chapter have been obtained for a relatively small number of molecular samples due to the limitations of the approach based on the solution of the quantum master equation. Other approaches have been considered in the literature [273] which allow for treating a large number of molecules within the effective Hamiltonian approach that takes advantage of the tensor-network description of the excitonic and vibrational states, but do not allow for calculation of the steady-state emission properties under coherent laser pumping. It would be desirable to implement the tensor-network approach within the open-quantum system approach and apply it to more realistic systems where large numbers of molecules couple with optical cavities.

Nevertheless, the results of this chapter provide an intuitive view of the processes that stand behind the experimental observations of light emission from molecules in optical cavities and can serve as a guideline for future implementations of dephasing in strongly-coupled systems.

Part IV

Surface-Enhanced Raman Scattering

Chapter 7

Optomechanical approach to resonant Surface-Enhanced Raman Scattering

Surface plasmon excitations in metallic particles are able to squeeze and enhance electromagnetic fields down to the nanometric scale and thus dramatically enhance the interaction of nearby molecules with the incident light. The plasmonic near-field enhancement has been exploited in plasmon-enhanced spectroscopies, particularly in the Surface Enhanced Raman Spectroscopy (SERS) [7–19], which enables detection of minute quantities of molecular samples. The improved design of plasmonic cavities has allowed for spectroscopic investigation of even single molecules that are placed into ultranarrow plasmonic gaps [9, 54]. Current experimental strategies have taken advantage of the properties of plasmonic cavity modes that allowed reaching the plasmon-exciton strong-coupling regime with single molecules [238], as well as intramolecular optical mapping of single-molecule vibrations in SERS [54] or in electroluminescence [56]. These results suggest the possibility to push the use of plasmonic modes to further and actively control the quantum state of a single molecule and thus influence its chemistry [95–100]. Recent theoretical and experimental studies [101–105] have revealed that off-resonant SERS can be understood as a quantum optomechanical process [101, 102, 287] where the single plasmon mode (sustained in a plasmonic cavity) of frequency ω_c plays the role of the macroscopic optical cavity and the molecular vibration of frequency Ω plays the role of the macroscopic oscillation of the mirror. The description of such process requires development of concepts and methods beyond the standard classical description of SERS [101–105].

In this chapter we address a quantum mechanical theory of *resonant* SERS (r-SERS), where an optical plasmonic mode supported in a metallic nanostructure resonantly excites a nearby single molecule described as an electronic two-level system (TLS), coupled to a vibrational mode. We discuss the similarities and differences between the r-SERS Hamiltonian and the off-resonant quantum optomechanical Hamiltonian, which has been described previously. To that end we adopt a range of the optomechanical parameters available in typical resonant situations. We then show that novel phenomena emerge in r-SERS under intense laser illumination, when the non-linearities of the molecule can trigger the coherent coupling of molecular electronic and vibrational degrees of freedom [63, 72, 234, 288–291]. We further exploit the analogy with quantum optomechanics to propose a mechanism of on-demand frequency-selective pumping of molecular vibrations [7, 10, 12, 13, 16] via the coherent laser illumination. Last, we expand the theory of molecular optomechanics to address r-SERS under conditions of strong coupling between the plasmon and the molecular electronic excitations. These phenomena may provide a means to drive plasmon-enhanced vibrational spectroscopy to the realm of the single-molecule selective chemistry or engineering of single-molecular optomechanical systems involving molecular vibrations on demand.

7.1 Optomechanical description of off-resonance Raman scattering

The standard theoretical approach to Raman scattering on molecules consists in performing a perturbative expansion of the molecular polarizability in the scope of the Placzek's or Albrecht's theory [292]. In this thesis we tackle the problem of plasmon-enhanced Raman scattering on molecules by applying the methodology of the quantum cavity optomechanics. We follow recent studies [101–105, 293] that have shown that off-resonant SERS can be understood as a quantum optomechanical process [287] where the single plasmon mode (the plasmonic cavity) of frequency ω_c plays the role of the macroscopic optical cavity and the molecular vibration of frequency Ω plays the role of the oscillating mirror. Here we extend the analogy between optomechanics and SERS and describe the r-SERS by means of cavity quantum electrodynamics (QED) as a hybrid-optomechnical process [294, 295].

In quantum optomechanics, the mirrors of optical cavity sustaining an electromagnetic mode are attached to a mechanical oscillator in such a way that the frequency of the optical mode $\omega_\mathrm{c}(q)$ depends on the displacement of the mirror, q, as schematically depicted in Fig. 7.1. The mechanical oscillations of the mirror are characterized by a frequency Ω which is constant. In quantum optomechanics, this dependence of the cavity frequency on the position leads to an interaction between the mode of the optical cavity and the mechanical mode of the mirror as follows. The Hamiltonian of the cavity $\hat{H}_\mathrm{c} = \hbar\omega_\mathrm{c}(q)\hat{a}^\dagger\hat{a}$ ($\hat{a}$ and $\hat{a}^\dagger$ being the bosonic annihilation and creation operators, respectively) is expanded in q and only the first-order term of the Taylor expansion is kept:

$$\hat{H}_\mathrm{c} \approx \hbar\omega_\mathrm{c}(0)\hat{a}^\dagger\hat{a} + \hbar\frac{\partial\omega_\mathrm{c}(q)}{\partial q}\Big|_{q=0} q\,\hat{a}^\dagger\hat{a}. \tag{7.1}$$

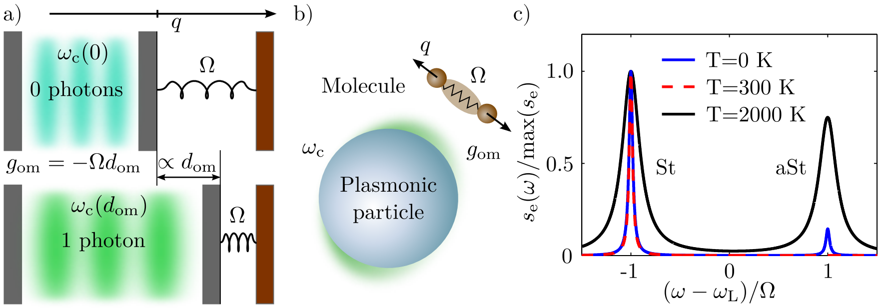

Figure 7.1: (a) Schematics of a typical optomechanical cavity. One of the cavity mirrors is attached to a mechanical oscillator of frequency Ω. The cavity supports a photonic mode of frequency $\omega_c(q)$, dependent on the displacement of the oscillating mirror, q. The q-dependence of the cavity mode then gives rise to the optomechanical coupling g_{om}, which can be also expressed in terms of the oscillation frequency Ω and a dimensionless displacement d_{om} of the mirror equilibrium position when one excitation is created in the cavity (as described in the main text). (b) In molecular optomechanics, the localized plasmonic mode of a metallic particle interacting with a molecule plays the role of the optical cavity and the molecule's vibrations play the role of the mechanical oscillation. (d) Example of off-resonant SERS spectra calculated using the quantum optomechanical formalism for three different temperatures: $T = 0\,$K (red dashed line), 300 K (blue line) and 2000 K (black line), and normalized to the maximum. The spectra exhibit two peaks, the Stokes peak (St), red detuned from the laser frequency ω_L, and the anti-Stokes peak (aSt), blue detuned from ω_L. The anti-Stokes peaks is practically absent when $T = 0\,$K. As the temperature increases, the anti-Stokes peak gains on intensity and for $T = 2000\,$K becomes comparable to the Stokes peak.

The displacement of the mechanical vibration is then promoted to an operator $q \rightarrow \hat{q}$, with $\hat{q} = q_0(\hat{b}^\dagger + \hat{b})$. Here $\hat{b}$ ($\hat{b}^\dagger$) is the bosonic annihilation (creation) operator and q_0 is the zero-point amplitude of the mirror's oscillation. The Hamiltonian $\hat{H}_c$ thus becomes:

$$\hat{H}_c \approx \hat{H}_{c,0} + \hat{H}_{c-vib} = \hbar\omega_c(0)\hat{a}^\dagger\hat{a} + \hbar \underbrace{\frac{\partial\omega_c(q)}{\partial q}\Big|_{q=0} q_0}_{\equiv\Omega d_{om} \equiv -g_{om}} \hat{a}^\dagger\hat{a}(\hat{b}^\dagger + \hat{b}), \tag{7.2}$$

where $\hat{H}_{c,0}$ is the bare-cavity Hamiltonian and

$$\hat{H}_{c-vib} = -\hbar g_{om}\hat{a}^\dagger\hat{a}(\hat{b}^\dagger + \hat{b}) \tag{7.3}$$

is the optomechnical Hamiltonian that contains the non-linear interaction between the cavity photons and the quanta of the mechanical vibration. We have also defined the optomechanical coupling constant g_{om} that can be alternatively expressed in terms of the optomechanical displacement parameter d_{om}, as discussed below.

The optomechanical Hamiltonian describing off-resonant SERS reads in close analogy with quantum optomechanics [101–104]

$$\boxed{\hat{H}_{\rm om} = \hat{H}_{\rm pl} + \hat{H}_{\rm vib} + \hat{H}_{\rm pl-vib} + \hat{H}_{\rm pump},} \tag{7.4}$$

where

$$\boxed{\begin{aligned} \hat{H}_{\rm pl} &= \hbar\omega_{\rm c}\hat{a}^\dagger\hat{a} \\ \hat{H}_{\rm vib} &= \hbar\Omega\hat{b}^\dagger\hat{b} \\ \hat{H}_{\rm pl-vib} &= -\hbar g_{\rm om}\hat{a}^\dagger\hat{a}(\hat{b}^\dagger + \hat{b}) \\ \hat{H}_{\rm pump} &= \hbar\mathcal{E}\left[\hat{a}\exp(\mathrm{i}\omega_{\rm L}t) + \hat{a}^\dagger\exp(-\mathrm{i}\omega_{\rm L}t)\right]. \end{aligned}} \tag{7.5}$$

Here operators $\hat{a}$ ($\hat{a}^\dagger$) and $\hat{b}$ ($\hat{b}^\dagger$) are the annihilation (creation) operators for plasmon and vibrations, respectively, $\mathcal{E}$ is the photon-plasmon coupling constant (with $|\mathcal{E}|^2$ proportional to the laser intensity) that characterizes the interaction Hamiltonian between the plasmon mode and the classical laser illumination of frequency $\omega_{\rm L}$, and $g_{\rm om}$ is the optomechanical coupling constant.

In the field of molecular optomechanics, the coupling constant $g_{\rm om}$ can be connected to the Raman tensor, $\partial\boldsymbol{\alpha}_{\rm eg}/\partial q$, of the molecule (with $\boldsymbol{\alpha}_{\rm eg}$ the molecule's electronic polarizability) interacting with the plasmonic cavity [101–103]. We do not discuss the details of this connection in the thesis. Instead, in what follows it will be convenient to interpret the optomechanical interaction as a displacement of the vibrational mode by a dimensionless value $n_{\rm PL}d_{\rm om}$, dependent on the number of excitations (plasmons) in the cavity, $n_{\rm PL}$. This becomes apparent after rearranging the bare optomechanical Hamiltonian, $\hat{H}_{\rm bom} = \hat{H}_{\rm pl} + \hat{H}_{\rm vib} + \hat{H}_{\rm pl-vib}$, into the form

$$\begin{aligned} \hat{H}_{\rm bom} =& \hbar(\omega_{\rm c} - \Omega d_{\rm om}^2\hat{a}^\dagger\hat{a})\hat{a}^\dagger\hat{a} \\ &+ \hbar\Omega(\hat{b}^\dagger + d_{\rm om}\hat{a}^\dagger\hat{a})(\hat{b} + d_{\rm om}\hat{a}^\dagger\hat{a}), \end{aligned} \tag{7.6}$$

with the dimensionless displacement $d_{\rm om} = -g_{\rm om}/\Omega$ (see Fig. 7.1 for a graphical depiction of the displacement in a standard optomechanical system). The first line of Eq. (7.6) is the non-linear Hamiltonian of the cavity excitations (photons or plasmons). In the limit of a weakly populated cavity we can neglect the small non-linear contribution to the cavity frequency $-\Omega d_{\rm om}^2\hat{a}^\dagger\hat{a} \approx 0$ and recover the linear cavity Hamiltonian $\hbar\omega_{\rm c}\hat{a}^\dagger\hat{a}$. The second line in Eq. (7.6) has the sought form of the vibrational mode displaced by an amount that depends on the number of cavity excitations $\hat{a}^\dagger\hat{a}$.

The level structure of the bare optomechanical Hamiltonian $\hat{H}_{\rm bom}$ [Eq. (7.6)] can be visualized as shown in Fig. 7.2 (a). The large grey dashed parabola illustrates an effective potential supporting the plasmonic mode. The vibrational potential is represented by the small parabolas that are displaced along the dimensionless normal coordinate q by a magnitude $n_{\rm PL}d_{\rm om}$ proportional to the plasmonic number state $|n_{\rm PL}\rangle$ [296, 297]. The energies of the plasmon Hamiltonian form an equidistant ladder, schematically drawn for the three lowest plasmon number states $|n_{\mathrm{PL}}\rangle$, and contain a fine-structure of vibrational sub-levels.

In realistic systems, the cavity excitations and the vibrations also undergo decay, pumping and dephasing processes. We consider losses and thermal pumping in the dynamics of the system by solving the master equation for the density matrix, $\hat{\rho}$, (see Section 3.1.3) with incoherent damping introduced via the phenomenological Lindblad terms for the plasmon and the vibration:

$$\mathscr{L}_{\hat{a}}^{\gamma_a}[\hat{\rho}] = \frac{\gamma_a}{2}\left(2\hat{a}\hat{\rho}\hat{a}^{\dagger} - \left\{\hat{a}^{\dagger}\hat{a}, \hat{\rho}\right\}\right), \tag{7.7}$$

$$\mathscr{L}_{\hat{b}}^{\gamma_b}[\hat{\rho}] = [n_{\mathrm{vib}}(T) + 1]\frac{\gamma_b}{2}\left(2\hat{b}\hat{\rho}\hat{b}^{\dagger} - \left\{\hat{b}^{\dagger}\hat{b}, \hat{\rho}\right\}\right), \tag{7.8}$$

$$\mathscr{L}_{\hat{b}^{\dagger}}^{\gamma_b}[\hat{\rho}] = n_{\mathrm{vib}}(T)\frac{\gamma_b}{2}\left(2\hat{b}^{\dagger}\hat{\rho}\hat{b} - \left\{\hat{b}\hat{b}^{\dagger}\hat{\rho}\right\}\right), \tag{7.9}$$

where γ_b is the vibrational decay rate and γ_a the plasmonic one, respectively, and

$$n_{\mathrm{vib}}(T) = \frac{1}{\exp\left(\frac{\hbar\Omega}{k_{\mathrm{B}}T}\right) - 1} \tag{7.10}$$

is the thermal population of the molecule's vibrational mode at temperature T where k_{B} is the Boltzmann constant. We do not consider the thermal population of the plasmonic mode as usually $\hbar\omega_{\mathrm{c}} \gg k_{\mathrm{B}}T$.

7.1.1 Off-resonant SERS spectra

As an illustrative example, we apply the off-resonant SERS model to calculate a typical Raman emission spectrum of a molecule interacting with a plasmonic cavity. To that end we choose a broad plasmonic cavity, setting $\hbar\omega_{\mathrm{c}} = 2\,\mathrm{eV}$, $\hbar\gamma_a = 500\,\mathrm{meV}$ and $\hbar g_{\mathrm{om}} = 1\,\mathrm{meV}$ for the cavity, and $\hbar\Omega = 50\,\mathrm{meV}$. We assume that the cavity is illuminated by an incident monochromatic laser of frequency $\hbar\omega_{\mathrm{L}} = \hbar\omega_{\mathrm{c}} = 2\,\mathrm{eV}$ of amplitude $\mathcal{E} = 0.1\,\mathrm{meV}$, which represents weak illumination conditions under which the laser only mildly perturbs the equilibrium of the molecular excitations.

The Hamiltonian in Eq. (7.4) can be further manipulated to simplify the calculations. First, we bring the Hamiltonian $\hat{H}_{\mathrm{om}}$ into a form that does not contain any explicit time dependence by transforming it into the appropriate interaction picture as $\hat{H}_{\mathrm{om}} \to \hat{U}_{\omega_{\mathrm{L}}}\hat{H}_{\mathrm{om}}\hat{U}_{\omega_{\mathrm{L}}}^{\dagger} - \mathrm{i}\hbar\hat{U}_{\omega_{\mathrm{L}}}\dot{\hat{U}}_{\omega_{\mathrm{L}}}^{\dagger}$ with $\hat{U}_{\omega_{\mathrm{L}}} = \exp(\mathrm{i}\hat{a}^{\dagger}\hat{a}\omega_{\mathrm{L}}t)$. After that we redefine the plasmonic creation and annihilation operators:

$$\hat{a} \to \hat{a} + \alpha_{\mathrm{S}},$$
$$\hat{a}^{\dagger} \to \hat{a}^{\dagger} + \alpha_{\mathrm{S}}^{*},$$

where $\alpha_{\mathrm{S}} = \frac{-\mathcal{E}}{\Delta - \mathrm{i}\frac{\gamma_a}{2}}$. This choice of α_{S} leads to a new form of the Hamiltonian

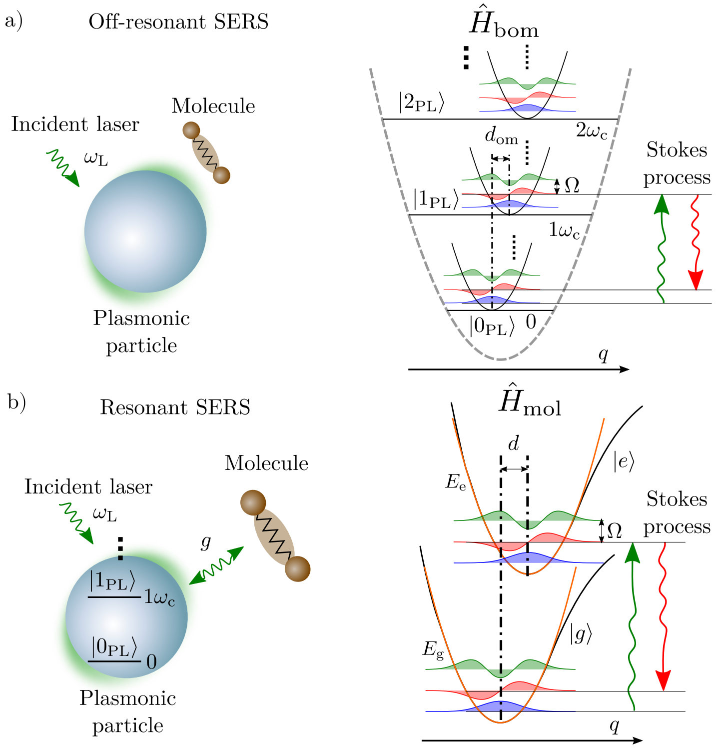

Figure 7.2: Schematics of (a) the off-resonant SERS process in a plasmonic particle and a vibrating molecule, and (b) the r-SERS process, both depicted with their corresponding level structure. (a) The plasmonic number states $|n_{\text{PL}}\rangle$ have equidistant energies $\hbar n_{\text{PL}}\omega_c$ (vertical axis) and vibrational fine-structure for each $|n_{\text{PL}}\rangle$. The vibrational parabolas are displaced by $n_{\text{PL}}d_{\text{om}}$ along the dimensionless normal coordinate q depending on the number of plasmonic excitations. (b) The r-SERS system consists of a plasmonic particle interacting with a molecule described by an electronic (two-level) and (bosonic) vibrational degrees of freedom: the potential energy surfaces (PES) for the vibrations of the ground electronic state, $|\text{g}|$, $E_{\text{g}}(q)$, and for those of the excited state, $|\text{e}\rangle$, $E_{\text{e}}(q)$, for the vibrations depend on the electronic states and are shifted with respect to the dimensionless normal coordinate q by a displacement d. The plasmon mode is excited by coherent laser illumination of frequency $\omega_L \approx \omega_c$.

$\hat{H}_{\mathrm{om}}$:

$$\hat{H}_{\mathrm{om}} = \hat{H}_{\mathrm{pl}} + \hat{H}_{\mathrm{pl-vib}} + \hat{H}_{\mathrm{vib}} \tag{7.11}$$

with

$$\begin{aligned} \hat{H}_{\mathrm{pl}} &= \hbar\Delta\hat{a}^\dagger\hat{a} \\ \hat{H}_{\mathrm{vib}} &= \hbar\Omega\hat{b}^\dagger\hat{b} \\ \hat{H}_{\mathrm{pl-vib}} &= -\hbar g_{\mathrm{om}}(\hat{a}^\dagger + \alpha_{\mathrm{S}}^*)(\hat{a} + \alpha_{\mathrm{S}})(\hat{b}^\dagger + \hat{b}), \end{aligned} \tag{7.12}$$

with $\Delta = \omega_{\mathrm{c}} - \omega_{\mathrm{L}}$. Under these transformations the Lindblad terms remain formally the same as in Eqs. (7.7) to (7.9). The optomechanical coupling Hamiltonian can be further simplified by assuming that $\langle\hat{a}\rangle_{\mathrm{SS}}$, evaluated in the steady state, is small ($\langle\hat{a}\rangle_{\mathrm{SS}} \ll 1$):

$$\hat{H}_{\mathrm{pl-vib}} = -\hbar g_{\mathrm{om}}(\hat{a}^\dagger + \alpha_{\mathrm{S}}^*)(\hat{a} + \alpha_{\mathrm{S}})(\hat{b}^\dagger + \hat{b}) \approx -\hbar g_{\mathrm{om}}(\alpha_{\mathrm{S}}^*\hat{a} + \alpha_{\mathrm{S}}\hat{a}^\dagger)(\hat{b}^\dagger + \hat{b}). \tag{7.13}$$

The approximated form of the optomechanical coupling Hamiltonian in Eq. (7.13) is nothing but a Rabi coupling term between the molecular vibrations and the cavity mode that is parametrically dependent on the amplitude of the driving laser via α_{S}.

Having simplified the Hamiltonian, we calculate the incoherent photon emission spectra of the cavity mode following the prescription of Section 3.3:

$$s_{\mathrm{e}}(\omega) = 2\mathrm{Re}\int_0^\infty \langle\langle\hat{a}^\dagger(0)\hat{a}(\tau)\rangle\rangle_{\mathrm{ss}}\, e^{\mathrm{i}\omega\tau}\mathrm{d}\,\tau, \tag{7.14}$$

where we use the notation $\langle\langle O_1O_2\rangle\rangle = \langle O_1O_2\rangle - \langle O_1\rangle_{\mathrm{SS}}\langle O_2\rangle_{\mathrm{SS}}$, where O_1 and O_2 are generic operators. This definition of the emission spectrum does not contain the coherent delta-peaked Rayleigh scattering at the frequency of the incident laser ω_{L}.

The resulting spectra normalized to their respective maximum values are plotted in Fig. 7.1 (c) for varying temperature T =0 K (red-dashed line), 300 K (blue line) and 2000 K (black line). The spectra are plotted as a function of frequency, normalized to the vibrational frequency Ω, and centred around ω_{L}. All the spectra exhibit a dominant Raman-Stokes peak at $\omega - \omega_{\mathrm{L}} = -\Omega$, which is apparent even for $T = 0$ K when the vibrational state is thermally unpopulated. As the temperature is increased and the vibrational thermal population, $n_{\mathrm{vib}}(T)$, appears, the Raman anti-Stokes peak becomes apparent in the spectrum. At room temperature ($T = 300$ K) the anti-Stokes peak is much weaker than the Stokes peak as the ratio of the two peak intensities is approximately $s_{\mathrm{e}}(-\Omega)/s_{\mathrm{e}}(\Omega) \approx [n_{\mathrm{vib}}(T) + 1]/n_{\mathrm{vib}}(T)$. For a rather high temperature of $T = 2000$ K, the Stokes and anti-Stokes peaks become comparable in magnitude as $n_{\mathrm{vib}}(T) + 1 \approx n_{\mathrm{vib}}(T)$. In the high-temperature limit the quantum model recovers the classical result that the Stokes and the anti-Stokes peaks should be equal in magnitude. Also, the increasing temperature results in a broadening of the emission peaks which follows from the dependence of the line broadening on the thermal population of the vibrations as $n_{\mathrm{vib}}(T)\gamma_b$.

7.1.2 Resonant SERS

We complete the previous picture of SERS by addressing the scenario where the frequency of the incident laser approaches the molecular electronic resonance. In r-SERS we describe the molecule as a TLS, composed of a ground, $|\mathrm{g}\rangle$, and an excited, $|\mathrm{e}\rangle$, electronic state, that interacts with the vibrational modes via a polaronic coupling term [81, 82, 274, 294, 298], and with the plasmonic cavity via the Jaynes-Cummings coupling term [see Fig. 7.2 (b)]. The molecular vibrations are modelled as bosons within the Born-Oppenheimer approximation, where the effective harmonic vibrational potential is given by the ground state $[E_{\mathrm{g}}(q)]$ and the excited state $[E_{\mathrm{e}}(q)]$ potential energy surfaces (PESs) along a normal vibrational coordinate q, respectively [77, 78, 156, 157]. We consider that the vibrational energies of the molecule, $\hbar\Omega$, are the same for the ground and for the excited state. The Hamiltonian describing the molecular vibrational end electronic excitations [see Eq. (2.44) in Section 2.3] thus simplifies to

$$\hat{H}_{\mathrm{mol}} = |\mathrm{g}\rangle\langle\mathrm{g}|(E_{\mathrm{e}} + \hbar\Omega\hat{b}^{\dagger}_{\mathrm{g}}\hat{b}_{\mathrm{g}}) + |\mathrm{e}\rangle\langle\mathrm{e}|(E_{\mathrm{e}} + \hbar\Omega\hat{b}^{\dagger}_{\mathrm{e}}\hat{b}_{\mathrm{e}}). \tag{7.15}$$

We further consider that the vibrations in the excited state are displaced with respect to the ground-state vibrations as $\hat{b}_{\mathrm{e}} \to \hat{b}_{\mathrm{g}} + d$ and define $\hat{b}_{\mathrm{g}} \equiv \hat{b}$. The parameter d is the dimensionless displacement between the minima of the ground and excited state PESs, which is related to the Huang-Rhys factor [81, 82, 156, 157, 299], S, as $S = d^2$, and is a measure of the coupling between the molecular vibration and the excitonic transition.

The polaronic Hamiltonian of the r-SERS system, $\hat{H}^{\mathrm{res}}_{\mathrm{om}}$, using the rotating wave approximation, can be thus expressed as [294, 299–301]:

$$\boxed{\hat{H}^{\mathrm{res}}_{\mathrm{om}} = \hat{H}_{\mathrm{pl}} + \hat{H}_{\mathrm{mol}} + \hat{H}_{\mathrm{pump}} + \hat{H}_{\mathrm{pl-e}},} \tag{7.16}$$

with

$$\boxed{\begin{aligned} \hat{H}_{\mathrm{mol}} =& [E_{\mathrm{e}} - E_{\mathrm{g}}]\hat{\sigma}^{\dagger}\hat{\sigma} \\ &+ \hbar\Omega(\hat{b}^{\dagger} + \hat{\sigma}_{\mathrm{e}}d)(\hat{b} + \hat{\sigma}_{\mathrm{e}}d), \\ \hat{H}_{\mathrm{pl-e}} =& \hbar g\hat{a}\hat{\sigma}^{\dagger} + \hbar g^{*}\hat{a}^{\dagger}\hat{\sigma} \end{aligned}} \tag{7.17}$$

with $\hat{H}_{\mathrm{pl}}$ and $\hat{H}_{\mathrm{pump}}$ as defined in Eq. (7.4). Here the operator $\hat{\sigma} = |\mathrm{g}\rangle\langle\mathrm{e}|$ ($\hat{\sigma}^{\dagger} = |\mathrm{e}\rangle\langle\mathrm{g}|$) is the lowering (raising) operator of the TLS, with $\hat{\sigma}_{\mathrm{e}} = \hat{\sigma}^{\dagger}\hat{\sigma}$ the TLS number operator. The interaction of the localized plasmon excitation and the molecular electronic levels is mediated by the coupling constant g.

The level diagram describing the r-SERS Hamiltonian $\hat{H}^{\mathrm{res}}_{\mathrm{om}}$ [Eq. (7.16)] is sketched in Fig. 7.2 (b). Strikingly, both the off-resonant Hamiltonian, $\hat{H}_{\mathrm{bom}}$, and the molecular Hamiltonian in r-SERS, $\hat{H}_{\mathrm{mol}}$, can be represented as a series of mutually displaced harmonic vibrational PESs. The electronic states in r-SERS thus play the role of the plasmon number states in the off-resonant case, an analogy which can be identified from the comparison of the Hamiltonians in Eqs. (7.17) and (7.6). In the limit of single-photon optomechanics [296, 297, 302], where the plasmon Hilbert space is spanned by the vacuum state and the singly excited state, the molecular Hamitonian $\hat{H}_{\mathrm{mol}}$ and $\hat{H}_{\mathrm{bom}}$ become formally identical. However, as we detail later, if the incident laser is strong, the non-linear character of the excitonic TLS Hamiltonian [Eq. (7.17)] leads to novel physical phenomena which cannot be achieved in the off-resonant SERS situation [Eq. (7.6)].

Finally, as in the off-resonant case, we can introduce incoherent processes into the dynamics of the cavity and molecule excitations via the Lindblad terms. On top of the terms introduced in Eqs. (7.7)-(7.9), we consider the decay of the molecule's electronic excitation via

$$\mathscr{L}_{\hat{\sigma}}^{\gamma_\sigma}[\hat{\rho}] = \frac{\gamma_\sigma}{2}\left(2\hat{\sigma}\hat{\rho}\hat{\sigma}^\dagger - \left\{\hat{\sigma}^\dagger\hat{\sigma}, \hat{\rho}\right\}\right), \tag{7.18}$$

where γ_σ is the electronic decay rate.

Assuming that the cavity interacts with the molecular electronic transition in the weak-coupling regime, we further include into the model the pure dephasing of the molecular electronic excitations in the form of a Lindblad term [158, 234, 303], as:

$$\mathscr{L}_{\hat{\sigma}_z/2}^{\gamma_\phi}(\hat{\rho}) = \frac{\gamma_\phi}{4}\left(2\hat{\sigma}_z\hat{\rho}\hat{\sigma}_z^\dagger - \{\hat{\sigma}_z^\dagger\hat{\sigma}_z, \hat{\rho}\}\right), \tag{7.19}$$

with $\hat{\sigma}_z = \hat{\sigma}^\dagger\hat{\sigma} - \hat{\sigma}\hat{\sigma}^\dagger$.

7.2 r-SERS in the plasmon-exciton weak coupling regime

As already discussed in Section 5.1.3, the decay of state-of-the-art plasmonic cavities γ_a is ultimately limited by the material properties of the metal [72, 227–230]. In plasmonic systems commonly reaches small quality factors, $Q = \omega_{\mathrm{c}}/\gamma_a$, in the range of $Q \approx 1 - 20$. As an example of a representative generic plasmonic resonator, we consider in this chapter a plasmonic cavity of energy $\hbar\omega_{\mathrm{c}} = 2\,\mathrm{eV}$ and broadening $\hbar\gamma_a = 500\,\mathrm{meV}$. Such parameters can represent, for instance, the leaky gap mode formed between a tip of a scanning tunnelling microscope and a metallic substrate, often used for single-molecule spectroscopy [52–56], and regarded as an example of a low-Q plasmonic cavity.

On the other hand, a typical decay rate of molecular excitations decoupled from the plasmonic cavity is usually much smaller than that of plasmons (as small as $\hbar\gamma_\sigma \sim 10^{-2}$ meV $\ll \gamma_a$). The line width of the molecular resonance is thus mostly limited by the pure dephasing γ_ϕ which strongly scales with temperature and is highly dependent on the environment surrounding the molecule (see Chapter 6 for a study of this aspect in molecular fluorescence). It is thus possible to engineer the conditions (low temperature vacuum experiment) under which pure dephasing becomes small and the line width of the molecular electronic excitation decreases below $< 10\,\mathrm{meV}$ and may even be limited only by the spontaneous decay. In this chapter we thus describe the molecule using the parameters $E_\mathrm{e} - E_\mathrm{g} = 2\,\mathrm{eV}$, $\hbar\gamma_\sigma = 0.02\,\mathrm{meV}$ and vary the value of the molecule's pure dephasing γ_ϕ.

We consider the bad cavity limit (or weak coupling if $\gamma_\phi > g$) where the plasmon-exciton coupling g is small compared to the plasmonic losses $\hbar\gamma_a$ but large with respect to the intrinsic decay γ_σ ($\gamma_\sigma \ll g \ll \gamma_a$). In particular, in this chapter we use two different values of relatively large coupling strengths between the plasmon and the molecular TLS ($\hbar g =$13 meV and $\hbar g =$50 meV), although still small enough to be in the bad cavity limit [63, 238]. These two selected values allow us to explore different regimes of plasmon-assisted interaction between molecular excitons and vibrations, as we detail below.

In the bad cavity limit, the parameter determining the regime of the off-resonant optomechanical coupling, d_om, and that defining the exciton-vibration coupling, d, in the resonant model, formally describe the same physical phenomena under weak-illumination conditions. In off-resonant SERS, the condition $|d_\mathrm{om}\Omega| > \gamma_a/2$ sets the so-called optomechanical strong coupling when the optomechanical non-linearity $-\Omega d_\mathrm{om}^2 \hat{a}^\dagger \hat{a}$ becomes relevant and the system thus becomes interesting for quantum applications. It has been estimated that $d_\mathrm{om} \sim 10^{-1}$ in most molecular species [101].

On the other hand, in r-SERS, for relevant dye molecules with electronic excitations in the visible, d ranges from $d \sim 10^{-1}$ for rigid molecules (such as porphyrines [304]) up to values of $d \sim 1$ for soft organic molecules [82, 305]. r-SERS might thus offer relatively high optomechanical coupling strengths even for a single organic molecule. Moreover, for small molecular dephasing, the broadening of the excitonic resonance, $\gamma_\sigma^\mathrm{tot} \approx \gamma_\sigma + \gamma_\phi + \Gamma_\mathrm{eff}$, containing the effects of pure dephasing but also other broadening mechanisms such as the Purcell effect due to the coupling to the plasmon (Γ_eff), becomes much smaller than the plasmon line width ($\gamma_\sigma^\mathrm{tot}/2 \ll \gamma_a/2$) and r-SERS may open the possibility to achieve large optomechanical coupling compared to the relevant line width: $|d\Omega| > \gamma_\sigma^\mathrm{tot}/2$ (strong optomechanical coupling).

In the following we describe the inelastic emission spectra and vibrational pumping in r-SERS for (i) the linear response regime (relatively weak laser illumination) and (ii) strong laser illumination where the molecular levels are dressed by the intense laser field and form a qualitatively new set of light-matter states.

7.2.1 Photon emission spectra in the linear regime of r-SERS

We first discuss the spectral response and the physics of hybrid-optomechanical vibrational pumping in r-SERS systems in the limit of weak incident laser intensities, for which the system can be treated within the linear-response theory (further denoted as *weak illumination*).

For convenience, we define the detuning parameters $\Delta = \omega_{\mathrm{c}} - \omega_{\mathrm{L}}$ and $\delta = \omega_{\mathrm{eg}} - \omega_{\mathrm{L}}$ (with the exciton frequency $\omega_{\mathrm{eg}} = [E_{\mathrm{e}} - E_{\mathrm{g}}]/\hbar$) and define the coherent amplitude of the plasmon annihilation operator induced by the incident monochromatic illumination $\alpha_{\mathrm{S}} = \frac{-\mathcal{E}}{\Delta - \mathrm{i}\gamma_a/2}$. We perform a similar set of transformations as performed for off-resonant SERS in Section 7.1.1. The solution of the dynamics of the hybrid optomechanical Hamiltonian and the respective Lindblad terms with the parameters described above allow for calculating the emission spectrum in such a system from the quantum regression theorem (QRT):

$$s_{\mathrm{e}}(\omega) = 2\mathrm{Re}\int_0^{\infty} \langle\langle \hat{a}^{\dagger}(0)\hat{a}(\tau)\rangle\rangle_{\mathrm{ss}}\, e^{\mathrm{i}\omega\tau}\mathrm{d}\,\tau.$$

As before, we remove the elastic scattering contribution from the spectrum.

To illustrate the emission properties of typical molecules we plot in Fig. 7.3 (a) the inelastic spectra in a r-SERS system [normalized to $s_{\mathrm{e}}(\omega_{\mathrm{eg}})$ and vertically shifted], calculated for weak illumination, $\hbar\mathcal{E} = 0.01\,\mathrm{meV}$, of a monochromatic laser of frequency $\hbar\omega_{\mathrm{L}} = 1.975\,\mathrm{eV}$ (green dashed line) and exciton-plasmon coupling $\hbar g = 13\,\mathrm{meV}$. The excitonic energy is $\hbar\omega_{\mathrm{eg}} = 2\,\mathrm{eV}$. We calculate the spectra for two large values of $d = 1,\ 0.5$ (top spectra) representing soft organic molecules and for a small value of $d = 0.1$ corresponding to a rigid molecule (two bottom spectra). We choose $\hbar\gamma_{\phi} = 20\,\mathrm{meV}$ for the three top spectra to demonstrate the effect of pure dephasing on the emission of molecules interacting with a decoherence-inducing environment. In the bottom spectrum no dephasing is considered, $\hbar\gamma_{\phi} = 0\,\mathrm{eV}$.

The bottom spectrum in Fig. 7.3 (a), calculated for weak exciton-vibration coupling, $d = 0.1$, and considering an absence of pure dephasing ($\hbar\gamma_{\phi} = 0\,\mathrm{meV}$), features two sharp emission peaks. The fluorescence peak appears at frequency $\omega = \omega_{\mathrm{eg}}$ regardless of the incident laser frequency. The second peak, appearing at $\omega = \omega_{\mathrm{L}} - \Omega$, is the Raman-Stokes emission line. The anti-Stokes line is not visible because the vibrations are not populated for $T = 0\,\mathrm{K}$. The Raman (SERS) line always appears at a constant detuning from the laser frequency which facilitates its identification in the spectrum. When the pure dephasing is increased, the fluorescence line starts to broaden and increase in intensity [note that the spectra are normalized in Fig. 7.3 (a)]. The SERS emission becomes hardly distinguishable on top of the strong fluorescence background for $d = 0.1$. As d increases, the fluorescence background becomes asymmetrical and broadens towards lower energies due to radiative transitions allowed by a simultaneous exchange of energy between electronic and vibrational states (*hot luminescence*). This so-called vibrational progression of the luminescence spectrum thus consists of a series of broad peaks, each peak positioned at frequency $\omega_{\mathrm{eg}} - n\Omega$ (with n a positive integer), with its amplitude determined by the overlap of the vibrational wave functions in the electronic ground and excited states, respectively (Franck-Condon factors) [156, 157, 296, 297, 302]. The Raman-Stokes lines appear on top of the fluorescence peaks at frequencies $\omega_{\mathrm{L}} - n\Omega$. The strength of the Raman lines

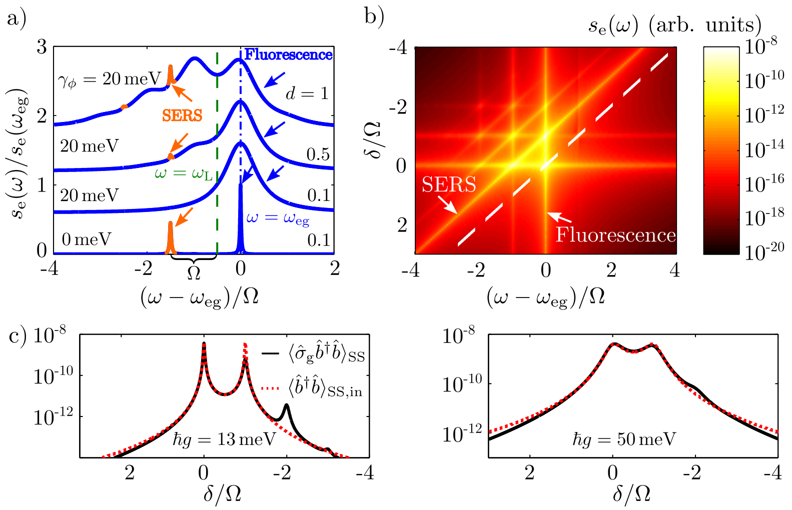

Figure 7.3: Inelastic emission spectra and vibrational populations of a r-SERS process where the molecular exciton is weakly coupled to the plasmon. (a) Normalized inelastic emission spectra $s_e(\omega)/s_e(\omega_{eg})$ for different values of pure dephasing γ_ϕ (for the three top spectra $\hbar\gamma_\phi = 20\,\mathrm{meV}$, for the bottom spectrum $\hbar\gamma_\phi = 0\,\mathrm{meV}$) and dimensionless displacement d (from the top: $d = 1$, 0.5, 0.1, 0.1). The blue dash-dotted line indicates the position of ω_{eg} and the green dashed line marks the excitation frequency ω_L. The spectra are vertically shifted for clarity. The vibrational frequency is $\hbar\Omega = 50\,\mathrm{meV}$. (b) Inelastic emission spectra as a function of detuning $\delta = \omega_{eg} - \omega_L$ of the incident laser frequency ω_L from the exciton frequency ω_{eg}. The white dashed line marks the laser frequency in each emission spectrum. In (a,b) $\hbar g = 13\,\mathrm{meV}$. (c) Population of the vibrational mode in the ground electronic state calculated numerically, $\langle\hat{\sigma}_g\hat{b}^\dagger\hat{b}\rangle_{SS}$ (black line), and an effective incoherent vibrational population calculated analytically, $\langle\hat{b}^\dagger\hat{b}\rangle_{SS,in}$ (red dashed line), as a function of laser detuning δ for illumination amplitude $\hbar\mathcal{E} = 0.01\,\mathrm{meV}$ and different values of plasmon-exciton coupling g. In the left panel $\hbar g = 13\,\mathrm{meV}$, and the molecule effective broadening Γ_{eff} due to the Purcell effect is similar to the line-width of the vibrational Raman lines γ_b. In the right panel $\hbar g = 50\,\mathrm{meV}$, a larger value of plasmon-exciton coupling that ensures $\Gamma_{\mathrm{eff}} > \gamma_b$.

is determined from a combination of the Franck-Condon overlaps, as in the case of the *hot luminescence*, and is further enhanced due to the proximity of the molecular electronic resonance that (i) enhances the interaction of the incident laser with the molecular transition and (ii) boosts the efficiency of the Raman-Stokes emission. The Raman peaks are also notably narrower than the fluorescence peaks when dephasing is large ($\hbar\gamma_\phi = 20$ meV), which facilitates their identification on top of the broad and intense fluorescence background.

The difference between the physical origin of the r-SERS lines and the fluorescence lines becomes clearer if we plot the emission spectra as a function of the laser detuning from the exciton frequency, $\delta = \omega_{eg} - \omega_L$. The emission spectra are shown in Fig. 7.3 (b) for a rigid molecule ($d = 0.1$) with no dephasing, similar to the bottom spectrum in Fig. 7.3 (a). The molecule is pumped by an incident laser of amplitude $\hbar\mathcal{E} = 1 \times 10^{-2}$ meV and we consider a smaller exciton-plasmon coupling, $\hbar g = 13$ meV. The incident laser frequency is marked in the spectra as a white dashed line diagonally crossing the color plot. The color plot with the spectra shows both the Raman-Stokes peaks that appear red-detuned from the incident-laser frequency ω_{L} by $n\Omega$ (diagonal bright lines), and the fluorescence peaks emerging at the energy of the excitonic transition regardless of δ (vertical bright lines).

Furthermore, the emission shown in Fig. 7.3 (b) is enhanced when $\hbar\delta = 0$ eV or $\hbar\delta = -\hbar\Omega = -50$ meV at the frequency of the first-order Raman-Stokes line, $\omega = \omega_{\mathrm{L}} - \Omega$. When the laser frequency is tuned to the molecular exciton (with $\hbar\delta = 0$ eV), the incident laser coherently (coherent population $n_\sigma^{\mathrm{coh}} = |\langle\hat{\sigma}\rangle_{\mathrm{SS}}|^2$) and incoherently (incoherent population $n_\sigma^{\mathrm{incoh}} = \langle\hat{\sigma}^\dagger\hat{\sigma}\rangle_{\mathrm{SS}} - |\langle\hat{\sigma}\rangle_{\mathrm{SS}}|^2$) populates the electronic excited state. Thereafter, the molecule efficiently emits both the Raman-Stokes ($\propto n_\sigma^{\mathrm{coh}}$) and the hot luminescence ($\propto n_\sigma^{\mathrm{incoh}}$) photons at $\omega = \omega_{\mathrm{eg}} - \Omega$. On the other hand, when $\hbar\delta = -\hbar\Omega = -50$ meV, the spectral position of the Raman-Stokes line coincides with the resonance frequency of the molecular exciton. In this case, the molecular fluorescence, now spectrally coinciding with the Raman-Stokes line, is suppressed as the molecule is not pumped resonantly. The off-resonance illumination does not efficiently populate the excited electronic state in this case and the emission peak appears mainly due to the SERS mechanism. Both mechanisms of SERS enhancement are closely related to the process of optomechanical vibrational pumping, as described for the off-resonant case [101–104].

Finally we remark that the spectral map in Fig. 7.3 (b) also features lines appearing due to higher-order Raman scattering and *hot luminescence*. These lines show much lower intensity than the lines of lower orders discussed above, but they exhibit the same mechanism of emission enhancement, as it is apparent from the spectral map.

7.2.2 Optomechanical vibrational pumping in the linear regime

Numerical calculations

Inasmuch as the emission of Raman-Stokes photons is accompanied by the creation of a vibrational quantum, the enhanced Raman-Stokes emission can be monitored through the steady-state vibrational population of the electronic ground state $\langle\hat{\sigma}_{\mathrm{g}}\hat{b}^\dagger\hat{b}\rangle_{\mathrm{SS}}$ ($\hat{\sigma}_{\mathrm{g}} = |\mathrm{g}\rangle\langle\mathrm{g}|$). To elucidate the role of Raman-Stokes scattering in the process of vibrational pumping of r-SERS, we plot in Fig. 7.3 (c) the vibrational population of the electronic ground state as a function of incident laser detuning for two values of plasmon-exciton coupling (black lines). The panel to the left corresponds to $\hbar g = \hbar\sqrt{\gamma_b\gamma_a/6} \approx 13$ meV, for which the broadening of the electronic resonance due to the plasmonic Purcell effect Γ_{eff} (see also Section 5.1.1),

$$\Gamma_{\text{eff}} \approx \frac{g^2\gamma_a}{\left[\left(\frac{\gamma_a}{2}\right)^2 + (\delta-\Delta)^2\right]}, \tag{7.20}$$

becomes comparable to the broadening of the vibrational line, γ_b, and in the panel to the right we use $\hbar g = 50\,\text{meV}$, ensuring that $\Gamma_{\text{eff}} > \gamma_b$ (with $\Gamma_{\text{eff}} = 20\,\text{meV}$). In the calculations we set $\hbar\mathcal{E} = 0.01\,\text{meV}$ to make sure that we stay in the linear regime. The numerically calculated values of $\langle\hat{\sigma}_{\text{g}}\hat{b}^\dagger\hat{b}\rangle_{\text{SS}}$ (black lines) are qualitatively similar in both cases. A set of peaks are clearly observed which correspond to the enhancement of the Raman-Stokes emission for detunings of $\hbar\delta = 0\,\text{eV}$, $\hbar\delta = -\hbar\Omega = -50\,\text{meV}$, and higher orders ($\delta = -n\Omega$, $n > 1$), respectively. The effect of a larger plasmon-exciton coupling g (right panel) is to broaden the peaks and to smear off the maxima of the populations associated with the enhancement of higher-order Raman-Stokes emission ($\delta = -n\Omega$, $n > 1$).

Analytical approximation

To shed light on the mechanism of the vibrational pumping in r-SERS, we derive the effective vibrational dynamics which results from the elimination of the plasmon and the TLS dynamics, following standard methods from the theory of open quantum systems [158], in close analogy with the procedure developed in hybrid quantum optomechanics [301]. Upon elimination of the plasmon, the effective reduced TLS-vibrational Hamiltonian, $\hat{H}_{\text{red}}$, becomes

$$\hat{H}_{\text{red}} = \hbar\delta\hat{\sigma}^\dagger\hat{\sigma} - \hbar\frac{1}{2}\mathcal{E}_{\text{pl}}\hat{\sigma}_x + \hbar\Omega(\hat{b}^\dagger + \hat{\sigma}_{\text{e}}d)(\hat{b} + \hat{\sigma}_{\text{e}}d), \tag{7.21}$$

where $\mathcal{E}_{\text{pl}} = -2g\alpha_{\text{S}}$ (with $\alpha_{\text{S}} = \frac{-\mathcal{E}}{\Delta - \text{i}\frac{\gamma_a}{2}}$) is the coherent coupling of the molecule mediated by the plasmon, $\hat{\sigma}_x$ is the Pauli x operator and $\hat{\sigma}_{\text{e}} = \hat{\sigma}^\dagger\hat{\sigma}$. Moreover, in the bad cavity limit, the molecular excitonic TLS is effectively broadened due to the plasmon via the Purcell effect. The total TLS decay rate thus becomes $\gamma_\sigma \to \Gamma_{\text{tot}} = \Gamma_{\text{eff}} + \gamma_\sigma$.

By further eliminating the TLS from the vibrational dynamics, by assuming $|d\Omega| \ll \Gamma_{\text{tot}}$, we obtain an effective vibrational Hamiltonian that includes the coherent pumping due to the TLS excited-state population

$$\hat{H}^{\text{red}}_{\text{vib}} = \hbar\Omega\hat{b}^\dagger\hat{b} + \hbar d\Omega\langle\hat{\sigma}_{\text{e}}\rangle_{\text{SS}}(\hat{b}^\dagger + \hat{b}), \tag{7.22}$$

together with the effective incoherent damping $\Gamma_{\text{v}}^{\text{dec}}$ and pumping $\Gamma_{\text{v}}^{\text{pump}}$ rates, which need to be added to the intrinsic vibrational dissipation rate (described by the original Lindblad term) via new Lindblad terms:

$$\mathscr{L}_{\hat{b}}^{\Gamma_{\text{v}}^{\text{dec}}}[\hat{\rho}] = \frac{\Gamma_{\text{v}}^{\text{dec}}}{2}\left(2\hat{b}\hat{\rho}\hat{b}^\dagger - \left\{\hat{b}^\dagger\hat{b}, \hat{\rho}\right\}\right) \tag{7.23}$$

for the effective damping, and

$$\mathscr{L}_{\hat{b}^\dagger}^{\Gamma_{\mathrm{v}}^{\mathrm{pump}}}[\hat{\rho}] = \frac{\Gamma_{\mathrm{v}}^{\mathrm{pump}}}{2}\left(2\hat{b}^\dagger\hat{\rho}\hat{b} - \left\{\hat{b}\hat{b}^\dagger, \hat{\rho}\right\}\right) \tag{7.24}$$

for the effective pumping. These rates are defined as $\Gamma_{\mathrm{v}}^{\mathrm{dec}} = 2\left(\Omega d\right)^2 \mathrm{Re}\{\tilde{S}(\Omega)\}$ and $\Gamma_{\mathrm{v}}^{\mathrm{pump}} = 2\left(\Omega d\right)^2 \mathrm{Re}\{\tilde{S}(-\Omega)\}$, respectively, where $\mathrm{Re}\{\cdot\}$ indicates the real part, and

$$\tilde{S}(s) = \int_0^\infty \langle\langle \hat{\sigma}_{\mathrm{e}}(\tau)\hat{\sigma}_{\mathrm{e}}(0)\rangle\rangle e^{\mathrm{i}s\tau}\mathrm{d}\tau \tag{7.25}$$

is the spectral function corresponding to the one-sided Fourier transform of the correlation function of the TLS for a generic frequency s, calculated for the TLS decoupled from the vibrations (details about the analytical calculation of $\tilde{S}(s)$ are provided in Appendix F). Finally, the incoherent steady-state vibrational population, $\langle\hat{b}^\dagger\hat{b}\rangle_{\mathrm{SS,in}}$, induced by the effective pumping of the vibrations via the TLS becomes in this approximation:

$$\begin{aligned}\langle\hat{b}^\dagger\hat{b}\rangle_{\mathrm{SS,in}} &= \frac{\Gamma_{\mathrm{v}}^{\mathrm{pump}}}{\gamma_b + \Gamma_{\mathrm{v}}^{\mathrm{dec}} - \Gamma_{\mathrm{v}}^{\mathrm{pump}}} \\ &\approx \frac{\Gamma_{\mathrm{v}}^{\mathrm{pump}}}{\gamma_b} \propto \mathrm{Re}\{\tilde{S}(-\Omega)\},\end{aligned} \tag{7.26}$$

where the last approximation assumes that under weak pumping $\gamma_b \gg \Gamma_{\mathrm{v}}^{\mathrm{dec}} - \Gamma_{\mathrm{v}}^{\mathrm{pump}}$. We note that in the linear regime $\langle\hat{b}^\dagger\hat{b}\rangle_{\mathrm{SS,in}} \approx \langle\hat{\sigma}_{\mathrm{g}}\hat{b}^\dagger\hat{b}\rangle_{\mathrm{SS,in}}$ which allows for direct comparison of the vibrational population calculated numerically and the one obtained analytically. From Eq. (7.26) it follows that the behavior of the spectral function $\tilde{S}(-\Omega;\delta)$ as a function of the incident laser frequency (i.e. δ) determines the conditions for which the vibrational pumping occurs. In the linear regime we can simplify the expression for $\mathrm{Re}\{\tilde{S}(-\Omega)\}$, in exact analogy with the off-resonant model [101–104]:

$$\begin{aligned}\mathrm{Re}\{\tilde{S}(-\Omega)\} &= \mathrm{Re}\left\{\int_0^\infty \langle\langle\hat{\sigma}_{\mathrm{e}}(\tau)\hat{\sigma}_{\mathrm{e}}(0)\rangle\rangle e^{-\mathrm{i}\Omega\tau}\mathrm{d}\tau\right\} \\ &\approx |\langle\hat{\sigma}\rangle_{\mathrm{SS}}|^2\mathrm{Re}\left\{\int_0^\infty \langle\langle\hat{\sigma}(\tau)\hat{\sigma}^\dagger(0)\rangle\rangle e^{-\mathrm{i}(\Omega-\omega_{\mathrm{L}})\tau}\mathrm{d}\tau\right\} \\ &\approx \underbrace{\frac{|\mathcal{E}_{\mathrm{pl}}|^2}{4(\delta^2+(\Gamma_{\mathrm{tot}}/2)^2)}}_{\tilde{S}^{\mathrm{R}}_{\mathrm{coh}}}\underbrace{\frac{\Gamma_{\mathrm{tot}}/2}{(\delta+\Omega)^2+(\Gamma_{\mathrm{tot}}/2)^2}}_{\tilde{S}^{\mathrm{R}}_{\mathrm{incoh}}}.\end{aligned} \tag{7.27}$$

The two terms,

$$\tilde{S}^{\mathrm{R}}_{\mathrm{coh}} \approx |\langle\hat{\sigma}\rangle_{\mathrm{SS}}|^2 \tag{7.28}$$

and

$$\tilde{S}^{\mathrm{R}}_{\mathrm{incoh}} \approx \mathrm{Re}\left\{\int_0^\infty \langle\langle\hat{\sigma}(\tau)\hat{\sigma}^\dagger(0)\rangle\rangle e^{-\mathrm{i}(\Omega-\omega_{\mathrm{L}})\tau}\mathrm{d}\tau\right\}, \tag{7.29}$$

can then be interpreted as the efficiency of the coherent driving ($\tilde{S}^{\mathrm{R}}_{\mathrm{coh}}$ resonant at $\delta = 0$) and the efficiency of the spontaneous Stokes-Raman emission ($\tilde{S}^{\mathrm{R}}_{\mathrm{incoh}}$ resonant at $\delta = -\Omega$), respectively.

The effective vibrational dynamics and its steady-state values derived in this section are an accurate approximation to the exact problem only if the decay rate, Γ_{tot}, of the dressed TLS is significantly larger than the intrinsic vibrational decay rate γ_b, and the exciton-vibration coupling is weak (moderate values of d). Some experimental situations in molecular spectroscopy might not satisfy these conditions. In such a case it is necessary to adopt a numerical treatment to obtain accurate results. Nevertheless, the properties of the TLS spectral function reveal the origin of the vibrational population associated with the pumping even beyond the limits of validity of the analytical-model.

We plot the analytical result for the evolution of the vibrational populations $\langle\hat{b}^\dagger\hat{b}\rangle_{\mathrm{SS,in}}$ as a function of detuning δ as a red dotted line in Fig. 7.3 (c). These analytical vibrational populations share with their numerically calculated counterparts (black lines) the same dominant peaks, i.e. peaks appearing for zero laser detuning from the exciton frequency, $\delta = 0$, and for detuning $\delta = -\Omega$, when the frequency of the first-order Raman-Stokes line coincides with the excitonic frequency. These two values of the laser detuning also lead to an enhancement of the Raman-Stokes emission [Fig. 7.3 (b)], i.e. creation of cavity photons, which gives rise to the optomechanical vibrational pumping.

Although the analytical model nicely describes the main features of the fully numerically calculated vibrational populations, it cannot explain the presence of the weaker higher-order peaks. This is due to the Markov approximation leading to (7.22), (7.23) and (7.24) which treats the exciton-vibration interaction perturbatively. In the full model, the vibrational pumping mechanism is present even for the vibrational transitions responsible for higher-order Raman scattering and hot luminescence. Moreover, in the case that $\hbar g = 13\,\mathrm{meV}$, the analytical model overestimates the vibrational populations induced by the optomechanical amplification for $\hbar\delta = -\hbar\Omega = -50\,\mathrm{meV}$, since the effective broadening of the TLS, $\Gamma_{\mathrm{tot}} = \Gamma_{\mathrm{eff}} + \gamma_\sigma$, is similar to the vibrational broadening γ_b, and the Markov approximation becomes less accurate in such situations. For $\hbar g = 50\,\mathrm{meV}$, the effective broadening $\Gamma_{\mathrm{tot}} > \gamma_b$ and the analytical model describes the low-order features of the vibrational populations accurately.

7.2.3 Photon emission spectra for strong laser intensities

Let us explore in the following the regime where the system is illuminated by a strong power incident laser, which induces the non-linear response of the molecule, and thus requires a treatment beyond the standard optomechanical description.

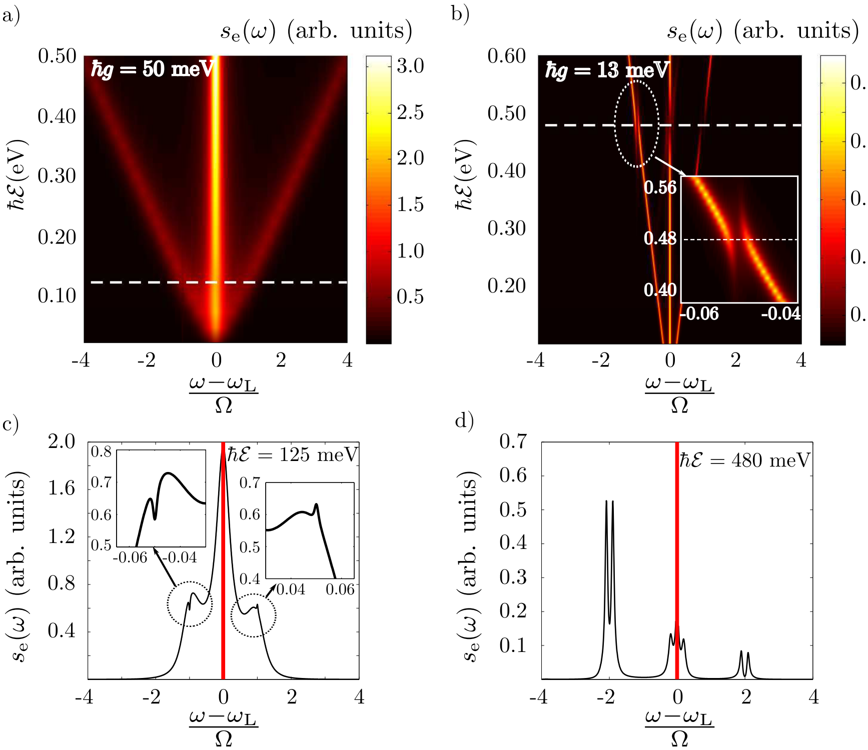

Figure 7.4: (a,b) Photon emission spectra of a plasmon coupled to molecular electronic and vibrational excitations as a function of incident laser amplitude $\mathcal{E}$, for $d = 0.1$. The molecule is coupled to the plasmonic cavity with (a) $\hbar g = 50$ meV and (b) $\hbar g = \hbar\sqrt{\gamma_b\gamma_a/6} \approx 13$ meV. The inset in (b) shows a detail of the peak splitting due to the hybridization of the Mollow triplet side peak and the Raman line. (c,d) Cuts of the spectral map shown in (a,b) along the white dashed lines, corresponding to (c) $\hbar\mathcal{E} = 125$ meV and (d) $\hbar\mathcal{E} = 480$ meV. The red lines indicate the position of the elastic Rayleigh peak, not included in the emission spectra.

The influence of the incident laser amplitude $\mathcal{E}$ is shown in Fig. 7.4 (a,b), where color maps of the emission spectra are displayed as a function of $\mathcal{E}$. The incident laser frequency is tuned to the TLS electronic transition, and we consider the results for $d = 0.1$, which show the well-known Mollow triplet, a spectral structure resulting from the resonance fluorescence (RF) of the dressed TLS [290, 291, 306–309]. The Mollow triplet consists of a strong emission line centered at the incident laser frequency and two side spectral peaks of similar spectral width that shift away as the laser intensity is increased [Figs. 7.4 (a) and (b)]. At a specific pumping amplitude $\mathcal{E}$ [white dashed lines in Fig. 7.4 (a) and (b)], the detuning of the Mollow triplet side peaks matches the vibrational frequency $\pm\Omega$ of the molecule and thus coherent effects emerge due to the interaction between the electronic RF and the vibrational Raman scattering. The visibility and nature of these effects depends on the width of the lines, which is dominated by the Purcell effect and hence on the coupling g. We thus consider again the two representative situations of interaction analysed in this chapter: (i) $\hbar g = 50$ meV, where the electronic peak is spectrally broader than the vibrational line, as the Purcell factor strongly broadens the former [Figs. 7.4 (a), (c)], and (ii) $\hbar g = 13$ meV, a situation where the broadening of the electronic peaks is approximately equal to the vibrational broadening [Figs. 7.4 (b), (d)].

For clarity, the emission spectra for the selected values of $\mathcal{E}$ that provide the matching ($\hbar\mathcal{E}$ =125 meV for $\hbar g$ =50 meV, and $\hbar\mathcal{E}$ =480 meV for $\hbar g \approx 13$ meV) are shown in Fig. 7.4 (c) and (d), respectively. When the RF peak is much broader than the width of the Raman line [Fig. 7.4 (c)], the interference results in small but sharp features that might be detectable in experimental spectra and remind of Fano-resonances[191]. On the other hand, when the linewidth of the RF is similar to the linewidth of the Raman lines, the two spectral lines exhibit a clear anticrossing [inset in Fig. 7.4 (b)] that results in a splitting of the spectral features of each branch of the Mollow triplet [Fig. 7.4 (d)]. This splitting occurs as a result of the strong coupling between the molecule's electronic (TLS) and its vibrational degrees of freedom [294], as predicted in the context of light emission from semiconductor quantum dots [310].

The onset of strong coupling between the electronic and vibrational degrees of freedom, and thus the clear line splitting, can be understood with the help of a simplified Hamiltonian of the system. This Hamiltonian is a result of an effective elimination of the plasmon cavity from the original Hamiltonian. Disregarding the vibrational part in (7.21), the simplified Hamiltonian $\hat{H}_{\mathrm{TLS}}$ becomes

$$\hat{H}_{\mathrm{TLS}} = \hbar\frac{1}{2}\delta\hat{\sigma}_z - \hbar\frac{1}{2}\mathcal{E}_{\mathrm{pl}}\hat{\sigma}_x + \hbar\frac{1}{2}\delta. \tag{7.30}$$

Here $\mathcal{E}_{\mathrm{pl}} = -2g\alpha_{\mathrm{S}} \propto \mathcal{E}$ again corresponds to the amplitude of the plasmon-enhanced electric field. The Hamiltonian in Eq. (7.30) can be diagonalized by a unitary transformation that rotates the TLS Pauli matrices in the $x-z$ plane, $(\hat{\sigma}_x,\, \hat{\sigma}_z \to \hat{\sigma}'_x,\, \hat{\sigma}'_z)$:

$$\begin{aligned}\hat{\sigma}_z &= \frac{\delta}{\lambda_{\mathrm{TLS}}}\hat{\sigma}'_z + \frac{\mathcal{E}_{\mathrm{pl}}}{\lambda_{\mathrm{TLS}}}\hat{\sigma}'_x,\\ \hat{\sigma}_x &= -\frac{\mathcal{E}_{\mathrm{pl}}}{\lambda_{\mathrm{TLS}}}\hat{\sigma}'_z + \frac{\delta}{\lambda_{\mathrm{TLS}}}\hat{\sigma}'_x.\end{aligned}$$

Under those operations, the simplified Hamiltonian describes the dynamics of an effective electronic TLS dressed by the incident coherent illumination with an effective frequency $\lambda_{\mathrm{TLS}} = (\mathcal{E}_{\mathrm{pl}}^2 + \delta^2)^{1/2}$. According to this simplified Hamiltonian, the effective electronic frequency λ_{TLS} can be tuned by either changing the intensity of the incident laser (i.e. $\mathcal{E}_{\mathrm{pl}} \propto \mathcal{E}$) or by detuning the incident laser frequency δ. This dressed TLS interacts with the molecular vibrations via the resonant Rabi interaction term [294]

$$\hbar\frac{1}{2}\Omega d\hat{\sigma}_z(\hat{b}^\dagger+\hat{b}) \rightarrow \underbrace{\hbar\frac{1}{2}\Omega d\frac{\mathcal{E}_{\mathrm{pl}}}{\lambda_{\mathrm{TLS}}}\hat{\sigma}'_x(\hat{b}^\dagger+\hat{b})}_{\text{Rabi term}} + \text{residual polaronic coupling}, \tag{7.31}$$

which becomes resonant if $\lambda_{\mathrm{TLS}} \approx \Omega$, the condition for the Mollow side peaks to coincide with the spectral position of the SERS lines.

On top of the effect of dressing the molecular levels, the plasmonic cavity increases the effective damping rate Γ_{eff} of the TLS by means of the Purcell effect (causing the broad peaks of the Mollow triplet). The condition to reach strong coupling in this situation can be derived by relating the decay rate of the molecular vibration and that of the dressed electronic transition with the exciton-vibration coupling strength:

$$\Omega d\frac{\mathcal{E}_{\mathrm{pl}}}{\lambda_{\mathrm{TLS}}} \gtrapprox |3\Gamma_{\mathrm{tot}}/4 - \gamma_b/2|. \tag{7.32}$$

This condition is at the origin of the strong coupling observed in the peaks of Fig. 7.4 (d) ($\hbar g = 13\,\mathrm{meV}$), but it is not reached in the case presented in Fig. 7.4 (c) ($\hbar g = 50\,\mathrm{meV}$) where Fano-type features appear as a sign of weak coupling. When the strong-coupling between the vibrational Raman emission and the resonance fluorescence is reached, the peak-splitting in the emission spectra in Fig. 7.4 (d) can be also interpreted using the dressed-(atom)molecule picture originally introduced by Cohen-Tanoudji [311, 312]. The dressed-atom picture allows for interpreting the splitting of the Raman and resonance-fluorescence in terms of the coherent interaction among molecular vibronic states, induced by the incident coherent laser illumination. This approach shows that the final emission peaks emerge from a coherent combination of both the resonance fluorescence-type transitions and the Raman-type transitions, making the two mechanisms inseparably connected. We elaborate on the dressed-molecule picture in the following section assuming small d, and provide a more general result allowing large d after that.

Small vibrational displacement d: dressed-molecule picture

The regime where the linewidth of the resonance fluorescence peaks is comparable to the width of the Raman peaks is a limiting case of Raman scattering in intense fields that has been studied in the context of atomic physics [311–314]. To understand the splitting of the lines that appear when the Mollow triplet side peaks have the frequency of the Raman lines, it is useful to rewrite the Hamiltonian into a form where the coupling among vibrational states is explicitly present.

This Hamiltonian can be derived from the original Hamiltonian $\hat{H}^{\mathrm{res}}_{\mathrm{om}}$ appearing in Eq. (7.16) by applying the so called *small polaron transformation* $\hat{H}^{\mathrm{res}}_{\mathrm{om}} \rightarrow \hat{H}'^{\mathrm{res}}_{\mathrm{om}} = \hat{U}_{\sigma_{\mathrm{e}}}\hat{H}^{\mathrm{res}}_{\mathrm{om}}\hat{U}^\dagger_{\sigma_{\mathrm{e}}}$, which is represented by the unitary matrix in the form of

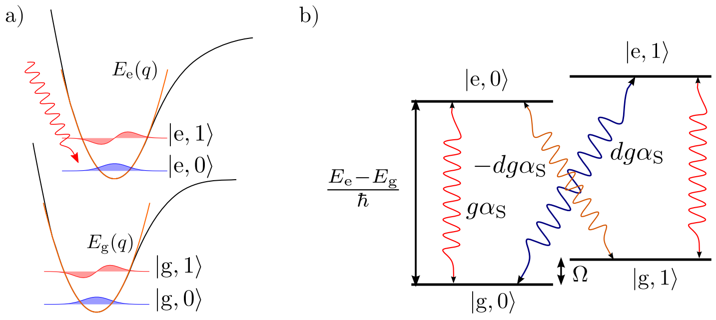

Figure 7.5: (a,b) Schematic representation of the energies of the simplified model of a TLS molecule with one vibrational excited state. In (b) the interaction terms of the simplified Hamiltonian, $\hat{H}_{\mathrm{om}}^{\prime\,\mathrm{res}}$, obtained after applying the *small polaron transformation*, are graphically depicted.

a displacement operator $\hat{U}_{\sigma_{\mathrm{e}}} = \exp\left[d\hat{\sigma}_{\mathrm{e}}(\hat{b}^{\dagger} - \hat{b})\right]$. This transformation has two effects on the Hamiltonian [defined in Eq. (7.16)]. First, the vibrational term in $\hat{H}_{\mathrm{mol}}$ transforms as:

$$\hbar\Omega(\hat{b}^{\dagger} + \hat{\sigma}_{\mathrm{e}}d)(\hat{b} + \hat{\sigma}_{\mathrm{e}}d) \to \hbar\Omega\hat{b}^{\dagger}\hat{b} \tag{7.33}$$

and the pumping term of the TLS given by $\hat{H}_{\mathrm{pump}}$ acquires an additional factor that includes the vibrational operators (which yield the well known Franck-Condon factors):

$$\hbar g\alpha_{\mathrm{S}}\hat{\sigma}^{\dagger} + \mathrm{H.c.} \to \hbar g\alpha_{\mathrm{S}}\hat{\sigma}^{\dagger}\exp\left[d(\hat{b}^{\dagger} - \hat{b})\right] + \mathrm{H.c.} = -\hbar\frac{\mathcal{E}_{\mathrm{pl}}}{2}\hat{\sigma}^{\dagger}\exp\left[d(\hat{b}^{\dagger} - \hat{b})\right] + \mathrm{H.c.} \tag{7.34}$$

We assume that the influence of the plasmon (given by $\hat{H}_{\mathrm{pl}}$ and $\hat{H}_{\mathrm{pl-e}}$ in Eq. (7.16)) is effectively included in the effect of enhancement of the incident laser field α_{S}. Furthermore we consider only the case where the splitting of the fluorescence and Raman spectral peaks is larger than their broadening (the so called secular limit). In such a case, the incoherent broadening does not influence the peaks positions and, therefore, in the following we consider that the system can be described only by the the simplified Hermitian Hamiltonian (we do not consider the Lindblad terms as we are mainly interested in the nature of the transitions). We further assume weak electron-phonon coupling in the molecule and expand the exponential terms containing the vibrational operators to the first order: $\exp\left[\pm d(\hat{b}^{\dagger} - \hat{b})\right] \approx I \pm d(\hat{b}^{\dagger} - \hat{b})$. Last, we reduce the system comprising the vibrations and the TLS into an effective four level system that consists of the ground and excited electronic states considering zero or one vibrational excitation for each electronic state. The diagram of the resulting effective system is drawn in Fig. 7.5 (a) and (b). By diagonalizing this 4×4 Hamiltonian we achieve a new level structure of the system that, in the dressed-molecule picture, provides the positions of the emission peaks (for detailed discussion of the dressed-molecule (atom) picture see e.g. chapter 10 of reference [161]). Below we briefly describe this procedure that will help understanding the origin of the features observed in the emission spectrum.

In the dressed-molecule picture we consider the simplified Hamiltonian, which can be formally defined in the basis of states $[|\mathrm{g},\mathcal{N},0\rangle, |\mathrm{e},\mathcal{N}-1,0\rangle, |\mathrm{g},\mathcal{N},1\rangle, |\mathrm{e},\mathcal{N}-1,1\rangle]$, with e (g) labeling the electronic excited (ground) state, $\mathcal{N}$ labeling the photon number state of the *exciting field* and 0 (1) labeling the number of vibrational excitations, respectively. The exciting field is not quantized explicitly in the original Hamiltonian [Eq. (7.16)] where it is represented by the plasmon coherent-state amplitude α_S. Without loss of generality, we assume that the exciting field is a highly populated bosonic field which peaks sharply around a (mean) occupation number $\tilde{\mathcal{N}}$ yielding $\alpha_\mathrm{S} = \sqrt{\tilde{\mathcal{N}}} g_{\mathrm{PL-L}}$, with $g_{\mathrm{PL-L}}$ formally defined as a small coupling constant (such that $\tilde{\mathcal{N}} \gg 1$) between the equivalent exciting field and the molecule. Note that the formal definition of the exciting field is not important for the following discussion as by introducing the quantized exciting field we only aim at mimicking the action of the semi-classical pumping term. However, the number states $|\mathcal{N}\rangle$ of the exciting field are advantageous to discuss the dressing of the molecular excited states in terms of the hybridization of the quantum-mechanical states.

We further define the total number of excitations as $n = \mathcal{N} + \delta_{i\mathrm{e}}$, with $i = \mathrm{e}, \mathrm{g}$ and δ_{ij} the Kronecker delta. We consider that the electronic levels, carrying the fine vibrational structure, are dressed by the strong laser illumination. The Hamiltonian is expressed in the interaction picture of the incident laser field which is exactly tuned to the electronic transition, $\hbar\delta = 0$ eV. In the basis $[|\mathrm{g},\mathcal{N},0\rangle, |\mathrm{e},\mathcal{N}-1,0\rangle, |\mathrm{g},\mathcal{N},1\rangle, |\mathrm{e},\mathcal{N}-1,1\rangle]$ the Hamiltonian, $\hat{H}'^{\mathrm{res}}_{\mathrm{om}}$, can be represented by a matrix:

$$\mathbf{H}'^{\mathrm{res}}_{\mathrm{om}} \approx \hbar \begin{bmatrix} 0 & -\mathcal{E}_{\mathrm{pl}}/2 & 0 & -d\mathcal{E}_{\mathrm{pl}}/2 \\ -\mathcal{E}_{\mathrm{pl}}/2 & 0 & d\mathcal{E}_{\mathrm{pl}}/2 & 0 \\ 0 & d\mathcal{E}_{\mathrm{pl}}/2 & \Omega & -\mathcal{E}_{\mathrm{pl}}/2 \\ -d\mathcal{E}_{\mathrm{pl}}/2 & 0 & -\mathcal{E}_{\mathrm{pl}}/2 & \Omega \end{bmatrix}. \tag{7.35}$$

For vanishing electron-phonon coupling, $d = 0$, the Hamiltonian in Eq. (7.35) reduces to the form describing a pair of TLSs dressed by the incident laser illumination. The process of dressing (i.e. diagonalization of the above Hamiltonian with $d = 0$) can be viewed as a mixing of the electronic states with the high number states of the exciting laser field, giving rise to the basis of hybridized states $[|n_-,0\rangle, |n_+,0\rangle, |n_-,1\rangle, |n_+,1\rangle]$ where the first quantum number, n, labels the total number of electronic plus laser excitations, and the second quantum number, m, belongs to the vibrational states [see Fig. 7.6 (a) for schematics of the corresponding energy levels]. The hybrid states are defined as $|n_\pm,m\rangle \equiv (|\mathrm{g},\mathcal{N},m\rangle \pm |\mathrm{e},\mathcal{N}-1,m\rangle)/\sqrt{2}$ with + labelling the state with higher energy. In

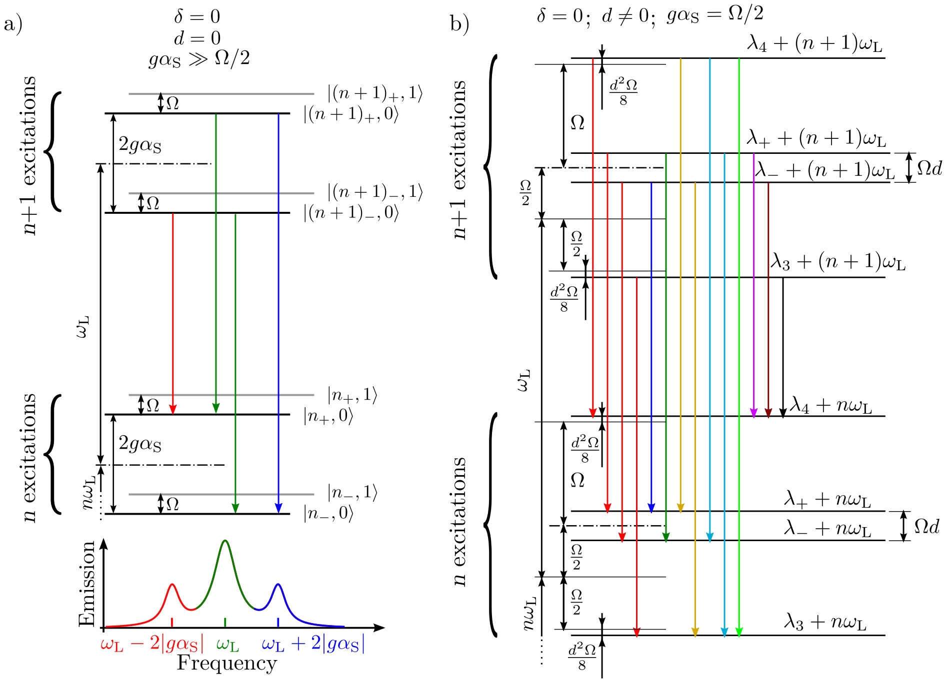

Figure 7.6: Energy level diagram in the dressed-molecule picture where the level structure of the effective four-level system describing the molecule is repeated for each manifold containing n excitation quanta: (a) a situation where no electron-phonon interaction is present ($d = 0$), and (b) a situation where all the interactions are present [λ_i are defined in Eq. (7.37)]. In (a) we further mark the transitions that give rise to Mollow triplet by coloured arrows (connecting only $m = 0$ states, for simplicity), and use the colour code to assign the transitions to the respective emission peaks in the spectrum below. The coloured lines in (b) represent all possible transitions that can contribute to the emission spectrum [shown in Fig. 7.7 (a)].

the new basis of such dressed states, we can represent the Hamiltonian as:

$$\mathbf{H}_{\mathrm{om}}^{\prime\mathrm{res,dr}} \approx \hbar \begin{bmatrix} \mathcal{E}_{\mathrm{pl}}/2 & 0 & 0 & 0 \\ 0 & -\mathcal{E}_{\mathrm{pl}}/2 & 0 & 0 \\ 0 & 0 & \Omega + \mathcal{E}_{\mathrm{pl}}/2 & 0 \\ 0 & 0 & 0 & \Omega - \mathcal{E}_{\mathrm{pl}}/2 \end{bmatrix} - \hbar \begin{bmatrix} 0 & 0 & 0 & -d\mathcal{E}_{\mathrm{pl}}/2 \\ 0 & 0 & -d\mathcal{E}_{\mathrm{pl}}/2 & 0 \\ 0 & -d\mathcal{E}_{\mathrm{pl}}/2 & 0 & 0 \\ -d\mathcal{E}_{\mathrm{pl}}/2 & 0 & 0 & 0 \end{bmatrix}, \tag{7.36}$$

For $d = 0$, the splitting of the states $|n_\pm\rangle$ for the TLS in each vibrational manifold is $|2g\alpha_S| = |\mathcal{E}_{\rm pl}|$. The two vibrational manifolds are mutually shifted by the vibrational frequency Ω along the energy axis. In the absence of electron-phonon coupling d, the resonance fluorescence emission (dominating in this case the inelastic emission) is given purely by the transitions within the individual vibrational manifolds and it changes the total number of excitations, n, by one. In particular, the central Mollow peak is given by transitions between $|(n+1)_+, 0(1)\rangle \rightarrow |n_+, 0(1)\rangle$ and $|(n+1)_-, 0(1)\rangle \rightarrow |n_-, 0(1)\rangle$, while the side peaks contain transitions $|(n+1)_-, 0(1)\rangle \rightarrow |n_+, 0(1)\rangle$ (red detuned) and $|(n+1)_+, 0(1)\rangle \rightarrow |n_-, 0(1)\rangle$ (blue detuned), respectively. The respective transitions and their corresponding emission peaks (the Mollow triplet) are schematically marked in Fig. 7.6 (a). In Fig. 7.6 (a) the colours of the spectral emission peaks correspond to the colour of the respective arrows marking the transitions.

If we switch on the electron-phonon interaction d, a mixing between the levels belonging to the two vibrational manifolds is introduced, simultaneously allowing additional transitions yielding the Raman emission (i.e. changing the vibrational manifolds). The details of the level mixing and the subsequent emission spectra depend on the particular choice of pumping strength, $\mathcal{E}_{\rm pl}$, in combination with the value of the electron-phonon coupling, d. In the following we consider a particular case where the Mollow triplet side peaks overlap with the Raman lines with the laser frequency exactly tuned to the TLS energy splitting ($\hbar\delta = 0$ eV and $|\mathcal{E}_{\rm pl}| = \Omega$). Upon diagonalization, the Hamiltonian in Eq. (7.35) [Eq. (7.36)] yields the following spectrum of energy levels:

$$\begin{aligned}
\lambda_- &= -\frac{1}{2}(d-1)\Omega,\\
\lambda_+ &= \frac{1}{2}(d+1)\Omega,\\
\lambda_3 &= -\frac{1}{2}\left(\sqrt{d^2+4}-1\right)\Omega \approx -\frac{1}{2}\left(1+\frac{d^2}{4}\right)\Omega,\\
\lambda_4 &= \frac{1}{2}\left(\sqrt{d^2+4}+1\right)\Omega \approx \frac{1}{2}\left(3+\frac{d^2}{4}\right)\Omega,
\end{aligned} \tag{7.37}$$

where we used the assumption that $d \ll 1$ to perform the Taylor expansion of the square root up to the first order. The states having energy $\lambda_\pm$ are a coherent admixture of states containing zero and one vibrational excitation $|n_-, 1\rangle$ and $|n_+, 0\rangle$, as discussed above, and the states of energy $\lambda_{3,4}$ can be identified (up to small $o(d)$ admixtures of other states) with $|n_-, 0\rangle$ and $|n_+, 1\rangle$ whose energy is renormalized due to the off-resonant electron-phonon coupling. This level structure of the molecule does not explicitly contain the quantized electromagnetic field of the incident laser. However, in the dressed-molecule picture the molecular level structure [Eq. (7.37)] is periodically repeated for each manifold represented by a specific number of excitations, n, and thus appears repeated along the energy axis displaced by integer values of the laser frequency $\omega_{\rm L}$, as schematically illustrated in Fig. 7.6 (b). In this picture, the emission events are represented by transitions between manifolds that differ by one excitation quantum of the electronic and

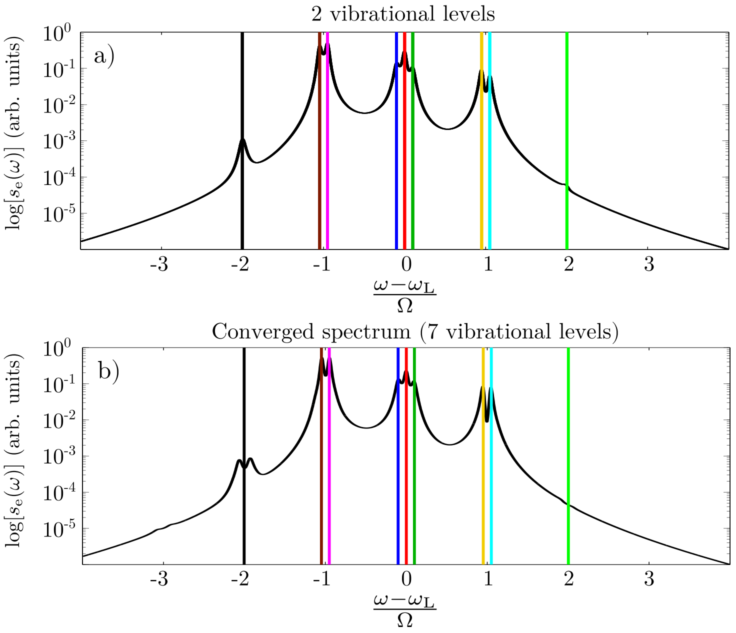

Figure 7.7: Particular example of an emission spectrum of a TLS in a plasmonic resonator obtained from the full model [Eq. (7.16)] using (a) two and (b) seven vibrational levels (converged spectrum) in both the ground and the excited electronic states. The spectrum is calculated for $d = 0.1$, $\hbar\Omega = 50$ meV, $\hbar g \approx 13$ meV, $\hbar\mathcal{E} = 480$ meV, $\hbar\gamma_\sigma = 2 \times 10^{-5}$ eV, $\hbar\gamma_b = 2$ meV, $\hbar\gamma_a = 500$ meV, $\hbar\delta = 0$ eV, $\hbar\Delta = 0$ eV and temperature $T = 0$ K. The colored lines represent the different transitions graphically depicted in Fig. 7.6 (b) using the same color code.

effective photonic states, i.e. transitions between the manifolds containing n and $n+1$ excitation quanta [represented by colored lines in Fig. 7.6 (b)].

The dressed-molecule picture above nicely allows us to identify the spectral peaks which appear in the complex photon emission spectra obtained from the numerical calculation of the complete Hamiltonian in Eq. (7.16) with its corresponding Lindblad terms. Figure 7.7 (a) shows such a situation where two vibrational levels corresponding to the ground vibrational state and the first excited vibrational state are considered. Nine main frequencies [coloured lines in Fig. 7.7 (a)] are identified in the spectrum which nicely coincide with the nine transitions marked in the energy diagram of Fig. 7.6 (b) (vertical lines marking $\lambda_i - \lambda_j$, where $i, j \in \{+, -, 3, 4\}$). For comparison, we show in Fig 7.7 (b) the results obtained using a sufficiently large number of vibrations to achieve results converged with respect to the size of the vibrational subspace. In this case, more spectral features appear [we observe higher order transitions and further peak splitting when compared with Fig. 7.7 (a)]. Nonetheless, the simple model introduced in this section still explains very well the spectral positions of the strongest peaks.

Large vibrational displacement d

We have so far used a moderate value of the displacement, $d = 0.1$, however, in realistic molecules significant exciton-vibration coupling can lead to larger values of d. Although the dressed-molecule picture developed in the previous section can be generalized for arbitrary displacement d, it becomes excessively complicated when d becomes large and we therefore opt for describing the situation with help of full numerical calculation. In Fig. 7.8 we show the evolution of the emission spectra with d [as schematically shown in Fig. 7.8 (a)] for the same two values of the plasmon-TLS coupling considered up to now, i.e. $\hbar g = 50$ meV [Fig. 7.8 (b)] and $\hbar g \approx 13$ meV [Fig. 7.8 (c)]. For all the values of d considered, the laser intensity is chosen such that the RF lines match the position of the Raman lines. For small values of $d \approx 0.1$, the RF profile follows the behavior described in Fig. 7.4. As d gradually increases, the spectra start exhibiting additional features due to the increasing importance of higher-order vibronic transitions. When the RF line is significantly broader than the Raman lines [Fig. 7.8 (b)], an increase of the coupling d gradually changes the spectral dip located at the frequency of the Stokes emission and the bump at the anti-Stokes emission [see Fig. 7.4 (c)] into positive Raman peaks. Additional peaks appear for values of $(\omega - \omega_{\mathrm{L}})$ that are multiple integers of Ω, together with a suppression of the broad background RF [top side of Fig. 7.8 (b)]. When the line width of the Mollow side peaks is similar to the width of the Raman lines [Fig. 7.8 (c)], the splitting of the strongly coupled hybrid lines becomes larger as d increases. For large values of d, all of the spectra in Figs. 7.8 (b,c) acquire a complex structure due to the generally complicated coherent interaction between the molecular vibrational and electronic degrees of freedom, with the emergence of additional peaks originating from higher-order Raman and resonance-fluorescence transitions.

7.2.4 Optomechanical vibrational pumping for strong laser intensities

In this section, we extend the treatment of resonant SERS within the linear response introduced previously to consider the case of strong incident illumination, where non-linear effects become important. To that end we invoke the effective vibrational Hamiltonian introduced in Eq. (7.22) together with the incoherent damping $\Gamma_{\mathrm{v}}^{\mathrm{dec}} = 2\,(\Omega d)^2\,\mathrm{Re}\{\tilde{S}(\Omega)\}$ and pumping $\Gamma_{\mathrm{v}}^{\mathrm{pump}} = 2\,(\Omega d)^2\,\mathrm{Re}\{\tilde{S}(-\Omega)\}$ rates in Eqs. (7.23) and (7.24), respectively. As described in Section 7.2.2, the spectral function $\tilde{S}(s)$ can be obtained from the effective dynamics of the TLS, which is effectively broadened by the plasmon via the Purcell effect (more details about the calculation of $\tilde{S}(s)$ are given in Appendix F). This hierarchy of approximations considered in this section is schematically depicted in Fig. 7.9 (a). These effective rates are dependent on the spectral function $\tilde{S}(s)$ of the reservoir

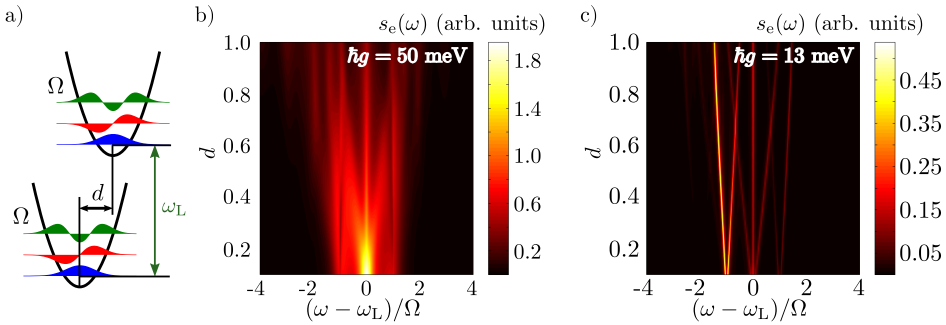

Figure 7.8: Emission spectra of a molecule for increasing value of coupling, d, as schematically depicted in (a), keeping the conditions $\delta = 0$ eV, for (b) $\hbar g$ =50 meV and $\hbar\mathcal{E} = 125$ meV, (c) $\hbar g$ =13 meV and $\hbar\mathcal{E} = 480$ meV. As d is increased, the spectra acquire a complicated form containing a number of RF and r-SERS peaks due to the increasing importance of higher-order vibronic transitions.

evaluated at frequencies Ω and $-\Omega$, respectively. Note that the analytical model is limited to cases where the electron-vibration coupling Ωd is smaller than the effective broadening Γ_{eff} of the electronic resonance. We thus perform full numerical calculations to obtain the results spanning the full range of model parameters and use the analytical model for qualitative discussion.

The effective optomechanical decay and pumping rates are dependent on the spectral function $\tilde{S}(s)$ of the reservoir, hence the value of the spectral function $\tilde{S}(s)$ at frequencies $\pm\Omega$ determines the strength of the effective vibrational pumping ($\Gamma_{\text{v}}^{\text{pump}}$) or damping ($\Gamma_{\text{v}}^{\text{dec}}$). It is therefore possible to achieve different regimes of interaction with the vibrations which range from pumping to damping by simply modifying the illumination conditions (laser intensity and frequency detuning) that provoke a variation of the shape of the spectral function. When the laser intensity is large, the reservoir function $\tilde{S}(s)$ reflects the structure of the TLS dressed by the incident laser, and therefore it becomes qualitatively different from the weak-illumination case.

In Fig. 7.9 (b) the spectral function, $\text{Re}\{\tilde{S}(s)\}$, for $d = 0.1$, $\hbar\mathcal{E} = 125$ meV, and $\hbar g = 50$ meV, is shown to peak around the effective frequencies of the dressed TLS ($s = \pm\lambda_{\text{TLS}}$). When the incident laser is detuned from the TLS transition ($\tilde{\delta} \neq 0$, with $\tilde{\delta} = \delta + d^2\Omega$), an additional peak appears at around $\hbar s = 0$ eV and the spectral function changes symmetry. For $\tilde{\delta} > 0$ (red detuning marked with a red line) a regime of vibrational damping can be reached ($\text{Re}\{\tilde{S}(\Omega)\} > \text{Re}\{\tilde{S}(-\Omega)\}$), whereas for $\tilde{\delta} < 0$ (blue detuning marked with a blue line) a regime of vibrational pumping ($\text{Re}\{\tilde{S}(\Omega)\} < \text{Re}\{\tilde{S}(-\Omega)\}$) is achieved. This effect is more pronounced for a situation where $\tilde{S}(\pm\Omega)$ corresponds to the maxima of $\tilde{S}(s)$.

To illustrate the possibility to achieve a controlled excitation of molecular vibrations on demand within this scheme of interactions, we numerically solve the full Hamiltonian of the system [Eq. (7.16)], and show in Figs. 7.9 (c,d) the

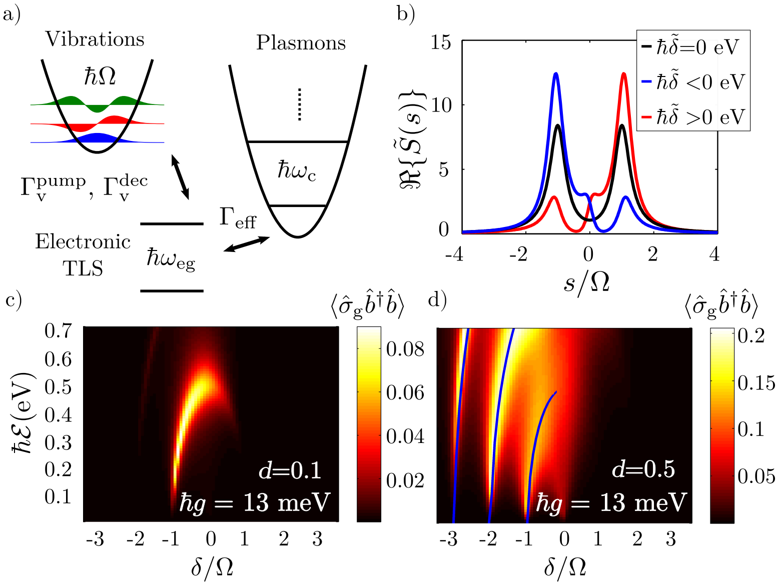

Figure 7.9: (a) Schematic depiction of the hierarchy considered in the theoretical model. The plasmons serve as an effective reservoir and broaden the TLS via the Purcell effect (Γ_{eff}). The broadened TLS then effectively influences the incoherent dynamics of the vibrations via the effective vibrational pumping ($\Gamma_{\mathrm{v}}^{\mathrm{pump}}$) and damping ($\Gamma_{\mathrm{v}}^{\mathrm{dec}}$). (b) Real part of the spectral function (calculated from the reduced Hamiltonian where the plasmonic cavity is eliminated), $\mathrm{Re}\{\tilde{S}(s)\}$, of the operator $\hat{\sigma}_{\mathrm{e}}$, for three different values of detuning $\hbar\tilde{\delta} = 0$ eV (black line), 0.02 eV (red line) and -0.02 eV (blue line). $\hbar\mathcal{E} = 125$ meV, and $\hbar g = 50$ meV. (c,d) Maps of vibrational population of a molecular vibration ($\hbar\Omega = 50$ meV) as a function of detuning from the effective TLS energy, $\tilde{\delta}$, and of the incident laser amplitude, $\mathcal{E}$, for $\hbar g = 13$ meV, with $d = 0.1$ (c), $d = 0.5$ (d). The blue lines in (d) indicate the condition $\lambda_{\mathrm{TLS}} = n\Omega$ with n integer (depicted only for $\delta < 0$).

result of the steady-state vibrational population of the electronic ground state, $\langle\hat{\sigma}_{\mathrm{g}}\hat{b}^\dagger\hat{b}\rangle$, for an electron-plasmon coupling of $\hbar g \approx 13$ meV and two different values of the dimensionless displacement ($d = 0.1$ and $d = 0.5$). The map of efficiency of vibrational pumping is non-trivially influenced by both the detuning $\tilde{\delta}$ of the incident laser frequency from the TLS transition frequency and by the incident laser intensity ($\propto |\mathcal{E}|^2$), so that the optimal laser intensity for the pumping depends on the laser detuning $\tilde{\delta}$. When the electron-vibration coupling is large ($d = 0.5$), the population reaches multiple local maxima [Fig. 7.9 (d)]. In this case, by adequately tuning the laser frequency one can efficiently excite Franck-Condon transitions involving a change of more than one vibrational transition (higher-order processes). As expected, the population maxima are found when the spectral position of the side peaks of the electronic spectral function matches the frequency of the higher order vibrational transitions ($\lambda_{\mathrm{TLS}} \approx n\Omega$, with n an

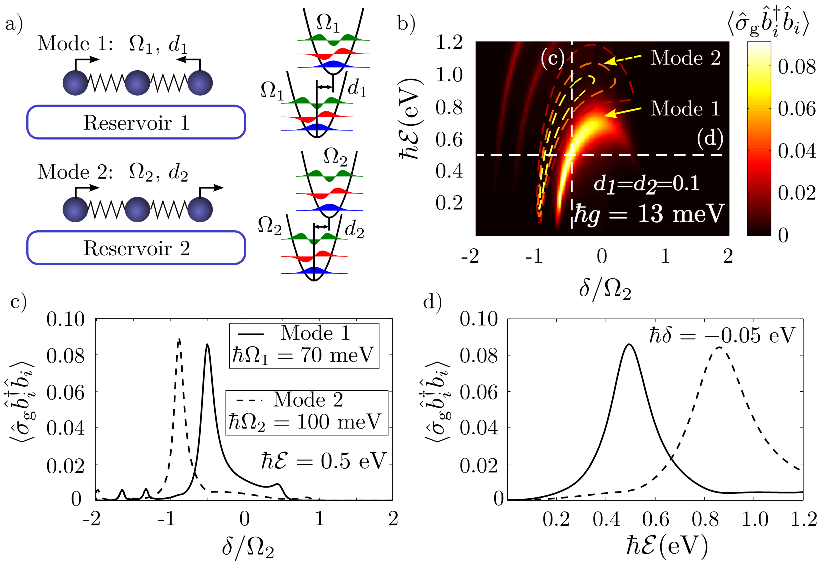

Figure 7.10: Selective vibrational pumping. (a) Schematic representation of an example of two different vibrational modes of frequencies Ω_1 and Ω_2, respectively, coupled with their electronic degrees of freedom via the displacement d_1 and d_2 of their respective PESs. The vibrational modes are assumed to interact independently with their corresponding reservoirs, 1 and 2. (b) Color map of the vibrational populations $\langle\hat{\sigma}_{\rm g}\hat{b}_i^\dagger\hat{b}_i\rangle$ of two different vibrational modes $\{i = 1, 2\}$ present in the same molecule, with frequency $\hbar\Omega_1 = 70$ meV (solid colors) and $\hbar\Omega_2 = 100$ meV (values expressed by dashed contour lines). (c,d) Populations of the modes Ω_1 (solid line) and Ω_2 (dashed line) extracted along the white dashed lines in (b). In (c) $\hbar\mathcal{E} = 0.5$ eV and δ is varied, whereas in (d) $\hbar\delta = -0.05$ eV and $\mathcal{E}$ is varied.

integer), a condition traced by the blue lines in Fig. 7.9 (d), and displayed only for negative detuning δ.

7.2.5 Selective optomechanical vibrational pumping

The potential to control the activation of molecular vibrations shown in the previous section can be exploited in the selective excitation of different vibrational modes. Let us consider the coupling of a plasmonic system with a molecule supporting two vibrations (labelled 1 and 2) at frequencies $\hbar\Omega_1 = 70$ meV and $\hbar\Omega_2 = 100$ meV, both coupled to independent reservoir modes (baths) with $\hbar\gamma_{b_1} = \hbar\gamma_{b_2} = 2$ meV, as schematically depicted in Fig. 7.10 (a). We simplify the description of the system and use the effective Hamiltonian where the plasmonic degrees of freedom are eliminated:

$$\begin{aligned}\hat{H}^{\text{two}}_{\text{red}} &= \hbar\delta\hat{\sigma}_{\text{e}} + \hbar\Omega_1(\hat{b}^\dagger_1 + d_1\hat{\sigma}_{\text{e}})(\hat{b}_1 + d_1\hat{\sigma}_{\text{e}}) \\ &+ \hbar\Omega_2(\hat{b}^\dagger_2 + d_2\hat{\sigma}_{\text{e}})(\hat{b}_2 + d_2\hat{\sigma}_{\text{e}}) + \hbar\frac{1}{2}\mathcal{E}_{\text{pl}}\hat{\sigma}_x\end{aligned} \tag{7.38}$$

Where we have assumed that the vibrational modes are coupled to the TLS via a polaronic coupling term ($d_1 = d_2 = 0.1$), and do not consider the direct coupling between the two vibrational modes. However, this model Hamiltonian naturally couples the two vibrational modes indirectly via the electronic TLS of the molecule. Our model thus partially accounts for thermalization effects, without considering the effect of the surrounding environment that may further incoherently couple the vibrational modes.

The resulting vibrational population of the electronic ground state, $\langle\hat{\sigma}_g\hat{b}^\dagger_i\hat{b}_i\rangle$, is shown in Fig. 7.10 (b) as a function of the intensity and detuning of the incoming laser. The color map depicting the population of the vibrational mode at frequency Ω_1 is displayed together with a dashed contour plot that shows the corresponding results for the mode at Ω_2. Each mode presents a clear maximum for adequate illumination conditions. The maxima are shifted with respect to each other both in frequency and amplitude, so that changing the illumination conditions serves to pump more efficiently one mode or another. To highlight the selectivity of the vibrational pumping mechanism, we extract line cuts of Fig. 7.10 (b) for constant laser pumping, $\hbar\mathcal{E} = 500$ meV, [Fig. 7.10 (c)], and for constant laser detuning $\hbar\delta = -50$ meV [Fig. 7.10 (d)]. As observed in Fig. 7.10 (c,d) the conditions of intensity and detuning for maximum population of one mode give a much weaker population of the other mode (solid versus dashed lines). This scheme of interactions makes it possible to achieve selective vibrational pumping by either tuning the laser frequency for a given illumination intensity or by modifying the laser intensity for a fixed illumination frequency.

7.3 Resonant-SERS in the plasmon-exciton strong coupling regime

We consider in this section that the coupling between the molecular exciton and the plasmon, g, is sufficiently large to overcome the plasmonic losses, $g \gtrsim \gamma_a/2$, and the system is thus in the plasmon-exciton strong-coupling regime. In this regime the plasmonic and excitonic states hybridize forming the Jaynes-Cummings ladder of plexcitonic states,which has been described in Section 5.1. The large g values necessary for strong coupling to occur are typically achieved by coupling plasmonic nanostructures with J-aggregates [80, 315–317], large complex dyes characterized by their large dipole moment, or with a large number of small molecules forming a collective bright mode of larger effective coupling strength [72, 238, 318]. However, recently it has become possible to achieve strong coupling even with a single small molecule conveniently aligned with the plasmonic field [238]. In this chapter we consider $\hbar g = 100\,\mathrm{meV}$ and $\hbar\gamma_a = 150\,\mathrm{meV}$ as representative values of strong coupling between a plasmonic cavity and a single molecule. As before, we consider $\hbar\gamma_\sigma = 2\times10^{-5}\,\mathrm{meV}$ for the intrinsic decay rate of the molecular electronic excited state and specify the other relevant parameters when necessary.

In the following it will be convenient to split the polaronic Hamiltonian, $\hat{H}^{\mathrm{res}}_{\mathrm{om}}$ [Eq. (7.16)], of the system of plasmons interacting with molecular excitations in a slightly different form than used in the previous sections:

$$\hat{H}^{\mathrm{res}}_{\mathrm{om}} = \hat{H}_{\mathrm{J-C,p}} + \hat{H}_{\mathrm{v}} + \hat{H}_{\mathrm{TLS-v}}, \tag{7.39}$$

where in the rotating frame

$$\hat{H}_{\mathrm{J-C,p}} = \hbar\Delta\hat{a}^\dagger\hat{a} + \hbar\tilde{\delta}\hat{\sigma}^\dagger\hat{\sigma} + \hbar g\hat{a}\hat{\sigma}^\dagger + \hbar g^*\hat{a}^\dagger\hat{\sigma} + \hbar\mathcal{E}(\hat{a} + \hat{a}^\dagger), \tag{7.40}$$

is the Hamiltonian of the pumped Jaynes-Cummings system, with $\tilde{\delta} = \delta + \Omega d^2$,

$$\hat{H}_{\mathrm{v}} = \hbar\Omega\hat{b}^\dagger\hat{b} \tag{7.41}$$

is the vibrational Hamiltonian, and

$$\hat{H}_{\mathrm{TLS-v}} = \hbar\Omega d\,\hat{\sigma}^\dagger\hat{\sigma}(\hat{b}^\dagger + \hat{b}) \tag{7.42}$$

is the Hamiltonian mediating the interaction between the Jaynes-Cummings system and the vibration.

7.3.1 Optomechanical vibrational pumping and photon emission in a simple situation

Optomechanical vibrational pumping

To provide insights into the scattering of light by the molecule we develop an analytical model describing the Raman process for a relatively simple scenario. We first consider that the electron-phonon coupling, described by the displacement value d, is in the low range of values obtained for rigid molecules [319, 320] ($d \sim 10^{-1}$). We further assume that the laser illumination is not too intense so that the linear response approximation is justified, and that the TLS is not affected by pure dephasing processes.

The condition of weak electron-phonon coupling, considering that the time scale of the electron-phonon interaction is larger than that of the dominant relaxation processes, can be roughly estimated as $\Omega d \ll |\gamma_a + \gamma_\sigma|/4$. This assumption allows us to separate the full system according to the hierarchy of time scales: the fast decaying and decohering reservoir part, which consists of the electronic TLS strongly coupled with the plasmon, and the slowly varying system part represented by the vibrational mode [158]. As we have shown in Section 7.2.2, under such conditions the vibrational dynamics then approximately follows the Hamiltonian H_{v} [Eq. (7.41)], and the effective incoherent decay, via the Lindblad superoperator

$\mathscr{L}_{\hat{b}}^{\Gamma_{\mathrm{v}}^{\mathrm{dec}}}(\hat{\rho})$ [Eq.(7.23)], and pumping, via the superoperator $\mathscr{L}_{\hat{b}^\dagger}^{\Gamma_{\mathrm{v}}^{\mathrm{pump}}}(\hat{\rho})$ [Eq.(7.24)], with $\Gamma_{\mathrm{v}}^{\mathrm{dec}}$ and $\Gamma_{\mathrm{v}}^{\mathrm{pump}}$ the effective incoherent damping and pumping rates due to the electronic TLS and the plasmon. As we have shown in Section 7.2.2, these rates are related to the steady-state reservoir spectral function:

$$\mathrm{Re}\{\tilde{S}(s)\} = \mathrm{Re}\left\{\int_0^\infty \langle\langle \hat{\sigma}^\dagger\hat{\sigma}(\tau)\hat{\sigma}^\dagger\hat{\sigma}(0)\rangle\rangle e^{\mathrm{i}s\tau}\mathrm{d}\tau\right\} \tag{7.43}$$

as:

$$\Gamma_{\mathrm{v}}^{\mathrm{dec}} = 2(\Omega d)^2\mathrm{Re}\{\tilde{S}(\Omega)\} \tag{7.44}$$

$$\Gamma_{\mathrm{v}}^{\mathrm{pump}} = 2(\Omega d)^2\mathrm{Re}\{\tilde{S}(-\Omega)\}, \tag{7.45}$$

In the considered scheme, the reservoir operators are obtained from the dynamics of the Jaynes-Cummings system decoupled from the vibrations.

As we have assumed that the pure dephasing of the TLS is negligible, we write $\langle\hat{\sigma}^\dagger\hat{\sigma}\rangle_{\mathrm{SS}} \approx |\langle\hat{\sigma}\rangle_{\mathrm{SS}}|^2$. In this case, after decomposing the lowering operator of the TLS into its steady state value $\langle\hat{\sigma}\rangle_{\mathrm{SS}}$ and the fluctuating part with zero mean $\delta\hat{\sigma}$ as $\hat{\sigma} = \langle\hat{\sigma}\rangle_{\mathrm{SS}} + \delta\hat{\sigma}$, we can approximate the population operator as $\hat{\sigma}^\dagger\hat{\sigma} \approx |\langle\hat{\sigma}\rangle_{\mathrm{SS}}|^2 + \langle\hat{\sigma}\rangle_{\mathrm{SS}}\delta\hat{\sigma}^\dagger + \langle\hat{\sigma}^\dagger\rangle_{\mathrm{SS}}\delta\hat{\sigma}$.

We then transform the spectral function $\mathrm{Re}\{\tilde{S}(s)\}$ from an expression depending on the correlation function of the full operator $\langle\langle\hat{\sigma}^\dagger\hat{\sigma}(\tau)\hat{\sigma}^\dagger\hat{\sigma}(0)\rangle\rangle$, to a simpler one where the expression depends on the correlation function $\langle\langle\delta\hat{\sigma}(\tau)\delta\hat{\sigma}^\dagger(0)\rangle\rangle = \langle\langle\hat{\sigma}(\tau)\hat{\sigma}^\dagger(0)\rangle\rangle$ as:

$$\begin{aligned}\mathrm{Re}\{\tilde{S}(s)\} &= \mathrm{Re}\left\{\int_0^\infty \langle\langle \hat{\sigma}^\dagger\hat{\sigma}(\tau)\hat{\sigma}^\dagger\hat{\sigma}(0)\rangle\rangle e^{\mathrm{i}s\tau}\mathrm{d}\tau\right\} \\ &\approx |\langle\hat{\sigma}\rangle_{\mathrm{SS}}|^2 \underbrace{\mathrm{Re}\left\{\int_0^\infty \langle\langle\hat{\sigma}(\tau)\hat{\sigma}^\dagger(0)\rangle\rangle e^{\mathrm{i}(s+\omega_{\mathrm{L}})\tau}\mathrm{d}\tau\right\}}_{\mathcal{J}_0(s)}.\end{aligned} \tag{7.46}$$

Equation (7.46) thus factorizes the full spectral function into two contributions: (i) the coherent population of the TLS, $|\langle\hat{\sigma}\rangle_{\mathrm{SS}}|^2$, and (ii) the absorption spectrum of the TLS, here strongly coupled with the plasmon, $\mathcal{J}_0(s)$. We obtain an approximate expression of both quantities analytically using the quantum regression theorem and considering the low pumping regime.

Under weak illumination, we consider the dynamics of the operators in the single-excitation manifold [234]. We define a vector of operator mean values $\mathbf{v} = (\langle\hat{a}\rangle, \langle\hat{\sigma}\rangle)^{\mathrm{T}}$ [$(\cdot)^{\mathrm{T}}$ denotes transposition, and with $\hat{a}$ and $\hat{\sigma}$ the standard bosonic annihilation operator and Pauli lowering operator, respectively] that approximately satisfies the differential equation

$$\frac{\mathrm{d}}{\mathrm{d}t}\mathbf{v} = \mathbf{M}_{\mathrm{C}}\,\mathbf{v} + \mathbf{rhs}, \tag{7.47}$$

where $\mathbf{M}_\mathrm{C}$ is a matrix of coefficients

$$\mathbf{M}_\mathrm{C} = \begin{bmatrix} -\mathrm{i}\Delta - \gamma_a/2 & -\mathrm{i}g \\ -\mathrm{i}g & -\mathrm{i}\Delta - \gamma_\sigma/2 \end{bmatrix}, \tag{7.48}$$

and **rhs** is a constant vector that represents the coherent pumping of the system, $\mathbf{rhs} = (0, -\mathrm{i}g\alpha_\mathrm{S}^*)^\mathrm{T}$. The steady-state value $\langle\hat{\sigma}\rangle_\mathrm{SS}$ follows from Eq. (7.47) after setting the time derivative equal to zero obtaining:

$$|\langle\hat{\sigma}\rangle_\mathrm{SS}|^2 \approx \langle\hat{\sigma}^\dagger\hat{\sigma}\rangle_\mathrm{SS} \approx \frac{g^2|\alpha_\mathrm{S}|^2(\Delta^2+\gamma_a^2/4)}{\Delta^4+(g^2+\gamma_\sigma\gamma_a/4)^2+\Delta^2(\gamma_\sigma^2/4+\gamma_a^2/4-2g^2)}. \tag{7.49}$$

To finally evaluate the correlation function, $\mathcal{J}_0(s)$, in the last integral of Eq. (7.46) we apply the QRT. We concentrate on the calculation of the fluctuating part of the correlation functions which are responsible for the incoherent damping and pumping effects. These go to zero in the limit $\tau \to \infty$. The time dynamics of the two-time correlation functions is then given by the homogeneous part of the differential equation for the operator mean values. More specifically,

$$\frac{\mathrm{d}}{\mathrm{d}\tau}\mathbf{w} = \mathbf{M}_\mathrm{C}\,\mathbf{w},$$

with $\mathbf{w} = (\langle\langle\hat{a}(\tau)\hat{\sigma}^\dagger(0)\rangle\rangle, \langle\langle\hat{\sigma}(\tau)\hat{\sigma}^\dagger(0)\rangle\rangle)^\mathrm{T}$. Finally, the initial values ($\tau = 0$) of the two-time correlators for $\mathbf{w}$ are:

$$\langle\langle\hat{a}\hat{\sigma}^\dagger\rangle\rangle_\mathrm{SS} \approx 0,$$
$$\langle\langle\hat{\sigma}\hat{\sigma}^\dagger\rangle\rangle_\mathrm{SS} \approx 1,$$

where we have neglected the terms $O(\alpha_\mathrm{S}^2)$. Finally, we obtain:

$$\mathcal{J}_0(s) = \frac{g^2\gamma_a/2+\gamma_\sigma/2[\gamma_a^2/4+(\Delta-s)^2]}{g^4-2g^2[(\Delta-s)^2-\gamma_\sigma\gamma_a/4]+[\gamma_\sigma^2/4+(\Delta-s)^2][\gamma_a^2/4+(\Delta-s)^2]}. \tag{7.50}$$

In the strong coupling regime, $\mathcal{J}_0(s)$ contains two peaks approximately located at frequencies $s_\pm^\mathcal{J} \approx \Delta \pm \sqrt{g^2-(\gamma_\sigma^2+\gamma_a^2)/8}$ (assuming a slowly varying numerator). We notice that the double-peaked structure can be resolved only if $g^2 > (\gamma_\sigma^2+\gamma_a^2)/8$, which is a stronger condition than the one for the plasmon-exciton strong coupling $g^2 > (\gamma_a-\gamma_\sigma)^2/16$.

The expressions for the effective damping [Eqs. (7.44)] and pumping [Eq. (7.45)], proportional to $\mathrm{Re}\{\tilde{S}(s)\}$, can then be interpreted as the consequence of a two step process. First, the $|\langle\hat{\sigma}\rangle_\mathrm{SS}|^2$ indicates that the pumping laser of frequency ω_L induces the coherent population of the molecular excited state, which triggers the Raman process and thus increases $\Gamma_\mathrm{v}^\mathrm{dec}$ and $\Gamma_\mathrm{v}^\mathrm{pump}$. In the second stage, the Stokes and anti-Stokes excitations appearing at frequencies $\omega_\mathrm{L} \pm \Omega$ are absorbed and partially emitted to the far field by the resonance of the J-C system,

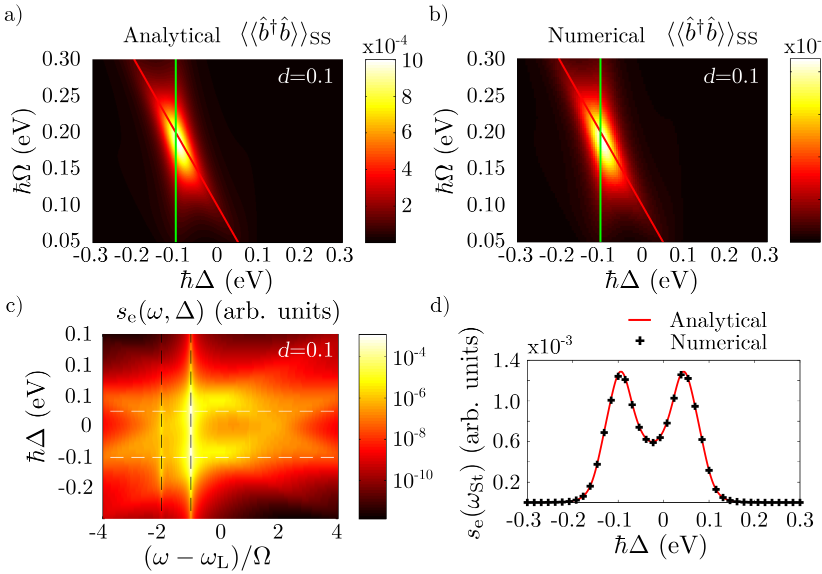

Figure 7.11: Resonant SERS for weak illumination $\hbar\mathcal{E} = 1$ meV, no pure dephasing and weak coupling between the electronic and vibrational levels of the molecule, $d = 0.1$. (a,b) Population of the vibrational mode under laser excitation as a function of laser detuning Δ and vibrational frequency Ω, calculated (a) from the analytical model as explained in the text and (b) from the full numerical calculation solving Eq. (7.39) with the corresponding Lindblad terms. The lines mark the conditions where the frequency of one of the bare J-C absorption peaks coincides with the frequency of the first order Stokes line (red line) or the incident laser (green line). (c) Numerical SERS spectra $s_{\rm e}(\omega,\Delta)$ at emission frequency ω as a function of plasmon detuning Δ, for a vibrational mode energy $\hbar\Omega = 50\,$meV. (d) Maximum intensity of the Stokes-Raman line (at $\omega = \omega_{\rm L} - \Omega$) as a function of the detuning of the incident laser from the plasmon Δ, calculated with the analytical model [Eq. (7.63)] (red line) and with the full numerical model (black crosses). The other parameters used for the calculation in (a-d) are $\hbar\gamma_b = 2$ meV, $\hbar\gamma_\sigma = 2\times10^{-5}$ eV, $\hbar\gamma_a = 150$ meV, $\hbar g = 100$ meV, $\gamma_\phi = 0\,$eV. $\Delta = \tilde{\delta}$.

as determined by $\mathcal{J}_0(s)$ [the emission at the Raman frequencies corresponds to $\mathcal{J}_0(\pm\Omega)$]. The enhancement of the Stokes scattering at frequency $\omega_{\rm L}-\Omega$ leads to an enhancement of the vibrational pumping $\Gamma_{\rm v}^{\rm pump}$ (a vibrational quantum is created with each emitted Stokes photon), while the anti-Stokes emission at frequency $\omega_{\rm L}+\Omega$ contributes to the vibrational damping $\Gamma_{\rm v}^{\rm dec}$. A similar interpretation has also been shown to be valid for off-resonant SERS [103, 104, 321, 322]. Figure 7.11 illustrates the validity of our model. We show in Fig. 7.11 (a,b) 2D color map plots of the incoherent part of the vibrational population $\langle\langle \hat{b}^\dagger \hat{b} \rangle\rangle_{\rm SS} = \langle \hat{b}^\dagger \hat{b} \rangle_{\rm SS} - |\langle \hat{b} \rangle_{\rm SS}|^2$ as a function of vibrational frequency Ω and of detuning Δ of the laser from the plasmon frequency. We display the incoherent part of the population, as the coherent part $|\langle \hat{b} \rangle_{\rm SS}|^2$ represents a constant static displacement of the vibration due to the coherent laser pumping. We compare numerical results with the analytical calculations using

$$\langle\langle\hat{b}^\dagger\hat{b}\rangle\rangle_{\mathrm{SS}} \approx \langle\hat{b}^\dagger\hat{b}\rangle_{\mathrm{SS,in}} = \frac{\Gamma_{\mathrm{v}}^{\mathrm{pump}}}{\gamma_b + \Gamma_{\mathrm{v}}^{\mathrm{dec}} - \Gamma_{\mathrm{v}}^{\mathrm{pump}}}. \tag{7.51}$$

The approximate [Fig. 7.11 (a)] and exact [Fig. 7.11 (b)] results are very similar, both exhibiting a clear population maximum for detuning ≈ −100 meV and frequency of the vibrational mode ≈ 180 meV. This maximum can be understood as a consequence of the two-step process described above.

r-SERS spectra

Although the vibrational populations provide important information about the system dynamics, the quantity typically accessible in experiments is the inelastic Raman emission spectrum [Eq. (7.14)]. By using the separation of the system into the slowly decaying vibrational mode and the fast decaying excitations of the J-C reservoir, we are able to isolate the Raman contribution to the scattering spectrum from the fluorescence background. Due to the separation of time scales described in Section 7.3.1, we can assume that the vibrations induce changes of the reservoir (J-C) operators which immediately (adiabatically) follow the changes at the vibrational operators. In the adiabatic approximation we assume that the vibrational operators satisfy the effective vibrational dynamics given by the Hamiltonian $\hat{H}_{\mathrm{v}}$ [Eq. (7.41)], the incoherent intrinsic damping $\mathscr{L}_{\hat{b}}^{\gamma_b}(\hat{\rho})$, and also that they are implicitly dependent on the reservoir via the reservoir-induced coherent and incoherent pumping, $\mathscr{L}_{\hat{b}^\dagger}^{\Gamma_{\mathrm{v}}^{\mathrm{pump}}}(\hat{\rho})$ [Eq. (7.24)], and damping, $\mathscr{L}_{\hat{b}}^{\Gamma_{\mathrm{v}}^{\mathrm{dec}}}(\hat{\rho})$ [Eq. (7.23)]. Based on these assumptions, we write the following set of Heisenberg-Langevine equations describing the dynamics of the J-C system operators coupled to the vibrations (in the frame rotating with the laser frequency ω_{L}). The Heisenberg-Langevine equations have almost the same form as the equations governing the dynamics of the operator mean values, but they additionally include the noise terms that are needed to preserve the operators commutation relations [158, 161]. The relevant equations can be derived from $\hat{H}_{\mathrm{J-C,p}}$, $\hat{H}_{\mathrm{TLS-v}}$ [Eqs. (7.40) and (7.42)], and adding the damping terms that arise from $\mathscr{L}_{\hat{\sigma}}^{\gamma_a}[\hat{\rho}]$ [Eq. (7.7)] and $\mathscr{L}_{\hat{\sigma}}^{\gamma_\sigma}[\hat{\rho}]$ [Eq. (7.18)]:

$$\begin{bmatrix}\dot{\hat{a}}\\ \dot{\hat{\sigma}}\end{bmatrix} \approx \begin{bmatrix}-\mathrm{i}\Delta - \gamma_a/2 & -\mathrm{i}g\\ -\mathrm{i}g & -\mathrm{i}\Delta - \gamma_\sigma/2\end{bmatrix}\cdot\begin{bmatrix}\hat{a}\\ \hat{\sigma}\end{bmatrix} + \begin{bmatrix}0\\ -\mathrm{i}\Omega d\langle\hat{\sigma}\rangle_{\mathrm{SS}}(\hat{b}^\dagger + \hat{b})\end{bmatrix} + \text{Noise terms}, \tag{7.52}$$

The inhomogeneous term in Eq. (7.52) has been derived with the use of the decomposition of the lowering operator of the TLS, $\hat{\sigma} = \langle\hat{\sigma}\rangle_{\mathrm{SS}} + \delta\hat{\sigma}$, and $\hat{\sigma}^\dagger\hat{\sigma} \approx |\langle\hat{\sigma}\rangle_{\mathrm{SS}}|^2 + \langle\hat{\sigma}\rangle_{\mathrm{SS}}\delta\hat{\sigma}^\dagger + \langle\hat{\sigma}^\dagger\rangle_{\mathrm{SS}}\delta\hat{\sigma}$, and neglecting $\delta\hat{\sigma}(\hat{b}^\dagger + \hat{b})$. This assumption restricts our further calculations to the first-order Raman scattering.

The solution for the plasmon annihilation operator relevant for the SERS process is represented by the inhomogeneous solution of these differential equations [Eq. (7.52)]. We first solve the homogeneous part by diagonalizing the matrix:

$$\begin{bmatrix} -\mathrm{i}\Delta - \gamma_a/2 & -\mathrm{i}g \\ -\mathrm{i}g & -\mathrm{i}\Delta - \gamma_\sigma/2 \end{bmatrix} = \\ = \mathbf{P}_\mathrm{C}\,\mathbf{D}_\mathrm{C}\,{\mathbf{P}_\mathrm{C}}^{-1}.$$

where $\mathbf{D}_\mathrm{C} = \mathrm{diag}\{\lambda_1^{\mathrm{SC}}, \lambda_2^{\mathrm{SC}}\}$ contains the eigenvalues $\lambda_{1(2)}^{\mathrm{SC}}$ of the matrix and the columns of $\mathbf{P}_\mathrm{C}$ contain the respective eigenvectors.

The inhomogeneous solution of the equations $\mathbf{v}_{\mathrm{inh}}$ in the steady state becomes

$$\mathbf{v}_{\mathrm{inh}}(t) \approx \int_{-\infty}^{t} \mathbf{P}_\mathrm{C}\, e^{\mathbf{D}_\mathrm{C}(t-t')}\, {\mathbf{P}_\mathrm{C}}^{-1}\, \mathbf{RHS}(t')\, \mathrm{d}t', \tag{7.53}$$

where $\mathbf{RHS}(t')$ is

$$\mathbf{RHS}(t') = \begin{bmatrix} 0 \\ -\mathrm{i}\Omega d\langle\hat{\sigma}\rangle_{\mathrm{SS}}[\hat{b}(t')^\dagger + \hat{b}(t')] \end{bmatrix}. \tag{7.54}$$

In particular, the steady-state inhomogeneous solution for the plasmon annihilation operator, $\hat{a}_{\mathrm{inh}}(t)$, adiabatically depends on the vibrational operators as follows:

$$\hat{a}_{\mathrm{inh}}(t) \approx -\mathrm{i}\Omega d\langle\hat{\sigma}\rangle_{\mathrm{SS}} \int_{-\infty}^{t} e^{-\lambda_1^{\mathrm{SC}}(t'-t)} \frac{g}{\sqrt{4g^2 - (\gamma_a - \gamma_\sigma)^2/4}} [\hat{b}(t')^\dagger + \hat{b}(t')]\mathrm{d}t' + \\ + \mathrm{i}\Omega d\langle\hat{\sigma}\rangle_{\mathrm{SS}} \int_{-\infty}^{t} e^{-\lambda_2^{\mathrm{SC}}(t'-t)} \frac{g}{\sqrt{4g^2 - (\gamma_a - \gamma_\sigma)^2/4}} [\hat{b}(t')^\dagger + \hat{b}(t')]\mathrm{d}t'. \tag{7.55}$$

In the adiabatic approximation, the slowly varying part of the vibrational operators $\hat{\hat{b}}(t')$ [with $\hat{b}(t') = \hat{\hat{b}}(t')e^{-\mathrm{i}\Omega t'}$] can be evaluated at time $t' \to t$ and the integration can then be performed explicitly, giving:

$$\begin{aligned} \hat{a}_{\mathrm{inh}}(t) \approx & -\mathrm{i}\Omega d\langle\hat{\sigma}\rangle_{\mathrm{SS}} \frac{g}{\sqrt{4g^2 - (\gamma_a - \gamma_\sigma)^2/4}} \left[\frac{1}{(\mathrm{i}\Omega - \lambda_1^{\mathrm{SC}})} - \frac{1}{(\mathrm{i}\Omega - \lambda_2^{\mathrm{SC}})}\right] \hat{b}^\dagger(t) \\ & -\mathrm{i}\Omega d\langle\hat{\sigma}\rangle_{\mathrm{SS}} \frac{g}{\sqrt{4g^2 - (\gamma_a - \gamma_\sigma)^2/4}} \left[\frac{1}{(-\mathrm{i}\Omega - \lambda_1^{\mathrm{SC}})} - \frac{1}{(-\mathrm{i}\Omega - \lambda_2^{\mathrm{SC}})}\right] \hat{b}(t) \\ & + \text{Noise terms} \\ & \equiv -\mathrm{i}\Omega d\langle\hat{\sigma}\rangle_{\mathrm{SS}}\mathcal{A}_0(-\Omega)\hat{b}^\dagger(t) - \mathrm{i}\Omega d\langle\hat{\sigma}\rangle_{\mathrm{SS}}\mathcal{A}_0(\Omega)\hat{b}(t) + \text{Noise terms}, \end{aligned} \tag{7.56}$$

where we have defined

$$\mathcal{A}_0(\Omega) = \frac{g}{\sqrt{4g^2 - (\gamma_a - \gamma_\sigma)^2/4}} \left[\frac{1}{(-\mathrm{i}\Omega - \lambda_1^{\mathrm{SC}})} - \frac{1}{(-\mathrm{i}\Omega - \lambda_2^{\mathrm{SC}})}\right]. \tag{7.57}$$

Finally, the calculation of the emission spectra requires the evaluation of the two-time correlation function $\langle\langle a^\dagger(0)a(\tau)\rangle\rangle$ as

$$s_{\mathrm{e}}(\omega) \approx 2\,\mathrm{Re}\left\{\int_0^\infty \left\langle\left\langle \hat{a}^\dagger_{\mathrm{inh}}(0)\hat{a}_{\mathrm{inh}}(\tau)\right\rangle\right\rangle e^{\mathrm{i}\omega\tau}\,\mathrm{d}\tau\right\}. \tag{7.58}$$

Using the expression in Eq. (7.56) we obtain:

$$\begin{aligned}
&\left\langle\left\langle \hat{a}^\dagger_{\mathrm{inh}}(0)\hat{a}_{\mathrm{inh}}(\tau)\right\rangle\right\rangle \approx \\
&\approx \Omega^2 d^2 |\langle\hat{\sigma}\rangle_{\mathrm{SS}}|^2 |\mathcal{A}_0(-\Omega)|^2 \left\langle\left\langle \hat{b}(0)\hat{b}^\dagger(\tau)\right\rangle\right\rangle && (7.59)\\
&+ \Omega^2 d^2 |\langle\hat{\sigma}\rangle_{\mathrm{SS}}|^2 |\mathcal{A}_0(\Omega)|^2 \left\langle\left\langle \hat{b}^\dagger(0)\hat{b}(\tau)\right\rangle\right\rangle && (7.60)\\
&+ \Omega^2 d^2 |\langle\hat{\sigma}\rangle_{\mathrm{SS}}|^2 \mathcal{A}_0^*(\Omega)\mathcal{A}(-\Omega) \left\langle\left\langle \hat{b}^\dagger(0)\hat{b}^\dagger(\tau)\right\rangle\right\rangle && (7.61)\\
&+ \Omega^2 d^2 |\langle\hat{\sigma}\rangle_{\mathrm{SS}}|^2 \mathcal{A}_0^*(-\Omega)\mathcal{A}(\Omega) \left\langle\left\langle \hat{b}(0)\hat{b}(\tau)\right\rangle\right\rangle, && (7.62)
\end{aligned}$$

from which the first two contributions represent the Stokes [Eq. (7.59)] and the anti-Stokes [Eq. (7.60)] contributions, respectively. The other terms can be neglected in the regime considered as the expectation values operators $\hat{b}\hat{b}$ and $\hat{b}^\dagger\hat{b}^\dagger$ are only sensitive to coherences between higher vibrational excited states.

The resulting expressions for the Stokes ($s_{\mathrm{e,St}}$) and anti-Stokes ($s_{\mathrm{e,aSt}}$) emission spectral lines are

$$s_{\mathrm{e,St}}(\omega) = \Omega^2 d^2 |\langle\hat{\sigma}\rangle_{\mathrm{SS}}|^2 |\mathcal{A}_0(-\Omega)|^2\, 2\,\mathrm{Re}\left\{\int_0^\infty \langle\langle \hat{b}(0)\hat{b}^\dagger(\tau)\rangle\rangle e^{\mathrm{i}(\omega-\omega_{\mathrm{L}})\tau}\mathrm{d}\tau\right\}, \tag{7.63}$$

$$s_{\mathrm{e,aSt}}(\omega) = \Omega^2 d^2 |\langle\hat{\sigma}\rangle_{\mathrm{SS}}|^2 |\mathcal{A}_0(\Omega)|^2\, 2\,\mathrm{Re}\left\{\int_0^\infty \langle\langle \hat{b}^\dagger(0)\hat{b}(\tau)\rangle\rangle e^{\mathrm{i}(\omega-\omega_{\mathrm{L}})\tau}\mathrm{d}\tau\right\}, \tag{7.64}$$

where $|\langle\hat{\sigma}\rangle_{\mathrm{SS}}|^2$ is given by Eq. (7.49) and it can be shown that $|\mathcal{A}_0|^2$ is the reservoir spectral function that describes the enhancement of the emission of the Raman photons into the far field due to the presence of the Jaynes-Cummings system (we assume that the emission from the molecule via the plasmon is much stronger than its direct far-field emission):

$$\begin{aligned}
|\mathcal{A}_0(s)|^2 &= \left|\int_0^\infty \langle\langle \hat{a}(\tau)\hat{\sigma}^\dagger(0)\rangle\rangle e^{\mathrm{i}s\tau}\mathrm{d}\tau\right|^2 = \\
&= \frac{g^2}{g^4 - 2g^2[(\Delta-s)^2 - \gamma_\sigma\gamma_a/4] + [\gamma_\sigma^2/4 + (\Delta-s)^2][\gamma_a^2/4 + (\Delta-s)^2]}.
\end{aligned} \tag{7.65}$$

This function is double peaked since we assume the plasmon-exciton strong coupling regime, and, for the conditions considered here, the peak positions, $s_\pm^{\mathcal{A}} = \Delta \pm \sqrt{g^2 - (\gamma_\sigma^2 + \gamma_a^2)/8}$, are similar to $s_\pm^{\mathcal{J}}$ for the spectral function $\mathcal{J}_0(s)$.

Last, the integrals of the vibrational correlation functions in Eqs. (7.63) and (7.64) represent the emission line shape (as a function of ω) that can be obtained from the equations describing the dynamics of the vibration coupled with the reservoir [104]:

$$\dot{\hat{b}} \approx -\mathrm{i}\Omega\hat{b} - \gamma_{\mathrm{vdp}}\hat{b} + \text{Noise terms}, \tag{7.66}$$

with $\gamma_{\mathrm{vdp}} = \gamma_b + \Gamma_{\mathrm{v}}^{\mathrm{dec}} - \Gamma_{\mathrm{v}}^{\mathrm{pump}}$. Applying the quantum regression theorem to these equations we obtain

$$\mathrm{Re}\left\{\int_0^\infty \langle\langle\hat{b}(0)\hat{b}^\dagger(t)\rangle\rangle e^{\mathrm{i}(\omega-\omega_{\mathrm{L}})t}\right\} = \frac{\gamma_{\mathrm{vdp}}/2}{(\omega-\omega_{\mathrm{L}}+\Omega)^2+\gamma_{\mathrm{vdp}}^2/4}\left(1+\langle\langle\hat{b}^\dagger\hat{b}\rangle\rangle_{\mathrm{SS}}\right), \tag{7.67}$$

$$\mathrm{Re}\left\{\int_0^\infty \langle\langle\hat{b}^\dagger(0)\hat{b}(t)\rangle\rangle e^{\mathrm{i}(\omega-\omega_{\mathrm{L}})t}\right\} = \frac{\gamma_{\mathrm{vdp}}/2}{(\omega-\omega_{\mathrm{L}}-\Omega)^2+\gamma_{\mathrm{vdp}}^2/4}\langle\langle\hat{b}^\dagger\hat{b}\rangle\rangle_{\mathrm{SS}}. \tag{7.68}$$

The emitted signal [Eq. (7.63) and (7.64)] is thus proportional to the efficiency of the excitation of the system $\propto |\langle\hat{\sigma}\rangle_{\mathrm{SS}}|^2$ and to the emission enhancement due to the coupled TLS-plasmon, $|\mathcal{A}_0(s)|^2$. Furthermore, the anti-Stokes and Stokes lines are proportional to the incoherent population of the vibrations $\langle\langle\hat{b}^\dagger\hat{b}\rangle\rangle_{\mathrm{SS}}$ and to $1+\langle\langle\hat{b}^\dagger\hat{b}\rangle\rangle_{\mathrm{SS}}$ [323], respectively [Eqs. (7.68) and (7.67)], where $\langle\langle\hat{b}^\dagger\hat{b}\rangle\rangle_{\mathrm{SS}}$ itself is enhanced by the effect of the reservoir on the excitation and emission process [Eqs. (7.44) to (7.46)]. The line width of the Raman peaks is finally given by the interplay between the damping rates γ_b together with $\Gamma_{\mathrm{v}}^{\mathrm{dec}}$, both broadening the peak, and the pumping rate $\Gamma_{\mathrm{v}}^{\mathrm{pump}}$ that narrows the peak. These properties again mirror the behavior discussed for off-resonant Raman [102–104], except for the presence of a more complex reservoir.

Figure 7.11 (c,d) illustrates the behavior of the resulting Raman emission for a vibrational mode of energy $\hbar\Omega = 50$ meV and $d = 0.1$. We first show in Fig. 7.11 (c) the emission spectra obtained from the numerical solution of the full system [Hamiltonian in Eq. (7.39) and the corresponding loss terms], as a function of the detuning Δ of the laser from the plasmon frequency. As discussed above, the inelastic emission can be split into two components. The emission resulting from the resonant fluorescence of the J-C system, and the Raman emission yielding the vibrational lines. The former is present in the emission spectra of Fig. 7.11 (c) as a broad symmetrical background around zero detuning $\Delta = 0$, in agreement with previous studies [234]. The strong Raman-Stokes line is also clearly distinguishable on top of the background at $\omega_{\mathrm{L}} - \Omega$, accompanied by a second-order Stokes transition line (not described by the analytical model that accounts only for the first-order transition) at $\omega_{\mathrm{L}} - 2\Omega$ and a very weak anti-Stokes line at $\omega_{\mathrm{L}} + \Omega$.

To better analyse the Δ dependence of the Raman signal, we focus in Fig 7.11 (d) on the maximum of the Stokes line, which we plot as a function of the laser detuning Δ as calculated from the full numerical model (black dots) and as given by the analytic expression in Eq. (7.63) (red line). The agreement between the two is excellent. We observe a double-peaked structure, a clear signature of plasmon-exciton coupling considered here, which, however, is not symmetric with respect to $\Delta = 0$, but its central minimum is blue-detuned by 25 meV. This blue detuning can be seen as the result of having to optimize the product of the enhancement at the excitation ω_{L} and emission $\omega_{\mathrm{L}} - \Omega$ frequencies, given by $|\langle\hat{\sigma}\rangle_{\mathrm{SS}}|^2$ and $|\mathcal{A}_0(s)|^2$, respectively (assuming that the vibrational population remains small $\langle\langle\hat{b}^\dagger\hat{b}\rangle\rangle_{\mathrm{SS}} \ll 1$).

7.3.2 Effect of strong electron-vibration coupling

We now consider scenarios that go beyond the assumptions of the previous section. Up to know, we have assumed that the coupling between the molecular vibrational and electronic states, characterized by the dimensionless displacement d, is weak. However, when the interaction becomes stronger, and thus the time scale of the coupling between the electronic TLS and the phonon is shortened, the dynamics of the J-C system coupled to the vibrational mode are no longer separable into a slow vibrational dynamics driven by the fast relaxing reservoir. For large d, we thus cannot apply the formalism developed in the previous section and we need to use the full numerical solution to obtain the response of the system.

We show in Fig. 7.12 (a,b) the vibrational population maps for relatively large electron-vibration coupling (a) $d = 0.5$ and (b) $d = 1$ as a function of laser detuning and vibrational frequency. The lines in Fig. 7.12 (a,b) are similar to those in Fig. 7.11 (a,b), indicating the detuning Δ at which the first-order Stokes line (red line) or the incident laser frequency (green line) match the position of the absorption peaks of the J-C system. For $d = 0.5$ [Fig. 7.12 (a)] the strongest vibrational pumping appears approximately when both conditions are met and the lines cross each other, similarly as for low $d = 0.1$ [Fig. 7.11 (a,b)]. Nonetheless, while for $d = 0.1$ a single clear peak was observed, in this situation two close maxima start emerging near this optimal condition for $d = 0.5$. The effect of large electron-vibration coupling is more apparent when we set $d = 1$ [Fig. 7.12 (b)]. In this case, the dependence of phonon population on the vibrational frequency and detuning becomes very complex as it involves the influence of the higher-order vibronic transitions.

The emission spectra for (c) weak ($d = 0.1$) and (d) strong ($d = 1$) electron-vibration coupling constant and two selected values of pumping amplitude, $\mathcal{E} = 1$ meV and 11 meV, are shown in Fig. 7.12. For $d = 0.1$ the results for both illumination intensities show a clear lower order Stokes peak at $\omega = \omega_{\mathrm{L}} - \Omega$ and a weak anti-Stokes peak at $\omega = \omega_{\mathrm{L}} + \Omega$. A weak second order Stokes peak at $\omega = \omega_{\mathrm{L}} - 2\Omega$ is visible for $\mathcal{E} \approx 1$ meV (for $\mathcal{E} \approx 11$ meV the second order Stokes peak is hidden by the fluorescence background). Increasing the displacement d of the excited state vibrations naturally leads to larger overlaps among vibrational wave functions belonging to different numbers of vibrational excitations, thus facilitating higher-order Raman transitions that yield intense higher-order Raman peaks. This can be seen in Fig. 7.12 (d) where for $d = 1$ intense Raman peaks of higher orders emerge on both the Stokes and anti-Stokes sides of the spectra, most notably for

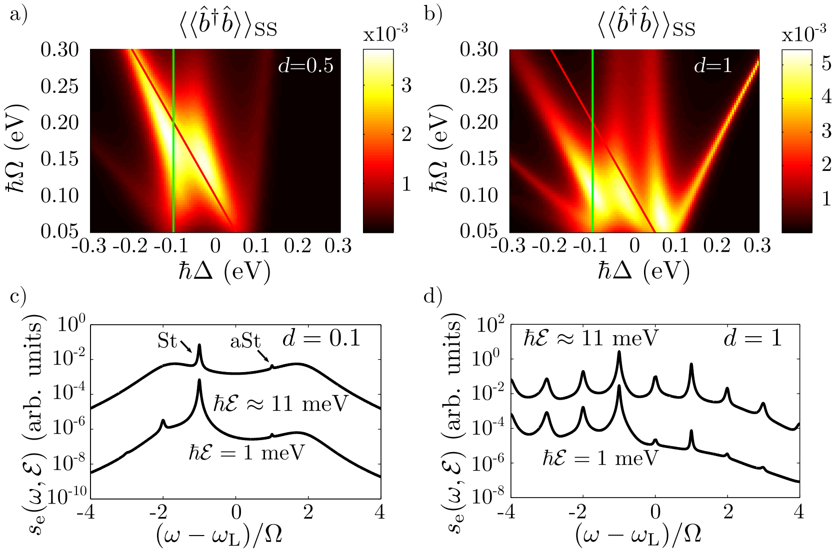

Figure 7.12: Effect of electron-vibration coupling on resonant SERS. (a,b) Populations of the vibrational mode as a function of detuning Δ and vibrational frequency Ω for electron-vibration coupling (Huang-Rhys) parameter (a) $d = 0.5$ and (b) $d = 1$. In both cases, $\mathcal{E} = 1\,\text{meV}$ and there is no pure dephasing. The straight lines mark the conditions where the peak frequency of one of the bare J-C absorption peaks coincides with the frequency of the incident laser (green line) or the first order Stokes line (red line). (c,d) SERS spectra of a molecule supporting a single vibrational mode of energy $\hbar\Omega = 50\,\text{meV}$, for two values of the electron-vibration coupling, (c) $d = 0.1$ and (d) $d = 1$. Two illumination intensities $\mathcal{E} = 1\,\text{meV}$ and $11\,\text{meV}$ are considered in both cases. The other parameters used for all the calculation are: $\hbar\gamma_b = 2$ meV, $\hbar\gamma_\sigma = 2\times10^{-5}$ eV, $\hbar\gamma_a = 150$ meV, $\hbar g = 100$ meV, $\gamma_\phi = 0\,\text{eV}$, $\Delta = \tilde{\delta}$.

$\mathcal{E} \approx 11\,\text{meV}$.

7.3.3 Effect of pure dephasing

So far we have always assumed negligible dephasing. This is the case for optimized experiments at low temperature, however for a typical situation at finite temperature the electronic transition is subjected to a large pure dephasing rate, γ_ϕ, due to interactions with the environment. In molecules decoupled from the plasmonic cavity, the pure dephasing introduces a loss of coherence between the states of the TLS but without directly inducing the decay of the excited state [324]. A careful analysis of the microscopic dephasing mechanism shows that when the plexcitonic states $|N,\pm\rangle$ are formed in the strong-coupling regime, the interaction of the system with the originally purely dephasing reservoir can lead to novel incoherent mechanisms including the energy transfer from the upper plexciton states $|N, +\rangle$ to the lower ones $|N, -\rangle$ within the same manifold [89, 91] (see also Chapter 6). In the following, we again consider that the system is illuminated by a *weak* laser and hence only the single-excitation manifold containing the states $|1, \pm\rangle \equiv |\pm\rangle$ is important for the description of the inelastic light emission from the plexcitons.

We implement the dephasing processes via the following Lindblad terms

$$\mathscr{L}^{\gamma_\phi}_{\hat{\sigma}_{--++}}(\hat{\rho}) = \gamma_\phi \left(2\hat{\sigma}_{--++}\hat{\rho}\hat{\sigma}_{--++} - \{\hat{\sigma}_{--++}\hat{\sigma}_{--++}, \hat{\rho}\}\right) \tag{7.69}$$

$$\mathscr{L}^{\gamma_{\sigma_{-+}}}_{\hat{\sigma}_{-+}}(\hat{\rho}) = \frac{\gamma_{\sigma_{-+}}}{2}\left(2\hat{\sigma}_{-+}\hat{\rho}\hat{\sigma}^\dagger_{-+} - \{\hat{\sigma}^\dagger_{-+}\hat{\sigma}_{-+}, \hat{\rho}\}\right), \tag{7.70}$$

where $\hat{\sigma}_{--++} = |+\rangle\langle+| + |-\rangle\langle-|$ and $\hat{\sigma}_{-+} = |-\rangle\langle+|$. We neglect any further incoherent processes such as the energy transfer from the lower to the upper plexciton as we assume that they are less important [89, 299]. We further set $\hbar\gamma_{-+} = 40\,\mathrm{meV}$ whenever we consider $\hbar\gamma_\phi \neq 0\,\mathrm{eV}$, a rate which leads to relatively strong transfer of populations towards the lower plexcitonic state via the vibrational reservoir of the molecule [271, 285].

To illustrate the effect of dephasing, we start by plotting the absorption spectrum, $s_\mathrm{a}(\omega)$, [Fig. 7.13 (a)] and emission, $s_\mathrm{e}(\omega)$, [Fig. 7.13 (b)] spectra for the bare plasmon-excition J-C system, without vibrations. In both cases we set $\hbar\mathcal{E} = 1\,\mathrm{meV}$, and we show results for intrinsic dephasing $\hbar\gamma_\phi = 0\,\mathrm{meV}$, $10\,\mathrm{meV}$ and 50 meV. For clarity the spectra are vertically shifted. When the dephasing is increased, we observe a clear broadening of the plexciton peaks in the absorption spectrum [Fig. 7.13 (a)], which is larger for the upper plexcitonic peak due to the population transfer to the lower polariton given by Eq. (7.70).

The dephasing-induced broadening also affects the J-C emission spectra $s_\mathrm{E}(\omega)$ shown in Fig. 7.13 (b) for $\mathcal{E} = 1\,\mathrm{meV}$ and $\Delta = 0\,\mathrm{eV}$. When the dephasing is switched on, there appears a strong inelastic light emission originating predominantly from the lower plexciton branch, since the upper branch is efficiently depopulated by the incoherent energy transfer. Without dephasing the emission spectrum practically vanishes as the incoherent population of the plexcitons is low.

Finally, we turn on the interaction between the molecular electronic and vibrational levels and calculate the effect of dephasing on the emission spectra of the complete system. The resulting emission spectra are shown in Fig. 7.13 (c) for the same parameters as the emission spectra of the bare plexcitons in Fig. 7.13 (b). All of the spectra feature a sharp Stokes-Raman peak at frequency $\omega_\mathrm{L} - \Omega$, which for $\hbar\gamma_\phi = 10\,\mathrm{meV}$ and $50\,\mathrm{meV}$ is accompanied by a broad and intense fluorescence background similar in nature to the one already discussed in Fig. 7.13 (b). Particularly for $\hbar\gamma_\phi = 50\,\mathrm{meV}$ the background overwhelms the relatively weak SERS signal. For no dephasing, this background is strongly reduced, and becomes negligible in comparison with the Raman peak.

For completeness, we show in Fig. 7.13 (d) the population of the vibrational level for the same parameter $d = 0.1$, illumination amplitude $\hbar\mathcal{E} = 1$ meV, and for $\hbar\gamma_\phi = 10\,\mathrm{meV}$. The obtained values can be compared with those in Fig. 7.11 (a),

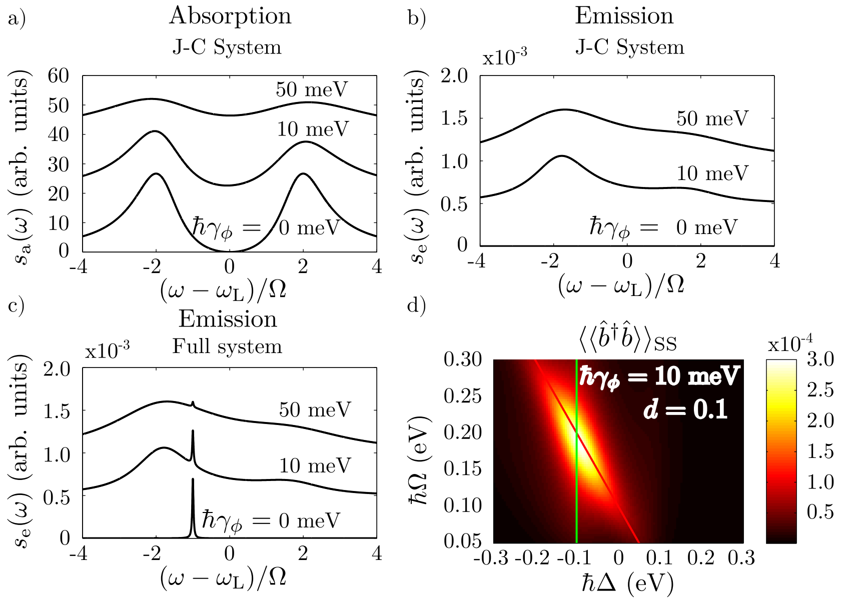

Figure 7.13: Effect of pure dephasing for weak illumination $\hbar\mathcal{E} = 1$ meV and electron-vibration coupling d=0.1. (a) Absorption spectra and (b) emission spectra for the simple J-C system (not considering the vibrations), displayed for three different values of pure dephasing: $\hbar\gamma_\phi = 0\,$meV, $10\,$meV and 50 meV, pumped by monochromatic illumination tuned to the plasmonic resonance $\hbar\Delta = \hbar\omega_c - \hbar\omega_L = 0$. (c) Emission spectra of the full molecule-plasmon system including the vibrational mode of frequency $\hbar\Omega = 50$ meV, for $\hbar\Delta = 0\,$eV and the same γ_ϕ values as in (a,b). The spectra in (a-c) are offset from each other by a constant value of $s_a = 20$ in (a) and $s_e = 0.5 \times 10^{-3}$ in (b,c). (d) Incoherent populations of the vibrational mode as a function of detuning and vibrational frequency for pure dephasing $\hbar\gamma_\phi = 10$ meV. The lines drawn into the color maps mark the detuning Δ for which the first order Stokes line (red line) or the incident laser (green line) coincides with one of the bare J-C absorption peaks. The other parameters used for all the calculations in (a-d) are: $\hbar\gamma_b = 2\,$meV, $\hbar\gamma_\sigma = 2 \times 10^{-5}\,$eV, $\hbar\gamma_a = 150\,$meV, $\hbar g = 100$ meV, $\hbar\Delta = \hbar\tilde{\delta} = 0\,$eV.

where we plotted the same results except that $\hbar\gamma_\phi = 0\,$eV. As could be expected, the most noticeable feature introduced by dephasing is the larger width of the displayed spectral features and the lower populations.

7.3.4 Effect of strong illumination

We consider again in this section a situation of weak electron-vibration coupling, and assume that there is no pure dephasing in the system. However, we turn our attention to situations where the intensity of the incident laser can be strong. An intense laser populates the different manifolds of the J-C ladder and thus leads

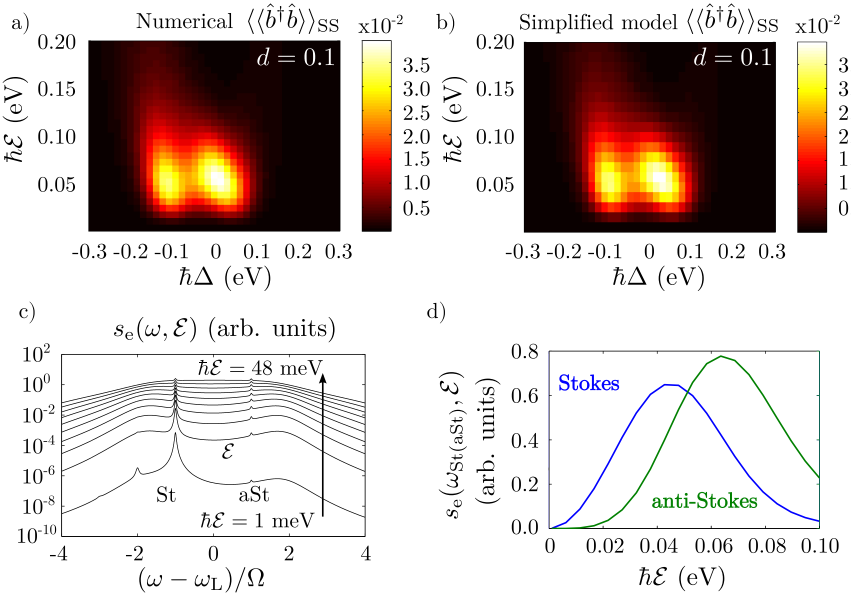

Figure 7.14: Non-linear resonant SERS response for strong laser illumination. (a,b) Populations of a vibrational mode of energy $\hbar\Omega = 50$ meV as a function of the detuning and incident laser amplitude $\mathcal{E}$ calculated from (a) the full numerical model and (b) the simplified model. The vibrations are weakly coupled to the electronic states ($d = 0.1$) and there is no pure dephasing. (c,d) Evolution of the SERS emission with laser illumination amplitude ($\mathcal{E}$), calculated numerically for a single vibrational mode of energy $\hbar\Omega = 50$ meV that is weakly coupled to the electronic states ($d = 0.1$) (c) Emission spectra as a function of $\mathcal{E}$ for detuning of the incident laser $\hbar\Delta = 0$ eV and $d = 0.1$. (d) Maximum intensity of the Stokes (blue line) and anti-Stokes (green line) Raman line as a function of $\mathcal{E}$ (shown in (c) for up to $\hbar\mathcal{E}$ =48 meV). To obtain the value of the Raman peaks, we first subtracted the background, defined as the inelastic emission of the J-C system. The other parameters used for all calculations are: $\hbar\gamma_b = 2$ meV, $\hbar\gamma_\sigma = 2 \times 10^{-5}$ eV, $\hbar\gamma_a = 150$ meV, $\hbar g = 100$ meV, $\hbar\gamma_\phi = 0$ eV, $\Delta = \tilde{\delta}$.

to non-linear effects in the resonant SERS signal that were not included in our weak-illumination expressions. A full analytical treatment of this situation is very challenging, however, we can still gain insight into the vibrational dynamics by assuming the separation of time-scales discussed in Section 7.3.1, and thus inserting the numerically-calculated reservoir spectral function $\tilde{S}(s)$ into the expression of the decay and pumping rates [Eq. (7.51)]. We complement this simplified approach with full numerical calculations.

We plot in Fig. 7.14 the vibrational population as a function of the amplitude $\mathcal{E}$ and detuning Δ of the illumination laser, obtained using the full-numerical [Fig. 7.14 (a)] and semi-analytical [Fig. 7.14 (b)] approaches. The excellent agreement between the two supports the assumption that using very intense laser illumination does not invalidate the separation of the system into a slowly evolving vibrations and a fast J-C reservoir.

Strikingly, the population is strongly non-linear with respect to the intensity $\propto |\mathcal{E}|^2$ of the incident laser. For weak illumination we are in the linear regime, where the population shows local maxima for two different moderate detunings, given by the optomechanical vibrational pumping and damping [Eq. (7.51), together with Eqs. (7.44), (7.45) and Eq. (7.46)], as discussed in the previous section. The population of these peaks initially grows as more energy is pumped into the system by increasing $\mathcal{E}$, but, for a certain laser intensity, the population reaches a maximum and starts to decay. We attribute this behavior to the underlying non-linearity of the J-C system contained in the uneven spacing of the energy levels sketched in Fig. 5.1 (c).

An intense illumination can also affect very strongly the SERS spectra measured in an experiment. We study this situation using full-numerical calculations. As an example we show the inelastic emission spectra as a function of laser amplitude $\mathcal{E}$ for zero detuning $\Delta = 0$ [Fig. 7.14 (c)]. The calculated emission spectra can still be regarded as a combination of the resonance fluorescence background and the Raman lines. For low illumination intensities the spectra in Fig. 7.14 (c) feature a clear Raman-Stokes peak at emission frequency $\omega = \omega_{\text{L}} - \Omega$ with a strength that is comparable to that of the background. One can also distinguish a second-order Stokes peak at $\omega = \omega_{\text{L}} - 2\Omega$ and the anti-Stokes peak at $\omega = \omega_{\text{L}} + \Omega$. As the intensity of the laser is increased, still remaining sufficiently small, the strength of both the background and Raman peaks increases, with the latter being clearly visible. In contrast, for very large laser intensities $\mathcal{E} \gtrapprox 100$ meV the amplitude of the Raman peaks is reduced and the spectrum is fully dominated by the background.

The laser intensity also affects the spectral shape of the background. For example, the two broad background peaks in Fig. 7.14 (c) for $\hbar\mathcal{E} = 1\,\text{meV}$ become a single broad flat feature for $\hbar\mathcal{E} = 48\,\text{meV}$. From these results one can conclude that the laser intensity does not simply scale the emission spectra by a frequency-independent factor, but it changes the overall shape and affects the relative weights of the Raman lines and the background (not shown).

We highlight the non-linear dependence of the maximum of the SERS signal on the incident laser amplitude by plotting the background-free amplitude of the Raman-Stokes (blue line) and anti-Stokes (green line) lines in Fig. 7.14 (d). The background that we subtract from the total signal corresponds to the inelastic emission spectrum of the J-C system uncoupled from the vibrational modes. Fig. 7.14 (c) showed that the intensity dependence of the Stokes and anti-Stokes amplitude resembled the result of the vibrational populations shown in Fig. 7.14 (a,b), with a broad maximum that peaks at an optimal illumination amplitude $\mathcal{E}$. This is consistent with the results in Fig. 7.14 (d), however, interestingly the optimal illumination-field amplitude is different for the Stokes and the anti-Stokes lines. The maximum of the anti-Stokes line appears at roughly the same illumination amplitude $\hbar\mathcal{E} \approx 70\,\text{meV}$ as for the vibrational populations, while the Stokes emission peaks are maximized at lower powers $\mathcal{E} \approx 45\,\text{meV}$.

7.4 Summary

After having introduced the basic concepts of the Raman activity of molecular vibrations, we have shown that the (resonant) Raman process can be described within the scope of the theory of cavity-QED as a hybrid optomechanical system. We have applied this cavity-QED approach to calculate the r-SERS spectra of molecules illuminated by a coherent monochromatic pumping laser, tuned close to the frequency of an electronic transition of a molecule under both weak and strong illumination conditions.

For weak laser illumination the molecule emits both Raman photons, creating sharp emission peaks at the Stokes and anti-Stokes frequencies, and fluorescence photons contributing to a generally broad emission background of the molecule. We have further exploited the optomechanical mechanism to study the mean vibrational populations as a function of the incident laser frequency. We have found that the mechanism of optomechanical vibrational pumping gives rise to higher steady-state mean vibrational populations whenever the generation of the Stokes-Raman emission is enhanced. This occurs either when the incident laser or the emitted Stokes-Raman photon is resonant with the molecular electronic transition.

As the intensity of the laser is increased, the non-linearity of the molecule's electronic transition notably influences its inelastic optical response. When illuminated by an intense pumping laser, the molecular electronic levels are dressed by the strong incident laser field and the resonant fluorescence acquires the form of the Mollow triplet. When the triplet's side peaks appear at the frequency of vibrational Raman photons, either interference features or a complete line splitting combining the Raman and the fluorescence emission mechanisms appear in the spectra. Furthermore, this dressing of the molecular electronic levels can be actively exploited to optically manipulate the populations of molecular vibrations. We note that the intensities of the dressing laser required to achieve the desired regime of the exciton-vibration interaction in the molecules may exceed the damage threshold of many organic molecules. This serious experimental challenge may thus require more stable sample molecules or the use of methods involving pulsed illumination of the sample to avoid excessive heating.

Finally we have explored the situation where the molecular electronic transition is strongly coupled with the plasmonic resonance of the metallic particle. We have shown that even under the conditions of vacuum strong coupling the system can be described in the scope of molecular optomechanics. We have derived analytical expressions for the vibrational pumping and damping rates induced by the optomechanical Stokes and anti-Stokes process, respectively, in a simple situation where the vibrations weakly couple to the Jaynes-Cummings system formed by the hybrid plexcitonic states, no dephasing is considered, and the system is illuminated by a weak incident laser.

We have then studied more complex situations. We have first considered the influence of two intrinsic parameters of the system: the electron-phonon coupling, d, and the pure dephasing γ_ϕ. Larger values of d promote higher-order vibrational transitions and generally increase the interaction strength between the electronic and vibrational states of the molecule, leading to breakdown of the simple reservoir-system picture introduced for small d and to the emergence of higher order Raman peaks in the emission spectra. On the other hand, pure dephasing reduces the efficiency of vibrational pumping, leading to smaller final vibrational populations, and diminishes the vibrational Raman peaks in the inelastic emission spectra. Pure dephasing also significantly broadens and enhances the fluorescence background. As a consequence of the weaker lines and stronger background, the visibility of the Raman lines becomes considerably smaller, complicating resonant-SERS experiments.

Conclusions and outlook

This thesis has been written with an intention to provide a brief but closed and thorough theoretical description of the coupling between light, plasmons, and molecular excitations including vibrations and excitons. In the opening of the thesis (Part I) we have introduced the underlying concepts in the quantum and classical description of light-matter interaction. We have intended to build theoretical tools starting from basic concepts involving classical Maxwell's equations and the quantum many-body Hamiltonian of an interacting electron gas, to end up with the use of cavity-QED models to address the dynamics of molecular and plasmonic excitations. All this effort has been inspired by the aim to describe situations of practical importance in nanophotonics. By applying these models, we have studied surface-enhanced infrared spectroscopy (SEIRS) in Part II, surface-enhanced fluorescence (SEF) in Part III, and surface-enhanced Raman scattering (SERS) in Part IV. Since SEIRS, SEF, and SERS have attained significant theoretical and experimental attention over the last decades, we have attempted to address original aspects of these spectroscopic.

In Part II we have analysed how the ability of plasmonic antennas (plasmonic substrate) to scatter and absorb infrared radiation impacts the formation of molecular spectral fingerprints in SEIRS. We have developed an analytical model to analyse absorption, scattering, and extinction spectral fingerprints of vibrationally active samples interacting with plasmonic substrates. By performing a systematic numerical study, we have found a practical rule of thumb for the design of linear plasmonic antennas for SEIRS: in order to optimize the performance of SEIRS, it is important to utilize antennas whose scattering and absorption efficiency is approximately equal.

In Chapter 5 of Part III we have focused on the description of the microscopic details governing the coupling between molecular excitons and plasmons in atomically-sharp plasmonic cavities. We have identified situations where the geometrical extent of the organic dye molecules supporting the excitons becomes important to obtain a more faithful description of the plasmon-exciton coupling. We have theoretically demonstrated that the highly localized and inhomogeneous plasmonic fields arising around atomistic protrusions in metallic particles are able to break selection rules of optical spectroscopy and thus render the otherwise dark excitonic transitions bright.

In Chapter 6 of Part III we have analysed fluorescence from plasmonic cavities strongly coupled with molecular excitons and coherently driven by a monochromatic laser. We have shown that light emission in such a situation is substantially influenced by incoherent effects arising from the effect of internal (vibrations) and external (solvent) dephasing reservoirs. These incoherent effects give rise to transfer of population between the hybrid plasmon-exciton states and yield spectral asymmetries in the light emission spectra, as often observed in experiments.

Last, in Part IV we have applied the theory of quantum optomechanics to describe resonant and off-resonant SERS. The framework of quantum optomechanics has allowed us to calculate the characteristic Raman spectra of a coupled system containing a plasmonic particle and a molecule. We have described the system by a range of parameters which can characterise both typical SERS systems, as well as state-of-the-art experimental configurations requiring strong plasmon-exciton coupling or strong laser intensities. In the quantum-optomechanical model, the Stokes- and anti-Stokes-Raman emission is intimately connected with processes of optomechanical vibrational pumping and damping which we have addressed in detail for the resonant SERS situation. The vibrational pumping described in this thesis is a plausible mechanism to optically drive chemical reactions involving on-demand selective pumping of molecular vibrations.

We hope that this thesis has also generated many interesting questions and opened several directions worth exploring in future. For example, quantum aspects of the interaction between infrared plasmonic modes and molecular vibrations can be further explored. The quantum nature of the plasmon-vibration coupling may impact, for instance, chemical properties of molecules or could be exploited to engineer collective quantum states of molecular vibrational modes with yet unforeseen applications. The theoretical models used across this thesis could be further combined and extended to account for both coherent and incoherent effects involving plasmons, molecular excitons, molecular vibrations, and interactions of these with their respective environment. It should be possible to exploit such complex modelling to describe, for example, quantum correlations of light emitted by realistic molecules under state-of-the-art experimental conditions. Another field worth exploring is the quantum-chemical description of the plasmon-exciton (and vibration) interaction beyond the model developed in Chapter 5. A worthwhile extension of the model developed here would be to self-consistently account for effects of static and dynamical plasmonic screening on the molecular electronic and vibrational quantum states. Another challenging task is to describe in its full complexity the experimental situation where a molecule of an organic dye is excited by an electric tunneling current and the light emitted by the molecule is recorded. Theory of such spectral mapping would require merging the quantum-optical model of the plasmon-exciton interaction developed in this thesis with a theory of electron tunneling through the dye molecule.

Hopefully, this thesis succeeds in planting a seed for future research directions and helps to discover unexplored and exciting novel aspects of light-matter interaction.

Part V

Appendices

Appendix A

Quantization of surface plasmons

A.1 Condition of quantization for plasmonic surface charge and potential

In this appendix we show how the condition of quantization for the surface-plasmon polarization density $\mathbf{P}_n$ [Eq. (1.57)] can be transformed into the condition for the plasmonic surface charge density σ_n and potential ϕ_n [Eq. (1.58)].

Equation (1.58) naturally emerges from the boundary-integral approach as follows. First one realizes that $\sigma_n^{(+)} = \mathbf{P}_\mathbf{n}^{(+)} \cdot \mathbf{n}$ ($\sigma_n^{(-)} = \mathbf{P}_\mathbf{n}^{(-)} \cdot \mathbf{n}$), and $\nabla\phi_n^{(+)} = L_n\mathbf{P}_\mathbf{n}^{(+)}/\varepsilon_\mathbf{0}$ ($\nabla\phi_n^{(-)} = L_n\mathbf{P}_\mathbf{n}^{(-)}/\varepsilon_\mathbf{0}$). We further apply the Green's first identity together with Laplace's equation to obtain the relationship:

$$\iiint_{V_\mathrm{par}} \nabla\phi_n^{(+)} \cdot \nabla\phi_n^{(-)}\, \mathrm{d}^3\mathbf{r} = \iint_{\partial V_\mathrm{par}} \phi_n^{(+)} \left(\nabla\phi_n^{(-)} \cdot \mathbf{n}\right) \mathrm{d}^2\mathbf{s}, \tag{A.1}$$

which leads to

$$\begin{aligned}\frac{L_n^2}{\varepsilon_0^2} \iiint_{V_\mathrm{par}} \mathbf{P}_n^{(+)} \cdot \mathbf{P}_n^{(-)}\, \mathrm{d}^3\mathbf{r} &= \iiint_{V_\mathrm{par}} \nabla\phi_n^{(+)} \cdot \nabla\phi_n^{(-)}\, \mathrm{d}^3\mathbf{r} \\ = \iint_{\partial V_\mathrm{par}} \phi_n^{(+)} \left(\nabla\phi_n^{(-)} \cdot \mathbf{n}\right) \mathrm{d}^2\mathbf{s} &= \iint_{\partial V_\mathrm{par}} \phi_n^{(+)} \frac{\left(L_n\sigma_n^{(-)}\right)}{\varepsilon_0}\, \mathrm{d}^2\mathbf{s}.\end{aligned} \tag{A.2}$$

The quantization condition for the surface charge density and the potential then follows from the first and the last expressions in Eq. (A.2), by inserting the polarization density from Eq. (1.57), and integrating:

$$\iint_{\partial \mathrm{V}_{\mathrm{par}}} \phi_n^{(+)}\sigma_n^{(-)}\,\mathrm{d}^2\mathbf{s} = \iint_{\partial \mathrm{V}_{\mathrm{par}}}\iint_{\partial \mathrm{V}_{\mathrm{par}}} \frac{\sigma_n^{(+)}(\mathbf{s}')\sigma_n^{(-)}(\mathbf{s})}{4\pi\varepsilon_0|\mathbf{s}-\mathbf{s}'|}\mathrm{d}^2\mathbf{s}\mathrm{d}^2\mathbf{s}'$$
$$= \frac{L_n}{\varepsilon_0}\iiint_{\mathrm{V}_{\mathrm{par}}} \mathbf{P}_n^{(+)}\cdot\mathbf{P}_n^{(-)}\,\mathrm{d}^3\mathbf{r} = \frac{L_n}{\varepsilon_0}\frac{N_e e^2\hbar}{2m_e\omega_n}\iiint_{\mathrm{V}_{\mathrm{par}}} \mathbf{f}_n\cdot\mathbf{f}_n^*\mathrm{d}^3\mathbf{r} = \frac{1}{2}\hbar\omega_n, \qquad \text{(A.3)}$$

where we have used $\omega_n = \sqrt{L_n N_e e^2/(\varepsilon_0 m_e)}$ and employed the integral representation of the potential,

$$\phi_n^{(+)}(\mathbf{s}) = \iint_{\partial \mathrm{V}_{\mathrm{par}}} \frac{\sigma_n^{(+)}(\mathbf{s}')}{4\pi\varepsilon_0|\mathbf{s}-\mathbf{s}'|}\mathrm{d}^2\mathbf{s}'. \qquad \text{(A.4)}$$

The quantization condition then follows from the equality of the initial and the final expression in Eq. (A.3) and adopts the form of Eq. (1.58) in the main text:

$$\iint_{\partial \mathrm{V}_{\mathrm{par}}} \phi_n^{(+)}\sigma_n^{(-)}\,\mathrm{d}^2\mathbf{s} = \frac{1}{2}\hbar\omega_n, \qquad \text{(A.5)}$$

A.2 Interaction of point-like excitons and spherical-particle plasmons

In this appendix we quantize the plasmonic modes of a spherical particle of radius R_{d} and calculate the plasmon-exciton coupling coefficients within the point-dipole approximation of the molecule. In the point-dipole approximation the coupling strength can be described as:

$$\hbar g = \iiint \rho_{\mathrm{PD}}\phi^{(+)}\,\mathrm{d}^3\mathbf{r}, \qquad \text{(A.6)}$$

where $\rho_{\mathrm{PD}} = -\mathbf{d_0}\cdot\nabla\delta(\mathbf{r}-\mathbf{r}')$ is the charge transition density of the point-like molecule with a transition dipole moment $\boldsymbol{d}_0$. Notice that the above definition of the charge density leads to the commonly assumed expression for the coupling between a point-like molecule and the local electric field, $\mathbf{E}_{\mathrm{loc}}^{(+)} = -\nabla\phi^{(+)}$, as:

$$\hbar g = -\mathbf{E}_{\mathrm{loc}}^{(+)}\cdot\mathbf{d}_0. \qquad \text{(A.7)}$$

Outside of the spherical particle, the quantized plasmonic modes (the positive-frequency part) can be described by the corresponding distribution of the electrostatic potential in spherical coordinates $(\theta,\,\varphi,\,r)$ as:

$$\phi_{lm}^{\mathrm{OUT}}(\theta,\varphi,r) = \sqrt{\frac{\hbar\omega_l R_{\mathrm{d}}^{2l+1}}{2\varepsilon_0(2l+1)}}Y_l^m(\theta,\phi)r^{-l-1} \equiv \mathcal{C}_l Y_l^m(\theta,\varphi)r^{-l-1}. \qquad \text{(A.8)}$$

Here $\omega_l = \omega_\mathrm{p}\sqrt{\frac{l}{2l+1}}$ is the frequency of the (lm) plasmonic mode (does not depend on m) and we have defined

$$\mathcal{C}_l = \sqrt{\frac{\hbar\omega_l R_\mathrm{d}^{2l+1}}{2\varepsilon_0(2l+1)}}. \tag{A.9}$$

The spherical harmonics are defined as

$$Y_l^m(\theta,\varphi) = \sqrt{\frac{(2l+1)}{4\pi}\frac{(l-m)!}{(l+m)!}}P_l^m[\cos(\theta)]e^{\mathrm{i}m\varphi}, \tag{A.10}$$

where $P_l^m[\cos(\theta)]$ are the associated Legendre functions [325]. The corresponding surface charge density is

$$\sigma_{lm} = \varepsilon_0(2l+1)\mathcal{C}_l Y_l^m(\theta,\varphi)R_\mathrm{d}^{-l}. \tag{A.11}$$

For completeness we also describe explicitly the potential inside the particle:

$$\phi_{lm}^{\mathrm{IN}}(\theta,\varphi,r) = \mathcal{C}_l R_\mathrm{d}^{-2l-1} Y_l^m(\theta,\varphi) r^l. \tag{A.12}$$

If we consider a point-like dipole positioned at a generic point near the spherical particle $[\theta = 0, \varphi = 0, R_0]$, oriented along the radial direction $(\hat{z})$, we obtain the following expression for the coupling constant $g_{lm}^{\perp}$:

$$\hbar g_{l0}^{\perp} = -\sqrt{\frac{\hbar\omega_l R_\mathrm{d}^{2l+1}}{8\pi\varepsilon_0}} d_0(l+1)R_0^{-l-2}, \tag{A.13}$$

being zero for $m \neq 0$ and where $d_0 = |\mathbf{d}_0|$

A similar calculation of the coupling constants for a point dipole transversally oriented with respect to the radial direction yields the expression for the coupling constant, $g_{lm}^{\parallel}$, which is nonzero only for $m = \pm 1$:

$$\hbar g_{l1}^{\parallel} = \hbar g_{l(-1)}^{\parallel} = -\mathrm{i}d_0\sqrt{\frac{\hbar\omega_l R_\mathrm{d}^{2l+1} l(l+1)}{32\pi\varepsilon_0}} R_0^{-l-2}. \tag{A.14}$$

Appendix B

Numerical implementation of quantum dynamics

In this appendix we provide further details about the numerical procedures that allow for solving the dynamics of the open-quantum systems studied in this thesis and introduced in Chapter 3. We summarize here the numerical approach to the solution of the quantum master equation for the density matrix introduced in Section 3.1.3 and the numerical solution of the Wigner-Weisskopf problem discussed in Section 3.2.

B.1 Numerical implementation of the quantum master equation

In Section 3.1.3 we have derived the quantum master equation for the density matrix, $\hat{\rho}_{\mathrm{S}}$, of an open quantum system [Eq. (3.26)]:

$$\frac{\mathrm{d}}{\mathrm{d}t}\hat{\rho}_{\mathrm{S}} = \frac{1}{\mathrm{i}\hbar}[\hat{\tilde{H}}_{\mathrm{S}}, \hat{\rho}_{\mathrm{S}}] + \sum_{\beta\beta'\alpha} \frac{\gamma^{\mathrm{Lin}}_{\beta'\beta}(\omega_\alpha)}{2} \left(2\hat{\mathcal{A}}_{\alpha\beta}\hat{\rho}_{\mathrm{S}}\hat{\mathcal{A}}^{\dagger}_{\alpha\beta'} - \{\hat{\mathcal{A}}^{\dagger}_{\alpha\beta'}\hat{\mathcal{A}}_{\alpha\beta}, \hat{\rho}_{\mathrm{S}}\}\right). \tag{B.1}$$

and we have remarked that Eq. (3.26) can be written in the form of a vector equation:

$$\dot{\vec{\hat{\rho}}}_{\mathrm{S}} = \mathcal{L}\vec{\hat{\rho}}_{\mathrm{S}}, \tag{B.2}$$

which can be expressed in a suitable matrix representation

$$\boldsymbol{\rho}_{\mathrm{S}} = \begin{bmatrix} \rho_{\mathrm{S}11} & \rho_{\mathrm{S}12} & \cdots \\ \rho_{\mathrm{S}21} & \rho_{\mathrm{S}22} & \cdots \\ \vdots & \vdots & \ddots \end{bmatrix} \rightarrow \vec{\rho}_{\mathrm{S}} = \begin{bmatrix} \rho_{\mathrm{S}11} \\ \rho_{\mathrm{S}21} \\ \vdots \\ \rho_{\mathrm{S}12} \\ \rho_{\mathrm{S}22} \\ \vdots \end{bmatrix}. \tag{B.3}$$

The matrix representation of the superoperator $\mathcal{L}$ can be constructed from the matrix representations of the respective system operators. Eq. (3.26) contains expressions where the operators act on the density matrix from the right or from the left (e.g. the term $\hat{\mathcal{A}}_{\alpha\beta}\hat{\rho}_{\mathrm{S}}\hat{\mathcal{A}}^{\dagger}_{\alpha\beta'}$). In the technical implementation, the expressions are transformed as:

$$\mathbf{O}_1\boldsymbol{\rho}_{\mathrm{S}}\mathbf{O}_2 \rightarrow \left(\mathbf{O}_2^{\mathrm{T}} \otimes \mathbf{O}_1\right)\vec{\rho}_{\mathrm{S}}, \tag{B.4}$$

where $\otimes$ represents a Kronecker product, $^{\mathrm{T}}$ denotes transposition and $\mathbf{O}_1$, $\mathbf{O}_2$ are matrix representations of the respective operators $\hat{O}_1$ and $\hat{O}_2$.

In practise, if the dimension of the truncated Hilbert space is set to N_{H}, the vectorised density matrix has length N_{H}^2 and the matrix $\left(\boldsymbol{O}_2^{\mathrm{T}} \otimes \boldsymbol{O}_1\right)$ is of dimension $N_{\mathrm{H}}^2 \times N_{\mathrm{H}}^2$. This scaling sets a practical constraint to the applicability of the numerical method as large matrices (although often sparse) have to be stored and handled in order to obtain the system dynamics.

B.2 Numerical solution of the Wigner-Weisskopf equation

Here we describe an efficient numerical implementation of the solution of the integro-differential equation (IDE) given by the Wigner-Weisskopf approach in Eq. (3.54) of the main text (Section 3.2), as given in Ref. [326]. Equation (3.54) can be written as an IDE of the general form:

$$\dot{c}_{\mathrm{e}}(t) = -\int_0^t f(t-\tau)c_{\mathrm{e}}(\tau)\mathrm{d}\tau, \tag{B.5}$$

with $f(t-\tau)$ a kernel function which has the Fourier transform

$$F(s) = \frac{1}{\sqrt{2\pi}}\int_{-\infty}^{\infty}\mathrm{d}u f(u)\exp(-\mathrm{i}su). \tag{B.6}$$

By defining a new auxiliary function $\lambda_{\mathrm{W}}(t,u)$, with $u = t - \tau$, we can rewrite Eq. (B.5) as

$$\begin{aligned} \dot{c}_{\mathrm{e}}(t) &= -\lambda_{\mathrm{W}}(t,0), \\ \dot{\lambda}_{\mathrm{W}}(t,u) &= f(u)c_{\mathrm{e}}(t) + \frac{\partial \lambda_{\mathrm{W}}(t,u)}{\partial u}. \end{aligned} \tag{B.7}$$

By introducing the Fourier transform of the second equation in variable u we obtain:

$$\begin{aligned} \dot{c}_{\mathrm{e}}(t) &= -\frac{1}{\sqrt{2\pi}} \int_{-\infty}^{\infty} \mathrm{d}s \Lambda_{\mathrm{W}}(t,s), \\ \dot{\Lambda}_{\mathrm{W}}(t,s) &= F(s)c_{\mathrm{e}}(t) + \mathrm{i}s\Lambda_{\mathrm{W}}(t,s), \end{aligned} \tag{B.8}$$

where $\Lambda_{\mathrm{W}}(t,s) = \frac{1}{\sqrt{2\pi}} \int_{-\infty}^{\infty} \mathrm{d}u \lambda_{\mathrm{W}}(t,u) \exp(-\mathrm{i}su)$, is the Fourier transform of the original function.

The discretization of the Fourier transform leads to the final set of differential equations which need to be solved numerically:

$$\begin{aligned} \dot{c}_{\mathrm{e}}(t) &= -\frac{\Delta s}{\sqrt{2\pi}} \sum_{k \in \mathrm{Grid}} \Lambda_{\mathrm{W}}(t,s_k), \\ \dot{\Lambda}_{\mathrm{W}}(t,s_k) &= F(s_k)c_{\mathrm{e}}(t) + \mathrm{i}s_k\Lambda_{\mathrm{W}}(t,s_k). \end{aligned} \tag{B.9}$$

The set of the differential equations above can be explicitly written in matrix notation as:

$$\begin{bmatrix} \dot{c}_{\mathrm{e}}(t) \\ \dot{\Lambda}_{\mathrm{W}}(t,s_1) \\ \dot{\Lambda}_{\mathrm{W}}(t,s_2) \\ \vdots \end{bmatrix} = \begin{bmatrix} 0 & -\frac{\Delta s}{\sqrt{2\pi}} & -\frac{\Delta s}{\sqrt{2\pi}} & \cdots \\ F(s_1) & \mathrm{i}s_1 & 0 & \\ F(s_2) & 0 & \mathrm{i}s_2 & \\ \vdots & & & \ddots \end{bmatrix} \begin{bmatrix} c_{\mathrm{e}}(t) \\ \Lambda_{\mathrm{W}}(t,s_1) \\ \Lambda_{\mathrm{W}}(t,s_2) \\ \vdots \end{bmatrix} \tag{B.10}$$

In the integration scheme, the generally infinite set of equations [Eq. (B.9)] is evaluated on a grid of finite frequency spacing, Δs, and for a finite range of frequencies around the excitonic particle, $[-s_{\mathrm{max}}, s_{\mathrm{max}}]$. In our implementation, we have selected the spectral range $[-s_{\mathrm{max}}, s_{\mathrm{max}}]$ broad enough so as to contain the entire non-trivial spectral structure of $F(s)$, and a step parameter, Δs, short enough as to avoid an unphysical revival of the dynamics in the time interval of interest.

Appendix C

TDDFT calculations of molecular excitations

In Chapter 5 the transition densities of the dominant optically excited states of methylene blue (MB) and zinc phtalocyanine (ZnPc) molecules are calculated within the linear-response of the time-dependent density functional theory, at the level of the Tamm-Dancoff approximation (TDDFT-TDA) as implemented in NWchem 6.5 [154]. In all the cases the excitations have been calculated for the ground-state equilibrium geometry.

The results presented in this thesis have been calculated using a valence double zeta Pople basis set with a polarization function (6-31G*) and the hybrid functional B3LYP. We further tested the influence of the basis set and functional chosen on the results of the TDDFT calculations. The results are summarized in Table C.1, where, as a figure of merit, we show the calculated excitation energy and transition dipole moment of the respective excitations for different basis sets and functionals. We have checked that the distributions of the transition charge densities of the excitations are not significantly altered when different basis sets/funcionals are utilized. We thus conclude that the particular choice of the basis set and functional does not strongly influence the general results of Chapter 5.

TDDFT results for MB

Functional/basis set	$\hbar\omega_{\mathrm{eg}}$ (eV)	d_z (e·nm)
B3LYP/6-31G*	2.84	0.23
B3LYP/6-31G**	2.84	0.23
B3LYP/6-311++G(2p,2d)	2.77	0.22
CAM-B3LYP/6-31G*	2.92	0.23

TDDFT results for ZnPc

Functional/basis set	$\hbar\omega_{\mathrm{eg}}$ (eV)	$d_{x,y}$ (e·nm)
B3LYP/6-31G*	2.30	0.17
B3LYP/6-31G**	2.30	0.17
B3LYP/6-311++G(2p,2d)[1]	2.27	0.18
CAM-B3LYP/6-31G*	2.33	0.18

Table C.1: Excitation energies, $\hbar\omega_{\mathrm{eg}}$, and values of the transition dipole moment, d_i, along the direction of the i-axis, for the MB and ZnPc excited states studied in Chapter 5.

Appendix D

Exciton dynamics as a function of plasmonic cavity quality factor

Throughout Chapter 5, we consider that the cavity has a broadening proportional to the plasma frequency of the electron gas. In particular, we consider the broadening to be $\gamma_a = 0.01\omega_\mathrm{p}$, which roughly corresponds to a quality factor, Q, of the n plasmon modes ($Q_n \approx \omega_n/\kappa$) of $Q_n \approx 60-70$. These values, appropriate for silver particles for example [227], have been chosen to clearly reveal the influence of the molecular size on the exciton dynamics, however, plasmonic quality factors commonly achieved in plasmonic systems can be slightly smaller, as those in gold, for example ($Q \approx 10-20$). Therefore, we also present here results of the dynamics of exciton population for different values of the plasmon broadening, γ_a. The results are presented in Fig. D.1. We calculate the dynamics for the MB molecule (left, green frame) and for ZnPc (right, yellow frame), using the full quantum model (FQM) (red lines) and thepoint-dipole model (PDM) (black lines), when the molecules are located close to the surface of a spherical particle, as shown in the insets. The molecular exciton frequency is tuned to the frequency of the plasmonic dipolar mode (a-d) and to the plasmonic pseudomode (e-l). The first row (a,e,i) represents the results shown in Chapter 5. We can observe that when the broadening of the plasmonic modes is increased, the oscillating dynamics of the exciton-plasmon state is damped, until it reaches a regime where the Rabi oscillations completely disappear, for $\gamma_a = 0.1\omega_\mathrm{p}$.

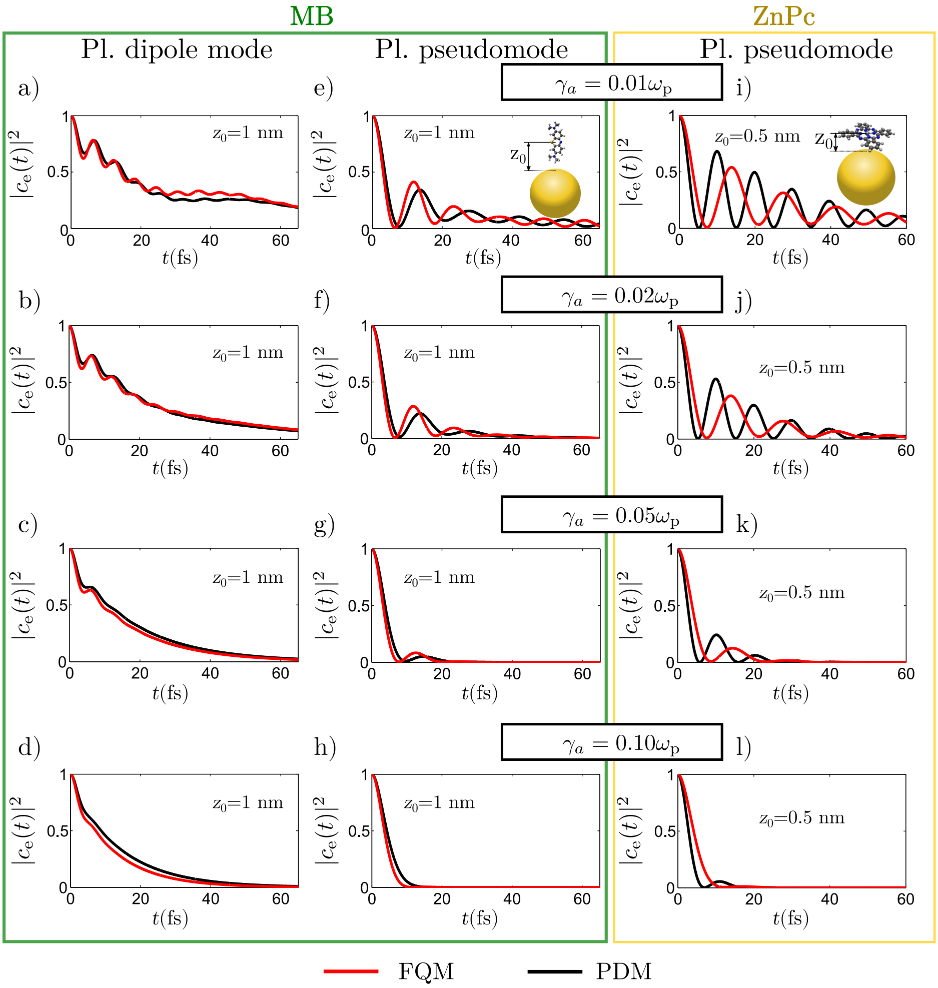

Figure D.1: Decay dynamics of a plasmon-exciton state for different values of the plasmon broadening $\gamma_a/\omega_\mathrm{p}$ (values displayed in the box above each row) for MB (green frame) and ZnPc (yellow frame) molecules. Calculations are performed within the FQM (red lines) and the PDM (black lines). The columns correspond to exciton frequency tuned to (a-d) the plasmonic (Pl.) dipole mode, and (e-l) to the plasmonic (Pl.) pseudomode. The values of the exciton energies are $\hbar\omega_\mathrm{eg} = 2.3$ eV (2.8 eV) for the ZnPc (MB) molecule.

Appendix E

Effects of dephasing reservoir in photon emission of coherently driven organic exciton-polaritons

E.1 Hilbert space for numerical calculations

In Chapter 6 we present a system Hamiltonian containing molecules interacting with their local dephasing reservoirs and a cavity mode. In order to solve the dynamics given by the system Hamiltonian and the Lindblad terms as described in Chapter 6, we need to define a suitable basis for the combined plasmonic, excitonic and vibrational Hamiltonian. We treat the plasmon and exciton on the same footing in the single-excitation manifold. The set of cavity mode-exciton states is written as:

$$\begin{aligned}|\psi_{\mathrm{P-E}}\rangle =&s_0|0_{\mathrm{p}},\,0,\,0,\ldots,\,0\rangle\\ &+s_{\mathrm{p}}|1_{\mathrm{p}},\,0,\,0,\ldots,\,0\rangle\\ &+s_1|0_{\mathrm{p}},\,1,\,0,\ldots,\,0\rangle\\ &+s_2|0_{\mathrm{p}},\,0,\,1,\ldots,\,0\rangle+...,\end{aligned}$$

where s_i are coefficients, the first occupation number represents the number of cavity excitations and the following ones belong to the respective molecular excitons. Alternatively, the states $|1_{\mathrm{p}},\,0,\,0,\ldots,\,0\rangle$ and $|0_{\mathrm{p}},\,1,\,0,\ldots,\,0\rangle$ can represent the lower $|-\rangle$ and upper $|+\rangle$ polaritons, respectively.

The reservoir states are represented in the double-excitation basis as

$$\begin{aligned}|\psi_{\mathrm{res}}\rangle =& v_1|0,\,0,\,0,\ldots,\,0\rangle\\ &+v_2|1,\,0,\,0,\ldots,\,0\rangle\\ &+v_3|0,\,1,\,0,\ldots,\,0\rangle+\ldots\\ &+w_1|2,\,0,\,0,\ldots,\,0\rangle\\ &+w_2|1,\,1,\,0,\ldots,\,0\rangle\\ &+w_3|1,\,0,\,1,\ldots,\,0\rangle+\ldots\\ &+w_{N+1}|0,\,2,\,0,\ldots,\,0\rangle\\ &+w_{N+2}|0,\,1,\,1,\ldots,\,0\rangle+\ldots,\end{aligned}$$

with respective coefficients v_i and w_i. The total state of the system is defined as a Kronecker product of the cavity-molecule and reservoir states

$$|\psi_{\mathrm{tot}}\rangle = |\psi_{\mathrm{P-E}}\rangle \otimes |\psi_{\mathrm{res}}\rangle.$$

This basis defines the dimension of the Hilbert space. With the number of molecules N_{mol} the dimension of the Hilbert space $\mathcal{H}$ grows as $\mathrm{Dim}\,\{\mathcal{H}\} = \mathrm{Dim}\,\{|\psi_{\mathrm{tot}}\rangle\} = (N_{\mathrm{mol}}+1)(N_{\mathrm{mol}}+2)^2/2$. Moreover, the superoperator space necessary for the solution of the quantum master equation has the dimension $\mathrm{Dim}\{\mathcal{S}\} = \mathrm{Dim}\,\{\mathcal{H}\}^4$, which makes the numerical treatment of systems containing larger number of molecules challenging. In the main text we thus present results for a maximum of $N_{\mathrm{mol}} = 5$ molecules.

E.2 Dependence of the emission and absorption spectra of polaritons on the effective reservoir frequency Ω_{R}

In Chapter 6 we describe the effective dephasing reservoir as a broad damped harmonic oscillator of energy $\hbar\Omega_{\mathrm{R}} = 400\,\mathrm{meV}$, width $\hbar\gamma_B = 400\,\mathrm{meV}$ and coupling to the molecular electronic levels via $d_{\mathrm{R}} \approx 0.173$, yielding the reservoir spectral density

$$J(\omega) = \frac{2\gamma_B d_{\mathrm{R}}^2 \Omega_{\mathrm{R}}^2}{(\Omega_{\mathrm{R}}-\omega)^2+\gamma_B^2}. \tag{E.1}$$

Here we briefly discuss the influence of the frequency Ω_{R} on the observed emission spectra. To that end we calculate the polariton emission and absorption spectra [Fig. E.1 (a) and (b), respectively] for $N_{\mathrm{mol}} = 4$ molecules illuminated at the frequency of the upper polariton ($\hbar\omega_{\mathrm{L}} = 2.2\,\mathrm{eV}$) for a constant broadening $\hbar\gamma_B = 400\,\mathrm{meV}$ and varying $\hbar\Omega_{\mathrm{R}} = 100\,\mathrm{meV}$, $200\,\mathrm{meV}$, $300\,\mathrm{meV}$ and $400\,\mathrm{meV}$. We adjust d_{R} such that $J(0)$ remains unchanged for all the cases. For clarity,

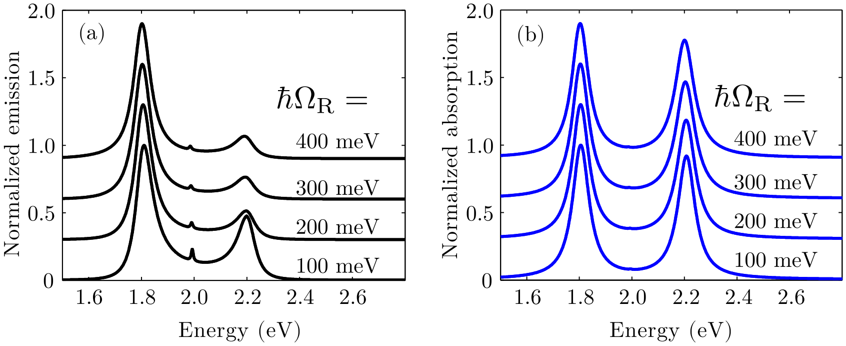

Figure E.1: Polariton (a) emission and (b) absorption spectra for $N_\mathrm{mol} = 4$ molecules illuminated at the frequency of the upper polariton ($\hbar\omega_\mathrm{L} = 2.2\,\mathrm{eV}$) for a constant broadening $\hbar\gamma_B = 400\,\mathrm{meV}$ and varying $\hbar\Omega_\mathrm{R} = 100\,\mathrm{meV}$, $200\,\mathrm{meV}$, $300\,\mathrm{meV}$ and $400\,\mathrm{meV}$. We adjust d_R such that $J(0)$ remains unchanged for all the cases. The spectra are calculated for $\hbar\omega_\mathrm{c} = 2\,\mathrm{eV}$, $\hbar g_i = \hbar g = 100\,\mathrm{meV}$, $\hbar\mathcal{E} = 0.1\,\mathrm{meV}$, $\hbar\gamma_a = 150\,\mathrm{meV}$ and $\hbar\gamma_\sigma = 2\times10^{-2}\,\mathrm{meV}$.

all of the spectra in Fig. E.1 are normalized to the maximal value and vertically displaced.

Fig. E.1 (a) shows that as Ω_R is decreased (from top to bottom), the emission spectra slightly change symmetry, making the emission from the upper polariton slightly more pronounced but preserving the qualitative picture. On the other hand, the absorption spectra remain practically identical for all Ω_R, as shown in Fig. E.1 (b).

Next we study the dependence of the polariton emission and absorption on the polariton splitting, $\omega_+ - \omega_- = 2\sqrt{N_\mathrm{mol}}g$. The spectra are calculated considering the parameters of the reservoir $\hbar\Omega_\mathrm{R} = 400\,\mathrm{meV}$, $\hbar\gamma_\mathrm{R} = 400\,\mathrm{meV}$ and $d_\mathrm{R} \approx 0.173$ and values of $\hbar g$ ranging from $\hbar g = 100\,\mathrm{meV}$ to $\hbar g = 300\,\mathrm{meV}$. In all the cases we consider $N_\mathrm{mol} = 4$ molecules and tune the pumping laser frequency to the frequency of the upper polariton ($\omega_\mathrm{L} = \omega_\mathrm{c} + \sqrt{N_\mathrm{mol}}g$). The emission and absorption spectra are plotted in Fig. E.2 (a) and (b), respectively. We normalize the spectra to the maximum of the lower-polariton peak and apply a constant vertical offset.

Increasing g leads to larger separation of the polariton spectral peaks in both the emission and the absorption spectra. In the emission spectra, the lower-polariton peak is more pronounced than the upper-polariton peak due to the asymetric population transfer. Interestingly, the relative intensity of the upper-polariton peak with respect to the intensity of the lower-polariton peak is decreased when $\approx 2\sqrt{N_\mathrm{mol}}g \approx \Omega_\mathrm{R}$, i.e. when the incoherent population transfer $|+\rangle \to |-\rangle$ becomes resonant [$J(\omega_+ - \omega_-)$ is maximized]. In the absorption spectra the upper- and lower-polariton peaks are of similar intensity.

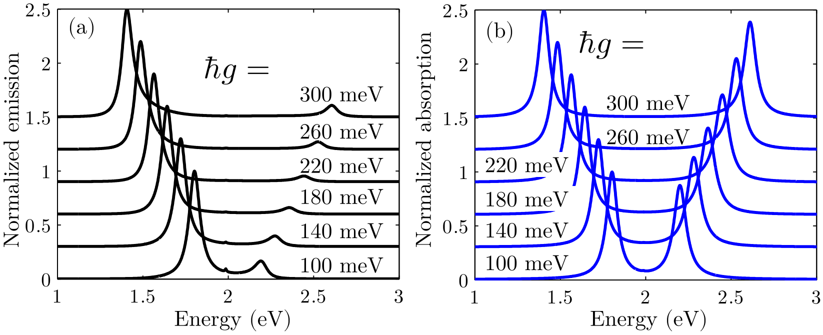

Figure E.2: Polariton (a) emission and (b) absorption spectra for $N_{\mathrm{mol}} = 4$ molecules illuminated at the frequency of the upper polariton for reservoir parameters $\hbar\gamma_B = 400\,\mathrm{meV}$, $\hbar\Omega_{\mathrm{R}} = 400\,\mathrm{meV}$ and $d_{\mathrm{R}} \approx 0.173$. The spectra are calculated for varying $\hbar g_i = \hbar g = 100\,\mathrm{meV}, 140\,\mathrm{meV}, 180\,\mathrm{meV}, 220\,\mathrm{meV}, 260\,\mathrm{meV}$ and $300\,\mathrm{meV}$. The other model parameters are $\hbar\omega_{\mathrm{c}} = 2\,\mathrm{eV}$, $\hbar\mathcal{E} = 0.1\,\mathrm{meV}$, $\hbar\gamma_a = 150\,\mathrm{meV}$ and $\hbar\gamma_\sigma = 2\times10^{-2}\,\mathrm{meV}$.

Appendix F

Vibrational pumping and damping for weak plasmon-exciton coupling and strong laser illumination

In Section 7.2.4 we discuss the effective incoherent dynamics of the molecular vibrations if the electronic and plasmonic degrees of freedom are eliminated from the total system Hamiltonian. We provide the effective damping, $\Gamma_{\mathrm{v}}^{\mathrm{dec}}$, and pumping, $\Gamma_{\mathrm{v}}^{\mathrm{pump}}$ rates [Eqs. (7.23) and (7.24), respectively] in terms of the real part of the reservoir spectral function $\mathrm{Re}\{\tilde{S}(s)\}$. Here we show how an analytical expression for $\mathrm{Re}\{\tilde{S}(s)\}$ can be obtained under the conditions of weak plasmon-exciton coupling and strong incident laser illumination.

We obtain the spectral function $\mathrm{Re}\{\tilde{S}(s)\}$ following the procedure described in references [301, 327]. We start with the master equation describing the TLS dynamics after effective elimination of the plasmonic cavity. In the case of no electron-phonon coupling, this contains the Hamiltonian:

$$\hat{H}_{\mathrm{TLS}} = \hbar\tilde{\delta}\hat{\sigma}_{\mathrm{e}} - \hbar\frac{1}{2}\mathcal{E}_{\mathrm{pl}}\hat{\sigma}_x$$

together with the Lindblad term:

$$\mathscr{L}_{\hat{\sigma}}^{\Gamma_{\mathrm{tot}}}[\hat{\rho}] = \frac{\Gamma_{\mathrm{tot}}}{2}\left(2\hat{\sigma}\hat{\rho}\hat{\sigma}^{\dagger} - \left\{\hat{\sigma}^{\dagger}\hat{\sigma}, \hat{\rho}\right\}\right).$$

Here $\Gamma_{\mathrm{tot}} = \Gamma_{\mathrm{eff}} + \gamma_\sigma$ [see Eq. (5.16) for definition of Γ_{eff}], with γ_σ the intrinsic decay rate of the exciton, and $\langle\langle\hat{\sigma}_{\mathrm{e}}(\tau)\hat{\sigma}_{\mathrm{e}}(0)\rangle\rangle = \langle\hat{\sigma}_{\mathrm{e}}(\tau)\hat{\sigma}_{\mathrm{e}}(0)\rangle - \langle\hat{\sigma}_{\mathrm{e}}\rangle_{\mathrm{SS}}\langle\hat{\sigma}_{\mathrm{e}}\rangle_{\mathrm{SS}}$ is the part of the correlation function that corresponds to the fluctuations of the operators around the steady-state value. We obtain the following equations of motion for the mean values of the operators:

$$\frac{\mathrm{d}}{\mathrm{d}t}\begin{bmatrix}\langle\hat{\sigma}\rangle\\ \langle\hat{\sigma}^{\dagger}\rangle\\ \langle\hat{\sigma}_{\mathrm{e}}\rangle\end{bmatrix}=\begin{bmatrix}-\mathrm{i}\tilde{\delta}-\frac{\Gamma_{\mathrm{tot}}}{2} & 0 & -\mathrm{i}\mathcal{E}_{\mathrm{pl}}\\ 0 & \mathrm{i}\tilde{\delta}-\frac{\Gamma_{\mathrm{tot}}}{2} & \mathrm{i}\mathcal{E}_{\mathrm{pl}}^{*}\\ -\mathrm{i}\mathcal{E}_{\mathrm{pl}}^{*}/2 & \mathrm{i}\mathcal{E}_{\mathrm{pl}}/2 & -\Gamma_{\mathrm{tot}}\end{bmatrix}\cdot\begin{bmatrix}\langle\hat{\sigma}\rangle\\ \langle\hat{\sigma}^{\dagger}\rangle\\ \langle\hat{\sigma}_{\mathrm{e}}\rangle\end{bmatrix}+\begin{bmatrix}\mathrm{i}\mathcal{E}_{\mathrm{pl}}/2\\ -\mathrm{i}\mathcal{E}_{\mathrm{pl}}^{*}/2\\ 0\end{bmatrix}. \tag{F.1}$$

According to the quantum regression theorem [158], the correlation functions $\langle\langle\hat{\sigma}(\tau)\hat{\sigma}_{\mathrm{e}}(0)\rangle\rangle$, $\langle\langle\hat{\sigma}^{\dagger}(\tau)\hat{\sigma}_{\mathrm{e}}(0)\rangle\rangle$ and $\langle\langle\hat{\sigma}_{\mathrm{e}}(\tau)\hat{\sigma}_{\mathrm{e}}(0)\rangle\rangle$ obey the same time evolution as $\langle\hat{\sigma}(\tau)\rangle$, $\langle\hat{\sigma}^{\dagger}(\tau)\rangle$ and $\langle\hat{\sigma}_{\mathrm{e}}(\tau)\rangle$, respectively:

$$\frac{\mathrm{d}}{\mathrm{d}t}\begin{bmatrix}\langle\langle\hat{\sigma}(\tau)\hat{\sigma}_{\mathrm{e}}(0)\rangle\rangle\\ \langle\langle\hat{\sigma}^{\dagger}(\tau)\hat{\sigma}_{\mathrm{e}}(0)\rangle\rangle\\ \langle\langle\hat{\sigma}_{\mathrm{e}}(\tau)\hat{\sigma}_{\mathrm{e}}(0)\rangle\rangle\end{bmatrix}=\begin{bmatrix}-\mathrm{i}\tilde{\delta}-\frac{\Gamma_{\mathrm{tot}}}{2} & 0 & -\mathrm{i}\mathcal{E}_{\mathrm{pl}}\\ 0 & \mathrm{i}\tilde{\delta}-\frac{\Gamma_{\mathrm{tot}}}{2} & \mathrm{i}\mathcal{E}_{\mathrm{pl}}^{*}\\ -\mathrm{i}\mathcal{E}_{\mathrm{pl}}^{*}/2 & \mathrm{i}\mathcal{E}_{\mathrm{pl}}/2 & -\Gamma_{\mathrm{tot}}\end{bmatrix}\cdot\begin{bmatrix}\langle\langle\sigma(\tau)\sigma_{\mathrm{e}}(0)\rangle\rangle\\ \langle\langle\sigma^{\dagger}(\tau)\sigma_{\mathrm{e}}(0)\rangle\rangle\\ \langle\langle\sigma_{\mathrm{e}}(\tau)\sigma_{\mathrm{e}}(0)\rangle\rangle\end{bmatrix} \tag{F.2}$$

with the initial values:

$$\begin{aligned}\langle\langle\hat{\sigma}(0)\hat{\sigma}_{\mathrm{e}}(0)\rangle\rangle&=\langle\hat{\sigma}\rangle_{\mathrm{SS}}(1-\langle\hat{\sigma}_{\mathrm{e}}\rangle_{\mathrm{SS}}),\\ \langle\langle\hat{\sigma}^{\dagger}(0)\hat{\sigma}_{\mathrm{e}}(0)\rangle\rangle&=-\langle\hat{\sigma}^{\dagger}\rangle_{\mathrm{SS}}\langle\hat{\sigma}_{\mathrm{e}}\rangle_{\mathrm{SS}},\\ \langle\langle\hat{\sigma}_{\mathrm{e}}(0)\hat{\sigma}_{\mathrm{e}}(0)\rangle\rangle&=\langle\hat{\sigma}_{\mathrm{e}}\rangle_{\mathrm{SS}}(1-\langle\hat{\sigma}_{\mathrm{e}}\rangle_{\mathrm{SS}}).\end{aligned}$$

Here SS denotes the steady-state values of the respective quantities. The inhomogeneous part in Eq. (F.2) disappears because of the conveniently chosen value of the correlation functions when $\tau\to\infty$.

Equation (F.2) can be solved numerically or analytically. We have obtained the analytical solutions of Eq. (F.2) and used it to evaluate $\tilde{S}(s)$, but we do not present it here due to its algebraic complexity.

List of publications

Publications related to the thesis:

1. **Neuman, T.**, Huck, C., Vogt, J., Neubrech, F., Hillenbrand, R., Aizpurua, J., Pucci, A., "Importance of Plasmonic Scattering for an Optimal Enhancement of Vibrational Absorption in SEIRA with Linear Metallic Antennas", J. Phys. Chem. C **119**, 26652-26662 (2015).

2. Huck, C., Vogt, J., **Neuman, T.**, Nagao, T., Hillenbrand, R., Aizpurua, J., Pucci, A., Neubrech, F., "Strong coupling between phonon-polaritons and plasmonic nanorods", Optics Express **24**, 25528-25539 (2016).

3. **Neuman, T.**, Esteban, R, Casanova, D.,García-Vidal, F. J., Aizpurua, J., "Coupling of molecular emitters and plasmonic cavities beyond the point-dipole approximation", Nano Lett., **18**, 2358-2367 (2018).

4. Konečná, A., **Neuman, T.**, Aizpurua, J., Hillenbrand, R., "Surface-enhanced molecular electron energy loss spectroscopy", ACS Nano, **12**, 4775-4786 (2018).

5. **Neuman, T.**, Aizpurua, J., "Asymmetric light emission from organic exciton-polaritons", Optica, **5**(10), 1247-1255 (2018).

6. **Neuman, T.**, Esteban, R, Giedke, G., Schmidt, M., Aizpurua, J., "Hybrid optomechanical model of resonant SERS for parametric all-optical control of molecular vibrations", Submitted.

7. **Neuman, T.**, Aizpurua, J., Esteban, R, "Theory of resonant SERS in strongly coupled plasmon-exciton systems", In preparation.

Other publications:

1. Dvořák, P., **Neuman, T.**, Břínek, L., Šamořil, T., Kalousek, R., Dub, P., Varga, P., Šikola, T. "Control and Near-Field Detection of Surface Plasmon Interference Patterns", Nano Lett. **13**, 2558-2563 (2013).

2. **Neuman, T.**, Alonso-González, P., Garcia-Etxarri, A., Schnell, M., Hillenbrand, R., Aizpurua, J., "Mapping the near fields of plasmonic

nanoantennas by scattering-type scanning near-field optical microscopy", Laser Photon. Rev. **9**, 637-649 (2015).

3. Schnell, M., Sarriugarte, P., **Neuman, T.**, Khanikaev, A. B., Shvets, G., Aizpurua, J., Hillenbrand, R., "Real-Space Mapping of the Chiral Near-Field Distributions in Spiral Antennas and Planar Metasurfaces", Nano Lett. **16**, 663-670 (2016).

List of symbols

Introduction

λ_{vis}	Wavelength of visible light
$\lvert x\rangle$	Quantum state specified by x: ground ($x = \mathrm{g}$) or excited ($x = \mathrm{e}$) electronic state, singly excited state of an environment ($x = \{1\omega_{k_n}\}$), unoccupied (ground) state of an environment ($x = \{0\omega_{k_n}\}$)
$E^{\mathrm{L}}_{\mathrm{inc}}$, E_{NF}, $E^{(0)}_{\mathrm{NF}}$, $E^{\mathrm{St}}_{\mathrm{NF}}$, $E^{\mathrm{St}}_{\mathrm{FF}}$, $E^{\mathrm{St}}_{\mathrm{inc}}$, E_{A}, E_{AS}, E_{BG}	Electric field of: incident light, plasmonic near field, near-field amplitude, at frequency of Raman-Stokes photon, plasmonic far field at Stokes frequency, incident auxiliary field at Stokes frequency, radiated by antenna, originating from antenna-sample interaction, background
$f^{\mathrm{L}}_{\mathrm{pl}}, f^{\mathrm{St}}_{\mathrm{pl}}$	Field enhancement of the incident light, and of the auxiliary field at the Stokes frequency
α_{mol}	Polarizability of the molecule
q, q_0	Vibrational displacement, amplitude of the vibrational displacement
d_{tot}, d_{St}, d_{aSt}, d_{Ray}, d_0	Dipole moment: Total dipole moment, Stokes dipole moment, anti-Stokes dipole moment , Rayleigh dipole moment, transition dipole moment
$\hat{d}$	Electronic dipole operator
ω_{L}, ω_{St}, ω_{aSt}, ω_{eg}, ω_{k_n}	Angular frequency of: incident light, Stokes, or anti-Stokes photons, the transition between $\lvert\mathrm{g}\rangle$ and $\lvert\mathrm{e}\rangle$, environmental modes
Ω	Vibrational angular frequency
$\mathscr{R}_{\mathrm{St}}$	Raman-Stokes signal
$\mathscr{A}, \mathscr{A}_{\mathrm{BG}}, \mathscr{A}_{\mathrm{AS}}$	Total signal of SEIRS, background signal, signal arising from the antenna-sample interaction
Γ_{eff}, $\Gamma^{\mathrm{rad}}_{\mathrm{eff}}$	Effective decay rate, effective radiative decay rate
η	Quantum yield
$\mathbf{r}_0$	Position of the molecule

Part I

Chapter 1

$\hbar$	Reduced Planck's constant
$\mathbf{r}, \mathbf{r}'$	Position vectors
x, y, z	Cartesian position coordinates
$\rho, \rho_\mathrm{ext}, \rho_\mathrm{tot}, \rho_\mathrm{ind}$	Electric charge density, and electric charge density of: external charge, total charge, induced charge
$\mathbf{J}_\mathrm{ext}, \mathbf{J}_\mathrm{ind}$	External current density, induced current density
$\mathbf{E}, \mathbf{D}, \mathbf{B}, \mathbf{H}, \mathbf{P}, \mathbf{M}$	Electric field, electric displacement field, magnetic field, magnetic H-field, macroscopic polarization field, macroscopic magnetization field
ε_0, μ_0	Vacuum permittivity, vacuum permeability
$\varepsilon, \varepsilon_x$	Dielectric function (relative permittivity), dielectric function of material specified by x
μ	relative permeability
c	Speed of light in vacuum
k	magnitude of the wave vector in vacuum $k = \omega/c$
$\mathbf{G}(\omega, \mathbf{r}, \mathbf{r}')$	Electric dyadic Green's function
$\delta(\mathbf{r} - \mathbf{r}')$	Dirac's delta function
$\mathbf{I}$	Identity dyadic
$\mathbf{R}, R$	$\mathbf{R} = \mathbf{r} - \mathbf{r}'$, $R = \lvert \mathrm{R} \rvert$
$\mathbf{K}(\mathbf{r}, \mathbf{r}')$	Quasi-static dyadic kernel
ϕ, ϕ_ext	Electric potential, external electric potential
σ	Surface charge density
$\mathbf{s}, \mathbf{s}'$	Surface positions
$\mathbf{n_s}$	Outer surface normal at point $\mathbf{s}$
$\mathcal{F}(\mathbf{s}, \mathbf{s}')$	Boundary-integral kernel $\mathcal{F}(\mathbf{s}, \mathbf{s}') = -\frac{\mathbf{n_s} \cdot (\mathbf{s} - \mathbf{s}')}{\lvert \mathbf{s} - \mathbf{s}' \rvert^3}$ for $\mathbf{s} \neq \mathbf{s}'$
$\mathbf{E}_\mathrm{ext}$	External electric field
V_par	Particle volume
$\mathbf{L}$	Depolarization dyadic (factor)
$\mathbf{e_R}$	$\mathbf{e}_\mathrm{R} = \mathbf{R}/R$
$\boldsymbol{\alpha}, \boldsymbol{\alpha}_0$	Particle's polarizability tensor, and quasi-static polarizability tensor
$P_\mathrm{ext}, P_\mathrm{abs}, P_\mathrm{sca}$	Total scattered and absorbed power, absorbed power, scattered power
$\sigma_\mathrm{abs}, \sigma_\mathrm{sca}, \sigma_\mathrm{ext}$	Absorption, scattering, and extinction cross section
I_0	Incident-light intensity
ω_p	Plasma frequency
e	Electron electric charge
N_e	Density of electrons
m_e	Electron mass
γ_e	Electron damping rate

L_n	Depolarization factor of a plasmonic mode n
σ_n	Surface-charge density of a plasmonic mode n
$\omega_{\text{bulk}}, \omega_{\text{sp}}, \omega_{L_n}$	Frequency of bulk, surface, and particle plasmon
$\mathbf{q}$	Wave vector
$\mathbf{P}_{\mathbf{q}}, \mathbf{E}_{\mathbf{q}}, P_{\mathbf{q}}$	Distribution of $\mathbf{q}-$dependent polarization density and electric field; $P_{\mathbf{q}} = \lvert\mathbf{P}_{\mathbf{q}}\rvert$
$\mathbf{q}_{\parallel}, \mathbf{r}_{\parallel}$	$\mathbf{q}-$vector and position vector parallel to the interface
ϕ_n^{IN}	Electrostatic potential induced by the surface-charge distribution of a plasmonic mode n
λ_n	Eigenvalue of surface-integral operator
$\sigma_n, \mathbf{P}_n$	Surface-charge density of a plasmonic mode n, Polarization density of a plasmonic mode n
δ_{nm}	Kronecker delta
$\mathbf{\Pi}_n$	$\mathbf{\Pi}_n \equiv \frac{m_e}{e}\dot{\mathbf{P}}_n$
$\mathbf{f}_n$	Mode function of a plasmonic mode n
$x(t)$, $x^{(+)}(t)$, $x^{(-)}(t)$	Generic real function $x(t)$, its positive [$x^{(+)}(t)$], and negative [$x^{(-)}(t)$] frequency part
$u_n, p_n, u_n^{(+)}, p_n^{(+)}$	Scalar amplitude of displacement, u_n, momentum, $p_n \equiv N_e m_e \frac{\mathrm{d}u_n}{\mathrm{d}t}$, and their respective positive-frequency parts
$\hat{u}_n, \hat{p}_n$	Scalar operators of displacement amplitude, $\hat{u}_n$, and momentum amplitude $\hat{p}_n$.
$\hat{a}, \hat{a}_n$	Annihilation bosonic operator, and annihilation bosonic operator of mode n
$\hat{\mathbf{P}}, \hat{\mathbf{P}}_n^{(+)}, \hat{\mathbf{P}}_n^{(-)}$	Operator of polarization density, positive and negative frequency part of the operator of polarization density for a plasmonic mode n
$\phi_n^{(+)}$, $\phi_n^{(-)}$, $\sigma_n^{(+)}$, $\sigma_n^{(-)}$	Positive- and negative-frequency part of the quantized amplitude of the scalar potential ($\phi_n^{(+)}, \phi_n^{(-)}$) and the surface-charge density ($\sigma_n^{(+)}, \sigma_n^{(-)}$) of a plasmonic mode n
$\hat{\phi}_n^{\text{pl}}, \hat{\sigma}_n^{\text{pl}}$	Operator of the scalar potential and surface charge density of a plasmonic mode n
$H_{\text{pl}}, \hat{H}_{\text{pl}}$	Classical Hamiltonian and quantum Hamiltonian operator of plasmons

Chapter 2

$H_{\text{mol}}, H_{\text{e}}, T_{\text{n}}$	Molecular Hamiltonian, electronic Hamiltonian and nuclear kinetic energy
$\mathbf{R}_I, Q_I, M_I$	Position, charge and mass of nucleus I
$\mathbf{r}_i$	Position of electron i
$\{\mathbf{r}\}, \{\mathbf{R}\}$	Set of electronic and nuclear coordinates
$\tilde{H}_{\text{e}}$	Electronic Hamiltonian free of inter-nuclear interaction
$\Psi(\{\mathbf{r}\}, \{\mathbf{R}\})$	Many-body electronic and nuclear wave function

$\varphi_\alpha(\{\mathbf{r}\};\{\mathbf{R}\})$	Many-body electronic Born-Oppenheimer wave function
$\chi_\alpha(\{\mathbf{R}\})$	Many-body nuclear Born-Oppenheimer wave function
$E_\alpha(\{\mathbf{R}\})$	$\{\mathbf{R}\}$-dependent eigenenergy of an electronic state α
ϵ	Vibrational eigenvalue
$\tau^{(1)}_{I,\alpha\beta}, \tau^{(2)}_{I,\alpha\beta}$	Non-adiabatic couplings
N_{el}	Number of electrons
$n(\mathbf{r})$	Electron density at position $\mathbf{r}$
$\phi_i^{\mathrm{KS}}(\mathbf{r})$	Kohn-Sham functions (orbitals)
λ_i^{KS}	Kohn-Sham eigenvalues
$V_s, V_{\mathrm{ext}}, V_{\mathrm{XC}}$	Effective single-particle potential, external potential and exchange-correlation potential
$E_{\mathrm{el}}, T_{\mathrm{s}}, f_{\mathrm{XC}}$	Total electronic energy, single-particle electronic kinetic energy, and exchange-correlation energy functional
A_{XC}	Exchange-correlation part of quantum mechanical action
$X_{ai}, Y_{ai}, \mathbf{X}, \mathbf{Y}$	Coefficients in linear-response TDDFT and their respective vector representations
$X^I_{ai}, Y^I_{ai}, \mathbf{X}^I, \mathbf{Y}^I$	Coefficients in linear-response TDDFT and their respective vector representations, belonging to the $I-$th electronic excitation
$\delta n, \delta n^I$	Linear perturbation of electronic density and linear perturbation of electronic density for the $I-$th electronic excitation
g_{XC}	$g_{\mathrm{XC}}(\mathbf{r}_1, \mathbf{r}_2) \approx \frac{\delta^2 f_{\mathrm{XC}}}{\delta n(\mathbf{r}_1)\delta n(\mathbf{r}_2)}$
$\mathcal{A}, \mathcal{B}$	Matrices of coefficients appearing in LR-TDDFT
$\rho_{\mathrm{e}_I\mathrm{g}}$	Transition charge density between states $\|\mathrm{g}\rangle$ and $\|\mathrm{e}_I\rangle$
$\tilde{q}_{I,\zeta}$	Mass-weighted coordinate ζ of nucleus I
$\mathbf{U}, U_{ab}$	Dynamical matrix and its components
$\boldsymbol{\Omega}$	Matrix of vibrational frequencies
H_{vib}	Vibrational Hamiltonian
$q_\alpha, p_\alpha, \hat{q}_\alpha, \hat{p}_\alpha$	Mass-weighted displacement, q_α, its conjugate momentum, p_α, of vibrational mode α, and operators of the respective classical variables
$\boldsymbol{\mu}^{\mathrm{M}}, \mu^{\mathrm{M}}_\alpha$	Matrix of reduced masses and its diagonal element
$\hat{b}_{i,\alpha}$	Annihilation operator of a vibrational mode α on top of Born-Oppenheimer surface of the electronic state $\|\mathrm{e}_i\rangle$
$\Omega_{i,\alpha}$	Vibrational frequency of mode α on top of Born-Oppenheimer surface of the electronic state $\|\mathrm{e}_i\rangle$

Chapter 3

$\hat{\rho}$, $\hat{\rho}_{\psi_{\mathrm{eg}}}$ ($\boldsymbol{\rho}_{\psi_{\mathrm{eg}}}$), $\hat{\rho}_{\mathrm{mix}}$ ($\boldsymbol{\rho}_{\mathrm{mix}}$), $\hat{\rho}_{\mathrm{T}}$, $\hat{\rho}_{\mathrm{S}}$, $\hat{\rho}_{\mathrm{E}}$	Density operator (matrix) of a state $\|\psi_{\mathrm{eg}}\rangle$, of a mixed state, of total system, reduced density operator, density operator of the environment
w_α	Classical probability coefficient

$\text{Tr}\{\}, \text{Tr}_\text{E}\{\}$	Trace, partial trace over environmental degrees of freedom E
$\hat{H}, \hat{H}_\text{S}, \hat{H}_\text{SE}, \hat{H}_\text{E}$	Hamiltonian of: the total system, the system of interest, the system-environment coupling, and the environment
$\hat{\mathcal{O}}, \hat{O}, \hat{O}_1, \hat{O}_2$	Generic operators
$\mathscr{L}(\hat{\rho}), \mathscr{L}^{\gamma_\mathcal{O}}_{\hat{\mathcal{O}}}(\hat{\rho})$	Lindblad term, Lindblad term of the form $\mathscr{L}^{\gamma_\mathcal{O}}_{\hat{\mathcal{O}}}(\hat{\rho}) = \frac{\gamma_\mathcal{O}}{2}\left(2\hat{\mathcal{O}}\,\hat{\rho}\,\hat{\mathcal{O}}^\dagger - \left\{\hat{\mathcal{O}}^\dagger\hat{\mathcal{O}}, \hat{\rho}\right\}\right)$
$\gamma^\text{Lin}_{\beta'\beta}, S^\text{Lamb}_{\beta'\beta}$	Decay rate and Lamb shift of an excitation specified by system operators $\hat{\mathcal{A}}_{\beta'}$ and $\hat{\mathcal{A}}_\beta$
$\gamma_\mathcal{O}$	Damping rate corresponding to a Lindblad term $\mathscr{L}^{\gamma_\mathcal{O}}_{\hat{\mathcal{O}}}(\hat{\rho})$ characterised by an operator $\hat{\mathcal{O}}$
$\hat{\mathcal{A}}_\beta, \hat{\mathcal{A}}_{\alpha\beta}(\omega_\alpha)$	System operators, system operators of eigenfrequency ω_α: $\hat{\mathcal{A}}_\beta = \sum_\alpha \hat{\mathcal{A}}_{\alpha\beta}(\omega_\alpha)$
$\hat{\mathcal{B}}_\alpha, \delta\hat{\mathcal{B}}_\alpha$	Reservoir operators: $\delta\hat{\mathcal{B}}_\alpha(s) = \hat{\mathcal{B}}_\alpha(s) - \langle\hat{\mathcal{B}}_\alpha\rangle_\text{res}$
$\hat{H}_\text{av}$	Effective Hamiltonian containing the non-vanishing averages of reservoir operators
$\hat{H}'_\text{S}$	Corrected system Hamiltonian: $\hat{H}'_\text{S} = \hat{H}_\text{S} + \hat{H}_\text{av}$
$\hat{H}_\text{Lamb}$	Hamiltonian containing the Lamb shift
$\hat{\hat{H}}_\text{S}$	Effective system Hamiltonian: $\hat{\hat{H}}_S = \hat{H}_\text{S} + \hat{H}_\text{av} + \hat{H}_\text{Lamb}$
$\hat{U}$, $\hat{U}_x$	Unitary operator, unitery operator specified by x
$\mathcal{L}$	Liouville superoperator
$\vec{\hat{\rho}}$	Vectorised density operator $\hat{\rho}$
$\hat{P}(t,t)$, $\vec{\hat{P}}(t,t)$	Auxiliary operator replacing the density operator in calculation of two-time correlators, $\hat{P}(t,t) = \hat{\rho}_\text{S}(t)\,\hat{O}_1$, and $\hat{P}(t,t)$ in its vectorised form
g^te_j	τ-dependent coefficient of term j appearing in operator dynamics
g_k	Coupling constant between cavity mode (plasmon) k and an exciton
$\omega_\text{eg}, \omega_k$	Frequencies of an electronic transition ($\vert\text{e}\rangle \to \vert\text{g}\rangle$) and an electromagnetic mode k
$J_\text{em}(\omega)$	Spectral density of the electromagnetic environment
$f(t-t_1)$	Integration kernel
$\hat{\sigma}, \hat{a}_k$	$\hat{\sigma} = \vert\text{g}\rangle\langle\text{e}\vert$, and $\hat{a}_k$ an annihilation bosonic operator
c_0, c_e, c_k	Coefficients characterising the state of the plasmon-exciton system
$\hat{N}$	Number operator
$\hat{H}_\text{sys}, \hat{H}_\text{I}$	Hamiltonian of a two-level electronic system and the electromagnetic modes, the interaction between the two-level system and the electromagnetic modes
$\hat{H}_{\text{det},\omega}, \hat{H}_{\text{det}-\text{ph}}$	Hamiltonian of the absorbing detector and the detector-photon interaction
$\hat{E}^{(+)}[\hat{E}^{(-)}]$	Positive (negative) frequency part operator of electric field

$\hat{d}_\omega$	Annihilation operator of the absorbing detector
$W(\omega)$	Rate of photon absorption at frequency ω
$s_{\mathrm{e}}(\omega), s_{\mathrm{a}}(\omega), s_{\mathrm{ta}}$	Normalized emission, absorption and total absorption as a function of frequency ω
$\hat{H}_{\mathrm{PR}}, \hat{H}_{\mathrm{P}}, \hat{H}_{\mathrm{PW}}$	Probe-field Hamiltonian, probe-driving Hamiltonian, and probe-driving Hamiltonian assuming coherent illumination
$\mathcal{E}_{\mathrm{P}}$	Amplitude of probe-system interaction
$\hat{c}$	Annihilation bosonic operator of a probe field
P_{abs}	Probe power absorbed by the system
ω_{P}	Probe angular frequency

Part II

Chapter 4

q, $q^{(+)}$, $q_0^{(+)}$	Vibrational (mass-weighted) coordinate, its positive-frequency part, and amplitude of its positive-frequency part
$\mathbf{d}(q)$	Ground-state dipole moment of a molecule
$\delta\mathbf{d}$, $\delta\mathbf{d}^{(+)}$	Induced dipole moment and its positive-frequency part
$\delta\mathbf{E}$, $\delta\mathbf{E}^{(+)}$, $\delta\mathbf{E}_0^{(+)}$	Incident electric field, its positive-frequency part, and amplitude of its positive-frequency part
$\boldsymbol{\alpha}_{\mathrm{vib}}$	Vibrational polarizability
$V_{\mathrm{vib-rad}}$, T_{vib}, V_{vib}	Potential energy of a dipole in an external electric field, vibrational kinetic energy, and vibrational potential
$\mathfrak{L}$	Lagrangian
Ω, γ_{v}	Vibrational frequency and damping
$\mathbf{F}$	Tensor of vibrational oscillator strength
$N_{\mathrm{mol}}^{\mathrm{d}}$	Density of molecules
ε_{S}, $\varepsilon_{\mathrm{SiO_2}}$	Effective dielectric function of a vibrational medium, and that of $\mathrm{SiO_2}$
ω_{OS}, ω_{TO}, ε_∞	Oscillator strength, transverse-optical phonon frequency, and background (relative) permittivity
α_{A}, α_{S}	Polarizability of an antenna and sample
Ω_{A}, Ω_{S}	Resonance frequency of an antenna and sample
f_{A}, f_{S}	Oscillator strength of an ntenna and sample
γ_{A}, γ_{S}	Damping of an antenna and sample
$\mathbf{r}_{\mathrm{A}}$, $\mathbf{r}_{\mathrm{S}}$	Position of antenna and sample
$\mathbf{d}_{\mathrm{A}}$, $\mathbf{d}_{\mathrm{S}}$	Dipole moment of antenna and sample
G	Scalar component of the electromagnetic dyadic Green's function mediating the antenna-sample interaction
α_{eff}, $\alpha_{\mathrm{eff}}^{\mathrm{AS}}$, $\alpha_{\mathrm{eff}}^{\mathrm{SA}}$	Effective polarizability of a plasmonic antenna, quasi-static effective polarizability of a plasmonic antenna, effective polarizability of the sample

$\sigma^{\mathrm{A}}_{\mathrm{abs}}$, $\sigma^{\mathrm{A}}_{\mathrm{abs}}$, $\sigma^{\mathrm{A}}_{\mathrm{sca}}$	Absorption, extinction, and scattering cross section of a bare antenna
σ_{CF}	Corrected Fano profile
a_{F}, b_{F}, c_{F}, d_{F}, y_{F}, R_{F}	$a_{\mathrm{F}} = \Omega^2_{\mathrm{A}} - \omega^2$, $b_{\mathrm{F}} = -\gamma_{\mathrm{A}}\omega$, $c_{\mathrm{F}} = \Omega^2_{\mathrm{S}} - \omega^2$, $d_{\mathrm{F}} = -\gamma_{\mathrm{S}}\omega$, and $y_{\mathrm{F}} = b_{\mathrm{F}} - R_{\mathrm{F}} f_{\mathrm{A}}$ with $R_{\mathrm{F}} = k^3/(6\pi\varepsilon_0)$
Δ_{F}, Γ, Γ_{c}, δ_{F}, β	$\Delta_{\mathrm{F}} = a_{\mathrm{F}} f_{\mathrm{A}} f_{\mathrm{S}} G^2/(a^2_{\mathrm{F}} + y^2_{\mathrm{F}})$, $\Gamma = \Gamma_{\mathrm{c}} + d_{\mathrm{F}}$, $\Gamma_{\mathrm{c}} = y_{\mathrm{F}} f_{\mathrm{A}} f_{\mathrm{S}} G^2/(a^2_{\mathrm{F}} + y^2_{\mathrm{F}})$, $\delta_{\mathrm{F}} = f_{\mathrm{A}} f_{\mathrm{S}} G^2/(y_{\mathrm{F}} d_{\mathrm{F}})$, $\beta = d^2_{\mathrm{F}}/\Gamma^2$
q_{F}, B_{F}, κ	Fano asymmetry parameter ($q_{\mathrm{F}} = \Delta_{\mathrm{F}}/\Gamma$), Fano dip parameter, Fano frequency parameter ($\kappa = (c_{\mathrm{F}} - \Delta_{\mathrm{F}})/\Gamma$)
δ'_{F}, Γ', Γ'_{c}, κ', q'_{F}, Δ'_{F}, β'	$\delta'_{\mathrm{F}} = f_{\mathrm{A}} f_{\mathrm{S}} G^2/(b_{\mathrm{F}} d_{\mathrm{F}})$, $\Gamma' = \Gamma'_{\mathrm{c}} + d$, $\Gamma'_{\mathrm{c}} = b_{\mathrm{F}} f_{\mathrm{A}} f_{\mathrm{S}} G^2/(a^2_{\mathrm{F}} + b^2_{\mathrm{F}})$, $\kappa' = (c_{\mathrm{F}} - \Delta'_{\mathrm{F}})/\Gamma'$, $q'_{\mathrm{F}} = \Delta'_{\mathrm{F}}/\Gamma'$, $\Delta'_{\mathrm{F}} = a_{\mathrm{F}} f_{\mathrm{A}} f_{\mathrm{S}} G^2/(a^2_{\mathrm{F}} + b^2_{\mathrm{F}})$, $\beta' = d^2_{\mathrm{F}}/\Gamma'^2$
B_{ext}, B_{sca}, B_{abs}	Fano dip parameter for extinction $B_{\mathrm{ext}} = \beta$, for scattering $B_{\mathrm{sca}} = \beta(1 + \delta_{\mathrm{F}})$, and for absorption $B_{\mathrm{abs}} = \beta(1 + \delta'_{\mathrm{F}})$
L_{A}, D_{A}, L, D, D_{phc}	Antenna length, antenna diameter, length of the sample patch, diameter of the sample patch, diameter of a spherical phononic sample
$\mathbf{E}_{\mathrm{A}}$, $\mathbf{P}_{\mathrm{S}}$, $\tilde{\mathbf{P}}_{\mathrm{S}}$	Electric near field induced by an antenna, polarization density in a sample, normalized polarization density in a sample
$\mathbf{E}_{\mathrm{BG}}$, $\mathbf{E}_{\mathrm{AS}}$	Background electric field scattered by an antenna, electric field scattered due to the antenna-sample interaction

Part III

Chapter 5

$\vert N, \mathrm{g(e)}\rangle$	Combined states of a plasmonic cavity and a TLS $\vert N, \mathrm{g(e)}\rangle = \vert N\rangle \otimes \vert\mathrm{g(e)}\rangle$
$\otimes$	Direct product
$\vert N\rangle$	Cavity number state containing N excitations
$\vert N, \pm\rangle$	Hybrid plasmon-exciton states $\vert N, \pm\rangle = (\vert N-1, \mathrm{e}\rangle \pm \vert N, \mathrm{g}\rangle)/\sqrt{2}$
g	Coupling rate (constant) between a plasmon and an electronic excitation in a molecule
$\mathbf{d}_0$	Molecular transition dipole moment
$\tilde{\mathbf{E}}$	Quantized electric field of a cavity mode
$\hat{\mathbf{r}}$	Position operator
$\hat{H}_{\mathrm{c}}$, $\hat{H}_{\mathrm{c-e}}$, $\hat{H}_{\mathrm{e}}$	Hamiltonian of: a cavity, a molecular electronic transition, and the coupling between the cavity modes and the electronic transition
V_{eff}	Effective volume of a cavity mode
$\mathbf{E}(\mathbf{r})$	Spatial distribution of the electric field of a plasmonic mode
$\mathbf{r}_{\mathrm{mol}}$	Position of a point-like molecule
$\hat{H}_{\mathrm{Rabi}}$, $\hat{H}_{\mathrm{J-C}}$	Rabi and Jaynes-Cummings coupling Hamiltonian

$\hat{a}$, $\hat{a}_n$	Bosonic annihilation operator of a plasmon and of a plasmonic mode n
$\tilde{\Omega}$	Real oscillation (Rabi) frequency
$\Delta E_{\mathrm{J-C}}(N)$	Energy splitting $\Delta E_{\mathrm{J-C}}(N) = 2\sqrt{N}\hbar g$
Q	Quality factor
ω_n	Angular frequency of the n-th plasmonic mode
$\hat{H}_{\mathrm{pl}}$	Plasmonic Hamiltonian
ρ_{eg}	Transition electric charge density
$\mathcal{G}$, α, R_{d}, R_{s}	Gap between plasmonic particles, cone opening angle, radius of plasmonic spheres, radius of the apex curvature
$\hat{\rho}_{\mathrm{c}}(\mathbf{r})$	Electronic-density operator
$\hat{H}_{\mathrm{pl-mol}}$	Interaction Hamiltonian between plasmons and molecular excitons
g_n, $g_{n,i}$	Coupling between plasmonic mode n and a molecular exciton, molecular exciton i
ω_{pl}	Lowest bonding dimer plasmon resonance frequency
$g^{\mathrm{ZnPc}}_{S_{\mathrm{x(y)}}}(\mathbf{r}_0)$, $g^{\mathrm{ZnPc}}_{S_{xz(yz)}}$	Effective coupling constant between the respective ZnPc excitons and a bonding dimer plasmon mode
S_x, S_y, S_z, S_{yz}, S_{xz}	Singlet excitations of ZnPc molecule (S_x, S_y, S_{yz}, S_{xz}), and MB molecule (S_z)
$\mathcal{Q}_{yz}$, $\mathcal{Q}_{xz}$	Quadrupolar moment of S_{yz} and S_{xz} excitons in ZnPc
ω_{dk}	angular frequency of S_{yz} and S_{xz} excitons in ZnPc
$\hat{H}^{\mathrm{dk}}_{\mathrm{mol}}$, $\hat{H}^{\mathrm{dk}}_{\mathrm{pl-mol}}$	Hamiltonian of of S_{yz} and S_{xz} excitons in ZnPc, and interaction Hamiltonian among S_{yz}, S_{xz} and plasmonic modes. dk stands for *dark* transition
g^{dk}_n	Constant of coupling between plasmonic mode n and a dark molecular exciton
ω_{ps}, ω_{dip}	Plasmon pseudomode frequency, dipolar plasmon frequency of a sphere
γ_0	Natural (vacuum) decay rate of molecular exciton

Chapter 6

N_{mol}	Number of molecules in a cavity
$\hat{H}_{\mathrm{e},i}$, $\hat{H}_{\mathrm{res},i}$, $\hat{H}_{\mathrm{e-res},i}$, $\hat{H}_{\mathrm{c}}$, $\hat{H}_{\mathrm{e-c},i}$, $\hat{H}_{\mathrm{e-e}}$, $\hat{H}_{\mathrm{tot}}$, $\hat{H}_{\mathrm{pump}}$, $\hat{H}^{\mathrm{col}}_{\mathrm{pump}}$	Excitonic Hamiltonian of molecule i, reservoir Hamiltonian of molecule i, Hamiltonian of exciton-reservoir coupling of molecule i, cavity Hamiltonian, Hamiltonian of coupling of a cavity mode with the $i-$th molecular exciton, exciton-exciton coupling, total system Hamiltonian, pumping Hamiltonian, and collective pumping Hamiltonian
Ω_{R}, d_{R}	Effective reservoir frequency and exciton-reservoir interaction (displacement)
g_i, G_{ij}	cavity mode-exciton coupling constant of molecule i, and a coupling constant between excitons of molecules i and j

$\hat{B}_i$ ($\hat{B}$), $\hat{\sigma}_i$ ($\hat{\sigma}$), $\hat{a}$	Bosonic annihilation operator of the reservoir of a molecule i (of a single molecule), Pauli lowering operator of the $i-$th molecular exciton (exciton of a single molecule), and bosonic annihilation operator of a cavity mode
$\vert 0\rangle$, $\vert +\rangle$, $\vert -\rangle$, $\vert \mathrm{D}_i\rangle$	Ground state, upper polariton state, lower polariton state, and dark state i
$\hat{F}$, $\hat{F}_i$	$\hat{F} = d_\mathrm{R}\Omega_\mathrm{R}(\hat{B}^\dagger + \hat{B})$, $\hat{F} = d_\mathrm{R}\Omega_\mathrm{R}(\hat{B}_i^\dagger + \hat{B}_i)$
$\hat{\sigma}_{\xi\zeta}$	$\hat{\sigma}_{\xi\zeta} = \vert \xi\rangle\langle\zeta \vert$, with ξ, $\zeta \in \{+, -\}$
$\hat{\sigma}_{--++}$	$\hat{\sigma}_{--++} = \vert +\rangle\langle+\vert + \vert -\rangle\langle-\vert$
ω_+, ω_-	Upper and lower polariton frequencies
$\hat{\mathcal{O}}(0)$	Schrödinger-picture operator
$J(\omega)$	Spectral function of a molecular reservoir
γ_ϕ	Dephasing rate
$\mathcal{E}$, ω_L	Laser pumping amplitude, laser frequency
$\hat{S}_i$	Collective excitonic operator $\hat{S}_i = \sum_\alpha c_{i\alpha}\hat{\sigma}_\alpha$, with coefficients $c_{i,\alpha}$
g_eff, θ (θ_eff)	Collective cavity mode-exciton coupling, polariton mixing angle (effective collective polariton mixing angle)
n_+, n_-, n_D	Upper polariton population, lower polariton population, dark polariton population
G_0, d_0, r_0	Constant of Exciton-exciton coupling, transition dipole moment of an exciton, intermolecular distance

Part IV

Chapter 7

$\vert \mathrm{g(e)}, \mathcal{N}, m\rangle$	Quantum state containing a molecule in its electronic ground, g, or excited, e, state, exciting field in a number state containing $\mathcal{N}$ photons, and a vibrational mode in a number state containing m phonons
$\vert n_\pm, m\rangle$	Hybrid states $\vert n_\pm, m\rangle = (\vert \mathrm{g}, \mathcal{N}, m\rangle \pm \vert \mathrm{e}, \mathcal{N}-1, m\rangle)/\sqrt{2}$ with $+$ labelling the state with higher energy, and $n = \mathcal{N} + \delta_{i\mathrm{e}}$, with $i = \mathrm{e}$, g and δ_{ij} the Kronecker delta
n_PL	Number of plasmonic excitations
$\hat{H}_\mathrm{c}$, $\hat{H}_\mathrm{c,0}$, $\hat{H}_\mathrm{c-vib}$	Cavity (plasmon) Hamiltonian, bare-cavity Hamiltonian, and plasmon-vibration coupling
d_om, g_om	Optomechanical displacement parameter, optomechanical coupling
$\hat{H}_\mathrm{om}$, $\hat{H}_\mathrm{pl}$, $\hat{H}_\mathrm{vib}$, $\hat{H}_\mathrm{pl-vib}$, $\hat{H}_\mathrm{pump}$	Optomechanical Hamiltonian, plasmon Hamiltonian, vibrational Hamiltonian, plasmon-vibration coupling Hamiltonian, and plasmon pumping Hamiltonian
$\boldsymbol{\alpha}_\mathrm{eg}$	Molecule's electronic polarizability
n_PL	Number of plasmonic excitations

$\hat{H}_{\mathrm{bom}}$	Bare optomechanical Hamiltonian
$n_{\mathrm{vib}}(T)$, k_{B}	Thermal vibrational population, Boltzmann constant
α_{S}	Coherent plasmon amplitude
$E_{\mathrm{g}}(q)$, $E_{\mathrm{e}}(q)$, d, S	Potential energy surface of ground electronic state, of excited electronic state, and displacement of electronic ground and excited potential-energy surfaces, Huang-Rhys factor
$\hat{H}^{\mathrm{res}}_{\mathrm{om}}$, $\hat{H}_{\mathrm{mol}}$, $\hat{H}_{\mathrm{pl-e}}$	Resonant optomechanical Hamiltonian, molecular Hamiltonian, and plasmon-exciton coupling Hamiltonian
$\hat{b}_{\mathrm{e}}$, $\hat{b}^{\dagger}_{\mathrm{e}}$, $\hat{b}_{\mathrm{g}}$, $\hat{b}^{\dagger}_{\mathrm{g}}$	Vibrational annihilation operator and creation operator in the ground electronic state, vibrational annihilation and creation operator in the excited electronic state
$\hat{b}$, $\hat{b}^{\dagger}$	Vibrational annihilation and creation operators
δ, Δ	$\delta = \omega_{\mathrm{eg}} - \omega_{\mathrm{L}}$, $\Delta = \omega_{\mathrm{c}} - \omega_{\mathrm{L}}$
$\tilde{\delta}$	Renormalized detuning: $\tilde{\delta} = \delta + d^2\Omega$
Q	Plasmonic quality factor
$\mathcal{E}_{\mathrm{pl}}$	Amplitude of TLS driving by the plasmon-enhanced field: $\mathcal{E}_{\mathrm{pl}} = -2g\alpha_{\mathrm{S}}$
$\hat{H}_{\mathrm{red}}$, $\hat{H}^{\mathrm{two}}_{\mathrm{red}}$	Effective reduced TLS-vibrational Hamiltonian, effective reduced TLS-vibrational Hamiltonian for two vibrational modes
$\hat{H}^{\mathrm{red}}_{\mathrm{vib}}$	Reduced vibrational Hamiltonian
$\hat{H}_{\mathrm{TLS}}$	Two-level-system reduced Hamiltonian
$\Gamma^{\mathrm{dec}}_{\mathrm{v}}$, $\Gamma^{\mathrm{pump}}_{\mathrm{v}}$	Effective vibrational decay rate and effective vibrational pumping rate
$\mathscr{L}_{\hat{b}}^{\Gamma^{\mathrm{dec}}_{\mathrm{v}}}[\hat{\rho}]$	Effective vibrational damping Lindblad term: $\mathscr{L}_{\hat{b}}^{\Gamma^{\mathrm{dec}}_{\mathrm{v}}}[\hat{\rho}] = \frac{\Gamma^{\mathrm{dec}}_{\mathrm{v}}}{2}\left(2\hat{b}\hat{\rho}\hat{b}^{\dagger} - \left\{\hat{b}^{\dagger}\hat{b}, \hat{\rho}\right\}\right)$
$\mathscr{L}_{\hat{b}^{\dagger}}^{\Gamma^{\mathrm{pump}}_{\mathrm{v}}}[\hat{\rho}]$	Effective vibrational pumping Lindblad term: $\mathscr{L}_{\hat{b}^{\dagger}}^{\Gamma^{\mathrm{pump}}_{\mathrm{v}}}[\hat{\rho}] = \frac{\Gamma^{\mathrm{pump}}_{\mathrm{v}}}{2}\left(2\hat{b}^{\dagger}\hat{\rho}\hat{b} - \left\{\hat{b}\hat{b}^{\dagger}, \hat{\rho}\right\}\right)$
$\tilde{S}(s)$	Spectral function of an electronic reservoir
$\tilde{S}^{\mathrm{R}}_{\mathrm{coh}}$, $\tilde{S}^{\mathrm{R}}_{\mathrm{incoh}}$	Coherent and incoherent part of $\tilde{S}(s)$
$\langle\hat{b}^{\dagger}\hat{b}\rangle_{\mathrm{SS,in}}$	Incoherent vibrational population
Γ_{tot}	Total decay rate $\Gamma_{\mathrm{tot}} = \Gamma_{\mathrm{eff}} + \gamma_{\sigma}$
λ_{TLS}	Effective frequency $\lambda_{\mathrm{TLS}} = (\mathcal{E}^2_{\mathrm{pl}} + \delta^2)^{1/2}$
$\hat{H}'^{\mathrm{res}}_{\mathrm{om}}$	Transformed resonant optomechanical Hamiltonian
$\mathbf{H}'^{\mathrm{res}}_{\mathrm{om}}$, $\mathbf{H}'^{\mathrm{res,dr}}_{\mathrm{om}}$	Matrices representing $\hat{H}'^{\mathrm{res}}_{\mathrm{om}}$ in different basis sets
$\mathcal{N}$	Number of photons in the exciting field
$n^{\mathrm{incoh}}_{\sigma}$, $n^{\mathrm{coh}}_{\sigma}$	Incoherent population of molecular TLS, coherent population of molecular TLS
$\hat{\sigma}_{\mathrm{g}}$, $\hat{\sigma}_{\mathrm{e}}$	Operator of ground, $\hat{\sigma}_{\mathrm{g}} = \hat{\sigma}\hat{\sigma}^{\dagger}$, and excited $\hat{\sigma}_{\mathrm{e}} = \hat{\sigma}^{\dagger}\hat{\sigma}$, state occupation
$\hat{\sigma}_x$, $\hat{\sigma}_y$, $\hat{\sigma}_z$	Pauli matrices x, y and z
$\hat{\sigma}'_x$, $\hat{\sigma}'_y$, $\hat{\sigma}'_z$	Transformed Pauli matrices x, y and z

$g_{\mathrm{PL-L}}$	Small coupling constant between an equivalent exciting field and a molecule
n	Number of field and excitonic excitations: $n = \mathcal{N} + \delta_{i\mathrm{e}}$
λ_+, λ_-, λ_3, λ_4	Eigenenergies of the effective Hamiltonian $\hat{H}_{\mathrm{om}}^{\prime\mathrm{res}}$
$\hat{b}_1$, $\hat{b}_1^\dagger$, $\hat{b}_2$, $\hat{b}_2^\dagger$	Vibrational annihilation operator of vibrational mode 1, vibrational creation operator of vibrational mode 1, vibrational annihilation operator of vibrational mode 2, and vibrational creation operator of vibrational mode 2
$\hat{H}_{\mathrm{J-C,p}}$, $\hat{H}_{\mathrm{v}}$, $\hat{H}_{\mathrm{TLS-v}}$	Hamiltonian of a pumped Jaynes-Cummings system, vibrational Hamiltonian, and exciton-vibration coupling Hamiltonian
$\mathcal{J}_0(s)$	Auxiliary spectral function of the TLS: $\mathcal{J}_0(s) = \mathrm{Re}\left\{\int_0^\infty \langle\langle\hat{\sigma}(\tau)\hat{\sigma}^\dagger(0)\rangle\rangle e^{\mathrm{i}(s+\omega_{\mathrm{L}})\tau}\mathrm{d}\tau\right\}$
$\mathbf{M}_{\mathrm{C}}$	Matrix of coefficients
$\mathbf{v}$, $\mathbf{w}$, $\mathbf{rhs}$	Shorthand vectorial notation for: $\mathbf{v} = (\langle\hat{a}\rangle, \langle\hat{\sigma}\rangle)^{\mathrm{T}}$, $\mathbf{w} = (\langle\langle\hat{a}(\tau)\hat{\sigma}^\dagger(0)\rangle\rangle, \langle\langle\hat{\sigma}(\tau)\hat{\sigma}^\dagger(0)\rangle\rangle)^{\mathrm{T}}$, $\mathbf{rhs} = (0, -\mathrm{i}g\alpha_{\mathrm{S}}^*)^{\mathrm{T}}$
$\mathbf{P}_{\mathrm{C}}$, $\mathbf{D}_{\mathrm{C}}$	Matrix of eigenvectors, matrix of eigenvalues
$\mathbf{RHS}$	Vector of right-hand side
λ_1^{SC}, λ_2^{SC}	Eigenvalues of $\mathbf{M}_{\mathrm{C}}$
$\mathbf{v}_{\mathrm{inh}}$	Vector of the inhomogeneous solution
$\hat{a}_{\mathrm{inh}}$	Inhomogeneous solution for the plasmon annihilation operator
$\mathcal{A}_0(s)$	Auxiliary spectral function of the TLS: $\mathcal{A}_0(\Omega) = \frac{g}{\sqrt{4g^2-(\gamma_a-\gamma_\sigma)^2/4}}\left[\frac{1}{(-\mathrm{i}\Omega-\lambda_1^{\mathrm{SC}})} - \frac{1}{(-\mathrm{i}\Omega-\lambda_2^{\mathrm{SC}})}\right]$
$s_{\mathrm{e,St}}$, $s_{\mathrm{e,aSt}}$	Stokes and anti-Stokes emission spectra
γ_{vdp}	$\gamma_{\mathrm{vdp}} = \gamma_b + \Gamma_{\mathrm{v}}^{\mathrm{dec}} - \Gamma_{\mathrm{v}}^{\mathrm{pump}}$

Appendices

$\mathbf{E}_{\mathrm{loc}}^{(+)}$	Positive-frequency part of quantized electric field at the position of an emitter
$\mathcal{C}_l$	$\mathcal{C}_l = \sqrt{\frac{\hbar\omega_l R_{\mathrm{d}}^{2l+1}}{2\varepsilon_0(2l+1)}}$
ρ_{PD}	Charge density of a point dipole
$\boldsymbol{\rho}_{\mathrm{S}}$	Matrix representation of density operator
$\vec{\rho}_{\mathrm{S}}$	Vectorized system density matrix
$\mathcal{L}$	Liouville superoperator
$\mathbf{O}_1$, $\mathbf{O}_2$	Matrix representations of operators $\hat{O}_1$ and $\hat{O}_2$
$F(s)$	Fourier transform of kernel function $f(t)$
$\lambda_{\mathrm{W}}(t,u)$	Auxiliary function
$\Lambda_{\mathrm{W}}(t,s)$	$\Lambda_{\mathrm{W}}(t,s) = \frac{1}{\sqrt{2\pi}}\int_{-\infty}^{\infty}\mathrm{d}u\lambda_{\mathrm{W}}(t,u)\exp(-\mathrm{i}su)$

Bibliography

[1] M. Andresen, A. C. Stiel, J. Fölling, D. Wenzel, A. Schönle, A. Egner, C. Eggeling, S. W. Hell, and S. Jakobs, "Photoswitchable fluorescent proteins enable monochromatic multilabel imaging and dual color fluorescence nanoscopy," Nat. Biotechnol **26**, 1035 (2008).

[2] T. A. Klar and S. W. Hell, "Subdiffraction resolution in far-field fluorescence microscopy," Opt. Lett. **24**, 954–956 (1999).

[3] E. Betzig, G. H. Patterson, R. Sougrat, O. W. Lindwasser, S. Olenych, J. S. Bonifacino, M. W. Davidson, J. Lippincott-Schwartz, and H. F. Hess, "Imaging intracellular fluorescent proteins at nanometer resolution," Science **313**, 1642–1645 (2006).

[4] W. E. Moerner and D. P. Fromm, "Methods of single-molecule fluorescence spectroscopy and microscopy," Rev. Sci. Instrum. **74**, 3597–3619 (2003).

[5] P. Genevet, F. Capasso, F. Aieta, M. Khorasaninejad, and R. Devlin, "Recent advances in planar optics: from plasmonic to dielectric metasurfaces," Optica **4**, 139–152 (2017).

[6] L. Novotny and N. Van Hulst, "Antennas for light," Nat. Photonics **5**, 83 (2011).

[7] K. Kneipp, Y. Wang, H. Kneipp, I. Itzkan, R. R. Dasari, and M. S. Feld, "Population pumping of excited vibrational states by spontaneous surface-enhanced Raman scattering," Phys. Rev. Lett. **76**, 2444–2447 (1996).

[8] K. Kneipp, Y. Wang, H. Kneipp, L. T. Perelman, I. Itzkan, R. R. Dasari, and M. S. Feld, "Single molecule detection using surface-enhanced Raman scattering (SERS)," Phys. Rev. Lett. **78**, 1667–1670 (1997).

[9] H. Xu, E. J. Bjerneld, M. Käll, and L. Börjesson, "Spectroscopy of single hemoglobin molecules by surface enhanced Raman scattering," Phys. Rev. Lett. **83**, 4357–4360 (1999).

[10] T. L. Haslett, L. Tay, and M. Moskovits, "Can surface-enhanced Raman scattering serve as a channel for strong optical pumping?" J. Chem. Phys. **113**, 1641–1646 (2000).

[11] H. Xu, J. Aizpurua, M. Käll, and P. Apell, “Electromagnetic contributions to single-molecule sensitivity in surface-enhanced Raman scattering,” Phys. Rev. E **62**, 4318–4324 (2000).

[12] A. G. Brolo, A. C. Sanderson, and A. P. Smith, “Ratio of the surface-enhanced anti-Stokes scattering to the surface-enhanced Stokes-Raman scattering for molecules adsorbed on a silver electrode,” Phys. Rev. B **69**, 045424 (2004).

[13] R. C. Maher, L. F. Cohen, P. Etchegoin, H. J. N. Hartigan, R. J. C. Brown, and M. J. T. Milton, “Stokes/anti-Stokes anomalies under surface enhanced Raman scattering conditions,” J. Chem. Phys. **120**, 11746–11753 (2004).

[14] A. J. Haes, C. L. Haynes, A. D. McFarland, G. C. Schatz, R. P. Van Duyne, and S. Zou, “Plasmonic materials for surface-enhanced sensing and spectroscopy,” MRS Bulletin **30**, 368–375 (2005).

[15] M. Moskovits, “Surface-enhanced Raman spectroscopy: a brief retrospective,” Journal of Raman Spectroscopy **36**, 485–496 (2005).

[16] E. C. Le Ru and P. G. Etchegoin, “Vibrational pumping and heating under SERS conditions: fact or myth?” Faraday Discuss. **132**, 63–75 (2006).

[17] P. L. Stiles, J. A. Dieringer, N. C. Shah, and R. P. V. Duyne, “Surface-enhanced Raman spectroscopy,” Annu. Rev. Anal. Chem. **1**, 601–626 (2008).

[18] L. Tong, H. Xu, and M. Käll, “Nanogaps for SERS applications,” MRS Bulletin **39**, 163–168 (2014).

[19] A. B. Zrimsek, N. Chiang, M. Mattei, S. Zaleski, M. O. McAnally, C. T. Chapman, A.-I. Henry, G. C. Schatz, and R. P. Van Duyne, “Single-molecule chemistry with surface- and tip-enhanced Raman spectroscopy,” Chem. Rev. **117**, 7583–7613 (2017).

[20] O. Neumann, A. S. Urban, J. Day, S. Lal, P. Nordlander, and N. J. Halas, “Solar vapor generation enabled by nanoparticles,” ACS Nano **7**, 42–49 (2013).

[21] Y. Zhang, S. He, W. Guo, Y. Hu, J. Huang, J. R. Mulcahy, and W. D. Wei, “Surface-plasmon-driven hot electron photochemistry,” Chem. Rev. **118**, 2927–2954 (2018).

[22] M. I. Stockman, K. Kneipp, S. I. Bozhevolnyi, S. Saha, A. Dutta, J. Ndukaife, N. Kinsey, H. Reddy, U. Guler, V. M. Shalaev, A. Boltasseva, B. Gholipour, H. N. S. Krishnamoorthy, K. F. MacDonald, C. Soci, N. I. Zheludev, V. Savinov, R. Singh, P. Groß, C. Lienau, M. Vadai, M. L. Solomon, D. R. B. III, M. Lawrence, J. A. Dionne, S. V. Boriskina, R. Esteban, J. Aizpurua, X. Zhang, S. Yang, D. Wang, W. Wang, T. W. Odom, N. Accanto, P. M.

de Roque, I. M. Hancu, L. Piatkowski, N. F. van Hulst, and M. F. Kling, “Roadmap on plasmonics,” J. Opt. **20**, 043001 (2018).

[23] R. F. Aroca, “Plasmon enhanced spectroscopy,” Phys. Chem. Chem. Phys. **15**, 5355–5363 (2013).

[24] S. Cataldo, J. Zhao, F. Neubrech, B. Frank, C. Zhang, P. V. Braun, and H. Giessen, “Hole-mask colloidal nanolithography for large-area low-cost metamaterials and antenna-assisted surface-enhanced infrared absorption substrates,” ACS Nano **6**, 979–985 (2011).

[25] K. Chen, R. Adato, and H. Altug, “Dual-band perfect absorber for multispectral plasmon-enhanced infrared spectroscopy,” ACS Nano **6**, 7998–8006 (2012).

[26] L. V. Brown, K. Zhao, N. King, H. Sobhani, P. Nordlander, and N. J. Halas, “Surface-enhanced infrared absorption using individual cross antennas tailored to chemical moieties,” J. Am. Chem. Soc. **135**, 3688–3695 (2013).

[27] J. M. Hoffmann, X. Yin, J. Richter, A. Hartung, T. W. W. Maß, and T. Taubner, “Low-cost infrared resonant structures for surface-enhanced infrared absorption spectroscopy in the fingerprint region from 3 to 13 μm,” J. Phys. Chem. C **117**, 11311–11316 (2013).

[28] P. Alonso-González, P. Albella, F. Neubrech, C. Huck, J. Chen, F. Golmar, F. Casanova, L. E. Hueso, A. Pucci, J. Aizpurua, and R. Hillenbrand, “Experimental verification of the spectral shift between near- and far-field peak intensities of plasmonic infrared nanoantennas,” Phys. Rev. Lett. **110**, 203902 (2013).

[29] C. D’Andrea, J. Bochterle, A. Toma, C. Huck, F. Neubrech, E. Messina, B. Fazio, O. M. Maragò, E. Di Fabrizio, M. Lamy de La Chapelle, P. G. Gucciardi, and A. Pucci, “Optical nanoantennas for multiband surface-enhanced infrared and Raman spectroscopy,” ACS Nano **7**, 3522–3531 (2013).

[30] C. Huck, F. Neubrech, J. Vogt, A. Toma, D. Gerbert, J. Katzmann, T. Härtling, and A. Pucci, “Surface-enhanced infrared spectroscopy using nanometer-sized gaps,” ACS Nano **8**, 4908–4914 (2014).

[31] T. Wang, V. H. Nguyen, A. Buchenauer, U. Schnakenberg, and T. Taubner, “Surface enhanced infrared spectroscopy with gold strip gratings,” Opt. Express **21**, 9005–9010 (2013).

[32] L. V. Brown, X. Yang, K. Zhao, B. Y. Zheng, P. Nordlander, and N. J. Halas, “Fan-shaped gold nanoantennas above reflective substrates for surface-enhanced infrared absorption (SEIRA),” Nano Lett. **15**, 1272–1280 (2015).

[33] C. Huck, A. Toma, F. Neubrech, M. Chirumamilla, J. Vogt, F. De Angelis, and A. Pucci, “Gold nanoantennas on a pedestal for plasmonic enhancement in the infrared,” ACS Photonics **2**, 497–505 (2015).

[34] F. Neubrech, A. Pucci, T. W. Cornelius, S. Karim, A. García-Etxarri, and J. Aizpurua, “Resonant plasmonic and vibrational coupling in a tailored nanoantenna for infrared detection,” Phys. Rev. Lett. **101**, 157403 (2008).

[35] F. Neubrech and A. Pucci, “Plasmonic enhancement of vibrational excitations in the infrared,” IEEE J. Sel. Top. Quantum Electron. **19**, 4600809–4600809 (2013).

[36] S. Bagheri, H. Giessen, and F. Neubrech, “Large-area antenna-assisted seira substrates by laser interference lithography,” Adv. Opt. Mater. **2**, 1050–1056 (2014).

[37] T. Neuman, C. Huck, J. Vogt, F. Neubrech, R. Hillenbrand, J. Aizpurua, and A. Pucci, “Importance of plasmonic scattering for an optimal enhancement of vibrational absorption in seira with linear metallic antennas,” J. Phys. Chem. C **119**, 26652–26662 (2015).

[38] A. Marini, I. Silveiro, and F. J. García de Abajo, “Molecular sensing with tunable graphene plasmons,” ACS Photonics **2**, 876–882 (2015).

[39] F. Neubrech, C. Huck, K. Weber, A. Pucci, and H. Giessen, “Surface-enhanced infrared spectroscopy using resonant nanoantennas,” Chem. Rev. **117**, 5110–5145 (2017).

[40] J. B. Khurgin and G. Sun, “Enhancement of optical properties of nanoscaled objects by metal nanoparticles,” J. Opt. Soc. Am. B **26**, B83–B95 (2009).

[41] R. C. Dunn, “Near-field scanning optical microscopy,” Chem. Rev. **99**, 2891–2928 (1999).

[42] F. Keilmann and R. Hillenbrand, “Near-field microscopy by elastic light scattering from a tip,” Philos. Trans. Royal Soc. A **362**, 787–805 (2004).

[43] A. M. Gobin, M. H. Lee, N. J. Halas, W. D. James, R. A. Drezek, and J. L. West, “Near-infrared resonant nanoshells for combined optical imaging and photothermal cancer therapy,” Nano Lett. **7**, 1929–1934 (2007).

[44] T. Liebermann and W. Knoll, “Surface-plasmon field-enhanced fluorescence spectroscopy,” Colloids Surf. A: Physicochem. Eng. Asp. **171**, 115 – 130 (2000).

[45] A. Kinkhabwala, Z. Yu, S. Fan, Y. Avlasevich, K. Müllen, and W. Moerner, “Large single-molecule fluorescence enhancements produced by a bowtie nanoantenna,” Nat. Photonics **3**, 654–657 (2009).

[46] A. Merlen, F. Lagugné-Labarthet, and E. Harté, “Surface-enhanced Raman and fluorescence spectroscopy of dye molecules deposited on nanostructured gold surfaces,” J. Phys. Chem. C **114**, 12878–12884 (2010).

[47] M. Bauch, K. Toma, M. Toma, Q. Zhang, and J. Dostalek, “Plasmon-enhanced fluorescence biosensors: a review,” Plasmonics **9**, 781–799 (2014).

[48] J.-F. Li, C.-Y. Li, and R. F. Aroca, “Plasmon-enhanced fluorescence spectroscopy,” Chem. Soc. Rev. **46**, 3962–3979 (2017).

[49] G. Sun, J. B. Khurgin, and D. P. Tsai, “Comparative analysis of photoluminescence and raman enhancement by metal nanoparticles,” Opt. Lett. **37**, 1583–1585 (2012).

[50] T. Neuman, R. Esteban, D. Casanova, F. J. García-Vidal, and J. Aizpurua, “Coupling of molecular emitters and plasmonic cavities beyond the point-dipole approximation,” Nano Lett. **18**, 2358–2364 (2018).

[51] S. Trautmann, J. Aizpurua, I. Götz, A. Undisz, J. Dellith, H. Schneidewind, M. Rettenmayr, and V. Deckert, “A classical description of subnanometer resolution by atomic features in metallic structures,” Nanoscale **9**, 391–401 (2017).

[52] H. Imada, K. Miwa, M. Imai-Imada, S. Kawahara, K. Kimura, and Y. Kim, “Single-molecule investigation of energy dynamics in a coupled plasmon-exciton system,” Phys. Rev. Lett. **119**, 013901 (2017).

[53] Y. Zhang, Q.-S. Meng, L. Zhang, Y. Luo, Y.-J. Yu, B. Yang, Y. Zhang, R. Esteban, J. Aizpurua, Y. Luo, J.-L. Yang, Z.-C. Dong, and J. G. Hou, “Sub-nanometre control of the coherent interaction between a single molecule and a plasmonic nanocavity,” Nat. Commun. **8**, 15225 (2017).

[54] R. Zhang, Y. Zhang, Z. C. Dong, S. Jiang, C. Zhang, L. G. Chen, L. Zhang, Y. Liao, J. Aizpurua, Y. Luo, J. L. Yang, and J. G. Hou, “Chemical mapping of a single molecule by plasmon-enhanced Raman scattering,” Nature **498**, 82–86 (2013).

[55] Y. Zhang, Y. Luo, Y. Zhang, Y.-J. Yu, Y.-M. Kuang, L. Zhang, Q.-S. Meng, Y. Luo, J.-L. Yang, Z.-C. Dong, and J. G. Hou, “Visualizing coherent intermolecular dipole–dipole coupling in real space,” Nature **531**, 623–627 (2016).

[56] B. Doppagne, M. C. Chong, E. Lorchat, S. Berciaud, M. Romeo, H. Bulou, A. Boeglin, F. Scheurer, and G. Schull, “Vibronic spectroscopy with submolecular resolution from STM-induced electroluminescence,” Phys. Rev. Lett. **118**, 127401 (2017).

[57] G. Reecht, F. Scheurer, V. Speisser, Y. J. Dappe, F. Mathevet, and G. Schull, “Electroluminescence of a polythiophene molecular wire suspended between a metallic surface and the tip of a scanning tunneling microscope,” Phys. Rev. Lett. **112**, 047403 (2014).

[58] D. G. Lidzey, D. Bradley, M. Skolnick, T. Virgili, S. Walker, and D. Whittaker, “Strong exciton–photon coupling in an organic semiconductor microcavity,” Nature **395**, 53 (1998).

[59] P. A. Hobson, W. L. Barnes, D. G. Lidzey, G. A. Gehring, D. M. Whittaker, M. S. Skolnick, and S. Walker, “Strong exciton-photon coupling in a low-Q all-metal mirror microcavity,” Appl. Phys. Lett. **81**, 3519–3521 (2002).

[60] J. Bellessa, C. Bonnand, J. C. Plenet, and J. Mugnier, “Strong coupling between surface plasmons and excitons in an organic semiconductor,” Phys. Rev. Lett. **93**, 036404 (2004).

[61] J. Dintinger, S. Klein, F. Bustos, W. L. Barnes, and T. W. Ebbesen, “Strong coupling between surface plasmon-polaritons and organic molecules in subwavelength hole arrays,” Phys. Rev. B **71**, 035424 (2005).

[62] P. Michetti and G. C. La Rocca, “Polariton states in disordered organic microcavities,” Phys. Rev. B **71**, 115320 (2005).

[63] A. Trügler and U. Hohenester, “Strong coupling between a metallic nanoparticle and a single molecule,” Phys. Rev. B **77**, 115403 (2008).

[64] T. Schwartz, J. A. Hutchison, C. Genet, and T. W. Ebbesen, “Reversible switching of ultrastrong light-molecule coupling,” Phys. Rev. Lett. **106**, 196405 (2011).

[65] D. M. Coles, P. Michetti, C. Clark, W. C. Tsoi, A. M. Adawi, J.-S. Kim, and D. G. Lidzey, “Vibrationally assisted polariton-relaxation processes in strongly coupled organic-semiconductor microcavities,” Adv. Funct. Mater. **21**, 3691–3696 (2011).

[66] V. Agranovich, Y. N. Gartstein, and M. Litinskaya, “Hybrid resonant organic–inorganic nanostructures for optoelectronic applications,” Chem. Rev. **111**, 5179–5214 (2011).

[67] A. Salomon, R. J. Gordon, Y. Prior, T. Seideman, and M. Sukharev, “Strong coupling between molecular excited states and surface plasmon modes of a slit array in a thin metal film,” Phys. Rev. Lett. **109**, 073002 (2012).

[68] S. Kéna-Cohen, S. A. Maier, and D. D. C. Bradley, “Ultrastrongly coupled exciton-polaritons in metal-clad organic semiconductor microcavities,” Adv. Opt. Mater. **1**, 827–833 (2013).

[69] P. Vasa, W. Wang, R. Pomraenke, M. Lammers, M. Maiuri, C. Manzoni, G. Cerullo, and C. Lienau, "Real-time observation of ultrafast Rabi oscillations between excitons and plasmons in metal nanostructures with J-aggregates," Nat. Photonics **7**, 128 (2013).

[70] A. E. Schlather, N. Large, A. S. Urban, P. Nordlander, and N. J. Halas, "Near-field mediated plexcitonic coupling and giant Rabi splitting in individual metallic dimers," Nano Lett. **13**, 3281–3286 (2013).

[71] G. Zengin, G. Johansson, P. Johansson, T. J. Antosiewicz, M. Käll, and T. Shegai, "Approaching the strong coupling limit in single plasmonic nanorods interacting with J-aggregates," Sci. Rep. **3**, 3074 (2013).

[72] A. Delga, J. Feist, J. Bravo-Abad, and F. J. Garcia-Vidal, "Quantum emitters near a metal nanoparticle: Strong coupling and quenching," Phys. Rev. Lett. **112**, 253601 (2014).

[73] T. J. Antosiewicz, S. P. Apell, and T. Shegai, "Plasmon-exciton interactions in a core-shell geometry: From enhanced absorption to strong coupling," ACS Photonics **1**, 454–463 (2014).

[74] G. Zengin, M. Wersäll, S. Nilsson, T. J. Antosiewicz, M. Käll, and T. Shegai, "Realizing strong light-matter interactions between single-nanoparticle plasmons and molecular excitons at ambient conditions," Phys. Rev. Lett. **114**, 157401 (2015).

[75] P. Törmä and W. L. Barnes, "Strong coupling between surface plasmon polaritons and emitters: a review," Rep. Prog. Phys. **78**, 013901 (2015).

[76] J. George, S. Wang, T. Chervy, A. Canaguier-Durand, G. Schaeffer, J.-M. Lehn, J. A. Hutchison, C. Genet, and T. W. Ebbesen, "Ultra-strong coupling of molecular materials: spectroscopy and dynamics," Faraday Discuss. **178**, 281–294 (2015).

[77] J. Galego, F. J. Garcia-Vidal, and J. Feist, "Cavity-induced modifications of molecular structure in the strong-coupling regime," Phys. Rev. X **5**, 041022 (2015).

[78] J. Galego, F. J. Garcia-Vidal, and J. Feist, "Suppressing photochemical reactions with quantized light fields," Nat. Commun. **7** (2016), 10.1038/ncomms13841.

[79] G. Zengin, T. Gschneidtner, R. Verre, L. Shao, T. J. Antosiewicz, K. Moth-Poulsen, M. Käll, and T. Shegai, "Evaluating conditions for strong coupling between nanoparticle plasmons and organic dyes using scattering and absorption spectroscopy," J. Phys. Chem. C **120**, 20588–20596 (2016).

[80] D. Melnikau, R. Esteban, D. Savateeva, A. Sánchez-Iglesias, M. Grzelczak, M. K. Schmidt, L. M. Liz-Marzán, J. Aizpurua, and Y. P. Rakovich, "Rabi splitting in photoluminescence spectra of hybrid systems of gold nanorods and J-aggregates," J. Phys. Chem. Lett. **7**, 354–362 (2016).

[81] J. A. Ćwik, P. Kirton, S. De Liberato, and J. Keeling, "Excitonic spectral features in strongly coupled organic polaritons," Phys. Rev. A **93**, 033840 (2016).

[82] F. Herrera and F. C. Spano, "Absorption and photoluminescence in organic cavity QED," Phys. Rev. A **95**, 053867 (2017).

[83] R. Sáez-Blázquez, J. Feist, A. I. Fernández-Domínguez, and F. J. García-Vidal, "Enhancing photon correlations through plasmonic strong coupling," Optica **4**, 1363–1367 (2017).

[84] F. Herrera and F. C. Spano, "Dark vibronic polaritons and the spectroscopy of organic microcavities," Phys. Rev. Lett. **118**, 223601 (2017).

[85] D. G. Baranov, M. Wersäll, J. Cuadra, T. J. Antosiewicz, and T. Shegai, "Novel nanostructures and materials for strong light-matter interactions," ACS Photonics **5**, 24–42 (2018).

[86] F. Herrera and F. C. Spano, "Theory of nanoscale organic cavities: The essential role of vibration-photon dressed states," ACS Photonics **5**, 65–79 (2018).

[87] M. A. Zeb, P. G. Kirton, and J. Keeling, "Exact states and spectra of vibrationally dressed polaritons," ACS Photonics **5**, 249–257 (2018).

[88] J.-J. Greffet, P. Bouchon, G. Brucoli, and F. Marquier, "Light emission by nonequilibrium bodies: Local Kirchhoff law," Phys. Rev. X **8**, 021008 (2018).

[89] T. Neuman and J. Aizpurua, "Origin of the asymmetric light emission from molecular exciton-polaritons," Optica **5**, 1247–1255 (2018).

[90] V. M. Agranovich, M. Litinskaia, and D. G. Lidzey, "Cavity polaritons in microcavities containing disordered organic semiconductors," Phys. Rev. B **67**, 085311 (2003).

[91] J. del Pino, J. Feist, and F. J. Garcia-Vidal, "Quantum theory of collective strong coupling of molecular vibrations with a microcavity mode," New J. Phys. **17**, 053040 (2015).

[92] R. Sáez-Blázquez, J. Feist, A. I. Fernández-Domínguez, and F. J. García-Vidal, "Organic polaritons enable local vibrations to drive long-range energy transfer," Phys. Rev. B **97**, 241407 (2018).

[93] R. F. Ribeiro, L. A. Martínez-Martínez, M. Du, J. Campos-Gonzalez-Angulo, and J. Yuen-Zhou, “Polariton chemistry: controlling molecular dynamics with optical cavities,” Chem. Sci. **9**, 6325–6339 (2018).

[94] M. Du, L. A. Martínez-Martínez, R. F. Ribeiro, Z. Hu, V. M. Menon, and J. Yuen-Zhou, “Theory for polariton-assisted remote energy transfer,” Chem. Sci. **9**, 6659–6669 (2018).

[95] B. C. Stipe, M. A. Rezaei, W. Ho, S. Gao, M. Persson, and B. I. Lundqvist, “Single-molecule dissociation by tunneling electrons,” Phys. Rev. Lett. **78**, 4410–4413 (1997).

[96] T. Komeda, “Chemical identification and manipulation of molecules by vibrational excitation via inelastic tunneling process with scanning tunneling microscopy,” Prog. Surf. Sci. **78**, 41–85 (2005).

[97] F. F. Crim, “Bond-selected chemistry: vibrational state control of photodissociation and bimolecular reaction,” J. Phys. Chem. **100**, 12725–12734 (1996).

[98] W. Ho, “Single-molecule chemistry,” J. Chem. Phys. **117**, 11033–11061 (2002).

[99] J. I. Pascual, N. Lorente, Z. Song, H. Conrad, and H.-P. Rust, “Selectivity in vibrationally mediated single-molecule chemistry,” Nature **423**, 525–528 (2003).

[100] J. R. Hahn and W. Ho, “Orbital specific chemistry: Controlling the pathway in single-molecule dissociation,” J. Chem. Phys. **122**, 244704 (2005).

[101] P. Roelli, C. Galland, N. Piro, and T. J. Kippenberg, “Molecular cavity optomechanics as a theory of plasmon-enhanced Raman scattering,” Nat. Nanotechnol. **11**, 164–169 (2015).

[102] M. K. Schmidt, R. Esteban, A. González-Tudela, G. Giedke, and J. Aizpurua, “Quantum mechanical description of Raman scattering from molecules in plasmonic cavities,” ACS Nano **10**, 6291–6298 (2016).

[103] M. K. Schmidt, R. Esteban, F. Benz, J. J. Baumberg, and J. Aizpurua, “Linking classical and molecular optomechanics descriptions of SERS,” Faraday Discuss. **205**, 31–65 (2017).

[104] M. Kamandar Dezfouli and S. Hughes, “Quantum optics model of surface-enhanced Raman spectroscopy for arbitrarily shaped plasmonic resonators,” ACS Photonics **4**, 1245–1256 (2017).

[105] F. Benz, M. K. Schmidt, A. Dreismann, R. Chikkaraddy, Y. Zhang, A. Demetriadou, C. Carnegie, H. Ohadi, B. de Nijs, R. Esteban, J. Aizpurua, and J. J. Baumberg, “Single-molecule optomechanics in "picocavities",” Science **354**, 726–729 (2016).

[106] J. D. Jackson, *Classical electrodynamics* (Wiley, 1999).

[107] J. Schwinger, L. L. Deraad, K. A. Milton, W. Tsai, and J. Norton, *Classical electrodynamics* (Perseus Books, Reading, Massachusetts, 1998).

[108] J. A. Stratton, *Electromagnetic theory* (John Wiley & Sons, 2007).

[109] L. Novotny and B. Hecht, *Principles of Nano-Optics* (Cambridge University Press, 2006).

[110] U. Hohenester and A. Trügler, "MNPBEM – A Matlab toolbox for the simulation of plasmonic nanoparticles," Comp. Phys. Commun. **183**, 370–381 (2012).

[111] F. J. García de Abajo and J. Aizpurua, "Numerical simulation of electron energy loss near inhomogeneous dielectrics," Phys. Rev. B **56**, 15873–15884 (1997).

[112] A. D. Yaghjian, "Electric dyadic Green's functions in the source region," Proc. IEEE **68**, 248–263 (1980).

[113] M. Meier and A. Wokaun, "Enhanced fields on large metal particles: dynamic depolarization," Opt. Lett. **8**, 581–583 (1983).

[114] S. Albaladejo, R. Gómez-Medina, L. S. Froufe-Pérez, H. Marinchio, R. Carminati, J. F. Torrado, G. Armelles, A. García-Martín, and J. J. Sáenz, "Radiative corrections to the polarizability tensor of an electrically small anisotropic dielectric particle," Opt. Express **18**, 3556–3567 (2010).

[115] E. Castanié, R. Vincent, R. Pierrat, and R. Carminati, "Absorption by an optical dipole antenna in a structured environment," Int. J. Optics **2012**, 452047 (2012).

[116] P. Drude, "Zur Elektronentheorie der Metalle," Ann. Phys. **306**, 566–613 (1900).

[117] P. Drude, "Zur Elektronentheorie der Metalle; II. Teil. Galvanomagnetische und thermomagnetische Effecte," Ann. Phys. **308**, 369–402 (1900).

[118] R. H. Ritchie, "Plasma losses by fast electrons in thin films," Phys. Rev. **106**, 874–881 (1957).

[119] E. A. Stern and R. A. Ferrell, "Surface plasma oscillations of a degenerate electron gas," Phys. Rev. **120**, 130–136 (1960).

[120] D. Pines, *Theory of Quantum Liquids: Normal Fermi Liquids* (CRC Press, 2018).

[121] J. Pitarke, V. Silkin, E. Chulkov, and P. Echenique, "Theory of surface plasmons and surface-plasmon polaritons," Rep. Prog. Phys. **70**, 1–87 (2007).

[122] M. S. Tame, K. McEnery, Ş. Özdemir, J. Lee, S. Maier, and M. Kim, "Quantum plasmonics," Nat. Phys. **9**, 329–340 (2013).

[123] V. H. Nguyen and B. H. Nguyen, "Basics of quantum plasmonics," Adv. Nat. Sci: Nanosci. Nanotechnol. **6**, 023001 (2015).

[124] O. Keller, *Quantum theory of near-field electrodynamics* (Springer Berlin Heidelberg, Berlin, 2011).

[125] F. Ouyang and M. Isaacson, "Surface plasmon excitation of objects with arbitrary shape and dielectric constant," Philos. Mag. B **60**, 481–492 (1989).

[126] I. D. Mayergoyz, D. R. Fredkin, and Z. Zhang, "Electrostatic (plasmon) resonances in nanoparticles," Phys. Rev. B **72**, 155412 (2005).

[127] P. Morse and H. Feshbach, *Methods of Theoretical Physics vol. I* (McGraw-Hill, 1953).

[128] R. Englman and R. Ruppin, "Optical lattice vibrations in finite ionic crystals: I," J. Phys. C: Solid State Phys. **1**, 614 (1968).

[129] R. Englman and R. Ruppin, "Optical lattice vibrations in finite ionic crystals: II," J. Phys. C: Solid State Phys. **1**, 630 (1968).

[130] R. Englman and R. Ruppin, "Optical lattice vibrations in finite ionic crystals: III," J. Phys. C: Solid State Phys. **1**, 1515 (1968).

[131] B. Huttner and S. M. Barnett, "Quantization of the electromagnetic field in dielectrics," Phys. Rev. A **46**, 4306–4322 (1992).

[132] S. M. Barnett, B. Huttner, and R. Loudon, "Spontaneous emission in absorbing dielectric media," Phys. Rev. Lett. **68**, 3698–3701 (1992).

[133] T. Gruner and D.-G. Welsch, "Correlation of radiation-field ground-state fluctuations in a dispersive and lossy dielectric," Phys. Rev. A **51**, 3246–3256 (1995).

[134] R. Matloob, R. Loudon, M. Artoni, S. M. Barnett, and J. Jeffers, "Electromagnetic field quantization in amplifying dielectrics," Phys. Rev. A **55**, 1623–1633 (1997).

[135] S. Scheel, L. Knöll, and D.-G. Welsch, "QED commutation relations for inhomogeneous kramers-kronig dielectrics," Phys. Rev. A **58**, 700–706 (1998).

[136] H. T. Dung, L. Knöll, and D.-G. Welsch, "Three-dimensional quantization of the electromagnetic field in dispersive and absorbing inhomogeneous dielectrics," Phys. Rev. A **57**, 3931–3942 (1998).

[137] A. Dreuw and M. Head-Gordon, “Single-reference ab initio methods for the calculation of excited states of large molecules,” Chem. Rev. **105**, 4009–4037 (2005).

[138] C. Møller and M. S. Plesset, “Note on an approximation treatment for many-electron systems,” Phys. Rev. **46**, 618 (1934).

[139] F. Coester and H. Kümmel, “Short-range correlations in nuclear wave functions,” Nucl. Phys. **17**, 477–485 (1960).

[140] R. J. Bartlett, “Many-body perturbation theory and coupled cluster theory for electron correlation in molecules,” Annu. Rev. Phys. Chem. **32**, 359–401 (1981).

[141] R. J. Bartlett and M. Musiał, “Coupled-cluster theory in quantum chemistry,” Rev. Mod. Phys. **79**, 291–352 (2007).

[142] A. L. Fetter and J. D. Walecka, *Quantum theory of many-particle systems* (Courier Corporation, 2012).

[143] B. L. Hammond, W. A. Lester, and P. J. Reynolds, *Monte Carlo methods in ab initio quantum chemistry*, Vol. 1 (World Scientific, 1994).

[144] B. M. Austin, D. Y. Zubarev, and W. A. Lester, “Quantum monte carlo and related approaches,” Chem. Rev. **112**, 263–288 (2012).

[145] P. Hohenberg and W. Kohn, “Inhomogeneous electron gas,” Phys. Rev. **136**, B864–B871 (1964).

[146] K. Burke, “Perspective on density functional theory,” J. Chem. Phys. **136**, 150901 (2012).

[147] R. O. Jones, “Density functional theory: Its origins, rise to prominence, and future,” Rev. Mod. Phys. **87**, 897–923 (2015).

[148] R. A. Donnelly and R. G. Parr, “Elementary properties of an energy functional of the first-order reduced density matrix,” J. Chem. Phys. **69**, 4431–4439 (1978).

[149] E. Runge and E. K. U. Gross, “Density-functional theory for time-dependent systems,” Phys. Rev. Lett. **52**, 997–1000 (1984).

[150] W. Kohn and L. J. Sham, “Self-consistent equations including exchange and correlation effects,” Phys. Rev. **140**, A1133–A1138 (1965).

[151] T. Tsuneda, *Density functional theory in quantum chemistry* (Springer, 2016).

[152] K. Burke, J. Werschnik, and E. K. U. Gross, “Time-dependent density functional theory: Past, present, and future,” J. Chem. Phys. **123**, 062206 (2005).

[153] M. A. Marques, C. A. Ullrich, F. Nogueira, A. Rubio, K. Burke, and E. K. Gross, *Time-dependent density functional theory* (Springer Science & Business Media, 2006).

[154] M. Valiev, E. J. Bylaska, N. Govind, K. Kowalski, T. P. Straatsma, H. J. J. Van Dam, D. Wang, J. Nieplocha, E. Apra, T. L. Windus, and W. de Jong, "Nwchem: a comprehensive and scalable open-source solution for large scale molecular simulations," Comput. Phys. Commun. **181**, 1477–1489 (2010).

[155] M. E. Casida, "Time-dependent density functional response theory for molecules," in *Recent Advances In Density Functional Methods: (Part I)* (World Scientific, 1995) pp. 155–192.

[156] M. Klessinger and J. Michl, *Excited states and photochemistry of organic molecules* (Wiley-VCH, 1995).

[157] V. May and O. Kühn, *Charge and energy transfer dynamics in molecular systems* (John Wiley & Sons, 2008).

[158] H.-P. Breuer and F. Petruccione, *The theory of open quantum systems* (Oxford University Press, 2003).

[159] K. Blum, *Density matrix theory and applications* (Springer Science & Business Media, 2013).

[160] D. A. Steck, "Quantum and atom optics," (2018), revision 0.12.2, [http://steck.us/teaching, 4 September 2018].

[161] M. O. Scully and M. S. Zubairy, *Quantum optics* (Cambridge University Press, 1997).

[162] L. Mandel and E. Wolf, *Optical coherence and quantum optics* (Cambridge university press, 1995).

[163] S. Bloom and H. Margenau, "Quantum theory of spectral line broadening," Phys. Rev. **90**, 791–794 (1953).

[164] B. R. Mollow, "Stimulated emission and absorption near resonance for driven systems," Phys. Rev. A **5**, 2217–2222 (1972).

[165] P. Zhou and S. Swain, "Quantum interference in probe absorption: Narrow resonances, transparency, and gain without population inversion," Phys. Rev. Lett. **78**, 832–835 (1997).

[166] A. Campion and P. Kambhampati, "Surface-enhanced Raman scattering," Chem. Soc. Rev. **27**, 241–250 (1998).

[167] B. Pettinger, B. Ren, G. Picardi, R. Schuster, and G. Ertl, "Nanoscale probing of adsorbed species by tip-enhanced Raman spectroscopy," Phys. Rev. Lett. **92**, 096101 (2004).

[168] C. Ciracì, R. T. Hill, J. J. Mock, Y. Urzhumov, A. I. Fernández-Domínguez, S. A. Maier, J. B. Pendry, A. Chilkoti, and D. R. Smith, "Probing the ultimate limits of plasmonic enhancement," Science **337**, 1072–1074 (2012).

[169] J. F. Li, Y. F. Huang, Y. Ding, and et al., "Shell-isolated nanoparticle-enhanced Raman spectroscopy," Nature **464**, 392–395 (2010).

[170] L. H. Oakley, D. M. Fabian, H. E. Mayhew, S. A. Svoboda, and K. L. Wustholz, "Pretreatment strategies for SERS analysis of indigo and prussian blue in aged painted surfaces," Anal. Chem. **84**, 8006–8012 (2012).

[171] M. Paulite, C. Blum, T. Schmid, L. Opilik, K. Eyer, G. C. Walker, and R. Zenobi, "Full spectroscopic tip-enhanced Raman imaging of single nanotapes formed from β-amyloid(1-40) peptide fragments," ACS Nano **7**, 911–920 (2013).

[172] D. van Lierop, I. A. Larmour, K. Faulds, and D. Graham, "SERS primers and their mode of action for pathogen dna detection," Anal. Chem. **85**, 1408–1414 (2013).

[173] F. S. Ameer, W. Hu, S. M. Ansar, K. Siriwardana, W. E. Collier, S. Zou, and D. Zhang, "Robust and reproducible quantification of SERS enhancement factors using a combination of time-resolved Raman spectroscopy and solvent internal reference method," J. Phys. Chem. C **117**, 3483–3488 (2013).

[174] E. A. Pozzi, M. D. Sonntag, N. Jiang, J. M. Klingsporn, M. C. Hersam, and R. P. Van Duyne, "Tip-enhanced Raman imaging: An emergent tool for probing biology at the nanoscale," ACS Nano **7**, 885–888 (2013).

[175] B. H. Stuart, *Infrared Spectroscopy: Fundamentals and Applications* (John Wiley & Sons, 2005).

[176] H. Hu, X. Yang, F. Zhai, D. Hu, R. Liu, K. Liu, Z. Sun, and Q. Dai, "Far-field nanoscale infrared spectroscopy of vibrational fingerprints of molecules with graphene plasmons," Nat. Commun. **7**, 12334 (2016).

[177] D. Rodrigo, O. Limaj, D. Janner, D. Etezadi, F. J. G. de Abajo, V. Pruneri, and H. Altug, "Mid-infrared plasmonic biosensing with graphene," Science **349**, 165–168 (2015).

[178] R. Adato, A. A. Yanik, J. J. Amsden, D. L. Kaplan, F. G. Omenetto, M. K. Hong, S. Erramilli, and H. Altug, "Ultra-sensitive vibrational spectroscopy of protein monolayers with plasmonic nanoantenna arrays," Proc. Natl. Acad. Sci. U.S.A. **106**, 19227–19232 (2009).

[179] O. Limaj, D. Etezadi, N. J. Wittenberg, D. Rodrigo, D. Yoo, S.-H. Oh, and H. Altug, "Infrared plasmonic biosensor for real-time and label-free monitoring of lipid membranes," Nano Lett. **16**, 1502–1508 (2016).

[180] E. Talebian and M. Talebian, “A general review on the derivation of Clausius–Mossotti relation,” Optik **124**, 2324–2326 (2013).

[181] J. Kischkat, S. Peters, B. Gruska, M. Semtsiv, M. Chashnikova, M. Klinkmüller, O. Fedosenko, S. Machulik, A. Aleksandrova, G. Monastyrskyi, Y. Flores, and W. T. Masselink, “Mid-infrared optical properties of thin films of aluminum oxide, titanium dioxide, silicon dioxide, aluminum nitride, and silicon nitride,” Appl. Opt. **51**, 6789–6798 (2012).

[182] K. L. Kliewer and R. Fuchs, “Optical modes of vibration in an ionic crystal slab including retardation. i. nonradiative region,” Phys. Rev. **144**, 495–503 (1966).

[183] K. L. Kliewer and R. Fuchs, “Optical modes of vibration in an ionic crystal slab including retardation. ii. radiative region,” Phys. Rev. **150**, 573–588 (1966).

[184] R. Fuchs and K. Kliewer, “Optical modes of vibration in an ionic crystal sphere,” J. Opt. Soc. Am **58**, 319–330 (1968).

[185] R. Hillenbrand, T. Taubner, and F. Keilmann, “Phonon-enhanced light–matter interaction at the nanometre scale,” Nature **418**, 159 (2002).

[186] M. S. Anderson, “Surface enhanced infrared absorption by coupling phonon and plasma resonance,” Appl. Phys. Lett. **87**, 144102 (2005).

[187] A. Huber, N. Ocelic, T. Taubner, and R. Hillenbrand, “Nanoscale resolved infrared probing of crystal structure and of plasmon- phonon coupling,” Nano Lett. **6**, 774–778 (2006).

[188] R. Marty, A. Mlayah, A. Arbouet, C. Girard, and S. Tripathy, “Plasphonics : local hybridization of plasmons and phonons,” Opt. Express **21**, 4551–4559 (2013).

[189] C. Huck, J. Vogt, T. Neuman, T. Nagao, R. Hillenbrand, J. Aizpurua, A. Pucci, and F. Neubrech, “Strong coupling between phonon-polaritons and plasmonic nanorods,” Opt. Express **24**, 25528–25539 (2016).

[190] M. K. Gunde, “Vibrational modes in amorphous silicon dioxide,” Ph. B **292**, 286–295 (2000).

[191] A. E. Miroshnichenko, S. Flach, and Y. S. Kivshar, “Fano resonances in nanoscale structures,” Rev. Mod. Phys. **82**, 2257–2298 (2010).

[192] Y. Francescato, V. Giannini, and S. A. Maier, “Plasmonic systems unveiled by Fano resonances,” ACS Nano **6**, 1830–1838 (2012).

[193] A. Lovera, B. Gallinet, P. Nordlander, and O. J. Martin, "Mechanisms of Fano resonances in coupled plasmonic systems," ACS Nano **7**, 4527–4536 (2013).

[194] B. Gallinet and O. J. F. Martin, "Influence of electromagnetic interactions on the line shape of plasmonic Fano resonances," ACS Nano **5**, 8999–9008 (2011).

[195] T. Neuman, "Study of optical properties of metallic structures and their applications in nano-optics," (2014).

[196] R. Adato, A. Artar, S. Erramilli, and H. Altug, "Engineered absorption enhancement and induced transparency in coupled molecular and plasmonic resonator systems," Nano Lett. **13**, 2584–2591 (2013).

[197] U. Fano, "Effects of configuration interaction on intensities and phase shifts," Phys. Rev. **124**, 1866–1878 (1961).

[198] M. F. Limonov, M. V. Rybin, A. N. Poddubny, and Y. S. Kivshar, "Fano resonances in photonics," Nat. Photonics **11**, 543–554 (2017).

[199] B. Gallinet and O. Martin, "Ab initio theory of Fano resonances," Phys. Rev. B **83**, 235427 (2011).

[200] T. J. Seok, A. Jamshidi, M. Kim, S. Dhuey, A. Lakhani, H. Choo, P. J. Schuck, S. Cabrini, A. M. Schwartzberg, J. Bokor, E. Yablonovitch, and M. C. Wu, "Radiation engineering of optical antennas for maximum field enhancement," Nano Lett. **11**, 2606–2610 (2011).

[201] P. Tassin, L. Zhang, R. Zhao, A. Jain, T. Koschny, and C. M. Soukoulis, "Electromagnetically induced transparency and absorption in metamaterials: The radiating two-oscillator model and its experimental confirmation," Phys. Rev. Lett. **109**, 187401 (2012).

[202] E. Palik, *Handbook of Optical Constants of Solids*, Academic Press handbook series No. vol. 2 (Academic Press, 1991).

[203] "Lumerical inc., fdtd solutions," [http://www.lumerical.com/tcad-products/fdtd/, 5 July 2018].

[204] A. Priebe, M. Sinther, G. Fahsold, and A. Pucci, "The correlation between film thickness and adsorbate line shape in surface enhanced infrared absorption," J. Chem. Phys. **119**, 4887–4890 (2003).

[205] J. Bochterle, F. Neubrech, T. Nagao, and A. Pucci, "Angstrom-scale distance dependence of antenna-enhanced vibrational signals," ACS Nano **6**, 10917–10923 (2012).

[206] D. Dregely, F. Neubrech, H. Duan, R. Vogelgesang, and H. Giessen, "Vibrational near-field mapping of planar and buried three-dimensional plasmonic nanostructures," Nat. Commun. **4**, 2237 (2013).

[207] R. Adato and H. Altug, "In-situ ultra-sensitive infrared absorption spectroscopy of biomolecule interactions in real time with plasmonic nanoantennas," Nat. Commun. **4**, 2154 (2013).

[208] X. Chen, C. Ciracì, D. R. Smith, and S.-H. Oh, "Nanogap-enhanced infrared spectroscopy with template-stripped wafer-scale arrays of buried plasmonic cavities," Nano Lett. **15**, 107–113 (2015).

[209] E. M. Purcell, H. C. Torrey, and R. V. Pound, "Resonance absorption by nuclear magnetic moments in a solid," Phys. Rev. **69**, 37–38 (1946).

[210] M. L. Andersen, S. Stobbe, A. S. Sørensen, and P. Lodahl, "Strongly modified plasmon-matter interaction with mesoscopic quantum emitters," Nat. Phys. **7**, 215–218 (2011).

[211] K. H. Madsen, S. Ates, T. Lund-Hansen, A. Löffler, S. Reitzenstein, A. Forchel, and P. Lodahl, "Observation of non-markovian dynamics of a single quantum dot in a micropillar cavity," Phy. Rev. Lett. **106**, 233601 (2011).

[212] P. K. Jain, D. Ghosh, R. Baer, E. Rabani, and A. P. Alivisatos, "Near-field manipulation of spectroscopic selection rules on the nanoscale," Proc. Natl. Acad. Sci. U.S.A. **109**, 8016–8019 (2012).

[213] S. Stobbe, P. T. Kristensen, J. E. Mortensen, J. M. Hvam, J. Mørk, and P. Lodahl, "Spontaneous emission from large quantum dots in nanostructures: Exciton-photon interaction beyond the dipole approximation," Phys. Rev. B **86**, 085304 (2012).

[214] P. T. Kristensen, J. E. Mortensen, P. Lodahl, and S. Stobbe, "Shell theorem for spontaneous emission," Phys. Rev. B **88**, 205308 (2013).

[215] J. M. Gordon and Y. N. Gartstein, "Local field effects for spherical quantum dot emitters in the proximity of a planar dielectric interface," J. Opt. Soc. Am. B **31**, 2029–2035 (2014).

[216] M. Pelton, "Modified spontaneous emission in nanophotonic structures," Nat. Photonics **9**, 427–435 (2015).

[217] M. Cotrufo and A. Fiore, "Spontaneous emission from dipole-forbidden transitions in semiconductor quantum dots," Phys. Rev. B **92**, 125302 (2015).

[218] P. Tighineanu, A. S. Sørensen, S. Stobbe, and P. Lodahl, "Unraveling the mesoscopic character of quantum dots in nanophotonics," Phys. Rev. Lett. **114**, 247401 (2015).

[219] P. Lodahl, S. Mahmoodian, and S. Stobbe, “Interfacing single photons and single quantum dots with photonic nanostructures,” Rev. Mod. Phys. **87**, 347 (2015).

[220] C.-J. Yang and J.-H. An, “Resonance fluorescence beyond the dipole approximation of a quantum dot in a plasmonic nanostructure,” Phys. Rev. A **93**, 053803 (2016).

[221] S. Corni and J. Tomasi, “Enhanced response properties of a chromophore physisorbed on a metal particle,” J. Chem. Phys. **114**, 3739–3751 (2001).

[222] S. Corni and J. Tomasi, “Lifetimes of electronic excited states of a molecule close to a metal surface,” The Journal of Chemical Physics **118**, 6481–6494 (2003).

[223] O. Andreussi, S. Corni, B. Mennucci, and J. Tomasi, “Radiative and nonradiative decay rates of a molecule close to a metal particle of complex shape,” J. Chem. Phys. **121**, 10190–10202 (2004).

[224] N. Rivera, I. Kaminer, B. Zhen, J. D. Joannopoulos, and M. Soljačić, “Shrinking light to allow forbidden transitions on the atomic scale,” Science **353**, 263–269 (2016).

[225] E. T. Jaynes and F. W. Cummings, “Comparison of quantum and semiclassical radiation theories with application to the beam maser,” Proc. IEEE **51**, 89–109 (1963).

[226] N. T. Fofang, N. K. Grady, Z. Fan, A. O. Govorov, and N. J. Halas, “Plexciton dynamics: Exciton-plasmon coupling in a J-aggregate-Au nanoshell complex provides a mechanism for nonlinearity,” Nano Lett. **11**, 1556–1560 (2011).

[227] F. Wang and Y. R. Shen, “General properties of local plasmons in metal nanostructures,” Phys. Rev. Lett. **97**, 206806 (2006).

[228] A. F. Koenderink, “On the use of Purcell factors for plasmon antennas,” Opt. Lett. **35**, 4208–4210 (2010).

[229] C. Sauvan, J. P. Hugonin, I. S. Maksymov, and P. Lalanne, “Theory of the spontaneous optical emission of nanosize photonic and plasmon resonators,” Phys. Rev. Lett. **110**, 237401 (2013).

[230] P. T. Kristensen and S. Hughes, “Modes and mode volumes of leaky optical cavities and plasmonic nanoresonators,” ACS Photonics **1**, 2–10 (2013).

[231] F. Bloch and A. Siegert, “Magnetic resonance for nonrotating fields,” Phys. Rev. **57**, 522–527 (1940).

[232] J. H. Shirley, “Solution of the schrödinger equation with a hamiltonian periodic in time,” Phys. Rev. **138**, B979–B987 (1965).

[233] J. Fink, M. Göppl, M. Baur, R. Bianchetti, P. Leek, A. Blais, and A. Wallraff, "Climbing the jaynes–cummings ladder and observing its nonlinearity in a cavity QED system," Nature **454**, 315–318 (2008).

[234] E. del Valle, F. P. Laussy, and C. Tejedor, "Luminescence spectra of quantum dots in microcavities. II. Fermions," Phys. Rev. B **79**, 235326 (2009).

[235] K. M. Birnbaum, A. Boca, R. Miller, A. D. Boozer, T. E. Northup, and H. J. Kimble, "Photon blockade in an optical cavity with one trapped atom," Nature **436**, 87–90 (2005).

[236] A. Manjavacas, P. Nordlander, and F. J. Garciía de Abajo, "Plasmon blockade in nanostructured graphene," ACS Nano **6**, 1724–1731 (2012).

[237] S. Huang, T. Ming, Y. Lin, X. Ling, Q. Ruan, T. Palacios, J. Wang, M. Dresselhaus, and J. Kong, "Ultrasmall mode volumes in plasmonic cavities of nanoparticle-on-mirror structures," Small **12**, 5190–5199 (2016).

[238] R. Chikkaraddy, B. de Nijs, F. Benz, S. J. Barrow, O. A. Scherman, E. Rosta, A. Demetriadou, P. Fox, O. Hess, and J. J. Baumberg, "Single-molecule strong coupling at room temperature in plasmonic nanocavities," Nature **535**, 127–130 (2016).

[239] E. Prodan, C. Radloff, N. J. Halas, and P. Nordlander, "A hybridization model for the plasmon response of complex nanostructures," Science **302**, 419–422 (2003).

[240] P. Nordlander, C. Oubre, E. Prodan, K. Li, and M. Stockman, "Plasmon hybridization in nanoparticle dimers," Nano Lett. **4**, 899–903 (2004).

[241] E. Prodan and P. Nordlander, "Plasmon hybridization in spherical nanoparticles," J. Chem. Phys. **120**, 5444–5454 (2004).

[242] D. J. Bergman and M. I. Stockman, "Surface plasmon amplification by stimulated emission of radiation: Quantum generation of coherent surface plasmons in nanosystems," Phys. Rev. Lett. **90**, 027402 (2003).

[243] G. Ford and W. Weber, "Electromagnetic interactions of molecules with metal surfaces," Phys. Rep. **113**, 195 – 287 (1984).

[244] J. Crowell and R. H. Ritchie, "Radiative decay of Coulomb-stimulated plasmons in spheres," Phys. Rev. **172**, 436–440 (1968).

[245] T. V. Teperik, P. Nordlander, J. Aizpurua, and A. G. Borisov, "Robust subnanometric plasmon ruler by rescaling of the nonlocal optical response," Phys. Rev. Lett. **110**, 263901 (2013).

[246] Y. Luo, A. I. Fernandez-Dominguez, A. Wiener, S. A. Maier, and J. B. Pendry, “Surface plasmons and nonlocality: A simple model,” Phys. Rev. Lett. **111**, 093901 (2013).

[247] M. K. Dezfouli, C. Tserkezis, N. A. Mortensen, and S. Hughes, “Nonlocal quasinormal modes for arbitrarily shaped three-dimensional plasmonic resonators,” Optica **4**, 1503–1509 (2017).

[248] M. Urbieta, M. Barbry, Y. Zhang, P. Koval, D. Sánchez-Portal, N. Zabala, and J. Aizpurua, “Atomic-scale lightning rod effect in plasmonic picocavities: A classical view to a quantum effect,” ACS Nano **12**, 585–595 (2018).

[249] M. Barbry, P. Koval, F. Marchesin, R. Esteban, A. G. Borisov, J. Aizpurua, and D. Sánchez-Portal, “Atomistic near-field nanoplasmonics: Reaching atomic-scale resolution in nanooptics,” Nano Lett. **15**, 3410–3419 (2015).

[250] R.-Q. Li, D. Hernángomez-Pérez, F. J. García-Vidal, and A. I. Fernández-Domínguez, “Transformation optics approach to plasmon-exciton strong coupling in nanocavities,” Phys. Rev. Lett. **117**, 107401 (2016).

[251] A. Delga, J. Feist, J. Bravo-Abad, and F. J. Garcia-Vidal, “Theory of strong coupling between quantum emitters and localized surface plasmons,” J. Opt. **16**, 114018 (2014).

[252] J. A. Hutchison, T. Schwartz, C. Genet, E. Devaux, and T. W. Ebbesen, “Modifying chemical landscapes by coupling to vacuum fields,” Angew. Chem. Int. Ed. **51**, 1592–1596 (2012).

[253] A. Canaguier-Durand, E. Devaux, J. George, Y. Pang, J. A. Hutchison, T. Schwartz, C. Genet, N. Wilhelms, J.-M. Lehn, and T. W. Ebbesen, “Thermodynamics of molecules strongly coupled to the vacuum field,” Angew. Chem. Int. Ed. **52**, 10533–10536 (2013).

[254] A. Thomas, J. George, A. Shalabney, M. Dryzhakov, S. J. Varma, J. Moran, T. Chervy, X. Zhong, E. Devaux, C. Genet, J. A. Hutchison, and T. W. Ebbesen, “Ground-state chemical reactivity under vibrational coupling to the vacuum electromagnetic field,” Angew. Chem. Int. Ed. **55**, 11462–11466 (2016).

[255] F. Herrera and F. C. Spano, “Cavity-controlled chemistry in molecular ensembles,” Phys. Rev. Lett. **116**, 238301 (2016).

[256] J. Flick, C. Schäfer, M. Ruggenthaler, H. Appel, and A. Rubio, “Ab-initio optimized effective potentials for real molecules in optical cavities: Photon contributions to the molecular ground state,” ACS Photonics **5**, 992–1005 (2017).

[257] H. Deng, G. Weihs, C. Santori, J. Bloch, and Y. Yamamoto, “Condensation of semiconductor microcavity exciton polaritons,” Science **298**, 199–202 (2002).

[258] J. Kasprzak, M. Richard, S. Kundermann, A. Baas, P. Jeambrun, J. Keeling, F. Marchetti, M. Szymańska, R. Andre, J. Staehli, *et al.*, "Bose–einstein condensation of exciton polaritons," Nature **443**, 409 (2006).

[259] R. Balili, V. Hartwell, D. Snoke, L. Pfeiffer, and K. West, "Bose-einstein condensation of microcavity polaritons in a trap," Science **316**, 1007–1010 (2007).

[260] G. Tosi, G. Christmann, N. Berloff, P. Tsotsis, T. Gao, Z. Hatzopoulos, P. Savvidis, and J. Baumberg, "Sculpting oscillators with light within a nonlinear quantum fluid," Nat. Phys. **8**, 190 (2012).

[261] J. D. Plumhof, T. Stöferle, L. Mai, U. Scherf, and R. F. Mahrt, "Room-temperature bose–einstein condensation of cavity exciton–polaritons in a polymer," Nat. Mater. **13**, 247 (2014).

[262] K. Daskalakis, S. Maier, R. Murray, and S. Kéna-Cohen, "Nonlinear interactions in an organic polariton condensate," Nat. Mater. **13**, 271 (2014).

[263] D. Sanvitto and S. Kéna-Cohen, "The road towards polaritonic devices," Nat. Mater. **15**, 1061 (2016).

[264] C. P. Dietrich, A. Steude, L. Tropf, M. Schubert, N. M. Kronenberg, K. Ostermann, S. Hoefling, and M. C. Gather, "An exciton-polariton laser based on biologically produced fluorescent protein," Sci. Adv. **2**, e1600666 (2016).

[265] Y. Sun, P. Wen, Y. Yoon, G. Liu, M. Steger, L. N. Pfeiffer, K. West, D. W. Snoke, and K. A. Nelson, "Bose-einstein condensation of long-lifetime polaritons in thermal equilibrium," Phys. Rev. Lett. **118**, 016602 (2017).

[266] D. M. Coles, N. Somaschi, P. Michetti, C. Clark, P. G. Lagoudakis, P. G. Savvidis, and D. G. Lidzey, "Polariton-mediated energy transfer between organic dyes in a strongly coupled optical microcavity," Nat. Mater. **13**, 712 (2014).

[267] X. Zhong, T. Chervy, L. Zhang, A. Thomas, J. George, C. Genet, J. A. Hutchison, and T. W. Ebbesen, "Energy transfer between spatially separated entangled molecules," Angew. Chem. Int. Ed. **56**, 9034–9038 (2017).

[268] D. G. Lidzey, D. D. C. Bradley, T. Virgili, A. Armitage, M. S. Skolnick, and S. Walker, "Room temperature polariton emission from strongly coupled organic semiconductor microcavities," Phys. Rev. Lett. **82**, 3316–3319 (1999).

[269] N. Christogiannis, N. Somaschi, P. Michetti, D. M. Coles, P. G. Savvidis, P. G. Lagoudakis, and D. G. Lidzey, "Characterizing the electroluminescence emission from a strongly coupled organic semiconductor microcavity LED," Adv. Opt. Mater. **1**, 503–509 (2013).

[270] M. Wersäll, J. Cuadra, T. J. Antosiewicz, S. Balci, and T. Shegai, “Observation of mode splitting in photoluminescence of individual plasmonic nanoparticles strongly coupled to molecular excitons,” Nano Lett. **17**, 551–558 (2017).

[271] A. Canaguier-Durand, C. Genet, A. Lambrecht, T. W. Ebbesen, and S. Reynaud, “Non-markovian polariton dynamics in organic strong coupling,” Eur. Phys. J. D **69**, 24 (2015).

[272] S. Mukamel, “On the nature of intramolecular dephasing processes in polyatomic molecules,” Chem. Phys. **31**, 327–333 (1978).

[273] J. del Pino, F. A. Schröder, A. W. Chin, J. Feist, and F. J. García-Vidal, “Tensor network simulation of non-markovian dynamics in organic polaritons,” arXiv preprint arXiv:1804.04511 (2018).

[274] B. Li, A. E. Johnson, S. Mukamel, and A. B. Myers, “The brownian oscillator model for solvation effects in spontaneous light emission and their relationship to electron transfer,” J. Am. Chem. Soc. **116**, 11039–11047 (1994).

[275] J. Tomasi, B. Mennucci, and R. Cammi, “Quantum mechanical continuum solvation models,” Chem. Rev. **105**, 2999–3094 (2005).

[276] T.-S. Yang, P. Vöhringer, D. C. Arnett, and N. F. Scherer, “The solvent spectral density and vibrational multimode approach to optical dephasing: Two-pulse photon echo response,” J. Chem. Phys. **103**, 8346–8359 (1995).

[277] C. Roy and S. Hughes, “Influence of electron-acoustic-phonon scattering on intensity power broadening in a coherently driven quantum-dot-cavity system,” Phys. Rev. X **1**, 021009 (2011).

[278] L. A. Pachón and P. Brumer, “Direct experimental determination of spectral densities of molecular complexes,” J. Chem. Phys. **141**, 174102 (2014).

[279] K. Roy-Choudhury and S. Hughes, “Spontaneous emission from a quantum dot in a structured photonic reservoir: phonon-mediated breakdown of Fermi’s golden rule,” Optica **2**, 434–437 (2015).

[280] M. M. Toutounji and G. J. Small, “The underdamped brownian oscillator model with ohmic dissipation: Applicability to low-temperature optical spectra,” J. Chem. Phys. **117**, 3848–3855 (2002).

[281] J. Roden, W. T. Strunz, K. B. Whaley, and A. Eisfeld, “Accounting for intra-molecular vibrational modes in open quantum system description of molecular systems,” J. Chem. Phys. **137**, 204110 (2012).

[282] C. Kreisbeck and T. Kramer, “Long-lived electronic coherence in dissipative exciton dynamics of light-harvesting complexes,” J. Phys. Chem. Lett. **3**, 2828–2833 (2012).

[283] A. Kell, X. Feng, M. Reppert, and R. Jankowiak, "On the shape of the phonon spectral density in photosynthetic complexes," J. Phys. Chem. B **117**, 7317–7323 (2013).

[284] T. Virgili, D. Coles, A. M. Adawi, C. Clark, P. Michetti, S. K. Rajendran, D. Brida, D. Polli, G. Cerullo, and D. G. Lidzey, "Ultrafast polariton relaxation dynamics in an organic semiconductor microcavity," Phys. Rev. B **83**, 245309 (2011).

[285] T. Schwartz, J. A. Hutchison, J. Léonard, C. Genet, S. Haacke, and T. W. Ebbesen, "Polariton dynamics under strong light-molecule coupling," Chem. Phys. Chem. **14**, 125–131 (2013).

[286] S. Wang, T. Chervy, J. George, J. A. Hutchison, C. Genet, and T. W. Ebbesen, "Quantum yield of polariton emission from hybrid light-matter states," J. Phys. Chem. Lett. **5**, 1433–1439 (2014).

[287] M. Aspelmeyer, T. J. Kippenberg, and F. Marquardt, "Cavity optomechanics," Rev. Mod. Phys. **86**, 1391–1452 (2014).

[288] H. Xu, X.-H. Wang, M. P. Persson, H. Q. Xu, M. Käll, and P. Johansson, "Unified treatment of fluorescence and Raman scattering processes near metal surfaces," Phys. Rev. Lett. **93**, 243002 (2004).

[289] P. Johansson, H. Xu, and M. Käll, "Surface-enhanced Raman scattering and fluorescence near metal nanoparticles," Phys. Rev. B **72**, 035427 (2005).

[290] Y. Gu, L. Huang, O. J. F. Martin, and Q. Gong, "Resonance fluorescence of single molecules assisted by a plasmonic structure," Phys. Rev. B **81**, 193103 (2010).

[291] A. Ridolfo, O. Di Stefano, N. Fina, R. Saija, and S. Savasta, "Quantum plasmonics with quantum dot-metal nanoparticle molecules: Influence of the Fano effect on photon statistics," Phys. Rev. Lett. **105**, 263601 (2010).

[292] D. A. Long, *The Raman effect: a unified treatment of the theory of Raman scattering by molecules* (Wiley, 2002).

[293] A. Lombardi, M. K. Schmidt, L. Weller, W. M. Deacon, F. Benz, B. de Nijs, J. Aizpurua, and J. J. Baumberg, "Pulsed molecular optomechanics in plasmonic nanocavities: From nonlinear vibrational instabilities to bond-breaking," Phys. Rev. X **8**, 011016 (2018).

[294] T. Ramos, V. Sudhir, K. Stannigel, P. Zoller, and T. J. Kippenberg, "Nonlinear quantum optomechanics via individual intrinsic two-level defects," Phys. Rev. Lett. **110**, 193602 (2013).

[295] M. J. Akram, F. Ghafoor, and F. Saif, "Electromagnetically induced transparency and tunable fano resonances in hybrid optomechanics," J. Phys. B **48**, 065502 (2015).

[296] A. Nunnenkamp, K. Børkje, and S. M. Girvin, "Single-photon optomechanics," Phys. Rev. Lett. **107**, 063602 (2011).

[297] A. Nunnenkamp, K. Børkje, and S. M. Girvin, "Cooling in the single-photon strong-coupling regime of cavity optomechanics," Phys. Rev. A **85**, 051803 (2012).

[298] M. Galperin, M. A. Ratner, and A. Nitzan, "Raman scattering in current-carrying molecular junctions," J. Chem. Phys. **130**, 144109 (2009).

[299] J. del Pino, J. Feist, and F. J. Garcia-Vidal, "Signatures of vibrational strong coupling in Raman scattering," Phys. Chem. C **119**, 29132–29137 (2015).

[300] R. Betzholz, J. M. Torres, and M. Bienert, "Quantum optical master equation for solid-state quantum emitters," Phys. Rev. A **90**, 063818 (2014).

[301] K. Jaehne, K. Hammerer, and M. Wallquist, "Ground-state cooling of a nanomechanical resonator via a cooper-pair box qubit," New J. Phys. **10**, 095019 (2008).

[302] U. Akram, N. Kiesel, M. Aspelmeyer, and G. J. Milburn, "Single-photon opto-mechanics in the strong coupling regime," New J. Phys **12**, 083030 (2010).

[303] R. Esteban, J. Aizpurua, and G. W. Bryant, "Strong coupling of single emitters interacting with phononic infrared antennae," New J. Phys. **16**, 013052 (2014).

[304] Q. Huang, C. J. Medforth, and R. Schweitzer-Stenner, "Nonplanar heme deformations and excited state displacements in nickel porphyrins detected by Raman spectroscopy at soret excitation," J. Phys. Chem. A **109**, 10493–10502 (2005).

[305] R. S. Sánchez-Carrera, M. C. R. Delgado, C. C. Ferrón, R. M. Osuna, V. Hernández, J. T. L. Navarrete, and A. Aspuru-Guzik, "Optical absorption and emission properties of end-capped oligothienoacenes: A joint theoretical and experimental study," Org. Electron. **11**, 1701 – 1712 (2010).

[306] B. R. Mollow, "Power spectrum of light scattered by two-level systems," Phys. Rev. **188**, 1969–1975 (1969).

[307] R.-C. Ge, C. Van Vlack, P. Yao, J. F. Young, and S. Hughes, "Accessing quantum nanoplasmonics in a hybrid quantum dot–metal nanosystem: Mollow triplet of a quantum dot near a metal nanoparticle," Phys. Rev. B **87**, 205425 (2013).

[308] G. Wrigge, I. Gerhardt, J. Hwang, G. Zumofen, and V. Sandoghdar, "Efficient coupling of photons to a single molecule and the observation of its resonance fluorescence," Nat. Phys. **4**, 60–66 (2008).

[309] C. S. Muñoz, F. P. Laussy, E. del Valle, C. Tejedor, and A. González-Tudela, "Filtering multiphoton emission from state-of-the-art cavity quantum electrodynamics," Optica **5**, 14–26 (2018).

[310] J. Kabuss, A. Carmele, M. Richter, and A. Knorr, "Microscopic equation-of-motion approach to the multiphonon assisted quantum emission of a semiconductor quantum dot," Phys. Rev. B **84**, 125324 (2011).

[311] C. Cohen-Tannoudji and S. Reynaud, "Modification of resonance Raman scattering in very intense laser fields," J. Phys. B: At. Mol. Phys. **10**, 365 (1977).

[312] G. S. Agarwal and S. S. Jha, "Theory of resonant Raman scattering of intense optical waves," J. Phys. B: At. Mol. Phys. **12**, 2655 (1979).

[313] C. Cohen-Tannoudji and S. Reynaud, "Dressed-atom approach to resonance fluorescence," Multiphoton Processes , 103–118 (1978).

[314] C. Cohen-Tannoudji and S. Reynaud, "Dressed-atom description of resonance fluorescence and absorption spectra of a multi-level atom in an intense laser beam," J. Phys. B: At. Mol. Phys. **10**, 345 (1977).

[315] G. P. Wiederrecht, G. A. Wurtz, and J. Hranisavljevic, "Coherent coupling of molecular excitons to electronic polarizations of noble metal nanoparticles," Nano Lett. **4**, 2121–2125 (2004).

[316] N. T. Fofang, T.-H. Park, O. Neumann, N. A. Mirin, P. Nordlander, and N. J. Halas, "Plexcitonic nanoparticles: plasmon-exciton coupling in nanoshell- J-aggregate complexes," Nano Lett. **8**, 3481–3487 (2008).

[317] F. Würthner, T. E. Kaiser, and C. R. Saha-Möller, "J-aggregates: From serendipitous discovery to supramolecular engineering of functional dye materials," Angew. Chem. Int. Ed. **50**, 3376–3410 (2011).

[318] R. J. Thompson, G. Rempe, and H. J. Kimble, "Observation of normal-mode splitting for an atom in an optical cavity," Phys. Rev. Lett. **68**, 1132–1135 (1992).

[319] T. K. Hakala, J. J. Toppari, A. Kuzyk, M. Pettersson, H. Tikkanen, H. Kunttu, and P. Törmä, "Vacuum Rabi splitting and strong-coupling dynamics for surface-plasmon polaritons and rhodamine 6g molecules," Phys. Rev. Lett. **103**, 053602 (2009).

[320] S. Kéna-Cohen, M. Davanço, and S. R. Forrest, "Strong exciton-photon coupling in an organic single crystal microcavity," Phys. Rev. Lett. **101**, 116401 (2008).

[321] R. C. Maher, L. F. Cohen, E. C. Le Ru, and P. G. Etchegoin, “A study of local heating of molecules under surface enhanced Raman scattering (SERS) conditions using the anti-Stokes/Stokes ratio,” Faraday Discuss. **132**, 77–83 (2006).

[322] E. Le Ru, C. Galloway, and P. Etchegoin, “On the connection between optical absorption/extinction and SERS enhancements,” Phys. Chem. Chem. Phys. **8**, 3083–3087 (2006).

[323] R. C. Maher, P. G. Etchegoin, E. C. Le Ru, and L. F. Cohen, “A conclusive demonstration of vibrational pumping under surface enhanced Raman scattering conditions,” J. Phys. Chem. B **110**, 11757–11760 (2006).

[324] A. Gonzalez-Tudela, E. del Valle, E. Cancellieri, C. Tejedor, D. Sanvitto, and F. Laussy, “Effect of pure dephasing on the jaynes-cummings nonlinearities,” Opt. Express **18**, 7002–7009 (2010).

[325] “Digital library of mathematical functions,” [https://dlmf.nist.gov/14.3, 16 October 2018].

[326] J. Wilkie and Y. M. Wong, “A linearly scaling grid method for generalized langevin and other integrodifferential equations,” J. Phys. A: Math. Theor. **41**, 335005 (2008).

[327] P. Rabl, “Cooling of mechanical motion with a two-level system: The high-temperature regime,” Phys. Rev. B **82**, 165320 (2010).